ABSTRACT

Title of Document: THE TECTONICS OF INTRAPLATE REGIONS: QUANTIFYING STRESS AND SURFACE DEFORMATION IN THE CENTRAL AND EASTERN U.S. AND PLANETARY ANALOGS ON MERCURY AND THE MOON

Lisa Schleicher Walsh
Doctor of Philosophy, 2013

Dissertation Directed By: Assistant Professor Aaron Martin and Associate Professor Laurent Montési, Department of Geology

Occurring ~ 1 year apart, the magnitude 3.4 Germantown, Maryland, (16 July 2010) and magnitude 5.8 Mineral, Virginia, (23 August 2011) earthquakes rocked the U.S. national capital region, drawing renewed attention to the occurrence of seismicity within continental interiors. While the majority of earthquakes concentrate at tectonic plate boundaries, the processes that promote spatially diffuse zones of seismicity in intraplate regions are not well understood. The Mineral earthquake was one of the largest earthquakes to occur east of the Rocky Mountains in the past century and offers a rare opportunity to examine the role of stress transfer, long-distance triggering, and aftershock decay within an intraplate region.

Stress transfer from the Mineral and Germantown earthquakes relieved stress on the majority of Cenozoic faults in the Mid-Atlantic region, moving these faults

further away from future failure. The Everona fault and southern portion of the Mountain Run fault zone were the only locations (except in the aftershock region) that were loaded from the Mineral earthquake, although by only ~1 mbar. Accumulation of stress over time is required in order to significantly affect regional seismicity.

There is no evidence of remote triggering due to the passage of seismic waves in any of the major seismic zones in the central and eastern U.S. However, the slow decay rate of aftershocks suggests seismicity in the epicentral region might continue for a decade or longer. Aftershocks triggered by stress imparted by the mainshock imply that Coulomb stress transfer plays an important role in earthquake triggering processes within intraplate regions. Processes in the aftershock zone likely have the greatest influence on seismic hazard.

New imagery and altimetry data returned from the MErcury Surface, Space ENvironment, GEochemistry, and Ranging (MESSENGER) and Lunar Reconnaissance Orbiter (LRO) spacecraft provide new insight into processes driving intraplate tectonic deformation. Mercurian wrinkle ridges are ~2.2 larger in mean relief than wrinkle ridges on the Moon, suggesting a larger component of global contraction on Mercury. Patterns of faulting on Mercury and the Moon, as well as in the central and eastern U.S., indicate that intraplate seismicity can concentrate in zones of pre-existing weakness and spatially migrate.

THE TECTONICS OF INTRAPLATE REGIONS: QUANTIFYING STRESS AND SURFACE DEFORMATION IN THE CENTRAL AND EASTERN U.S. AND PLANETARY ANALOGS ON MERCURY AND THE MOON

By

Lisa Schleicher Walsh

Dissertation submitted to the Faculty of the Graduate School of the
University of Maryland, College Park, in partial fulfillment
of the requirements for the degree of
Doctor of Philosophy
2013

Advisory Committee:
Assistant Professor Aaron J. Martin, Chair
Associate Professor Laurent G.J. Montési, Co-Chair
Assistant Professor Vedran Lekic
Thomas R. Watters (Smithsonian Institution)
Jeanne Sauber (NASA-GSFC)
Martha Geores (Dean's Representative)

Dedication

I dedicate this research to my family, who always encouraged and supported me in everything I have chosen to work on in my life. In particular, I dedicate this dissertation to my husband, Ben, who has been there for me through both the highs and the lows of every aspect of this research and always welcomed listening to the details of my ideas even though they were sometimes abstract and outside his field of expertise. The countless hikes, dinners, and other adventures he planned for us throughout this process have helped me stay sane and maintain enthusiasm for my research. Ben is truly the love of my life, and I owe him a great deal of debt and gratitude for being there for me throughout the dissertation process.

My original interest in geology was spurred by fossil collecting trips I went on in Texas with my family as part of the paleontology group of the Houston Gem and Mineral Society. While my interests changed over time, I have always maintained an enthusiasm for the great outdoors and understanding the Earth. This work would not have been possible without the support from my Mom and my Dad, who each have always inspired me to always pursue my interests. My Dad taught me over the phone how to work in a Linux computing environment, which has been invaluable for working with planetary data and running geophysical models. My Mom has always been willing to help me edit my papers and presentations and keeps me up to date on the latest world geologic hazard which has maintained my excitement for working on research related to mitigating natural disasters. My sister, Jennifer, and my aunt, Mimi, always remind me to view my work from an artistic perspective, which has undoubtedly helped me craft illuminating maps and figures for my research. I also

want to thank my stepmother, Carol, mother and father in-law, Steve and Kathy, brother in-law, Andrew, adopted grandparents, Barbara, Dot, and Harry, and all other members of my family that have supported me during my dissertation research. This research is also devoted to my Oma and Opa, Patty and Hans Schleicher, Grandma and Grandpa, Martha and Harold Whisenhunt, and Aunt Sue, who, though they are no longer with us, continue to inspire me to always do my best, work hard, and make a difference in the world. Without the unwavering support of my family, I would not be where I am today.

I also dedicate this work towards the broader goal of improving our ability to understand earthquake and faulting processes, particularly in intraplate regions and on other planets where plate tectonics cannot explain tectonic deformation. My personal goal for this research has been to work on problems that help advance our ability to mitigate seismic hazards. I hope that this work will allow us to move one step closer towards reducing the loss of life and property from future earthquakes.

Finally, I include the following quote in tribute to the August 23, 2011 M_w 5.8 Mineral, VA, earthquake which occurred during the course of this dissertation and thus became a major focus of my research:

"I was awakened by a tremendous earthquake, and though I hadn't ever before enjoyed a storm of this sort, the strange thrilling motion could not be mistaken, and I ran out of my cabin, both glad and frightened, shouting "A noble earthquake! A noble earthquake feeling sure I was going to learn something."

- John Muir (The Wild Muir: Twenty-Two of John Muir's Great Adventures)

Acknowledgements

Most of all I would like to thank my adviser, Aaron Martin, who has guided my research since I arrived at the University of Maryland and started graduate school, first for my master's thesis research and now through each of the projects contained in this dissertation for my Ph.D. His continued dedication to improving our understanding of tectonic processes, and willingness to try new methods, techniques, and ideas has been an unwavering source of encouragement and motivation that enabled me to complete these projects. Our regular scientific discussions on a variety of topics for each project have inspired many aspects of the work presented in this dissertation. I also greatly appreciate the time and effort he has taken to help me improve my writing skills and move papers from my research towards publication. In particular, Aaron helped me learn about the geologic history that formed the Appalachians and inspired me to begin the search for recently active faults in the Mid-Atlantic region. He has also provided great insight into evaluating statistical significance for both my seismicity rate change analysis and study of tectonic features on Mercury and the Moon.

I also thank Laurent Montési who introduced me to the hypothesis of Coulomb stress transfer. Laurent stepped in as my co-adviser and has provided me with a great deal of advice relating to numerical modeling, programming, and statistical analysis that was essential to complete this research. I greatly appreciate the many meetings and discussions we had and his comments throughout each project's evolution. His effort to help me learn how to create models of Coulomb stress transfer from earthquakes in response to the Germantown earthquake prepared

me to rapidly produce models of stress transferred by the Mineral earthquake, which enabled me to participate in the active research and reconnaissance immediately following the Mineral earthquake.

I owe a great deal of gratitude to Tom Watters, who acted as my adviser at the Smithsonian Institution and provided me with the unique opportunity to study tectonic features on Mercury and the Moon at the Center for Earth and Planetary Studies (CEPS). The chance to work with new global imagery and altimetry datasets for Mercury and the Moon recently returned from the MESSENGER and LRO spacecraft has been very exciting and invaluable towards advancing my understanding of tectonic processes and a variety of useful techniques including image processing and rectification, IDL programming, numerical modeling, and mapping of tectonic features in GIS. I also thank Maria Banks who taught me in particular how to work with imagery from the Lunar Reconnaissance Orbiter Camera and continues to inspire me to explore ideas in the field of planetary tectonics. I also greatly appreciate the thoughtful discussions I had with Michelle Selvans relating to tectonic processes on Mercury. Sean Solomon, Christian Klimczak, Paul Byrne, Nathan Williams, Drew Enns, Lillian Ostrach, Keith Bennett, Brett Denevi and other members of the LROC and MESSENGER science teams have also contributed and provided great insight into my analysis of wrinkle ridges on Mercury and the Moon. I am especially grateful to Ramsey Gorchev and Bill Sneed who helped me get ISIS, IDL, and other advanced computer software running on the computers in CEPS; Rose Aiello and Laurenda Patterson for helping me deal with logistical issues; and all the other members of CEPS for their thoughtful discussions relating to planetary geology.

I thank Jeanne Sauber who helped me understand the basic science behind locating earthquakes and resolving earthquake focal mechanisms immediately following the occurrence of the Germantown earthquake and the fundamentals of Light Detection and Radar (LiDAR). Jeanne also introduced to me the idea of comparing the aftershock decay from the Mineral earthquake to the aftershock decay sequences produced by the Whittier Narrows and Kettleman Hills earthquakes of California. I also thank Vedran Lekic for joining my committee which provided me with a seismologist's perspective on my research. In particular, Ved helped me perform the Fourier Transform on the seismicity rate timeseries data from the New Madrid Seismic Zone and has given me insight into basic characterization of seismic catalogs such as the magnitude of completeness. I also thank the Dean's Representative, Martha Geores, from the Department of Geographical Sciences for expressing interest in my research and joining my committee.

I thank Karen Prestegaard for the thoughtful discussions we have shared regarding many aspects of my research, particularly relating to tectonic geomorphology and benchmark re-leveling. I also thank Diane Doser, professor at the University of El Paso, who served as my external mentor through the MentorNet program and provided great insight into research, teaching, and the dissertation process. Mike Evans, Wenlu Zhu, other members of the Geology Department faculty, the Geodynamics Research Group, Naijuin Zhou, and Ralph Dubayah in the Department of Geographical Sciences have also aided in various aspects of this research.

Several geoscientists involved in active research relating the Mineral and Germantown earthquakes have also contributed to my research. I thank Gisela Viegas Fernandes, Won-Young Kim, and Robert Herrmann for providing detailed information on the location and focal mechanisms for these earthquakes and Dave Prowell and Andy Bobyarchick for discussing in detail the geology of the study area and sharing unpublished fault maps. I would like to thank Mark Carter, Jeff Munsey, Martin Chapman, and Alena Leeds for allowing me to participate in the search for liquefaction features and ruptures and installation of a temporary seismic station in response to the Mineral earthquake. Won-Young Kim, Wayne Newell, Scott Southworth, Ross Stein, Jian Lin, Helaine Walsh Markewich, Seth Stein, Tish Tuttle, Oliver Boyd, Erica Emry, Diane Doser, Rich Briggs, Ryan Gold, Dan Clark, and John Ebel each provided valuable discussions and feedback in regard to my research related to the Mineral earthquake. In addition, I greatly appreciate collaborating with Fred Pollitz at the U.S. Geological Survey who produced the model of the dynamic shear strain created by the passage of seismic waves from the Mineral earthquake; Wright Horton, for sharing his delineation of aftershock-defined fault zones, and Daniel McNamara, for sharing his relocated aftershock database with me before publication; and Robert Williams and Wright Horton for providing me access to the recently collected LIDAR database for the epicentral region of the Mineral earthquake.

I also thank Bob Anderson, Dave Fenster, Stephanie Devlin, Jim McCalpin, Kris McCandless, Steve Self, and Allen Fetter who provided me a perspective into opportunities to apply my research to seismic hazard evaluations and other aspects of

applied geology important for safe siting and operation of nuclear reactors and other critical facilities. I have also received thoughtful comments returned by reviewers and editors from submission of the manuscript in Chapter 2 to Seismological Research Letters, the Journal of Geophysical Research – Solid Earth, and the Bulletin of the Seismological Society of America.

I greatly appreciate the friendships I developed with (in alphabetical order by last name): Rick and Paula Arevalo, Jeremy Bellucci, Kate Burgy, Huan Cui, John-Luke and Jennifer Henriquez, Palma Jarboe, Tom and Rachel Ireland, Stephanie Johnston, Ryan Kerrigan, Xiaoming Liu, Adam Mansur, Kristen Miller, Tammy Newcomer, Sara Peek, Leigh Ann Roble, Miriam and Nick Sharp, Emily Seldomridge, Sarah Sillin, Rose Smith, Brian and Becca Tattich, and everyone else in the department. I would also like to extend thanks to the Geology Department support staff, including Sandy Romeo, Dorothy Brown, Jeanne Martin, Suzanne Martin, and Joanna Patterson for their support regarding a variety of logistical issues and their constant encouragement. I am also very grateful to Todd Karwoski for fixing my computer issues.

Funding for this project was provided by grant NSF- EAR09-11151 and the Smithsonian Institution, the Graduate School at the University of Maryland through the Ann G. Wylie Dissertation Fellowship, the Geology Department through a teaching fellowship, and the American Federation of Mineralogical Societies Scholarship Foundation. I was funded to present my research at national meetings and attend workshops by the following organizations: UNAVCO travel grant to the Geological Society of American annual meeting (2013), Eastern Section

Seismological Society of America Meeting Travel Grant (2011), University of Maryland Geology Department Alumni Funded Travel Grant (2011), Seismological Society of America Annual Meeting Travel Grant (2011), UNAVCO – GAMIT/GLOBK and DEFNODE Workshop Travel Grant (2010), and the Jacob K. Goldhaber Travel Award from the University of Maryland Graduate School (2009).

Table of Contents

List of Tables

List of Figures

Chapter 1: Introduction

1.1 Motivation

The majority of seismicity on Earth occurs along the boundaries between tectonic plates [*Wilson*, 1965]. Tectonic plate boundary zones concentrate seismicity and deformation in spatially narrow bands, and are readily identifiable from global topography by large-scale mountain belts and trenches (Figure 1-1). Recent large magnitude earthquakes along plate boundaries include the 2013 Solomon Islands earthquake (M_w = 8.0), the 2013 southeastern Alaska earthquake (USA, M_w = 7.5), the 2012 Queen Charlotte Islands earthquake (Canada, M_w = 7.7), the 2012 Nicoya Peninsula earthquake (Costa Rica, M_w = 7.6), the 2011 Tohoku earthquake (Japan, M_w = 9.0), the 2010 El Mayor – Cucapah earthquake (Baja California, Mexico, M_w = 7.2), and the 2010 Port-Au-Prince earthquake (Haiti, M_w = 7.0).

Although less common, large and destructive earthquakes have been recorded within the interiors of tectonic plates far from plate boundary zones [*Schulte and Mooney*, 2005]. Intraplate seismicity has been recorded in stable continental regions (beyond passive margins) of North America, South America, Eurasia (subdivided into Europe, west of 20°E, and Russia, east of 20°E), Africa (including the Arabian Peninsula), India, China, and Australia [*Schulte and Mooney*, 2005; *Wang*, 2007; *Assumpcao et al.*, 2011; *Holford et al.*, 2011] (Figure 1-1). Notable earthquakes in these intraplate regions include the 1811 – 1812 New Madrid earthquakes along the Mississippi River (Central U.S., M 7.0 to 7.4), the 1886 Charleston, South Carolina earthquake (USA, M_w 7.3), the 1929 Grand Banks and 1933 Baffin Bay earthquakes

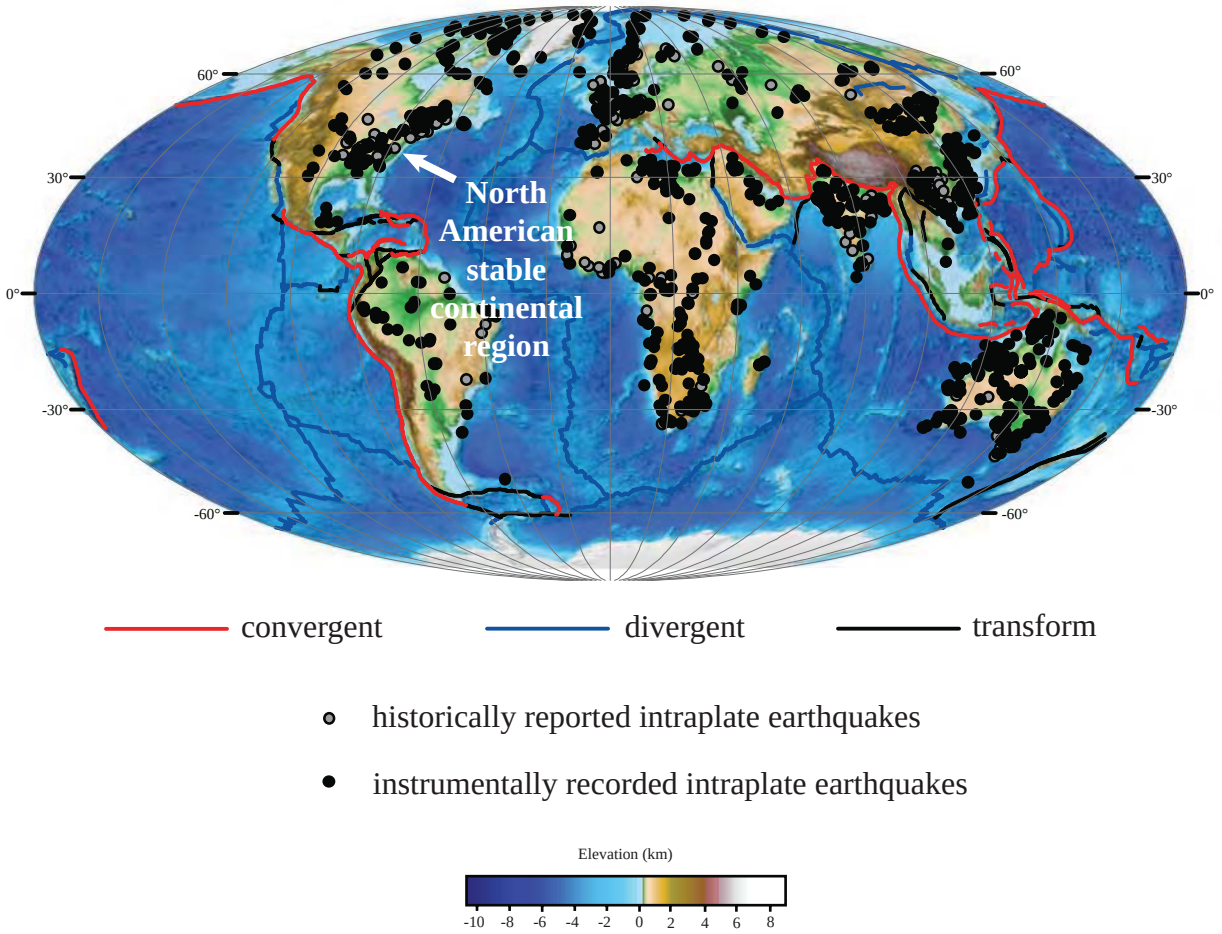

Figure 1-1. Global intraplate seismicity
Map of intraplate earthquakes occurring in stable continental regions [*Schulte and Mooney*, 2005] 2005), tectonic plate boundaries [*Coffin et al.*, 1998], and global topography and bathymetry [*Amante and Eakins*, 2009]. The North American stable continental region is the site of the Mineral and Germantown earthquakes.

(Eastern Canada, M_w =7.2 and M_w =7.4), the 1988 Tennant Creek earthquake sequence (Northern Territory, Australia, M_w 6.3 to 6.7), the 2001 Bhuj and 2011 Talala earthquakes (India, M_w = 7.2), and the 2008 Sao Vicente earthquake (Brazil, M_b = 5.2) [*Bowman et al.*, 1990; *Bent*, 1994; *Ebel et al.*, 2000; *Assumpcao et al.*, 2011; *Holford et al.*, 2011; *Rastogi et al.*, 2013a; *Rastogi et al.*, 2013b; *Stein et al.*, 1979]. On July 16, 2010, a M_w 3.4 earthquake struck near the town of Germantown, Maryland, and was followed ~1 year later by a M_w 5.8 earthquake near Mineral, Virginia within the North American continental plate interior in the central and eastern U.S. (Figure 1-2). Shaking from these earthquakes in the Washington, DC, metropolitan region and the surrounding area (and damage from the Mineral earthquake) rekindled concern for intraplate seismicity and highlighted our limited understanding of seismicity in stable continental regions.

1.1.1 The Mineral and Germantown earthquakes

The Mineral earthquake was one of the largest earthquakes to occur east of the Rocky Mountains in the past century [*Bollinger and Hopper*, 1971; *Kim and Chapman*, 2005] and offers a rare opportunity to examine the role of static stress transfer, long-distance triggering, and aftershock decay from a moderate magnitude intraplate event. The Germantown earthquake provides a chance to study stress transfer from a smaller magnitude earthquake that happened only ~1 year prior to the Mineral earthquake. Chapters 2 and 3 of this dissertation focus on understanding earthquake triggering in intraplate North America by focusing on the Mineral and Germantown earthquakes. Chapter 2 discusses not only stress transfer but also the tectonic framework of the Mineral and Germantown earthquakes. Chapter 3 presents

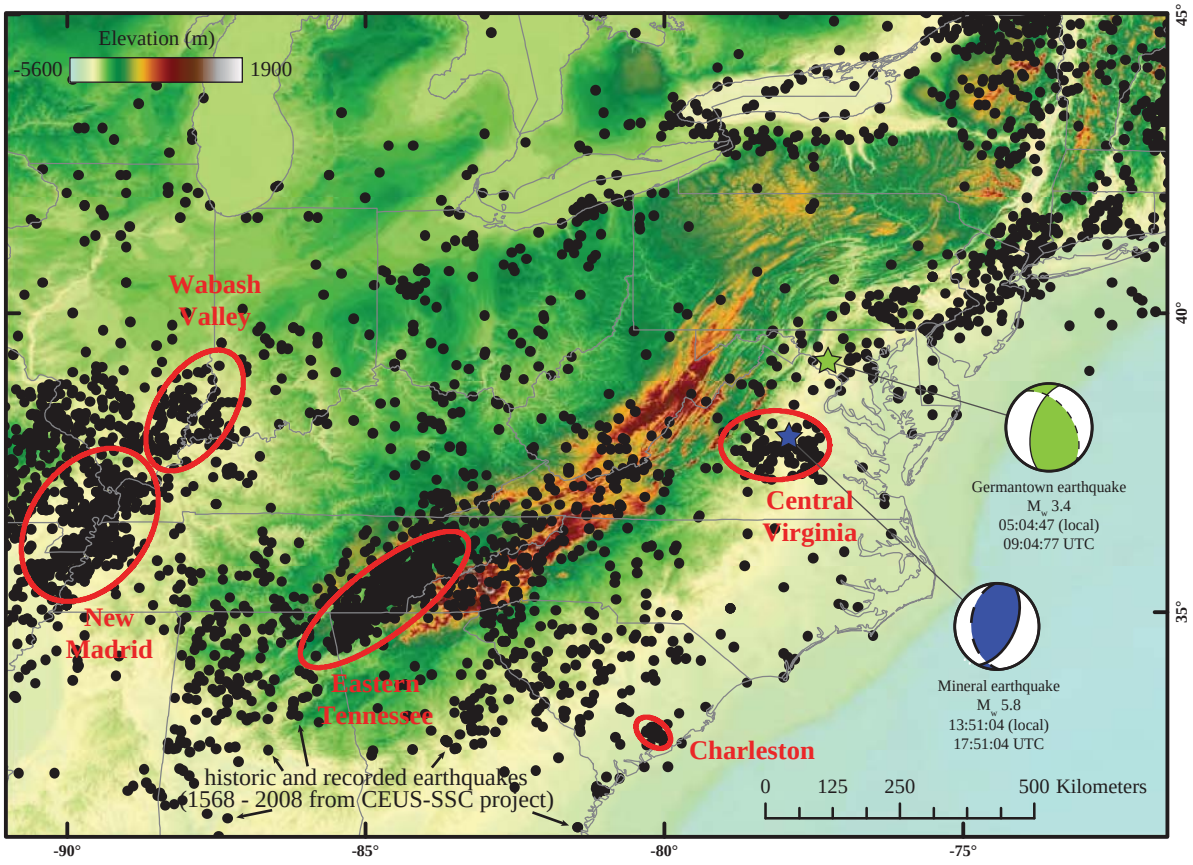

Figure 1-2: Location of Germantown and Mineral earthquakes

Locations and focal mechanisms for the Germantown and Mineral earthquake (Saint Louis University and the U.S. Geological Survey). Red ellipses shown major seismic zones in the central and eastern U.S. [*Bisrat et al.*, 2012; *Braile et al.*, 1982; *Csontos and Van Arsdale*, 2008; *Dunn and Chapman*, 2006; *Hildenbrand and Ravat*, 1997; *Kelson et al.*, 1996; *Kim and Chapman*, 2005; *Madabhushi and Talwani*, 1993; *Mazzotti and Townend*, 2010]. Historic and recorded earthquakes (all magnitudes) are from the CEUS-SSC Earthquake Catalog Compilation (http://www.ceus-ssc.com). Topography is from the CEUS-SCC Project basemap database and was created by the British Oceanographic Data Centre (BODC) General Bathymetric Chart of the Oceans (GEBCO) [2008] and has a spatial resolution of 30-arc-seconds. Boundaries are from the North American Atlas - Political Boundaries jointly compiled by the Government of Canada, USGS, and Instituto Nacional de Estadistica y Geografia [2010]. Geographic Coordinate System: WGS 1983. Projection: Datum WGS 1983.

an examination of seismicity rate changes in the near-field and the far-field associated with the Mineral earthquake.

In Chapter 2, I first compile an in-depth literature review of Cenozoic faulting, historical seismicity, and the geologic history of the Mid-Atlantic region in order to establish the tectonic framework for the Mineral and Germantown earthquakes. I then employ the orientations of fault systems active during the Cenozoic, notably the DC fault zone (Figure 1-3), Stafford fault system, Mountain Run fault zone, and Everona fault, to evaluate to what extent slip from the Mineral and Germantown earthquakes may have increased the risk of future failure on these or similarly oriented fault systems by calculating Coulomb failure stress change. I also quantify Coulomb failure stress changes on Paleozoic and Mesozoic faults in the epicentral region and assess the spatial relationships between the mainshock and its aftershocks with these pre-existing geologic structures. In addition, I present a numerical model that estimates the maximum amount of permanent vertical surface deformation expected from the Mineral earthquake (~9 cm).

The research presented in Chapter 3 statistically evaluated changes in the near-field, the aftershock zone, and the far-field, thousands of kilometers from the epicenter of the Mineral earthquake. In the near-field I evaluate the spatial and temporal distribution of aftershocks, while in the far-field I assess if there is any increase in the rate of seismicity related to the passage of seismic waves. The results in this chapter indicate that the aftershock decay sequence from the Mineral earthquake is occurring at a much slower rate than the 1985 Kettleman Hills and 1987 Whittier Narrows earthquakes in California which have similar magnitudes, focal

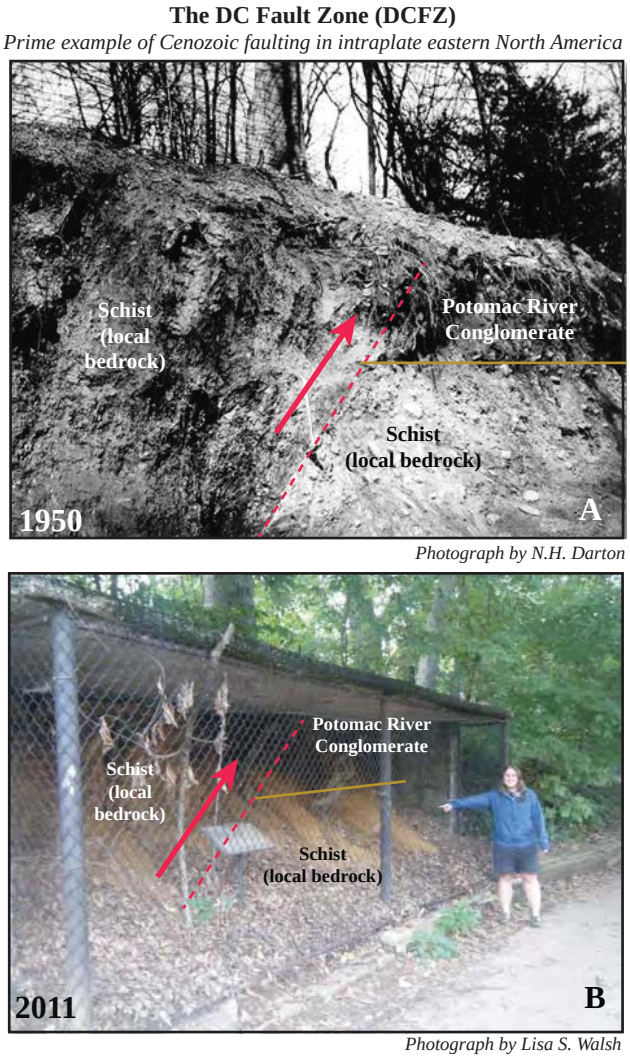

Figure 1-3. Photographs of the DC Fault Zone
Photographs taken in 1950 [*Darton*, 1950] (A) and 2011 (B) of outcrop of the DC fault zone located near the National Zoological Park at Clydesdale Place NW and Adams Mill Rd. NW in Washington, DC. The outcrop was first identified by N.H. Darton of the United States Geological Survey who cited it as a prime example of late-Cenozoic faulting in eastern North America and placed a cage around it to preserve it. The fault places conglomerates deposited by the ancestral Potomac River on schist, the local bedrock. Annotations added to both photos for clarification. The trace of the DC fault zone has been extended by a series of en echelon faults to the southeast of this outcrop from identification of the fault in drill cores extracted from Lafayette Square located immediately north of the White House. In Chapter 2, I evaluate the stress change on the DC fault zone resulting from the Mineral and Germantown earthquake.

mechanisms and depth. In the far-field, there appears to be no detectable signals of triggering at remote distances associated with the passage of seismic waves from the Mineral earthquake.

1.1.2 Tectonics on Mercury and the Moon

The surfaces of Mercury and the Moon exhibit no signatures of plate tectonics and are thus considered to be one-plate bodies. However, the presence of broadly distributed contractional landforms across their surfaces indicates that tectonic deformation occurred on both bodies (Figure 1-4). In general, loading or global radial contraction due to cooling are the primary processes driving tectonic deformation on Mercury and the Moon. Examining tectonic features on the surfaces of Mercury and the Moon, regions of intraplate deformation, may offer an analog for understanding tectonic deformation occurring in the central and eastern U.S. within the continental interior of North America.

On 18 March 2011 the MErcury Surface, Space ENvironment, GEochemistry, and Ranging (MESSENGER) spacecraft transitioned from orbiting the Sun to become the first spacecraft to orbit Mercury. Meanwhile, the Lunar Reconnaissance Orbiter (LRO) has been orbiting the Moon since 2009, compiling a database of high-resolution images and altimetry of the lunar surface. MESSENGER's orbital phase returned new images and altimetry of Mercury's northern hemisphere, where broad expanses of smooth plains material were deformed by wrinkle ridges, contractional tectonic features formed by thrust faulting and folding [*Watters and Johnston*, 2010; *Watters and Nimmo*, 2010; *Head et al*., 2011]. Data from MESSENGER's flybys and

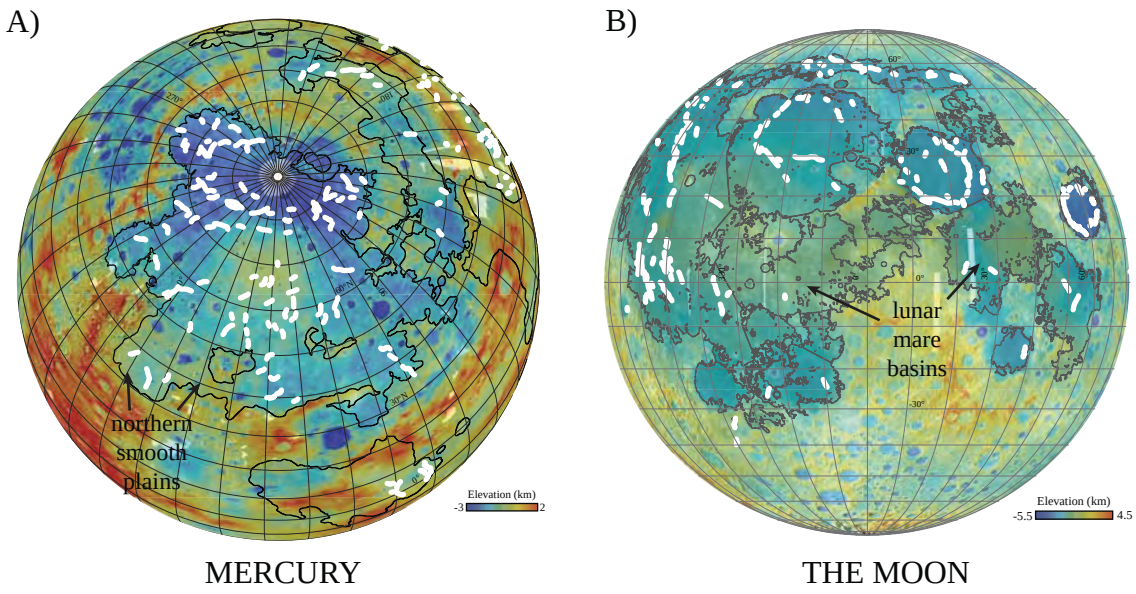

Figure 1-4. Wrinkle ridges on Mercury and the Moon
Wrinkle ridges (white lines) in A) the northern smooth plains (black line) of Mercury overlaid on a 500 m/pixel global monochrome mosaic and a MLA derived-DEM global mosaic [*Hawkins et al.*, 2007; *Zuber et al.*, 2012] (orthographic projection center latitude = 66.87°N, center longitude = 43°E) and B) the mare basins (black line) on the Moon overlaid on a 100 m/pixel global monochrome mosaic and 100 m/pixel DEM derived from stereo photogrammetric analysis of WAC images [*Robinson et al.*, 2010; *Scholten et al.*, 2012] (orthographic projection center latitude = 0°, center longitude = 0°). Red shades are high elevation and blue shades are low elevation. Mercury smooth plains boundary from Denevi et al. [2012] and mare basins boundary digitized by Steven Koeber.

orbital phase, together with earlier observations of Mercury by the Mariner 10 spacecraft, now provide a near-global look at the planet, indicating that smooth plains cover about 27% of Mercury's surface [*Solomon et al.*, 2008; *Denevi et al.*, 2009; *Watters et al.*, 2009c; *McNutt et al.*, 2010; *Denevi et al.*, 2012]. High-incidence angle (55–75°) images returned during MESSENGER's and LRO's orbital phases enable us to produce more comprehensive global tectonic maps. High-resolution images and altimetric data from MESSENGER and LRO offer an unprecedented opportunity to compare quantitatively the morphology of newly detected wrinkle ridges on Mercury with previously identified wrinkle ridges on the Moon [*Maxwell et al.*, 1975; *Watters*, 1988; *Strom*, 1970; *Solomon et al.*, 2008].

I use these datasets to characterize the length–relief relationships that define the morphology of wrinkle ridges on the Moon and Mercury, and then resolve the relative contributions of subsidence and global contraction to shortening on Mercury and the Moon. Most wrinkle ridges on Mercury are ~2.2 times higher than those on the Moon, suggesting a larger component of global contraction on Mercury. I then extend my observations of the patterns of faulting on Mercury and the Moon to the central and eastern U.S., site of the Mineral earthquake, in the synthesis (Chapter 5).

1.2 Importance

This research aims to advance our understanding of seismic activity in intraplate regions by focusing on the following topics:

1. **Cenozoic faulting in the Mid-Atlantic region:** Establish a geologic context for the July 2010 Germantown and August 2011 Mineral earthquakes by

compiling a literature review of neotectonic features in the Mid-Atlantic regions as well as geologic history of the region.

2. **Role of static stress transfer in earthquake triggering:** Determine if aftershocks occurred within the stress trigger zone produced by the Mineral earthquake and if nearby Cenozoic faults were moved closer to failure by the Mineral earthquake.
3. **Influence of the passage of seismic waves on the regional stress field:** Evaluate if seismic waves generated by the Mineral earthquake triggered seismicity at remote locations (spanning thousands of kilometers from the earthquake's epicenter), particularly in nearby seismic zones.
4. **Crustal properties of intraplate regions:** Compare the aftershock decay rate of events following the Mineral earthquake to the decay rate of aftershocks from the 1985 Kettleman Hills and 1987 Whittier Narrows earthquakes to evaluate if differences in the geologic environment affects aftershock triggering rate.
5. **Patterns of faulting and mechanisms driving intraplate faulting:** Examine tectonic deformation on Mercury and the Moon as an analog for deciphering factors that contribute to generating broad, spatially diffuse zones of seismicity.

1.3 Broader Impacts

Even though intraplate regions produce only 0.2% of Earth's seismic moment release [*McPherson et al.*, 2012], large, damaging earthquakes occur in intraplate

environments and cause loss of life and property. The Charleston earthquake killed 60 people and caused $6 million in property damage (1886 dollars; $146 million in 2012 dollars) [*Dutton*, 1889; *Schmidtlein et al.*, 2011]. The Mineral earthquake caused extensive damage to the Washington Monument and National Cathedral, and over $80 million in property damage in the epicentral region. Densely populated metropolitan regions and the concentration of nuclear power reactors in the central and eastern U.S. (CEUS) increase the possible loss of life and property from a large, destructive earthquake in intraplate North America, meriting the need to improve our understanding of seismic hazard in intraplate regions [*Braile et al.*, 1986; *Zoback*, 1992; *Wang*, 2007].

1.4 Dissertation Structure and Content

This dissertation is divided into five chapters. The purpose of the first chapter (this chapter) is to highlight the motivation behind the overall research in this dissertation and the questions addressed in each chapter. Three scientific papers form the core of the dissertation and each is included as a separate chapter (Chapters 2 through 4). The final chapter is a synopsis that provides a summary of the results from each of the core chapters.

The research questions, methods, and results in each chapter are discussed independently from the other chapters. I have written the core chapters in a manner that allows each chapter to be read and understood on its own.

1.5 Peer-reviewed publications expected from this research

Chapters 2, 3, and 4 are in various stages of the peer-review process. A version of Chapter 2, "Tectonic framework of the August 2011 Mineral Virginia and July 2010 Germantown Maryland earthquakes" with co-authors Laurent Montési and Aaron Martin, has been returned from review from the Bulletin of the Seismological Society of America. A revised version of this manuscript is presented in this dissertation and will be submitted to a Geological Society of America Special Book entitled "The August 23, 2011 Earthquake in Central Virginia and its Significances for Seismic Hazards in Eastern North America" with editors Wright Horton, Martin Chapman, and Russell Green. A version of chapter 4, "Wrinkle ridges on Mercury versus the Moon: Morphometric Characterization, elastic dislocation modeling, and tectonic evaluation of planetary contraction with co-authors Thomas Watters, Maria Banks, Sean Solomon, and Aaron Martin is pending submission to the Journal of Geophysical Research – Planets. I also plan to submit a version of Chapter 3, "Seismicity rate changes in the near-field and far-field from the August 2011 M_w 5.8 Mineral Virginia earthquake" for peer-reviewed publication.

Chapter 2: Tectonic framework and numerical modeling of the August 2011 Mineral, Virginia, and July 2010 Germantown, Maryland, earthquakes

2.1 Abstract

Occurring only 13 months apart, the magnitude 3.4 Germantown, MD, (16 July 2010) and magnitude 5.8 Mineral, VA, (23 August 2011) earthquakes rocked the U.S. national capital region, drawing renewed attention to the occurrence of intraplate seismicity in the Mid-Atlantic region in the eastern United States. I establish a reference for future research on the Mineral earthquake and intraplate seismicity of the eastern U.S. by: (1) Highlighting zones of relatively recent tectonic activity through a discussion of fault zones of the Mid-Atlantic region active during the Cenozoic, notably the DC fault zone (DCFZ), Stafford fault system (SFS), Mountain Run fault zone (MRFZ), and Everona fault (EF); (2) Assessing the spatial relationships between the mainshock and its aftershocks and pre-existing geologic structures in the epicentral region; (3) Calculating the amount of permanent vertical surface deformation expected from the Mineral earthquake; and (4) Evaluating to what extent slip from the Mineral and Germantown earthquakes may have increased the risk of future failure on the DCFZ, SFS, MRFZ, and EF by calculating Coulomb failure stress (σ_{CF}) change. The Mineral earthquake likely ruptured on a new fault, rather than a pre-existing Paleozoic or Mesozoic fault system and is expected to have generated a maximum of ~9 cm of permanent upward vertical surface deformation. In general, the Mineral earthquake brought the pre-existing Cenozoic faults further

from failure. The Mineral earthquake loaded only the EF and the southern portion of the MRFZ; the magnitude of the loading was very small and very unlikely to affect changes in the occurrence of earthquakes.

2.2 Introduction

At 5:04 local time (09:04:47 UTC) on 16 July 2010 the U.S. national capital region was awoken by a M_w 3.4 earthquake that ruptured approximately 35 km northwest of Washington, DC, between Germantown, Maryland, and Sugarloaf Mountain. Only 13 months later, at 13:51 local time (17:51:04 UTC) on 23 August 2011, the nation's capital was shaken again by the larger M_w 5.8 earthquake that ruptured approximately 135 km southwest of DC near the town of Mineral in Louisa County, Virginia (Figure 2-1). The Mineral earthquake occurred in the Central Virginia Seismic Zone (CVSZ), an east-west trending cluster of historic seismicity extending from Richmond to Lynchburg, Virginia [*Kim and Chapman*, 2005; *Petersen et al.*, 2008] (Figure 2-2). The Mineral earthquake, along with a M_w 5.8 earthquake centered on the New York-Ontario border in 1944, were the largest earthquakes in the U.S. east of the Rocky Mountains in more than a century. Ground motion from the Mineral earthquake was felt as far west as Minnesota and from Florida to Fredericton, New Brunswick, Canada [*Hough*, 2012b], over a much wider region than most western U.S. earthquakes of a similar magnitude (Figure 2-3). The occurrence of the Mineral and Germantown earthquakes rekindled concern about our rather poor understanding of intraplate seismicity and offers an opportunity to

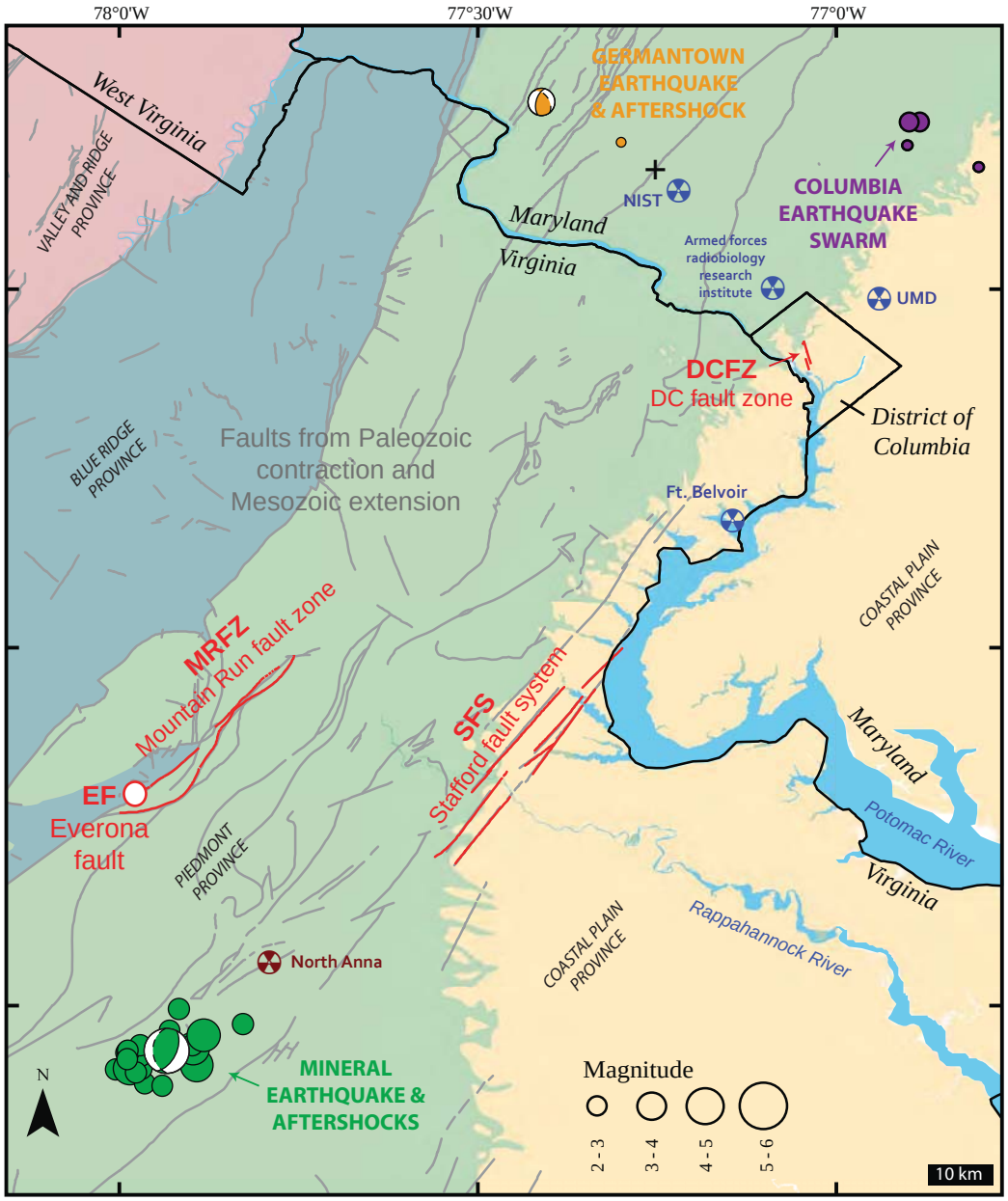

Figure 2-1. Locations of the Mineral and Germantown earthquakes
Focal mechanisms and epicenters of the Mineral and Germantown earthquakes, their aftershocks, and the Columbia earthquake swarm (circles) in relation to ancient faults from Paleozoic contraction and Mesozoic extension, younger fault zones active during the Cenozoic (red lines), and geologic provinces in the national capital region. The epicenter of the Germantown earthquake originally located by the USGS (plus) was relocated ~20 km northeast by Lamont-Doherty Earth Observatory at Columbia University. The locations of the earthquakes in the Columbia earthquake swarm are from the USGS National Earthquake Information Center catalog. The location of the Mineral earthquake's mainshock and aftershocks (> M_w 2.0) were provided the Saint Louis University Earthquake Center. Nuclear reactors used both for research and power generation are indicated by the nuclear symbol [*Fenneman and Johnson*, 1946; *Mixon and Newell*, 1977; *Prowell*, 1988; 2010; *Johnson*, 1999; *Davis et al*., 2001; *Southworth et al*., 2002; 2007]. Geographic Coordinate System: WGS 1984. Projection: Datum WGS 1984.

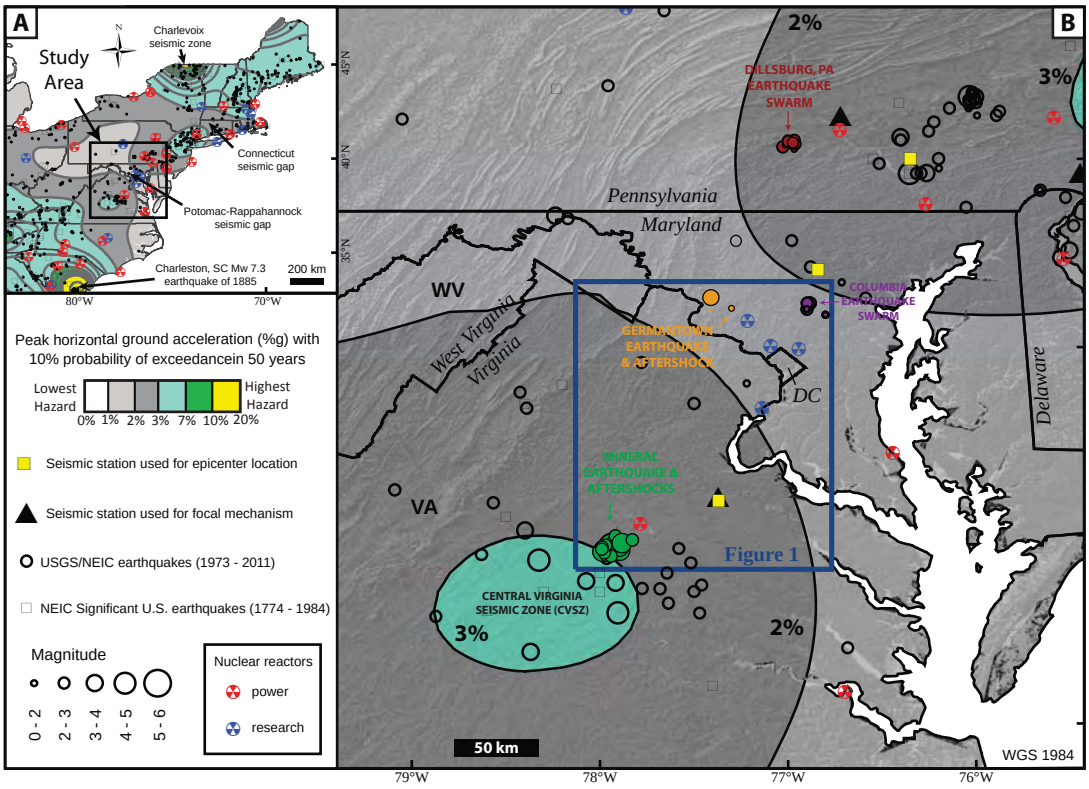

Figure 2-2. Seismic hazard map for the Mid-Atlantic region
A) USGS probabilistic seismic hazard map for the northern Atlantic coast of the United States and nearby regions [*Petersen et al.*, 2008]. Seismic hazard contours indicate 10% probability of exceedance of peak horizontal ground acceleration (%g) on a uniform firm rock site (760 m/s shear-wave velocity in the upper 30 m of the crust) in 50 years. B) Zoom in on the Mid-Atlantic region. Note that the Germantown earthquake occurred in a gap in the seismic hazard map. By contrast, the Mineral earthquake occurred in a zone of moderately high seismic hazard near the CVSZ. Geographic Coordinate System: WGS 1984. Projection: Datum WGS 1984. Location and magnitude of earthquakes on this map were obtained from the USGS National Earthquake Information Center, Saint Louis University Earthquake Center, and Lamont-Doherty Earth Observatory at Columbia University (Appendix 2-A).

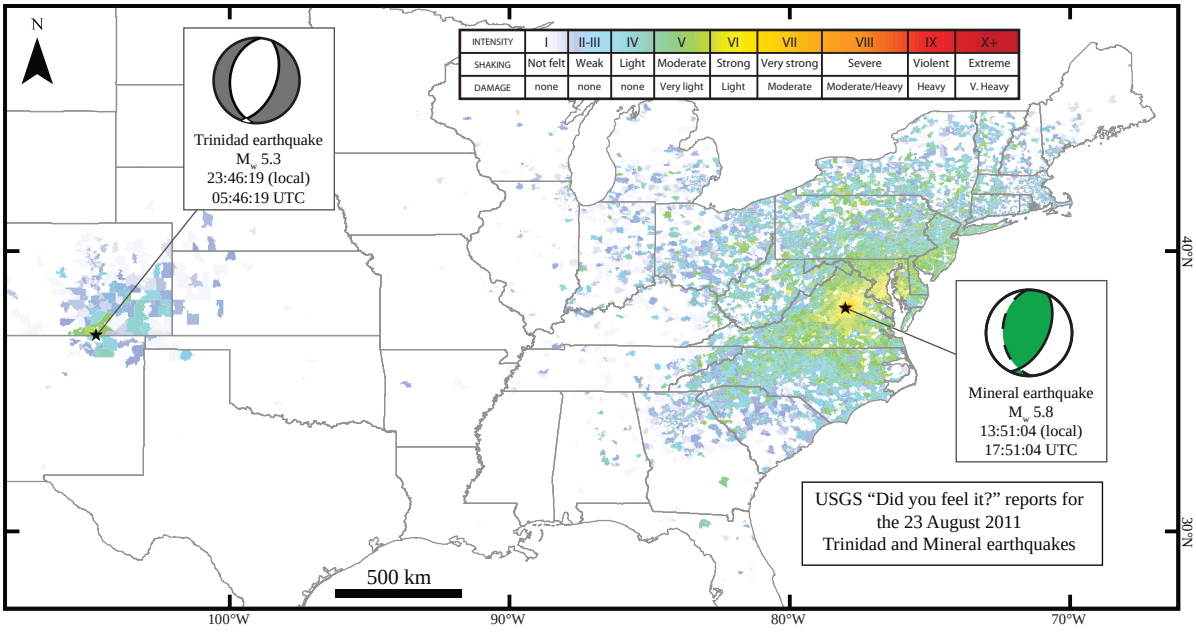

Figure 2-3. Shaking intensity from the Mineral, VA, versus the Trinidad, CO, earthquakes
Comparison of the USGS Community Internet Intensity maps for the August 23, 2011 M_w 5.8 Mineral, Virginia, and M_w 5.3 Trinidad, Colorado, earthquakes. Shaking from the Mineral earthquake was felt over a region at least three times larger than the Trinidad earthquake. Intensity is reported by zipcode was obtained from the USGS event pages from these earthquakes (Appendix 2-A). Earthquake times are in Coordinated Universal Time (UTC). Maximum intensity for the region surrounding the Mineral earthquake was VII and V for the Trinidad earthquake. Geographic Coordinate System: WGS 1984. Projection: Datum WGS 1984.

reevaluate seismic hazard in the Mid-Atlantic region of the eastern United States and intraplate environments in general.

Even though intraplate environments produce only 0.2% of Earth's seismic moment release [*McPherson et al.*, 2012], large damaging earthquakes occur in intraplate environments, causing loss of life and property [*Wilson*, 1965; *Braile et al.*, 1982; *Stein et al.*, 1979; 1989; *Zoback*, 1992; *Schulte and Mooney*, 2005; *Li et al.*, 2007; *Liu et al.*, 2011; *Wolin et al.*, 2012]. The Mineral and Germantown earthquakes occurred in the interior of the North American plate, far from plate boundaries. No damage was reported for the Germantown earthquake, however damage from the Mineral earthquake ranged from broken chimneys in the epicentral region to buildings in Washington, DC (Figure 2-4). The Mineral earthquake caused extensive damage to the Washington Monument and National Cathedral and over $80 million in property damage to schools, businesses, and homes in rural Louisa County [*National Park Service*, 2011; *Fenster and Walsh*, 2012]. Fortunately, no serious injuries or loss of life were reported from either earthquake. Ground motion exceeded safe operating parameters at the North Anna nuclear power reactor located ~18 km northeast of the Mineral epicenter, forcing an automatic shutdown [*Dominion Power*, 2011; *Fenster and Walsh*, 2012]. The large number of cities and nuclear reactors in the eastern U.S. increases the risk posed by future large-magnitude intraplate earthquakes (Figure 2-2).

Understanding the interaction of faults and associated seismicity is vital to improving evaluations of seismic hazard in intraplate environments [*Freed*, 2005; *Liu et al.*, 2011; *Wolin et al.*, 2012], which is important for (1) safe siting and operation of

Figure 2-4. Building damage caused by the Mineral earthquake
Photographs of building damage caused by the Mineral earthquake. No damage was reported after the Germantown earthquake. A and B) Chimneys were damaged in the town of Mineral, VA. C) A large crack in the top of the Washington Monument (Photographs by L.S. Walsh, except C, courtesy of the National Park Service).

nuclear power plants, (2) protecting national security, and (3) establishing mitigation strategies to reduce the loss of life and property during future intraplate earthquakes. In light of the Mineral earthquake, in this chapter I review our knowledge of recorded seismicity, paleotectonics, and neotectonics in the Mid-Atlantic region (Figure 2-2). I highlight zones of relatively recent tectonic activity in this region through a discussion of fault zones active during the Cenozoic, notably the DC fault zone (DCFZ), Stafford fault system (SFS), Mountain Run fault zone (MRFZ), and Everona fault (EF) and by determining how stress on each of these zones was affected by the Mineral earthquake. I intend this compilation of information to be used as a reference for further evaluation of the Mineral earthquake and more broadly for improving our understanding of intraplate seismicity.

2.3 Historical seismicity in the eastern United States

The Mineral earthquake was not the first occasion on which the national capital region experienced shaking from an earthquake. In 1828, President John Quincy Adams recorded in his diary an earthquake he experienced at the White House [*Adams*, 1828]. The location of this earthquake is unknown and it may have been quite distant from Washington, DC. Damaging earthquakes, particularly the Charleston, SC, M_w 7.3 earthquake of 1886 [*Dewey and Gordon*, 1984; *Talwani and Cox*, 1985; *Ebel*, 1986; *Nishenko*, 1990] and the 1811-1812 New Madrid Earthquake Sequence [*Nuttli*, 1987; *Li et al.*, 2007] have also struck the eastern U.S. and were felt in Washington, DC. The Charleston, SC, Mw 7.3 earthquake of 1886 killed 60 people and caused over $6 million (1886 dollars) in property damage [*Dutton*, 1889;

Schmidtlein et al., 2011]. No event of similar magnitude has been documented in the Mid-Atlantic region, but small or moderate earthquakes occur persistently. Larger earthquakes, like the 1933 Baffin Island M_s 7.3 event, are possible along the eastern margin of North America [*Stein et al.*, 1979; *Wolin et al.*, 2012]. At least ninety minor earthquakes have been recorded in the Mid-Atlantic region over the last 20 years (Figure 2-2B).

The Mineral earthquake was the largest to occur in the CVSZ. Before the Mineral earthquake, the magnitude 4.9 earthquake of 1875 was the largest recorded in the CVSZ [*Bollinger and Hopper*, 1971]. A sequence of magnitude 3.9 to 4.25 earthquakes that occurred in December 2003 were the most recent historical earthquakes ($M \geq 2.5$) recorded in the CVSZ [*Kim and Chapman*, 2005]. It is possible that the CVSZ, and the Mineral earthquake itself, reflect a long lived aftershock sequence initiated by a large magnitude prehistoric earthquake as was proposed for other intraplate seismic zones [*Li et al.*, 2007; *Stein and Liu*, 2009; *Wolin et al.*, 2012].

Swarms of small magnitude earthquakes (M_w 1.0 to 3.0) occurred in Columbia, MD, in 1993 and Dillsburg, PA from 2008 to 2009 [*Kim et al.*, 2009] (Figure 2-2). In addition, isolated events are scattered throughout the Mid-Atlantic region, including a M_w 2.5 earthquake that struck Manassas, VA, in May 2008 and the Germantown M_w 3.4 earthquake of July 2010. Only one M_w 2.1 aftershock was recorded 11 minutes after the Germantown earthquake (Figure 2-2A). Over 300 aftershocks were detected in the epicentral region of the Mineral earthquake by a

temporary seismic network deployed by several institutions between 23 August 2011 and 2 May 2012 (Appendix 2-A).

2.4 Seismic forecasting in intraplate regions

The short duration of the seismic record and paucity of sufficiently detailed geologic maps showing recently active Cenozoic faults make the evaluation of seismic hazard in intraplate regions challenging. Although the Mineral earthquake occurred in a previously identified zone of elevated seismic hazard [*Petersen et al.*, 2008], the CVSZ (Figure 2-2), the fault responsible for the earthquake was not identified prior to the event as being more likely to rupture than its neighbors.

A variety of mechanisms could be responsible for triggering intraplate seismicity in the Mid-Atlantic region [*Stein et al.*, 1989]: topographic relaxation of the Appalachians [*Ghosh et al.*, 2009], loading of water and sediments in the Chesapeake Bay and on the Atlantic margin [*Calais et al.*, 2010], isostatic uplift from melting of the Laurentide ice sheet from the last glacial maximum (12,000 years ago) [*Stewart et al.*, 2000; *Calais et al.*, 2006; *Sella et al.*, 2007], or ridge push generated by the cooling of the oceanic portion of the North American plate [*Zoback*, 1992].

Probabilistic Seismic Hazard Assessments (PSHA) have been calculated for the eastern U.S. by developing models of seismicity-derived hazard sources (tied to previously recorded seismicity), estimates of the maximum expected magnitude earthquakes on known faults, and models of ground shaking and attenuation [*Petersen et al.*, 2008]. Regions with high concentrations of previously recorded earthquakes, such as the CVSZ, the Charlevoix seismic zone of Quebec and northern

New York and the epicentral region of the 1885 Charleston earthquake stand out as high hazard zones on the USGS seismic hazard map (Figure 2-2). The Mineral earthquake was ~1 unit magnitude larger than previously recorded seismicity in the CVSZ that were used to make the PSHA maps for the eastern U.S. Therefore, PSHA in the Mid-Atlantic region needs to be revaluated.

The ground acceleration produced by the Mineral earthquake in the CVSZ was not wholly unexpected: Figure 2-2 indicates a 10% probability of Peak Ground Acceleration (PGA) exceeding 3% *g* in 50 years, where *g* is the acceleration due to gravity. By contrast, the Germantown earthquake occurred in a gap in the hazard map where seismic hazard is lower than surrounding areas, sometimes called the Potomac-Rappahannock gap (Figure 2-2A), and alone along the Appalachian belt, indicates a 10% probability of PGA exceeding less than 1% *g* in 50 years [*Petersen et al.*, 2008]. Juxtaposing the Mineral earthquake, which occurred in a high seismic hazard zone, with the Germantown earthquake, which occurred in a low seismic hazard zone, highlights the complexities of reliably forecasting earthquake activity in intraplate environments.

While some researchers emphasize that ancient collision structures and rift zones are pre-existing weaknesses in the crust that concentrate intraplate seismicity [*Mazzotti and Townend*, 2010]. Liu et al. [2011] proposed that intraplate earthquakes in North China migrate between fault systems and large earthquakes do not rupture the same fault segment twice. In addition, tectonic loading in intraplate regions is accommodated collectively by a complex system of interacting faults, which can become active for a short period after long dormancy [*Stein and Liu*, 2009*; Liu et al.*,

2011]. These hypotheses are consistent with the observation that the Germantown earthquake occurred in a gap in the seismic hazard map and may presage renewed activity at that location. Several large magnitude earthquakes have occurred in locations mapped with a low seismic hazard or produced accelerations of ground motion much larger than seismic hazard maps predicted, including: (1) the March 2011 M_w 9.1 Tohoku earthquake (Japan), (2) the 2008 M_w 8.0 Sichuan earthquake (China), and (3) the 2010 M_w 7.1 Haiti earthquake [*Geller*, 2011; *Kerr*, 2011; *Stein et al.*, 2011; *Stein and Okal*, 2011].

Stein and Liu [2009] proposed that intraplate seismicity is dominated by long-duration aftershock sequences, in which case the few centuries of available historical records are insufficient to produce reliable estimates of seismic hazard. It is possible that the Mineral earthquake and other recent seismicity in the CVSZ are aftershocks from a large magnitude pre-historic earthquake that occurred in the CVSZ. Alternatively, the Mineral earthquake could purely reflect reactivation of pre-existing faults in the CVSZ or the creation of a newly active fault system in central Virginia.

Assuming that fairly uniform long-term seismicity is expected along coherent tectonic entities such as the Appalachian orogen and Atlantic passive margin, seismic hazards should be higher than predicted where no earthquake has been recorded recently [*Mazzotti and Townend*, 2010]. A low seismicity area (and published hazard) extends along the Appalachians from the Virginia - North Carolina border to Pennsylvania near the site of the Germantown earthquake (Figure 2-2) [*Petersen et al.*, 2008]. It may be that this gap is present because major earthquakes have not happened recently and that the Germantown earthquake, although too small to fill the

gap, is a sign that seismicity will increase in this region to be comparable with nearby areas. Alternatively, activity in the CVSZ may release stress in this portion of the Appalachians.

Another region of low seismicity along the Appalachian Belt is present in Connecticut (Figure 2-2A). Large faults exist in that region, particularly in the Connecticut River Basin, a Triassic half-graben related to the opening of the Atlantic Ocean [*Brown and Oliver*, 1976; *Petersen et al.*, 2008]. If long-term seismicity is indeed uniform along the Appalachian belt and the Eastern seaboard, this region may be at a higher risk than implied by the USGS seismic hazard map. Of course, it would be a mistake to entirely ignore regions of documented seismicity. In fact, the application of cellular seismology for earthquake forecasting, which relies on the locations of previous earthquakes, has forecasted the spatial location of subsequent earthquakes in the Eastern U.S [*Wolin et al.*, 2012]. The occurrence of the Mineral earthquake in the CVSZ clearly shows that locations of previous seismic activity can still act as hotspots for future seismicity and highlights the complexities of the systems that drive the occurrence of intraplate earthquakes.

2.5 Geologic Setting

The lithologic assemblages in the Mid-Atlantic region record the tectonic history of the formation and destruction of the Appalachian orogen [*Poag and Sevon*, 1989; *Williams*, 1995]. The region extending from the Appalachian Mountains to the Atlantic Coast is typically divided into a set of physiographic provinces from west to east: the Appalachian Plateau, Valley and Ridge, Blue Ridge, Piedmont, and Coastal

Plain (Figure 2-1). The Piedmont, where the Mineral and Germantown earthquakes occurred, encompasses the foothills of the Appalachians and contains numerous faults and ductile shear zones created during Paleozoic contraction and Mesozoic extension [*Bobyarchick*, 1988; *Kunk et al.*, 2004; 2005; *Southworth et al.*, 2006]. However, younger fault zones active during the Cenozoic also pervade the Piedmont province where the Mineral earthquake occurred (Figure 2-1) [*Mixon and Newell*, 1977; *Prowell*, 1983; *Pavlides*, 1986; *Bobyarchick*, 1988; *Kunk et al.*, 2004; 2005; *Southworth et al.*, 2006; *Wheeler*, 2006]. Here I discuss recently active fault systems located in the Piedmont, all known to have experienced offset during the Cenozoic. Then I focus on the region of the Mineral earthquake to discuss known geologic structures in the local epicentral region.

2.5.1 Structures active during the Cenozoic in the Mid-Atlantic region

Some ancient fault systems in the Mid-Atlantic region created during the Paleozoic or Mesozoic have been reactivated in the Cenozoic. Other recently active fault systems do not correlate with the location of older Paleozoic and Mesozoic faults, suggesting the most recent stresses acting on the lithosphere have assumed a different orientation at these locations.

The Stafford fault system (SFS)

The Stafford fault system (SFS) accommodated extension during the Mesozoic opening of the Atlantic Ocean and then was reactivated in the late Cenozoic [*Pavlides et al.*, 1994; *Crone and Wheeler*, 2000; *Davis et al.*, 2001; *Southworth et al.*, 2002; *Mixon et al.*, 2005; *Southworth et al.*, 2007]. Mixon and Newell [1977] regard the SFS as a rare example of late Cenozoic faulting on the east

coast. The SFS displaces strata moderately, ranging from 6 to 61 meters, and is characterized by a series of right-stepping, *en-echelon*, northeast-striking, northwest-dipping, near-vertical reverse faults near the Piedmont-Coastal Plain boundary in northeastern Virginia [*Mixon and Newell*, 1977; *Mixon et al.*, 2005] (Figure 2-1). The SFS continues at least 56 km parallel to the Fall Zone, a series of knickzones where stress cross the Piedmont-Coastal Plain interface. The correlation between a northeast-trending reach of the Potomac estuary and the strike of the SFS suggests the river course may have been tectonically influenced (Figure 2-1) [*Mixon and Newell*, 1977; *Mixon et al.*, 2005]. Similarly, local structural features and lithologic contacts are thought to accentuate major knickzones at the Fall Line along the Susquehanna and upper reach of the Potomac River at Great Falls [*Hack*, 1973; *Pazzaglia and Gardner*, 1993].

The Mountain Run fault zone (MRFZ) and Everona fault (EF)

The Mountain Run fault zone (MRFZ) is a northeast-striking series of faults located near Culpeper, VA, in the central Appalachians (Figure 2-1). This fault zone juxtaposes the Laurentian outer continental margin and Ordovician accretionary complexes in the western Piedmont province with metamorphosed and deformed Laurentian terranes in the Blue Ridge province [*Bobyarchick*, 1999; *Bailey et al.*, 2007]. The MRFZ accommodated ductile deformation and retrograde metamorphism between the late Ordovician and Jurassic. However, two northwest-facing scarps indicate that brittle reverse faulting events overprint ductile fabrics in the MRFZ [*Pavlides*, 1986; *Bobyarchick*, 1999; *Crone and Wheeler*, 2000]. Although the MRFZ is thought to have been active primarily during the Paleozoic contraction and

Mesozoic extension episodes, these scarps are Quaternary in age and probably tectonically influenced, according to analyses of the topography and eroded soil horizons [*Pavlides*, 1986; *Pavlides et al.*, 1994]. These scarps may have controlled the northeasterly flow direction of the Mountain Run and the alignment of its associated northeast-trending valley, observations that also support their Quaternary age [*Drake and Pavlides*, 1993].

The MRFZ strikes northeast and dips 55° to the southeast. The southeast dip of the MRFZ comes from the subparallel dip of the regional primary foliation. Approximately 1 km to the west of the MRFZ, offset colluvial deposits identified in outcrop indicate a possibly related Tertiary or Quaternary fault that also strikes northeast but dips 20° to the northwest, known as the Everona fault (EF) [*Crone and Wheeler*, 2000]. The opposing dip of the EF makes it antithetic to the MRFZ. True slip for the EF based on gravel offset in outcrop is 1.5 m and the fault throw is 60 cm (*Bobyarchick*, 2012, personal communication). These faults are described as one collective fault system, the Everona fault – Mountain run fault zone because of their geographic closeness and evidence of Cenozoic offset [*Crone and Wheeler*, 2000].

The DC fault zone (DCFZ)

The DC fault zone (DCFZ) is a prime example of late Cenozoic faulting [*Darton*, 1950; *Prowell and Christopher*, 2004; *Prowell*, 2010]. Portions of the fault zone were first recognized in 1891 by N.H. Darton from outcrops at Clydesdale and Adams Mill Road and on Calvert Street NW in Washington, DC [*Darton*, 1950] (Figure 2-1). These faults are oriented at N28ºE, 64˚NW and N17˚W, 68˚SW and place Precambrian Piedmont metagreywake on top of Cretaceous Coastal Plain river

conglomerate [*Darton*, 1891; 1950]. Similar faults nearby cut Miocene sedimentary rocks, therefore the faulting is thought to be post-Miocene [*Darton*, 1891; 1950]. Later, the fault was recognized at the junction of 18th St., NW and California St., NW in Washington, DC, and from four U.S. Geological Survey cores extracted from Lafayette Square [*Mueser*, 1967; *Prowell and Christopher*, 2004; *Prowell*, 2010]. The DCFZ accommodated approximately 12 m of vertical displacement in its northern reaches and about 7 m of displacement in Lafayette Square, suggesting that fault displacement diminishes towards the south [*Darton*, 1950; *Prowell and Christopher*, 2004; *Prowell*, 2010]. The fault projects underneath the East wing of the White House. There is no evidence that the DCFZ is a reactivated ancient structure. Instead, the DCFZ probably formed during the activity period that resulted in the current displacement. When this activity occurred is not precisely known.

2.5.2 Local geology in the epicentral region of the Mineral earthquake

Geologic contacts and mapped faults in the epicentral region

Figure 2-5 presents the location of the Mineral earthquake's epicenter and aftershocks on a 1:500,000 scale local geologic map modified from the digital representation of the 1993 Geologic Map of Virginia [*Pavlides*, 1989; *Drake and Pavlides*, 1993; *Lampshire et al.*, 1994; *Aleinikoff et al.*, 1996; *Johnson*, 1999; *Coler et al.*, 2000; *Owens and Tucker*, 2003; *Virginia Department of Mines*, 2003; *Bailey et al.*, 2004; *Spears et al.*, 2004; *Horton et al.*, 2010; *Owens et al.*, 2010; *Hughes et al.*, 2012; *Martin*, 2012]. The epicenter of the mainshock is located east of the Chopawamsic thrust and west of the Spotsylvania fault within the Chopawamsic terrane of the Piedmont (Figure 2-5). The Chopawamsic terrane is composed of the

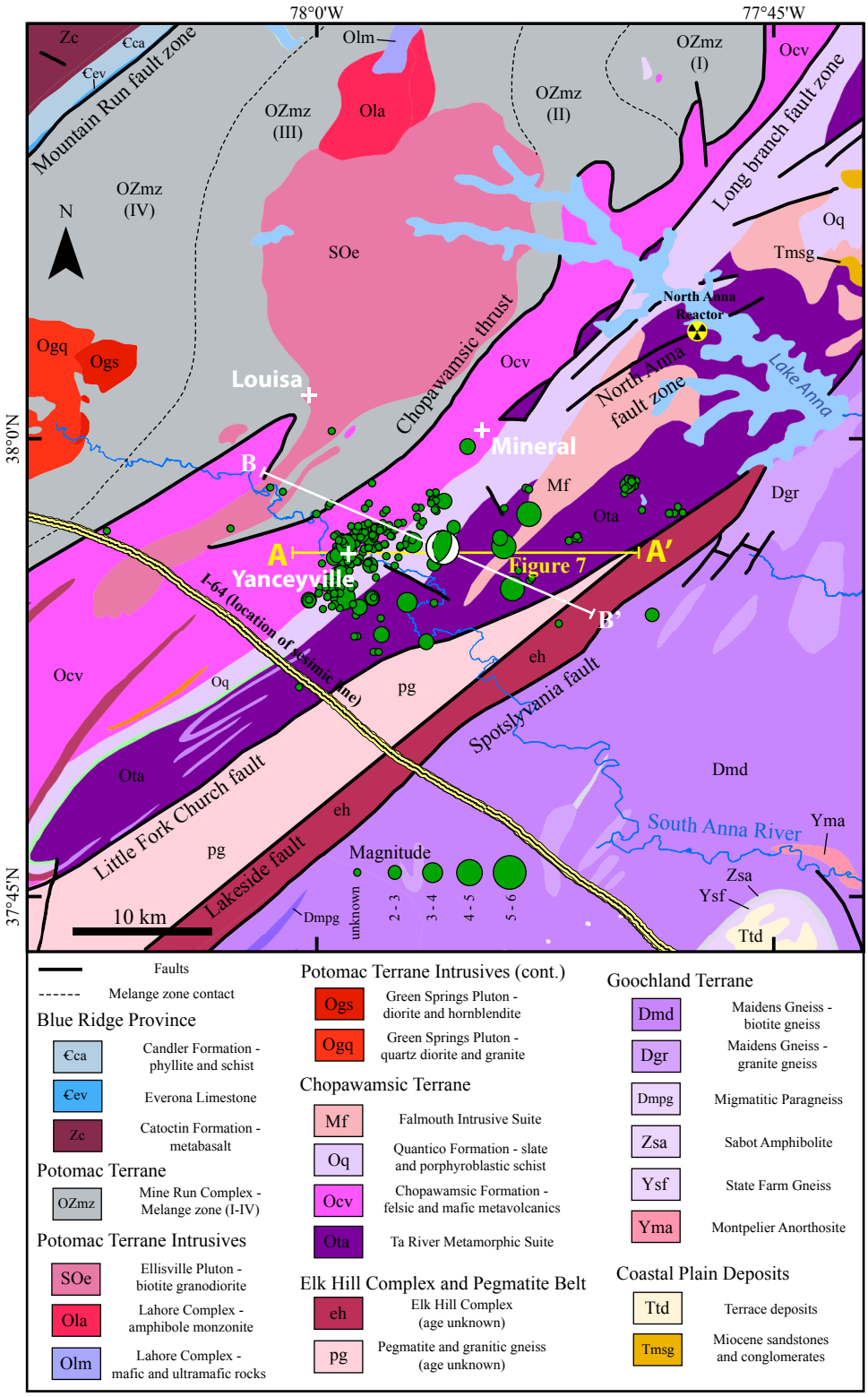

Figure 2-5. Local geologic map of epicentral region
Local geologic map of the region of the Mineral earthquake modified from the 1993 Virginia Department of Mines1:500,000 digital geologic map [*Pavlides*, 1989; *Drake and Pavlides*, 1993; *Lampshire et al.*, 1994; *Aleinikoff et al.*, 1996; *Johnson*, 1999; *Coler et al.*, 2000; *Owens and Tucker*, 2003; *Virginia Department of Mines*, 2003; *Bailey et al.*, 2004; *Horton et al.*, 2010; *Owens et al.*, 2010; *Spears et al.*, 2004; *Hughes et al.*, 2012; *Martin*, 2012]. The location of the mainshock and aftershocks was provided by the Saint Louis University Earthquake Center. Geographic Coordinate System: WGS 1984. Projection: Datum WGS 1984.

Mississippian – Pennsylvanian Falmouth intrusive suite, Ordovician Chopawamsic Formation, Ordovician Quantico Formation, and the Ordovician Ta River Metamorphic Suite all of which are interpreted as having formed in an island arc environment (Figure 2-5). The Chopawamsic Formation is composed of interlayered felsic and mafic metavolcanic rocks, the Ta River Metamorphic Suite primarily consists of amphibolites and amphibole-bearing gneiss and schist, the Quantico formation contains slates and porphyroblastic staurolite, kyanite, and garnet biotite muscovite schists, and the Falmouth intrusive suite is composed of granite, quartz monzonite, granodiorite, and tonalite intrusives [*Virginia Department of Mines*, 2003].

The Spotsylvania fault places biotite gneisses of the Goochland terrane (Maidens gneiss) on the Elk Hill Complex, Pegmatite Belt, and Chopawamsic terrane. Although the Department of Mines map shows these gneisses as Middle Proterozoic, recent zircon U/Pb isotopic dating indicates that the igneous protoliths of at least some of the Goochland gneisses cut by the Spotsylvania fault crystallized in the Devonian [*Owens et al.*, 2010]. Structural analyses indicate that the Spotsylvania fault zone is a transpressional high-strain zone with a complex history, including thrusting and right-handed strike-slip faulting [*Bailey et al.*, 2003; 2004; *Mixon et al.*, 2005]. The Chopawamsic thrust is interpreted as an early Paleozoic fault that placed the Chopawamsic terrane on the Mine Run Complex melange zone of the western Piedmont [*Pavlides*, 1986; *Virginia Department of Mines*, 2003] (Figure 2-5).

Other smaller-scale faults mapped within the Chopawamsic terrane are the Long Branch fault zone, Little Fork Church fault, Lakeside fault, and an unnamed fault that traverses the North Anna nuclear power plant site, herein referred to as the North Anna fault zone (NAFZ) (Figure 2-5). The Long Branch fault zone delineates

a northeast striking boundary between the Quantico formation and Chopawamsic formation [*Virginia Department of Mines*, 2003; *Mixon et al.*, 2005]. Previous studies of the Long Branch fault system indicate it accommodated predominately thrust sense motion [*Pavlides*, 1990; 1995], however more recent field mapping indicates the possible presence of late strike-slip movement [*Mixon et al.*, 2005]. Kinematic studies of mylonitic fabrics associated with the Long branch fault zone await future analysis. There is no evidence for recent activity on the fault.

Geologic and seismologic investigations documented in the Site Safety Analysis Report for Unit 3 of the North Anna nuclear power plant indicate that seismicity in the epicentral region is not associated with any of the known faults mapped at the surface [*Dominion Nuclear North Anna*, 2006]. The NAFZ was discovered in site excavations and mapped in trenches on-site. Based on direct evidence of no displacement of saprolitic soils, the absence of geomorphic expression, and K-Ar ages on undeformed chlorite ranging from 214-303 Ma, the fault is considered not active (Figure 2-5). Recent aerial and field reconnaissance and air photo interpretation did not reveal any evidence for an off-site extension of the fault [*Dominion Nuclear North Anna*, 2006; *Fenster and Walsh*, 2012].

Ground motion at the North Anna reactor due to the Mineral earthquake exceeded the safe operating parameters (0.12g) for operating units 1 and 2 causing both units to shut down safely as designed [*Fenster and Walsh*, 2012]. Note that because the earthquake rupture did not reach the surface, it cannot be associated directly with the faults currently identified in the vicinity of the power plant.

Rupture plane of the Mineral earthquake

The orientation and location of the rupture plane of the Mineral earthquake does not match previously mapped Paleozoic and Mesozoic faults in the epicentral region at the surface (Figure 2-5). The USGS/SLU regional moment tensor solution for the Mineral earthquake indicates predominately thrust sense motion (Figure 2-6). Aftershocks define a 1 km-thick southeast dipping tabular cluster ranging from ~3 to 7.5 km depth that corresponds to the north- northeast striking nodal plane of the focal mechanism, suggesting it was the mainshock's rupture plane (NP2: strike=177°, dip=39° SE, rake = 66°) (SLU, aftershock monitoring) (Figures 2-5, 2-6, and 2-7). Two clusters of aftershocks situated 4 and 8 km east of the rupture plane suggest activation of nearby faults in the epicentral region following the mainshock (Figure 2-7) [*Horton*, 2012; *Horton et al.*, 2012]. Empirical relations on fault geometry [*Wells and Coppersmith*, 1994] suggest that the rupture plane for the Mineral earthquake was ~38 times longer by ~18 times wider and accommodated 35 cm more thrust slip than the July 2010 Germantown earthquake, the most recent earthquake in the DC metropolitan area prior to the Mineral earthquake (Table 2-1).

Seismic reflection data collected along Interstate-64 offer the opportunity to compare the orientation of the rupture plane with geologic structures at depth in cross-section [*Harris et al.*, 1986] (Figure 2-8). The seismic line is only ~5.6 km southwest of the epicentral region, so major geologic contacts and structures detectable in the seismic data likely are present in the region of the Mineral earthquake. The rupture of the Mineral earthquake probably dips more steeply than mapped geologic contacts and structures. Therefore, the Mineral earthquake likely

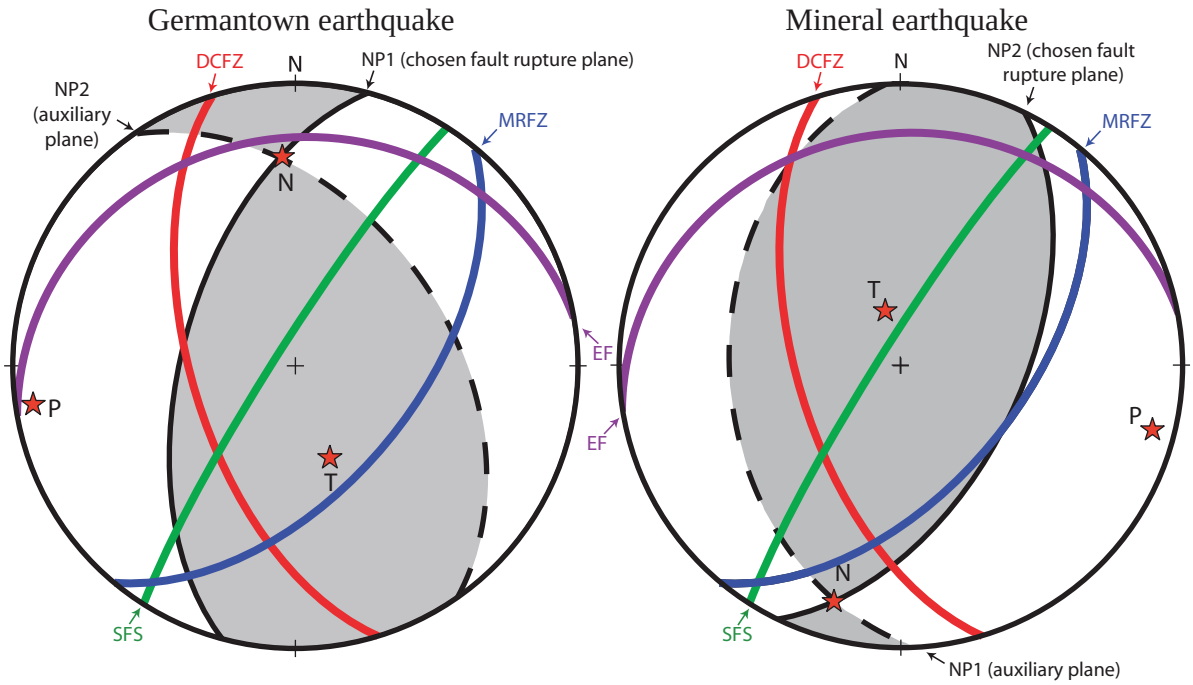

Figure 2-6. Earthquake focal mechanisms and Cenozoic fault orientations
Orientation of selected faults with Cenozoic motion (Figure 1) superposed on USGS/SLU focal mechanisms for the (A) Germantown and (B) Mineral earthquakes on an equal-area lower hemisphere projection.

Table 2-1. Magnitude, length, displacement relations

Earthquake	M_w	Moment (dyn·cm)	Fault length (km)*	Fault width (km)*	Reverse slip (cm)*	Expected right-lateral slip (cm)*	Maximum $\Delta\sigma_{CF}$ (bar)
Germantown	3.4	1.58×10^{21}	0.2	0.3	6	4	22.48
Mineral	5.8	6.31×10^{24}	7.5	5.4	41	-18	0.04
Difference	2.4		7.3	5.1	35	22	
Factor		3994	37.5	18			562

*Expected subsurface fault plane dimensions and slip from empirical relations (cf. Wells and Coppersmith, 1994).

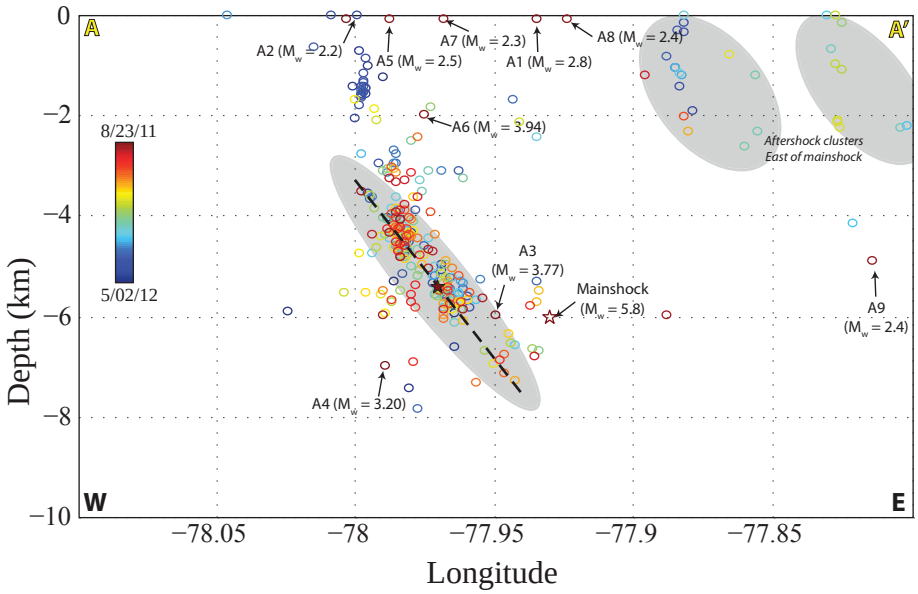

Figure 2-7. Cross-section of aftershock locations from the Mineral earthquake
Cross-section showing depth of aftershocks and their time of occurrence. Highlighted aftershocks A1 to A9 occurred within 48 hours of the mainshock. The majority of aftershocks define a southeast dipping tabular rupture plane that matches NP2 of the mainshock's focal mechanism. Two clusters of aftershocks to the east of the rupture suggest activation of nearby faults [*Horton*, 2012; *Horton et al*., 2012]. Gray ovals delineate the tabular rupture plane and the two clusters. The dashed line approximates a rupture plane width of ~5.4 km based on empirical relations. I centered the rupture plane on the original location and depth of the mainshock (open star) and then relocated it to the aftershock cluster (filled star). Aftershock locations were determined by the Saint Louis University Earthquake Center.

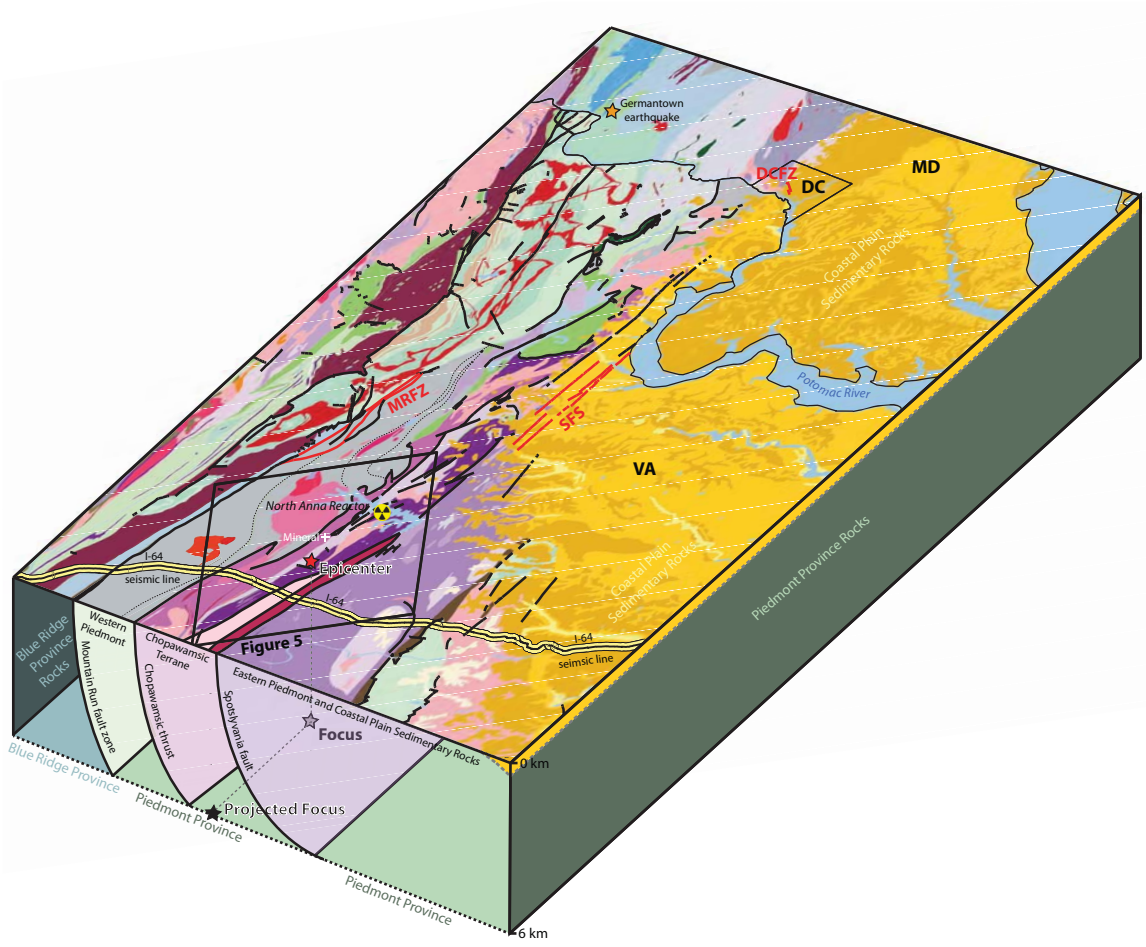

Figure 2-8. Block diagram of major geologic structures in epicentral region
Block diagram depicting the major geologic structures in the region of the Mineral earthquake. Produced by integrating the 1:500,000 scale digital representation of the 1993 Geologic Map of Virginia [*Virginia Department of Mines*, 2003] and a geologic interpretation of the Interstate 64 seismic line [*Harris et al.*, 1986]. This diagram indicates the Mineral earthquake ruptured within the Chopawamsic terrane, between the Chopawamsic and Spotsylvania faults. It is possible shallow aftershocks near the surface (Figure 2-5 and 2-7) may have ruptured new unmapped faults, but that these new fault converged with older faults and reactivated them at depth (i.e. the Chopawamsic or Spotsylvania faults). Geographic Coordinate System: WGS 1984. Projection: Datum WGS 1984.

ruptured on a new or unmapped fault zone, rather than reactivating known preexisting Paleozoic and Mesozoic fault systems in the epicentral region. It is worth noting, however, that the earthquake probably occurred at 5 to 10 km depth, probably below the penetration depth of the seismic line (6 km) and the orientation of seismically-determined faults could be in error by as much as 10° (*Varga*s, personal communication, 2011).

It is also possible that at shallow depths the earthquake ruptured a new fault, but that this new fault connects with older faults at depth. The orientation of the earthquake's rupture plane is similar to the orientation of the MRFZ (Figure 2-8), which shows evidence of Cenozoic offset. Perhaps a spatially widespread system of faults with similar orientations is active and responsible for the Mineral earthquake and recent seismicity in the CVSZ. These faults may be connected by a regional structure at depth, such as the Appalachian decollément at ~10 km depth [*Iverson and Smithson*, 1983].

2.6 Surface deformation generated by the Mineral earthquake

2.6.1 Liquefaction

A search for liquefication features by Obermeier and McNulty in the CVSZ in 1988 revealed (1) a few small sand dikes at one site estimated to be a few centuries old based on radiocarbon data and a lack of weathering in surrounding sediments and (2) a few small severely weathered sand dikes, suggesting they are older than the first set, at a second site a few tens of kilometers away across the structural grain [*Obermeier and McNulty*, 1998; *Crone and Wheeler*, 2000; *Wheeler*, 2006]. The scarcity of liquefaction features, ages of liquefied sediments, and close spacing of

searched streams led Obermeier and McNulty to conclude that the CVSZ has not had an earthquake larger than magnitude 7 in the last 2,000 to 3,000 years. These sand dikes have not been tied to previously recorded seismicity in the CVSZ and may indicate that faults within the seismic zone created large magnitude prehistoric earthquakes [*Kim and Chapman*, 2005; *Wheeler*, 2006].

Following the August 2011 Mineral earthquake, geologists from the Virginia Division of Geology and Mineral Resources (DMGR) and the U.S. Geological Survey (USGS) searched the epicentral region for possible surface ruptures and liquefaction features. No surface ruptures have been identified in the field; however sand boils attributed to liquefaction during the earthquake were discovered in Yanceyville, VA, by Jeff Munsey (Tennessee Valley Authority) and Mark Carter (USGS) (Figure 2-9).

2.6.2 Expected vertical surface deformation

To estimate expected vertical displacement of the surface from the Mineral earthquake, I created an elastic dislocation model using the Boundary Element software Coulomb version 3.3 [*Lin and Stein*, 2004; *Toda et al.*, 2005]. In my model, I assumed that nodal plane 2 (NP2) from the focal mechanism corresponds to the rupture plane (Table 2), as it is most consistent with the distribution of aftershocks (Figure 2-7). Empirical relations [*Wells and Coppersmith*, 1994] predict a rupture plane that is 7.5 km long and 5.4 km wide for a magnitude 5.8 earthquake (Table 2-1). The center of the rupture plane is placed at 6 km below the surface according to the best estimate of the earthquake depth (SLU/USGS).

Figure 2-9. Sandboils attributed to liquefaction from the Mineral earthquake
Photograph of sand boils attributed to liquefaction during the Mineral earthquake near Yanceyville, VA (location: 37.938387°, -77.982666) (see Figure 3-5). Identified and photographed by Jeff Munsey (Tennessee Valley Authority) and Mark Carter (USGS).

My results predict ~9 cm of permanent vertical surface deformation at the epicenter of the Mineral earthquake, decreasing rapidly to only ~ 1 mm 20 km away from the epicenter, for an earthquake with at depth of 6 km at the center of the rupture (Figure 2-10). Additional surface deformation may also be expected across the region from shallow aftershocks, previously recorded earthquakes in the CVSZ, and silent slip on Quaternary-active scarps. The maximum slip expected during previously recorded earthquakes in the CVSZ ranges from 0 to 15 cm, based on magnitude and length-displacement relations [*Wells and Coppersmith,* 1994]. Note that the expected amount of vertical deformation at the surface increases with decreasing earthquake depth. The depth of the earthquake (6 km) is uncertain by several kilometers, therefore predicted surface displacement from the Mineral earthquake could be in error by several centimeters. The small amplitude of surface deformation could only be detected by a dense geodetic network in place before the earthquake or with high-quality radar data, which is not available for this location. Lines of benchmarks used to create the National Vertical Datum of 1988 (NAVD88) offer a reference for the elevation of the surface before the earthquake, however the maximum displacement expected at the locations of the benchmarks is less than 3 cm and likely not resolvable from a re-leveling campaign (Figure 2-10A).

Table 2-2. Regional Coulomb source and receiver fault orientations

	Germantown earthquake	Mineral earthquake
Source Faults	**strike*** **/ dip / rake†**	**strike*** **/ dip / rake†**
NP1	195°/ 57°NW / 123° (chosen rupture plane)	177°/ 39°SW / 66° (auxiliary plane)
NP2	325° / 45°NE / 50° (auxiliary plane)	26° / 55° SE/ 108° (chosen rupture plane)
Receiver Faults	**strike*** **/ dip / rake†**	**strike*** **/ dip / rake†**
DCFZ	163° / 68°SW / 93°	163° / 68°SW / 41°
SFS	213° / 84°NW / 138°	213° / 84°NW / -152°
MRFZ	40° / 55°SE / 141°	40° / 55°SE / 114°
EF	260° / 20°NW / -36°	260° / 20°NW / 116°

*Strike defined using the right hand rule. †Rake resolved on the fault plane by the stress tensor associated with the focal mechanism for the Germantown and Mineral earthquakes (see Appendix A).

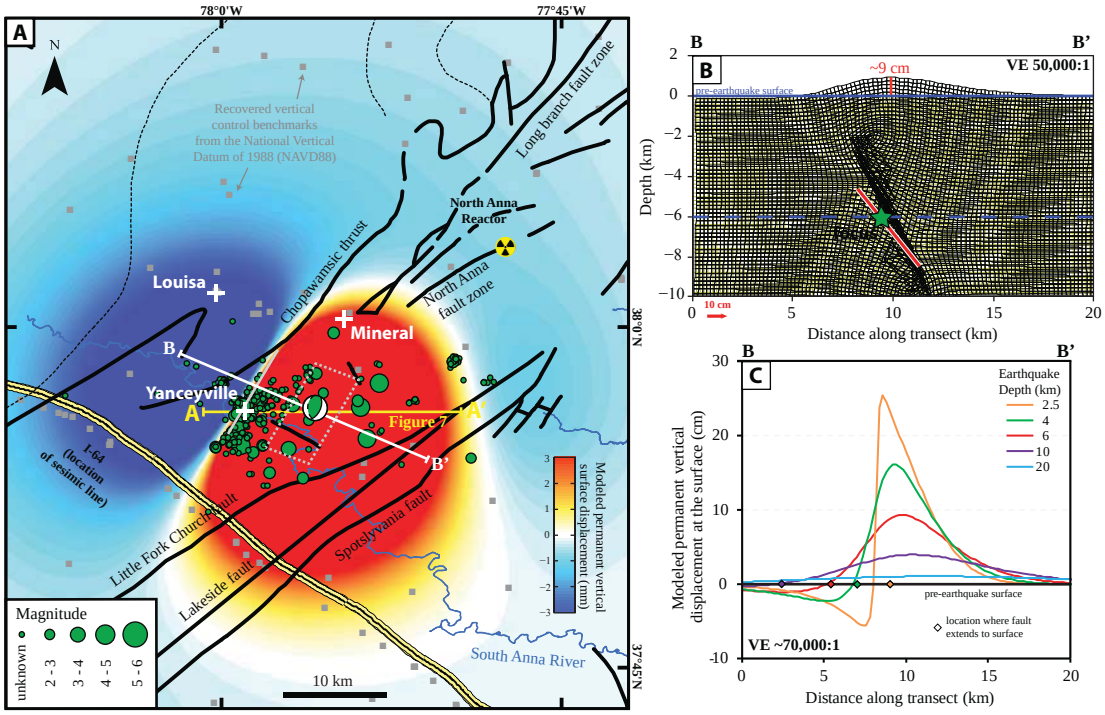

Figure 2-10. Permanent vertical surface displacement from the Mineral earthquake
A) Map of permanent vertical displacement expected at the surface from the Mineral earthquake for a focus depth of 6 km at the center of the rupture. Calculation is based on empirical relations for same slip and dimensions [*Wells and Coppersmith*, 1994] and a Coulomb elastic dislocation model. Benchmark locations are from the National Geodetic Survey. Geographic Coordinate System: WGS 1984. Projection: Datum WGS 1984. B) Rupture plane and corresponding displacement model for slip generated by a magnitude 5.8 earthquake with a depth of 6 km (preferred depth). Maximum displacement at the surface along transect B to B' crossing the rupture is ~9 cm. C) Profile of vertical displacement at the surface for a range of depths along B to B'.

2.7 Coulomb stress transferred by the Mineral and Germantown earthquakes

2.7.1 Fault interaction through static stress transfer

One way faults interact is by the transfer of static stress. After an earthquake, fault slip redistributes stress to nearby fault systems and can potentially trigger future seismicity on these faults [*Lin and Stein*, 2004; *Toda et al.*, 2005]. A fault plane's closeness to failure can be expressed by the Coulomb Failure Stress

$$\sigma_{CF} = \tau + \mu' \Delta\sigma_n - \sigma_0$$

where τ and σ_n are the shear stress and normal stress (positive in tension when unclamped) resolved on the fault plane and μ' is the effective friction coefficient, which combines the intrinsic friction coefficient of the fault plane and the effect of pore fluid pressure, and σ_0 is the cohesion of the fault [*King et al.*, 1994; *Stein*, 1999; *Toda et al.*, 2005]. The shear stress is projected along a predefined slip vector in the fault plane.

After a fault ruptures, regions where σ_{CF} increases or decreases define stress trigger zones and stress shadows around the earthquake hypocenter, where faults of a given orientation have been brought closer to or further from failure [*King et al.*, 1994]. The westward propagation of earthquakes during the 1939 to 1992 rupture of the North Anatolian fault in Turkey is perhaps the clearest manifestation of Coulomb stress transfer, or static triggering of earthquakes [*Stein et al.*, 1997]. Similarly, the M_w 6.4 Big Bear earthquake and several aftershocks occurred in the stress trigger zones produced by the June 28th M_w 7.3 Landers earthquake of 1992 in southern California, which itself was likely triggered by the M_w 6.1 Joshua Tree preshock on April 23rd [*Hauksson et al.*, 1993]. Coulomb stress transfer from the Landers

earthquake also promoted the M_w 7.1 Hector Mine shock that occurred in the stress trigger zone seven years later [*Stein et al.*, 1992; *Toda et al.*, 2005].

The importance of Coulomb stress transfer is still being evaluated for intraplate regions. Li et al. [2007] suggested that inherited strain energy accumulates from large magnitude earthquakes and can become trapped in intraplate regions for thousands of years, in contrast to plate boundaries where tectonic loading dominates. The Coulomb stress transfer from this accumulation of strain could promote intraplate seismicity on both new and pre-existing faults.

One major unresolved issue regarding intraplate seismicity is the importance of static vs. dynamic stress transfer [*Freed*, 2005]. Although there is clear evidence for dynamic triggering by seismic waves in the eastern U.S. [*Parsons et al.*, 2012] (see Chapter 3), unrelated to changes in σ_{CF}, the paucity of large magnitude earthquakes (> 5.0) in the eastern U.S. over the last ~50 years suggests the Mineral and Germantown earthquakes themselves are unlikely tied to the passage of seismic waves from a larger event. The influence of dynamic triggering from a global event remains unexplored. I restricted the analysis to regional changes in σ_{CF} that occurred in the broad DC metropolitan region as a result of the Mineral and Germantown earthquakes. Coulomb stress transfer and associated seismic hazard have not yet been assessed in the CVSZ, site of the Mineral earthquake, or for the identified Cenozoic fault systems in the Mid-Atlantic region. I calculated the change of σ_{CF} on the following Cenozoic-active fault systems: the DCFZ, SFS, MRFZ, and EF to evaluate to what extent slip from the Germantown and Mineral earthquakes may have transferred stress to these faults.

2.7.2 Methods: Coulomb stress change ($\Delta\sigma_{CF}$) calculations

I identified regions where faults were brought closer to failure (stress trigger zones) and locations where faults were moved further from failure (stress shadows) by the Mineral and Germantown earthquakes by producing maps of changes in σ_{CF} using USGS Coulomb software [*Lin and Stein*, 2004; *Toda et al.*, 2005]. Coulomb stress change, $\Delta\sigma_{CF}$, is given by:

$$\Delta\sigma_{CF} = \Delta\tau + \mu'\Delta\sigma_n$$

where Δ expresses the change in the associated stress component [*King et al.*, 1994; *Stein*, 1999; *Toda et al.*, 2005].

Coulomb stress change maps were calculated for a variety of source and receiver fault geometries, rupture depths, and coefficients of friction. My preferred model assumes μ'=0.8, which represents the high friction and stress drop expected in intraplate regions [*King et al.*, 1994; *Zoback*, 1992; *Li et al.*, 2007] and in particular for the Mineral and Germantown earthquakes [*Cramer et al.*, 2011; *Viegas*, 2012], a shear modulus of 3.2×10^5 bars and a Poisson's ratio of 0.25, which are similar to other $\Delta\sigma_{CF}$ calculations and representative of several rock types [*Toda et al.*, 2005].

In models of Coulomb failure stress change, the source fault slips and imparts stress to the surrounding crust and faults within it. Receiver faults do not slip, but receive stress transferred from the source fault. I used the rupture plane from the earthquake's focal mechanism as the source fault and the strike and dip of various fault zones in the DC metropolitan region as potential receiver faults.

The USGS/SLU regional moment tensor solutions for both the Mineral and Germantown earthquakes indicate predominantly thrust motion. I chose to use nodal

plane 1 (NP1) as the source fault for the Germantown earthquake because its strike is similar to Paleozoic and Mesozoic faults in the epicentral region (Appendix 2-B). However, since the Germantown earthquake may have ruptured on a new or unidentified fault, the auxiliary plane cannot be ruled out as the true rupture plane. Regardless, since the Coulomb stress analysis depends only on the principal stresses at the earthquake hypocenter (pressure - P, neutral - N, and tension - T axes), using either NP1 or NP2 as the source rupture plane for either earthquake generates similar results (Appendix 2-C). I chose nodal plane 2 (NP2) as the source fault for the Mineral earthquake since aftershocks subsequently defined this plane (Figure 2-6). In the absence of better constraints, fault dimensions were determined from the empirical relations of Wells and Coppersmith [1994] (Table 2-1). Rupture depth, which is poorly constrained, is set to 7 km for the Germantown earthquake and 6 km for the Mineral earthquake, following the best depth solutions from the USGS/SLU.

The geometry of the receiver fault is an important factor in determining the pattern of $\Delta\sigma_{CF}$ [*Lin and Stein*, 2004] (Appendix 2-C). For this analysis, I considered receiver faults that adopt the strike and dip representative of the DCFZ, SFS, MRFZ, and EF (Figure 2-1 Table 2-2). The rake, or expected direction of slip on the receiver fault surface, is unknown for these faults. If the P, N, and T axes determined in each earthquake's focal mechanism are taken as representative of the regional stress field, they imply a certain long-term slip direction on each Cenozoic fault system of interest. I used the geometry of each focal mechanism to determine a regionally consistent slip for each receiver fault (Table 2) and assume that the long-term slip is collinear with this orientation, giving the rake needed to calculate Coulomb failure

stress change (Appendices 2-C, 2-D, and 2-E). For the modeling, each fault system was mapped from pre-existing geologic maps. The orientation of the EF was measured in outcrop at 38.301714° latitude and -77.972286° longitude (*Bobyarchick*, 2012, personal communication). Since the length of the EF is unknown, I arbitrarily extend the fault ~30 km to the north along the strike of EF and MRFZ in order to visualize changes in σ_{CF} on possible extensions of the fault system. I chose to extend the fault system to the north of the outcrop due to the possible geologic connection between the EF and MRFZ.

2.7.3 Coulomb stress transfer results

I present $\Delta\sigma_{CF}$ for three cases: First, I calculate the regional $\Delta\sigma_{CF}$ field across the Mid-Atlantic region generated by the Mineral and Germantown earthquakes to visualize the stress change both on the Cenozoic fault systems of interest (DCFZ, SFS, MRFZ and EF) and on faults across the study area with similar orientations (Figure 2-11 and 2-12). Second, I resolved $\Delta\sigma_{CF}$ generated by the Mineral earthquake on subdivided fault plane segments for each Cenozoic fault system to evaluate the $\Delta\sigma_{CF}$ within each fault system and to view the $\Delta\sigma_{CF}$ on the fault segments with documented Cenozoic activity collectively (Figure 2-13, Table 2-3). Finally, I calculated the local $\Delta\sigma_{CF}$ field created by the Mineral earthquake across mapped faults located within 30 km of the epicenter [e.g. the rupture plane itself, the North Anna fault zone (NAFZ) which crosses under the North Anna reactor, the

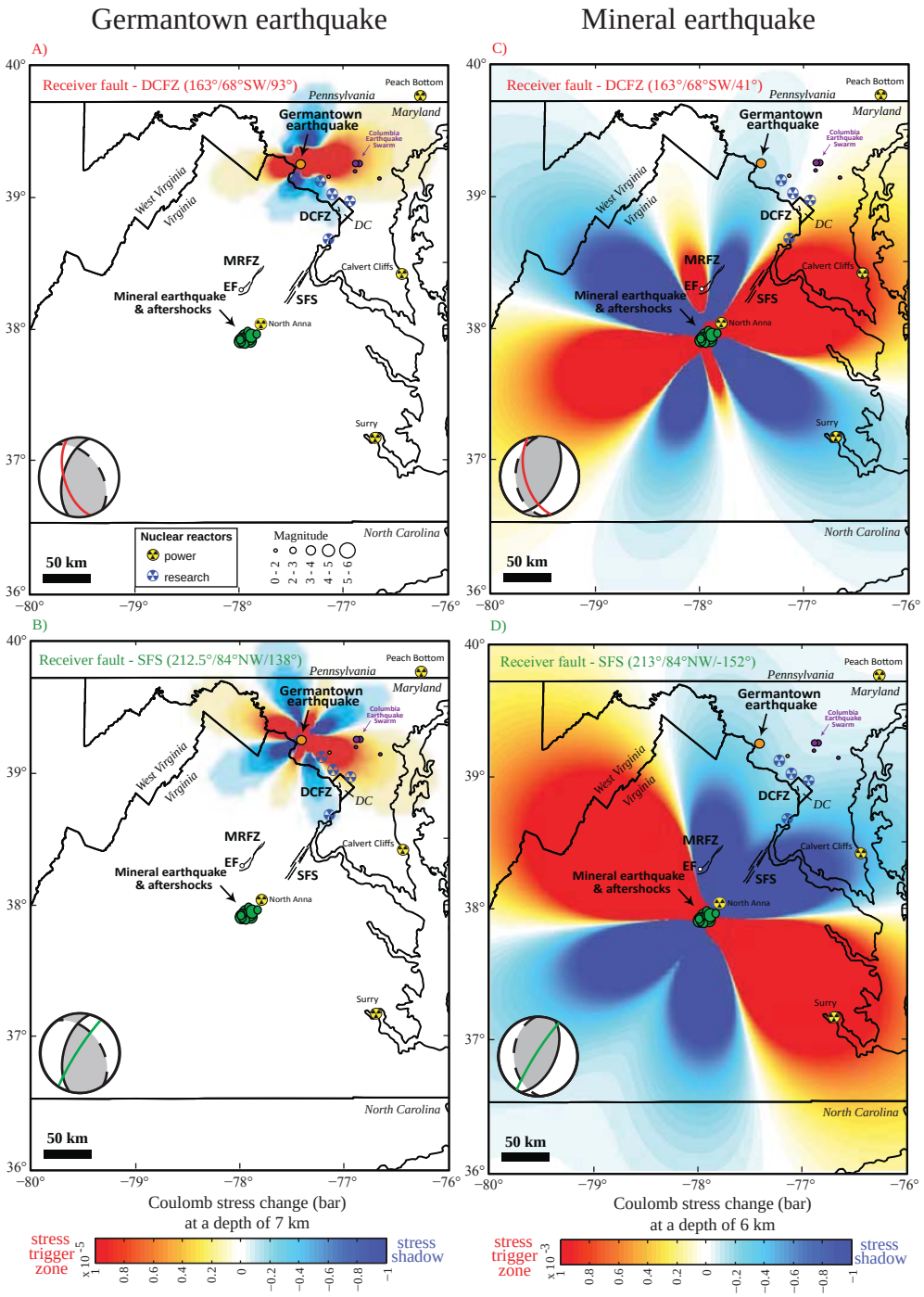

Figure 2-11. Stress transferred to the DC fault zone and the Stafford fault system
Regional Coulomb failure stress change ($\Delta\sigma_{CF}$) field for receiver faults oriented like the DC Fault Zone (DCFZ) (A and C), and Stafford fault system (SFS) (B and D) for the Germantown and Mineral earthquakes at 7 and 6 km depth, respectively. Source and receiver fault geometries are superposed on stereonets for each earthquake's focal mechanism. The Mineral and Germantown earthquakes did not affect the DCFZ, but moved faults oriented like the DCFZ near the Calvert Cliffs reactor and like the SFS near the Surry reactor closer to failure. The Germantown earthquake did not affect the SFS, but moved faults oriented like the DCFZ and SFS north of DC and in central Maryland, site of the 1993 Columbia, MD, earthquake swarm, closer to possible future failure. Geographic Coordinate System: WGS 1984. Projection: Datum WGS 1984.

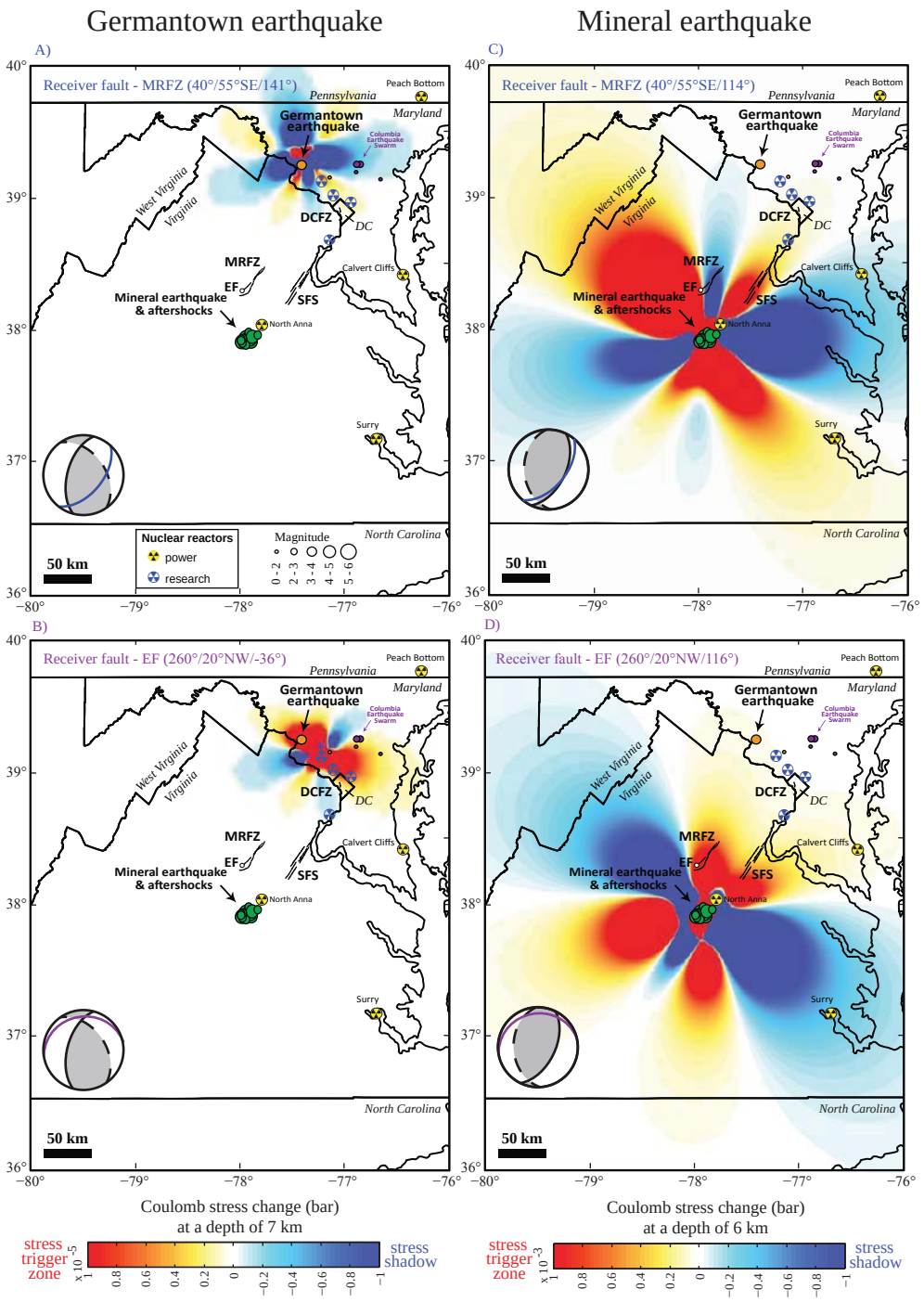

Figure 2-12. Stress transferred to the Mountain Run fault zone and the Everona fault
Regional Coulomb failure stress change ($\Delta\sigma_{CF}$) field for receiver faults oriented like the Mountain Run fault zone (MRFZ) (A and C), and Everona Fault (EF) (B and D) for the Germantown and Mineral earthquakes at 7 and 6 km depth, respectively. Source and receiver fault geometries are superposed on stereonets for each earthquake's focal mechanism. The EF and MRFZ are too far away to be affected by the Germantown earthquake. The Mineral earthquake moved the northern segment of the MRFZ farther away from failure, but moved the southern end of the MRFZ and the EF closer to failure. Geographic Coordinate System: WGS 1984. Projection: Datum WGS 1984.

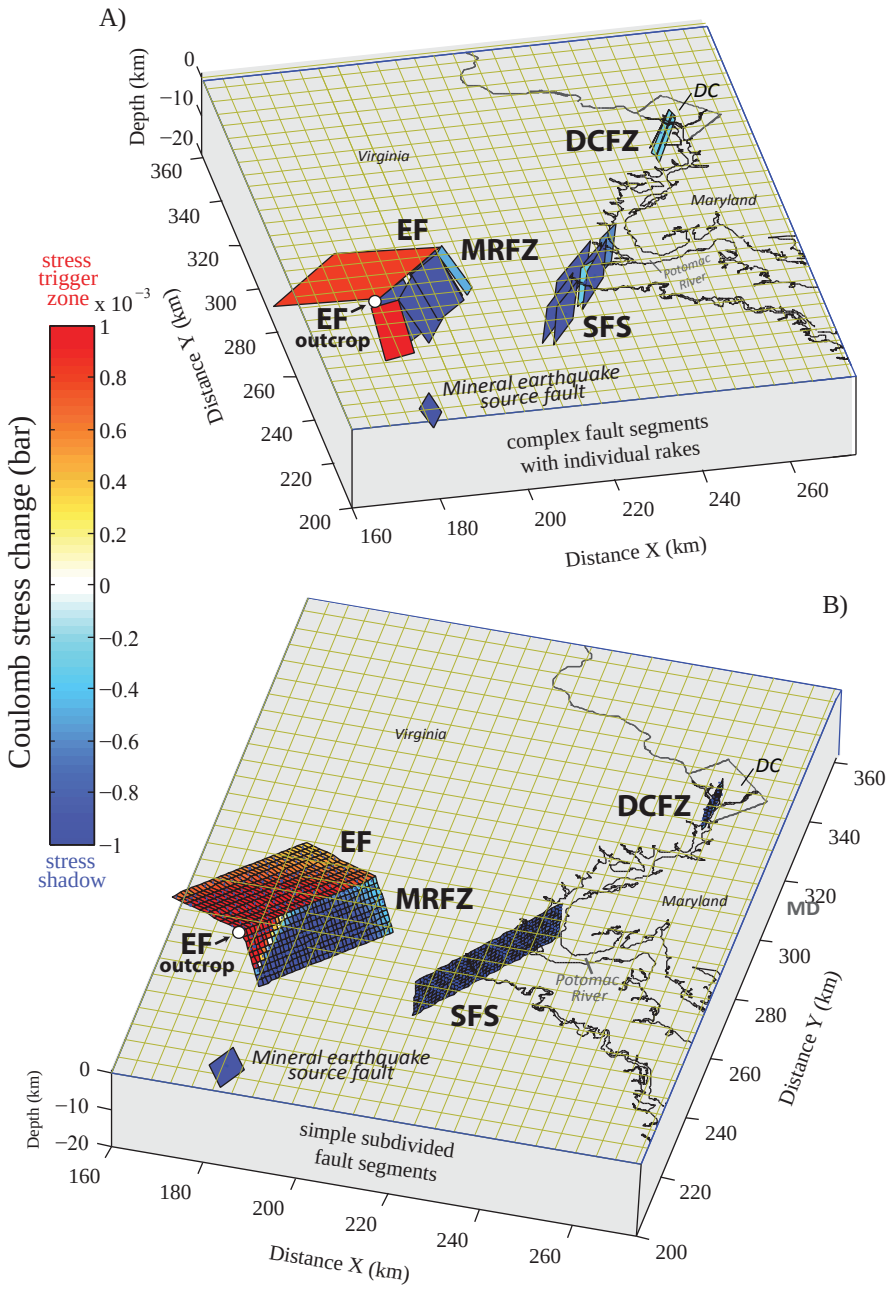

Figure 2-13. Stress transferred to all Cenozoic fault systems
Change in Coulomb failure stress ($\Delta\sigma_{CF}$) generated by the Mineral earthquake for all fault segments of the DCFZ, SFS, MRFZ, and EF. The length of EF is unknown because it was identified only in an outcrop at the location marked with the white circle. A) $\Delta\sigma_{CF}$ resolved on a more complex model that accounts for variation of strike and dip within each fault system and corresponding rake (Table 3). B) $\Delta\sigma_{CF}$ on simplified planes representing each fault system. Each fault segment is subdivided to reveal stress change within the fault plane. Each subdivision on the fault planes is ~1 km by 1 km. In general, the $\Delta\sigma_{CF}$ caused by the Mineral and Germantown earthquakes moved these fault systems further away from failure. The largest changes in σ_{CF} are on the southern portion of the MRFZ and on the EF (positive $\Delta\sigma_{CF}$), indicating that these faults were brought closer to failure as a result of the Mineral earthquake. The increase in σ_{CF} on the southern portion of the MRFZ depends more on receiver fault location than azimuth.

Table 2-3. $\Delta\sigma_{CF}$ resolved on non-divided complex fault segments (Figure 2-13A)

Fault ID	Description	Strike (°)	Dip (°)	Length (km)	Assumed rake (°)*	$\Delta\sigma_{CF}$ (bar)
1	Source fault - NP2	26.00	55	7.57	108	-23.10744
2	SFS	217	84	7.92	-154	-0.00050
3	SFS	215	84	19.71	-153	-0.00128
4	SFS	212	84	10.05	-152	-0.00121
5	SFS	208	84	14.63	-149	-0.00195
6	SFS	226	84	4.80	-156	0.00016
7	SFS	213	84	16.04	-152	-0.00369
8	SFS	213	84	12.26	-152	-0.00470
9	MRFZ	50	55	11.74	117	-0.00109
10	MRFZ	39	55	12.19	114	-0.00064
11†	MRFZ	74	55	7.36	114	**0.00353**
12	MRFZ	27	55	11.97	108	-0.00147
13	MRFZ	40	55	11.31	114	-0.00065
14	MRFZ	24	55	3.59	106	-0.00020
15	DCFZ	199	68	0.53	95	-0.00016
16	DCFZ	163	68	1.91	41	0.00006
17	DCFZ	163	68	1.45	41	0.00008
18	DCFZ	163	68	0.73	41	0.00009
19	DCFZ	163	68	1.92	41	0.00007
20†	EF	163	20	26.74	116	**0.00098**

*Resolved rakes determined using methods outlined in Appendix A.

†Fault segments with largest positive increase in σ_{CF}.

Chopawamsic thrust (CT), Long Branch fault zone (LBFZ), and Spotsylvania fault (SPFZ)] (Figure 2-14, Table 2-4).

Coulomb failure stress change ($\Delta\sigma_{CF}$) from the Germantown Earthquake

Because of its small magnitude, the Germantown earthquake induced only very small changes in σ_{CF} throughout the study area, which are unlikely to significantly alter the probably of failure on any regional fault like the SFS or the MRFZ. Similarly, the EF was too far away to be affected by the σ_{CF} generated by the earthquake (Figures 2-11 and 2-12). The earthquake increased σ_{CF} on putative faults oriented like the SFS, DCFZ, and EF north of DC and in central Maryland, including the location of the 1993 Columbia, MD, earthquake swarm. The closest Cenozoic fault system of interest to the epicenter is the DCFZ, which is located in a stress shadow, indicating the Germantown earthquake brought the DCFZ itself farther away from failure.

Faults oriented like the MRFZ near the region surrounding the epicenter have in general been brought farther away from failure by the earthquake. The orientation of the MRFZ corresponds with the predominant dip of the regional primary foliation and Paleozoic and Mesozoic faults in the epicentral region. The decrease in σ_{CF} on these regional structures may support the hypothesis that seismicity is migrating from older fault systems to newer fault systems in order to adjust to current stresses acting on the lithosphere. Note however that the locations and orientations of both pre-existing faults and the earthquake greatly influence the pathways through which stress may be transferred.

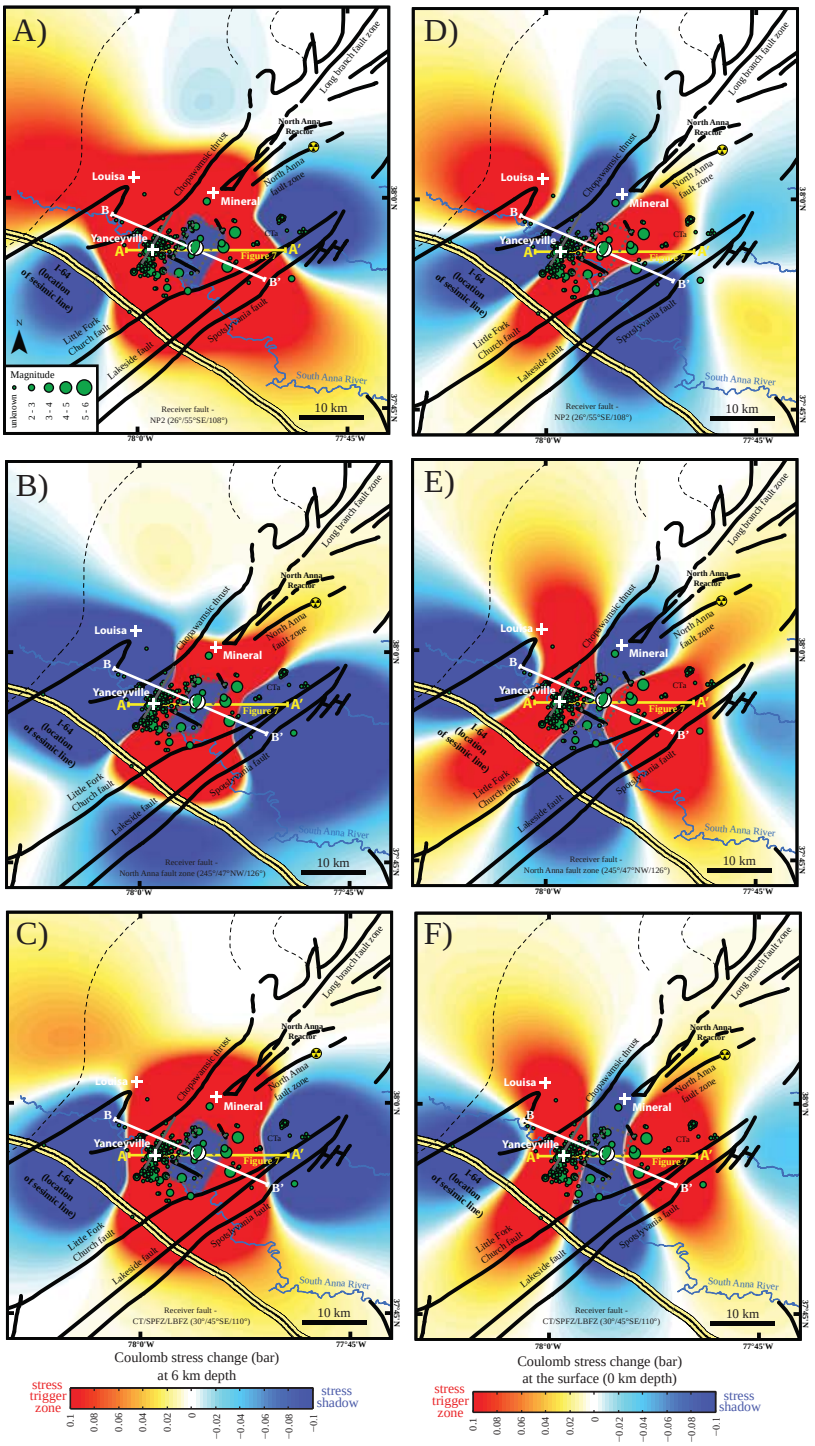

Figure 2-14. Stress transferred to Paleozoic and Mesozoic faults in the epicentral region
Regional Coulomb failure stress change ($\Delta\sigma_{CF}$) field generated by the Mineral earthquake for receiver faults oriented like the rupture plane (NP2) (A and D), the North Anna Fault Zone (NAFZ) (B and E), and the average orientation of Chopawamsic thrust fault, Long Branch fault zone, and Spotsylvania fault (C and F) (Table 4). Calculations are shown at the depth of the Mineral earthquake (6 km depth) and the surface (0 km depth). The Mineral earthquake moved the NAFZ closer to failure by ~0.02 bars at the North Anna reactor or a range of 0.1 to 0.11 bars along the fault at 6 km depth. σ_{CF} increased by a maximum of 1.5 bars on the Chopawamsic thrust, 2.1 bars on the Spotsylvania fault, and 0.6 bars on the southern end of the Long Branch fault zone. The rupture plane itself generated an increase in σ_{CF} of ~20 bars at the rupture's edge, and ~5 bars at 5 km and 0.5 bars at 10 km from the rupture. Geographic Coordinate System: WGS 1984. Projection: Datum WGS 1984.

Table 2-4. Local (<30 km from epicenter) Coulomb source and receiver fault orientations

	Mineral earthquake
Source Faults	**strike[*] / dip / rake[†]**
NP1	177°/ 39°SW / 66° (auxiliary plane)
NP2	26° / 55° SE/ 108° (chosen rupture plane)
Receiver Faults	**strike[*] / dip / rake[†]**
NP2	26° / 55° SE/ 108° (rupture plane itself)
NAFZ	245°/ 47°NW / 126 °
CT/SPFZ/LBFZ	30°/ 45°SE / 110°

Notes: [*]Strike defined using the right hand rule. [†]Rake resolved on the fault plane by the stress tensor associated with the focal mechanism for the Mineral earthquake (see Appendix A).

Coulomb failure stress change ($\Delta\sigma_{CF}$) from the Mineral Earthquake

The M_w 5.8 Mineral earthquake caused changes in σ_{CF} over two orders of magnitude greater than the Germantown earthquake (Figures 2-11 and 2-12), although probably still too small to have an effect on regional hazard. Changes in σ_{CF} on the order of 1 bar extend only to about 5 km from the rupture and hardly exceed 1 mbar over the remainder of the study area. These changes also moved most of the Cenozoic fault systems away from failure, particularly on the SFS and northern portion of the MRFZ. Stress was essentially unchanged along the DCFZ, however stress would be increased on faults oriented like the DCFZ south of DC and on faults oriented like the SFS southeast and northwest of the Mineral epicenter (Figure 2-11).

Among all the faults with documented Cenozoic slip, only the EF (~+0.00098) and southern end of the MRFZ (~+0.00353 bars) experienced an increase in σ_{CF} from the Mineral earthquake (Figures 2-12 and 2-13, Table 2-4). The EF and MRFZ are often described as one collective fault system, the Everona fault - Mountain Run fault zone, because of their geographic closeness, however whether a direct relationship exists between the two fault systems is unknown. The southern end of the MRFZ and the EF, which is located at the southern end of the MRFZ, are both located in the stress trigger zone produced by the Mineral earthquake. Note that the strike of the EF and MRFZ are both northeast, but the dips are antithetic to each other: the EF dips to the northwest and the MRFZ dips to the southeast. The opposing dips probably explain why the spatial patterns of the regional $\Delta\sigma_{CF}$ results for the EF almost reflect those for the MRFZ.

Figure 2-13 shows that σ_{CF} increased on the distal end of the MRFZ because of its location in the stress trigger zone of the Mineral earthquake rather than because this segment has a slightly different azimuth than the rest of the MRFZ (Table 3). Therefore, any extension of the MRFZ to the south would also be at increased risk for future seismic failure as a result of the Mineral earthquake. The stress trigger zone for faults oriented like the EF encompasses the MRFZ. Therefore, both the outcrop where the EF has been mapped in the field and any additional segments of the EF fault that extend north along the MRFZ have been moved closer to failure by the Mineral earthquake (Figure 2-13). This indicates that the Mineral earthquake moved faults striking northeast and dipping either southeast or northwest in the region at the southern end of the MRFZ closer to failure. Faults oriented like the EF greater than 10 km south of the outcrop of the EF would be brought farther away from failure by the Mineral earthquake, however there is no geologic indication that the EF would extend to the south (Figure 2-12).

Naturally, mapped faults closer to the epicenter of the earthquake had larger changes in σ_{CF}. The Mineral earthquake moved the NAFZ closer to failure by ~0.02 bars at the North Anna reactor, 1.5 bars on the Chopawamsic thrust, 2.1 bars on the Spotsylvania fault, and 0.6 bars on the Long Branch fault zone (Figure 2-14). The rupture plane itself increased σ_{CF} by ~20 bars at the rupture's edge, and ~5 bars at 5 km and 0.5 bars at 10 km from the rupture. An increase of 0.5 to 1 bars of stress change produced by the 1992 Landers earthquake (M_w = 7.3) was attributed to have triggered the 1999 Hector Mine earthquake (M_w = 7.1) (~20 km from the Landers earthquake's epicenter) [*Parsons and Dreger*, 2000]. Since the Mineral earthquake

caused a change in stress of 0.6 to 2.1 bars on the Chopawamsic thrust, Spotsylvania fault, and Long Branch fault zone it is possible that stress transfer from the Mineral earthquake could promote seismicity on these faults.

2.7.4 Assessment of seismic hazard from Coulomb stress transfer

Stress on Cenozoic-active fault systems in the Mid-Atlantic region changed by only minute amounts as a result of the Mineral (~±1 mbars) and Germantown (~±0.01 mbars) earthquakes. Some researchers argue that there is no lower threshold required to trigger seismicity from Coulomb stress transfer [*Ziv and Rubin*, 2000] and tidal stresses as small as 10 mbar have been shown to trigger earthquakes in some cases [*Tanaka et al.*, 2004; *Tanaka*, 2010; 2012]. Although the stress changes generated by the Mineral and Germantown earthquakes alone are unlikely to have a noticeable effect on the regional state of stress, except on faults that are extremely close to failure, repetition of similar events over time may be enough to influence regional seismicity.

In most cases, the Mineral earthquake decreased σ_{CF} on Cenozoic fault systems in the Mid-Atlantic region. If this relation is characteristic of CVSZ earthquakes, it is possible that activity of the CSVZ is responsible for the zones of low seismic activity present along the Appalachian belt in and around Maryland. Low seismic activity prevents a precise *a priori* identification of active fault systems in intraplate settings. My analysis focuses on fault systems with recognized Cenozoic motion. However, many Paleozoic and Mesozoic faults are present in the region, some of which may share the geometry of these Cenozoic fault systems and may have been brought closer to failure as a result of the Mineral earthquake (Figure 2-5).

Regional $\Delta\sigma_{CF}$ maps can be used to identify zones were σ_{CF} has increased on faults of a particular orientation. For example, σ_{CF} increased by ~1 mbar on faults oriented like the DCFZ near the Calvert Cliffs nuclear reactor and on faults oriented like the SFS near the Surry reactor (Figure 2-11). Because of the presence of these reactors, it is important to evaluate if such faults exist in these regions. Comparison of the Coulomb failure stress change on the MRFZ and EF show that stress triggering in the Mid-Atlantic region is particularly sensitive to fault dip.

The EF and southern segment of the MRFZ are the only Cenozoic faults considered here that may have been moved closer to failure by the Mineral earthquake, where the greatest increase in σ_{CF} (+0.00098 and +0.00353 bars respectively) exists (Table 2-3). Extremely small (+0.0015 bars) tidally induced shear stress change parallel to the San Andreas fault has been robustly correlated to non-volcanic tremor activity near Parkfield, California [*Thomas et al*., 2009]. Therefore, it is feasible that the amount of stress transferred from the Mineral earthquake to the EF and MRFZ could have been enough to promote future seismicity. However, tidally induced shear stress repeatedly applies stress over time so it is more likely that multiple earthquakes in the CVSZ would be required to move these faults to failure.

Stress also may have increased on possible continuations of the MRFZ south of the currently mapped fault zone or on other Piedmont faults in that location and on faults antithetic to the MRFZ, like the EF (Figure 2-13). The EF and MRFZ are less than 50 km from the earthquakes in the CVSZ. Perhaps the paleo-earthquakes that occurred in the CVSZ triggered slip on the EF and MRFZ. It is possible that

earthquakes in the CVSZ are feeding stress to these fault systems, perhaps explaining why they have been active in the Cenozoic.

Note there is no indication of how close to failure any of these fault systems were at prior to 2011. The accumulation of σ_{CF} over the last several million years on these fault systems and its effect on the state of stress is unknown, however this accumulation is likely the main constraint on seismicity in the eastern US. My quantification of $\Delta\sigma_{CF}$ for the Mineral and Germantown earthquakes is a first step towards evaluating the effects of stress transfer on intraplate seismicity and the state of stress in the Mid-Atlantic region of the eastern US.

2.8 Conclusions

Based on my modeling and compilation of seismic and geologic data, I reach the following main conclusions:

1. The maximum permanent vertical surface displacement at the epicenter of the Mineral earthquake (focus depth at 6 km) is ~9 cm based on length-displacement relations and Coulomb elastic dislocation modeling.
2. Overall, the Mineral and Germantown earthquakes brought the DCFZ, SFS, and northern section of the MRFZ further away from failure. The EF and southern portion of the MRFZ are the only locations that appear to have been loaded as a result of these earthquakes, although by only ~1 mbar. Accumulation of σ_{CF} on these fault systems from multiple earthquakes likely is needed to significantly affect regional seismicity.

3. Accumulation of stress sources in an intraplate environment can reactivate old faults or create new faults. The rupture plane of the Mineral earthquake occurred between the Chopawamsic thrust fault and the Spotsylvania fault zone within the Chopawamsic Terrane of the Piedmont province and does not match any previously mapped Paleozoic and Mesozoic fault systems in the epicentral region on the surface or in cross-section. Perhaps the earthquake occurred on a new fault.
4. The orientation of the Mineral earthquake's rupture plane is remarkably similar to the orientation of the MRFZ (~ 50 km north of the earthquake), which shows evidence of Cenozoic offset. These structures could be connected to each other at depth by the Appalachian décollement (~10 km). Possibly a spatially widespread system of faults with similar orientations is active and responsible for the Mineral earthquake and recent seismicity in the CVSZ.

2.9 Outlook

Although the Mineral earthquake occurred in a previously identified zone of elevated seismic hazard [*Petersen et al.*, 2008], the CVSZ, the fault responsible for the earthquake was not identified prior to the event as being more likely to rupture than its neighbors [*Davis et al.*, 2001; *Southworth et al.*, 2007]. Furthermore, the Mineral earthquake was about one magnitude unit larger than previously recorded earthquakes in the CVSZ. The PSHA maps for the eastern U.S. were created using previously recorded earthquakes, and are thus now outdated with the occurrence of

the Mineral earthquake. The Mineral earthquake fuels the need to revisit PSHA maps as well as policy regarding safe siting and operation of nuclear reactors in the eastern US. Future constraints on the structure of the lithosphere and modeling of seismic stress sources are required to improve our understanding of intraplate seismicity in general. In addition, perhaps monitoring of Coulomb failure stress change ($\Delta\sigma_{CF}$) after each earthquake could help quantify the accumulation and migration of stress in the lithosphere over time and thus improve forecasts of seismicity in the eastern U.S.

Chapter 3: Seismicity rate changes in the near-field and far-field from the August 2011, Mineral, Virginia earthquake

3.1 Abstract

Earthquakes generate static and dynamic changes in stress in both the near-field, the traditional aftershock zone, and the far-field, at long-distances up to thousands of kilometers from their epicenters. On August 23, 2011 a magnitude 5.8 earthquake struck near Mineral, Virginia, drawing renewed attention to intraplate seismicity in the eastern Unites States. I examine changes in the seismicity rate associated with the Mineral earthquake in both the aftershock zone and at distances spanning from the Mississippi River to the coast of the eastern seaboard. First I characterize the Mineral earthquake by comparing its aftershock decay rate with that of blind thrust earthquakes with similar magnitude, focal mechanism, and depth from a variety of tectonic settings. In particular, I compare aftershock decay relations of the Mineral earthquake with two well-studied California reverse faulting events, the August 4, 1985 Kettleman Hills (M_w = 6.1) and October 1, 1987 Whittier Narrows (M_w = 5.9) earthquakes. The aftershock decay rate from the Mineral earthquake is much slower than the Californian events, supporting the hypothesis that aftershocks in active tectonic margins typically last only a few years while aftershocks in intraplate regions could endure for a decade or more. In the near-field of the Mineral earthquake, aftershocks defining the Late Steep fault zone, a cluster of events occurring ~100 days after the mainshock, appear to be triggered by Coulomb stress transfer from the Mineral earthquake. In the far-field, we observe no seismicity rates greater than the

98% threshold in the Eastern Tennessee Seismic Zone, Middleton Place - Summerville Seismic Zone, Wabash Valley Seismic Zone, or New Madrid Seismic Zone. There is no clear evidence of remote triggering from the Mineral earthquake, however, the possibility that a swarm of earthquakes that occurred near Albany, New York, and one event in West Virginia that occurred on August 25, 2011 (two days after the mainshock) were triggered by the passage of seismic waves from the Mineral earthquake cannot be ruled out.

3.2 Introduction

On August 23, 2011, a M_w 5.8 earthquake, one of the largest earthquakes in the U.S. east of the Rocky Mountains in more than a century, struck near the town of Mineral, Virginia (Figure 1-1). Ground motion from the Mineral earthquake was felt as far west as Minnesota and from Florida to Fredericton, New Brunswick, Canada [*Hough*, 2012], over a much wider region than most western U.S. earthquakes of a similar magnitude (Figure 2-3). The Mineral earthquake also generated landslides and groundwater-level changes at long-distances from its epicenter (~245 km and ~560 km, respectively) [*Jibson and Harp*, 2012; *Roeloffs*, 2012] (Figure 3-1A). A multi-institution deployment of seismometers in the epicentral region of the Mineral earthquake has yielded the best recorded aftershock sequence in the eastern U.S. [*Horton and Williams*, 2012; *McNamara et al.*, 2013]. The Mineral earthquake offers a rare opportunity to examine the influence of a moderate magnitude earthquake on seismicity in intraplate North America and to gain insight into the mechanics of earthquake triggering.

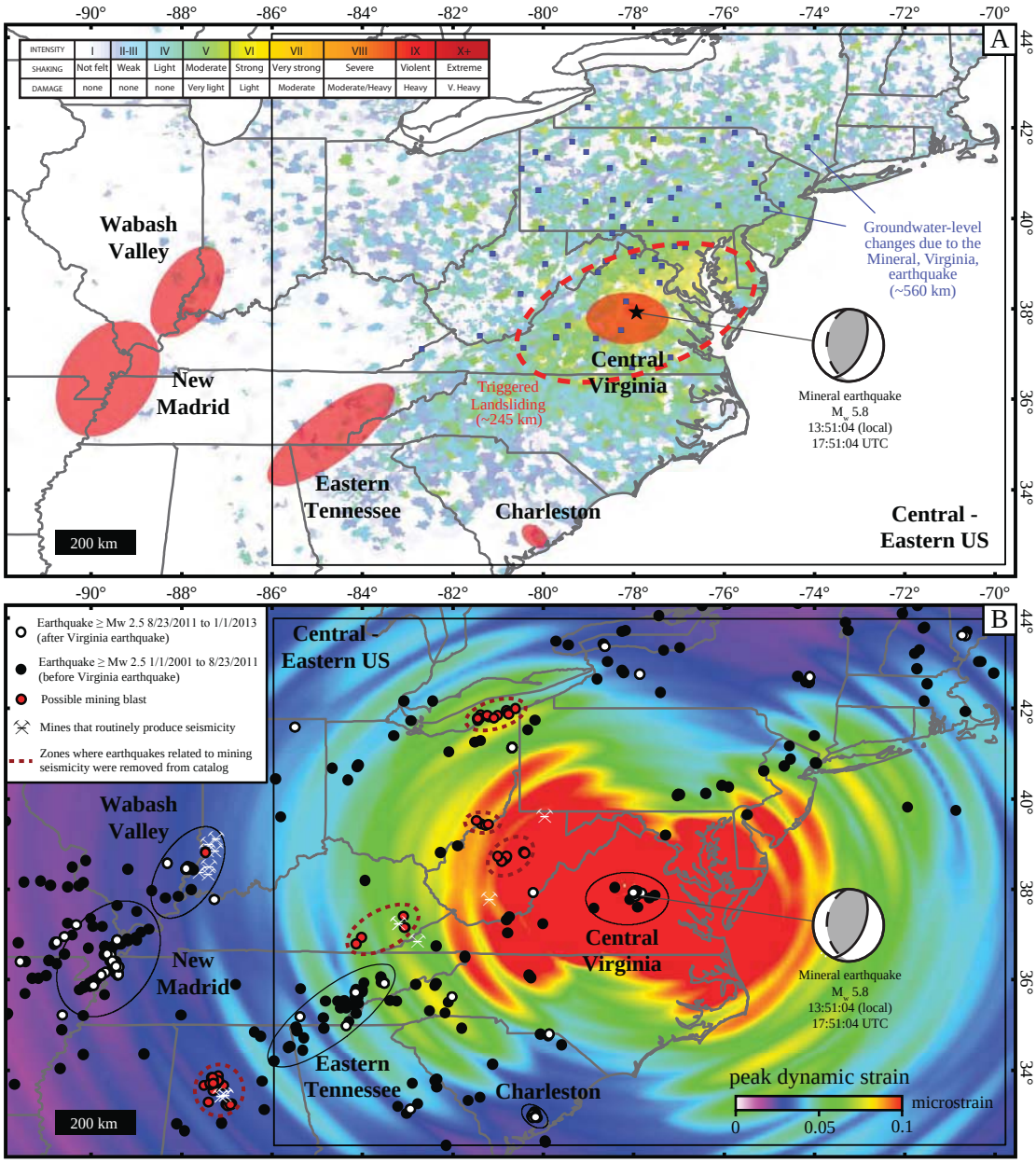

Figure 3-1. Seismic zones in the central and eastern U.S.
Seismic zones and regions of interest in the central and eastern U.S. examined for this study. A) Long-distance regional effects from the Mineral earthquake included (1) felt ground motion indicated by the USGS Community Internet Intensity maps, (2) landsliding (dashed ellipse) [Jibson and Harp , 2012], and 3) groundwater-level changes (blue squares) [*Roeloffs*, 2012; *USGS*, 2013a]. Intensity is reported by zipcode and was obtained from the USGS event pages for the Mineral earthquake. Maximum intensity for the region surrounding the Mineral earthquake was VII in the epicentral region. B) Peak dynamic strain generated by the passage of seismic waves from the Mineral earthquake (*Fred Pollitz*, USGS, personal communication). Ellipses delineated by red dashed lines indicate major mining regions known to produce blast large enough to be detected by regional seismic networks that were removed from the catalog. Boundaries are from the North American Atlas - Political Boundaries jointly compiled by the Government of Canada, USGS, and Instituto Nacional de Estadistica y Geografia [2010]. Geographic Coordinate System: WGS 1983. Projection: Datum WGS 1983.

Stress changes associated with earthquakes can induce or retard seismicity in the aftershock zone, the near-field, and at great distances far from its epicenter, in the far-field [*Gomberg and Davis*, 1996; *Freed*, 2005; *Hough*, 2007; *Hill*, 2008; *van der Elst and Brodsky*, 2010]. Aftershocks generally occur within 1 to 2 fault lengths from the mainshock's epicenter [*Kanamori*, 1977]. The spatial distribution of aftershocks are often controlled by the transfer of Coulomb stress from the mainshock [*Lin and Stein*, 2004]. However, the zone of earthquake triggering can extend to remote distances thousands of kilometers wider than the near-field aftershock zone surrounding the mainshock. Remotely triggered earthquakes from the 1992 Landers earthquake were the first instance in which the phenomenon of long-distance dynamic triggering was widely documented [*Hill et al.*, 1993; *Bodin et al.*, 1994]. Increases in both regional and global seismicity have been tied to remote triggering from earthquakes in a variety of tectonic settings [*Gomberg and Davis*, 1996; *Stark and Davis*, 1996; *Gomberg*, 2001; *Glowacka et al.*, 2002; *Hough and Kanamori*, 2002; *Parsons et al.*, 2012; *Pollitz et al.*, 2012]. Remotely triggered earthquakes succeeded the 1811-1812 New Madrid earthquake sequence, the 1886 Charleston, South Carolina, earthquake, and magnitude 4.9-6.1 events in eastern Canada, indicating that long-distance triggering can occur in intraplate regions such as the central and eastern U.S. (CEUS) as well as in tectonic plate boundary zones [*Hough*, 2001; *Hough et al.*, 2003; *Hough*, 2007]**.**

In this chapter, I first compare the Mineral earthquake's aftershock decay sequence to two similar Californian earthquakes, the 1985 M_w 6.1 Kettleman Hills and 1987 M_w 5.9 Whittier Narrows events [*Linde and Johnston*, 1989; *Ekstrom et al.*,

1992]. Then I evaluate the role of Coulomb stress transfer in the triggering of aftershock defined fault zones in the epicentral region of the Mineral earthquake. Next, I assess whether or not the Mineral earthquake triggered earthquakes at remote distances by evaluating if there was a significant change in the seismicity rate after the Mineral earthquake in the Mid-Atlantic region of central and eastern U.S. as a whole as well as in its major seismic zones.

3.3 Methodology

3.3.1 Regions of interest, earthquake catalogs, and magnitude of completeness

The Mineral earthquake's aftershock zone (near-field)

Multiple institutions including the United States Geological Survey (USGS), Virginia Polytechnic Institute and State University (Virginia Tech), Lamont-Doherty Earth Observatory of Columbia University, University of Memphis Center for Earthquake and Research Information (CERI), Lehigh University, Incorporated Research Institutions for Seismology (IRIS), and Cornell University deployed temporary seismometers in the source region immediately following the mainshock (Figure 3-2) [*Horton and Williams,* 2012]. This aftershock detection seismic network was in place approximately three days after the mainshock and deployed through May 2, 2012, allowing a timeframe of 253 days (~8 months) to capture the characteristics of the aftershock decay sequence. An initial catalog of detected aftershocks is available on the USGS website for the Mineral earthquake at http://earthquake.usgs.gov/regional/ceus/se082311a/aftershocks.php, however

Figure 3-2. Temporary seismic station in epicentral region of the Mineral earthquake
Steve Ploetz, a field engineer, installs a temporary USGS seismic station named PTRD in Spotsylvania County, Virginia, one of over 30 installed by a variety of organizations within three days after the mainshock. Photo taken thanks to Alana Leeds who agreed to meet with me during the days immediately following the mainshock in the epicentral region near the town of Mineral, VA.

seismologists are currently using a hypocentroidal decomposition algorithm to prepare a catalog of calibrated, relocated aftershocks spurred by the August 2011 Mineral earthquake [*McNamara et al.*, 2013]. I used a preliminary version of this catalog (*Daniel McNamara*, USGS, personal communication) to characterize the decay rate of aftershocks in the epicentral region of the Mineral earthquake and compare them to the aftershock decay rate produced by the California earthquakes.

I used earthquake catalogs publically available from the Northern California Earthquake Catalog and the Southern California Earthquake Data Center (based on permanent seismic networks) to characterize the aftershock decay rate of the Kettleman Hills, Northern California, and Whittier Narrows, Southern California, earthquakes for comparison to the Mineral earthquake. Tables 3-1 and 3-2 include the basic information for each aftershock sequence's mainshock. I only extracted earthquakes recorded within a 15 km radius of the mainshock in order to consistently examine the aftershock decay of regions with the same geographic extent (Table 3-3). Comparisons of the magnitude frequency relations indicated earthquakes less than magnitude 2.2 were not consistently detected from the temporary seismic network deployed in the epicentral region of the Mineral earthquake and events less than ~1.8 were not detectable in the region of the Kettleman Hills and Whittier Narrows events. Therefore I also used a M_c of 2.2 in order to consistently compare the aftershock decay rate of the Mineral earthquake to these California events (Figure 3-3).

The Mineral earthquake's aftershock sequence consists of four subdivisions or named fault zones: The Quail fault zone, Fredericks Hall fault zone, Late Steep fault zone, and North of Cuckoo fault zone [*Horton et al.*, 2012] (Figure 3-4). The Quail

Table 3-1. Earthquake information comparison

Earthquake Name	Location	Date	Lat. (°)	Long. (°)	Depth (km)	strike (°)	dip (°)	rake (°)
Mineral	Central Virginia	8/23/2011	37.936	-77.933	6	26	55SE	108
Kettleman Hills	Northern California	8/4/1985	36.1385	-120.159	10.1	145	25NE	110
Whittier Narrows	Southern California	10/1/1987	34.061	-118.079	14.6	90	27N	90

Table 3-2. Earthquake moment release, stress drop, duration, and surface displacement

Earthquake Name	M_w	Moment Release (N.m)	Stress Drop (MPa)	Source duration (seconds)	Maximum Predicted Vertical Surface Displacement (modeled) (mm)	Maximum Vertical Surface Displacement (observed) (mm)
Mineral	5.7	5.75E+17	40 -75	3	90	
Kettleman Hills	6.1	1.60E+18		16	60	10.18
Whittier Narrows	5.9	7.00E+17	17.5 ± 5.0		38	50

Table 3-3. Aftershock decay study parameters

Earthquake Name	Radial Distance from epicenter that defines area used to extract aftershocks	Magnitude threshold	b-value	p	c	k
Mineral Virginia	15	2.2	0.91	0.76	5	22.6
Kettleman Hills	15	2.2	0.68	1.13	0.746	34.5
Whittier Narrows	15	2.2	0.83	1.25	0.338	24.5

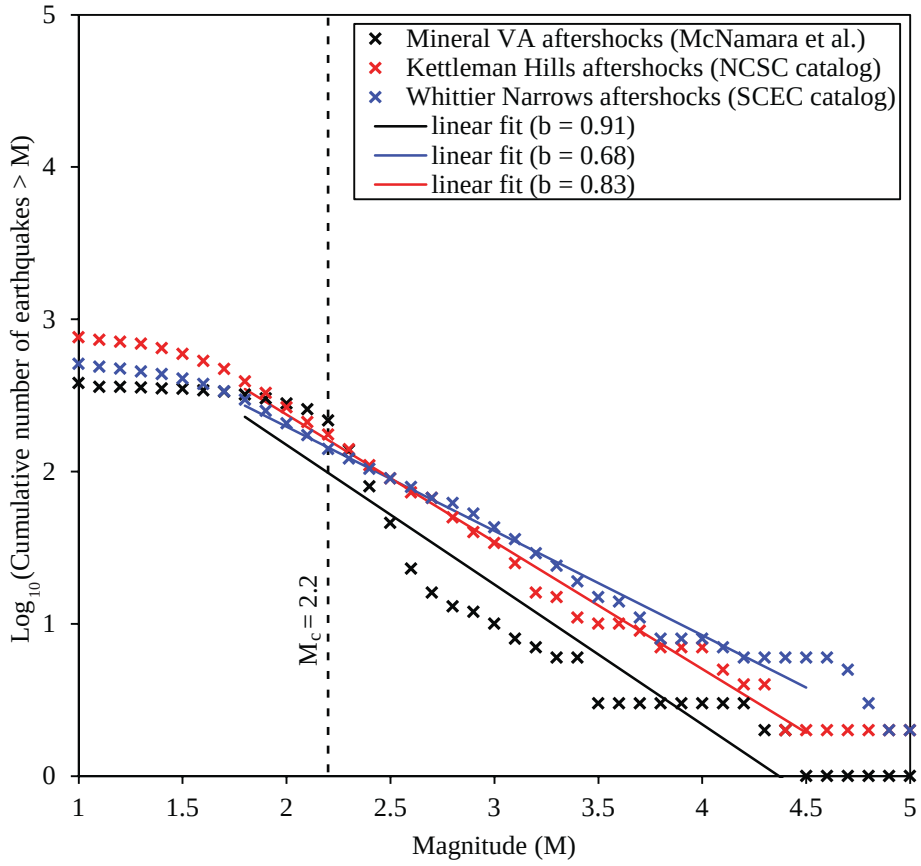

Figure 3-3. Magnitude of completeness for aftershock databases
Cumulative number of aftershocks by magnitude (M) within a 15 km radius of the Mineral, Kettleman Hills, and Whittier Narrows earthquakes. I applied a common magnitude of completeness (M_c) of 2.2 to each catalog before fitting the modified Omori's decay law curve. Corresponding b-values are derived from linear fits over the $1.8 \leq M \leq 4.5$ range. The p-values indicate that the aftershock decay rate of the Mineral earthquake was much slower than the decay rate of aftershocks triggered by the California earthquakes.

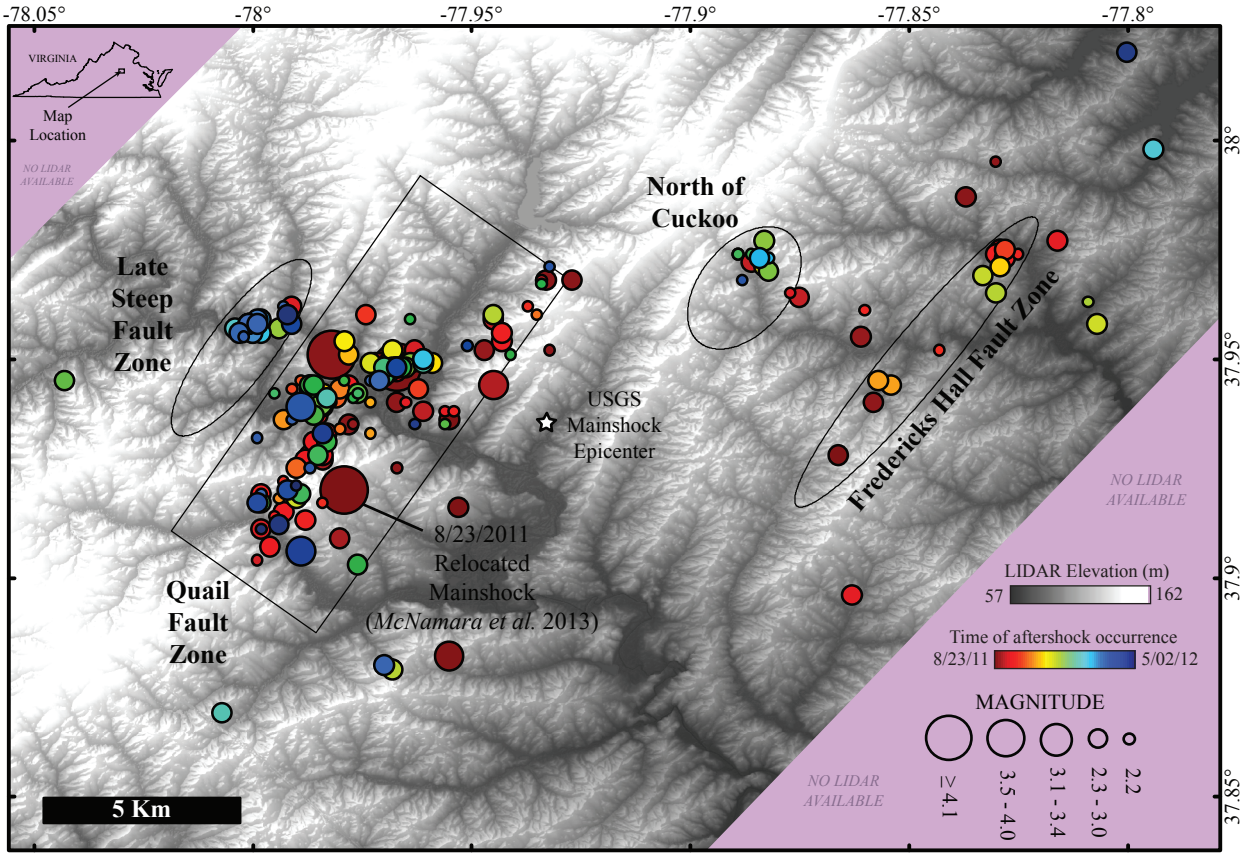

Figure 3-4. Aftershock delineated fault zones in the epicentral region of the Mineral earthquake Relocated aftershocks from McNamara et al. [2013] with aftershock fault zones delineated by Horton et al. [2012]. Aftershocks are superimposed on the 1/9 arc-second light detection and ranging (LIDAR) elevation data collected post-earthquake available from the National Elevation Dataset. Geographic Coordinate System: WGS 1983. Projection: Datum WGS 1983.

fault zone is defined by aftershocks that match the rupture plane defined by the mainshock's focal mechanism. The North of Cuckoo and Fredericks Hall fault zones are located east of and perpendicular to the strike of the rupture plane. Aftershocks in the Late Steep fault zone are shallower than those in the Quail fault zone and define a plane that dips more steeply than the mainshock's rupture plane (See Chapter 2, Figure 2-7). In the following sections, I will investigate the timing and spatial distributions of the aftershocks in each of these fault zones to assess their influence on the aftershock decay rate from the Mineral earthquake.

Seismicity rate changes at long-distances (far-field)

I primarily used the catalog of earthquakes from the National Earthquake Information Center (NEIC) to search for any changes in the regional seismicity rate related to dynamic triggering from the Mineral earthquake. I subdivided the catalog into the following regions of interest for this analysis: 1) the Central – Eastern U.S. (without seismic zones), 2) the Central Virginia seismic zone (CVSZ), 3) the Eastern Tennessee seismic zone (ETSZ), 4) the Middleton Place - Summerville seismic zone (MPSSZ) near Charleston, South Carolina, 5) the Wabash Valley seismic zone (WVSZ) and the 6) the New Madrid seismic zone (NMSZ) (Figure 3-1A). Ellipses shown in Figure 3-1 were delineated following publications on each of these seismic zones [*Braile et al.*, 1982; *Madabhushi and Talwani*, 1993; *Kelson et al.*, 1996; *Hildenbrand and Ravat*, 1997; *Kim and Chapman*, 2005; *Dunn and Chapman*, 2006; *Csontos and Van Arsdale*, 2008; *Bisrat et al.*, 2012]. The Central-Eastern U.S. region, with seismic zones removed, was chosen in order to examine changes in the background seismicity in the region ranging from ~100 to 600 km outside the

aftershock zone of the Mineral earthquake. I chose to examine each major seismic zone in the central and eastern U.S. since these zones have been identified as possible pre-existing zones of weakness in intraplate North America [*Mazzotti and Townend*, 2010], and thus may be most susceptible to triggering from the passage of seismic waves.

Over the last 50 years, seismicity generated by man-made engineering activities (including blasts from coal mining, waste water injection, and hydraulic fracturing) has played a prominent role in events recorded by the regional seismic network in the central and eastern U.S. [*Simpson*, 1986; *Chapman et al.*, 1993; *Eagar et al.*, 2006; *Ellsworth et al.*, 2012]. My preliminary analysis with the IRIS earthquake catalog indicated that 25% of events recorded in the Eastern U.S. (west of 86°W) are related to mining blasts or other non-tectonic events (Figure 3-5). Many man-made events range from magnitude 1 – 2, however mining blasts with magnitudes as large as 3.5 have been recorded in the Eastern U.S. Some researchers suggest human generated seismicity may have an influence on the way in which crustal stresses are released [*Simpson*, 1986], therefore many include these events in their global and regional catalogs (with the option for removal) to allow these events to be incorporated into evaluations of seismic hazard. Since the seismicity rate in my study area is low (typically significantly less than 1 event/day at a detection threshold of 2.5), the presence of mining blasts in the earthquake catalog has the potential to dramatically skew the seismicity rate per day. This artifact could lead us to interpret periods when tectonic earthquakes and mining blasts occurred on the same day to

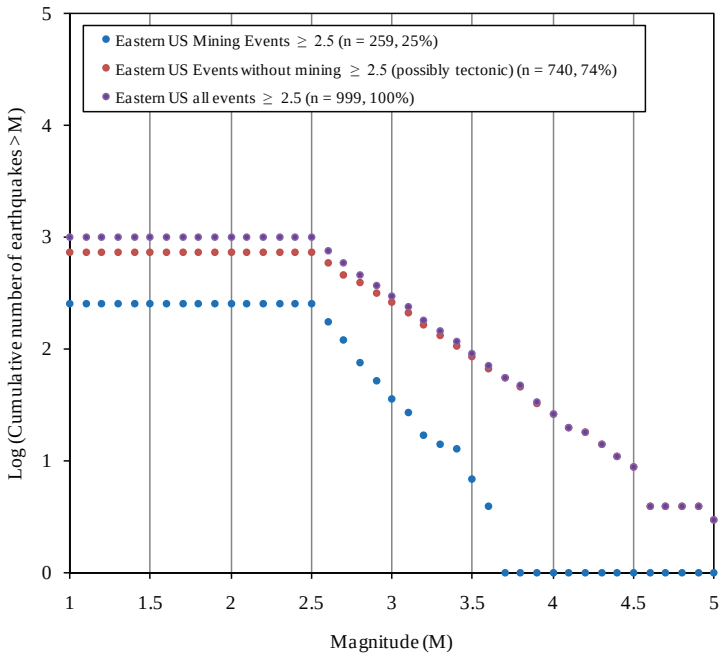

Figure 3-5. Number of events associated with mining activities
Cumulative number of events by magnitude (M) ≥ M 2.5 from the Incorporated Research Information for Seismology (IRIS) for the Eastern U.S. (east of 86°W). Events shown are in the time period between August 23, 2001 and January 1, 2013. Twenty-five percent of events in the catalog for the region are generated by man-made engineering activities (i.e. coal mining blasts, waste water injection, or hydrofracking). Blasts associated with coal mining can produce events with magnitudes as large as 3.5.

have a seismicity rates greater than the 98% threshold and ultimately an increase in seismicity related to long-distance triggering from the Mineral earthquake (Figure 3-6).

I chose to use the catalog from the National Earthquake Information Center which enabled us to filter events related to non-tectonic processes out of the catalog. Filtering the catalog removed many non-tectonic events, however events located in mining regions known to routinely produce blasts detectable by the seismic network remained in the catalog. Major mining regions known to generate detectable man-made seismicity are shown in Figure 3-1B [*USGS*, 2013b]. I took a conservative approach by removing all earthquakes within the ellipses encompassing mining regions shown in Figure 3-1B to ensure man-made events from these regions did not skew the catalog. However, it is impossible to remove all mining events from the catalog for this analysis because not all mining blasts are documented in the catalog. The magnitude of completeness (M_c) for the NEIC catalog in each seismic zone is 2.5 (Figure 3-7). Therefore, I also cut all earthquakes less than 2.5 out of the catalog before examining changes in the seismicity rate.

An increase in the seismicity rate from remote triggering can be subtle and may only be reflected by small magnitude earthquakes. Therefore, I also zoom into the New Madrid seismic zone (NMSZ), where there is a denser seismic network, allowing a smaller magnitude of completeness to be used. The earthquake catalog maintained by the Center for Earthquake Research and Information (CERI) (http://folkworm.ceri.memphis.edu/catalogs/html/cat_nm.html) enabled earthquakes with magnitudes as low as 1.6 to be detected (Figure 3-8).

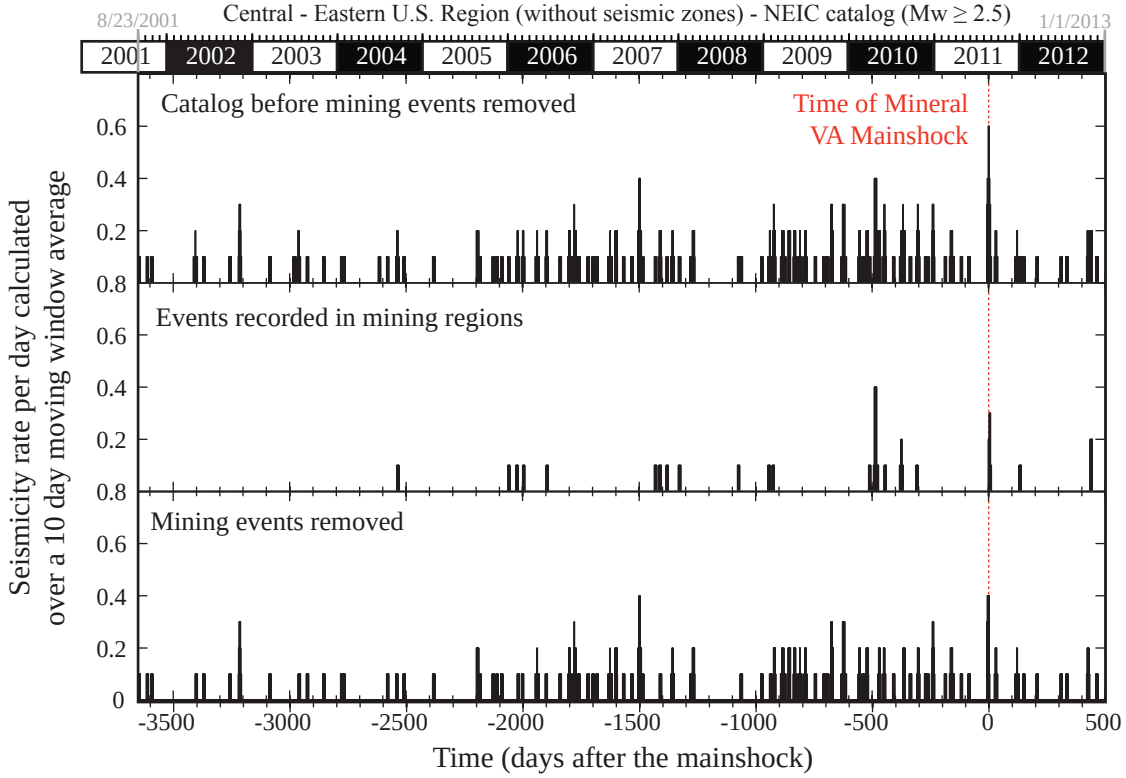

Figure 3-6. Influence of mining blasts on seismicity rate changes
Time series showing the influence of mining blasts not removed from the earthquake catalog can have on daily seismicity frequency. Notice mining related events occurred near the time of the Mineral earthquake. If these mining events were not removed, an artificial peak the day after the mainshock may lead us to interpret a long-distance triggering signal when in fact the events were purely human generated. A similar peak likely related to mining blasts also occurs ~500 days before the mainshock.

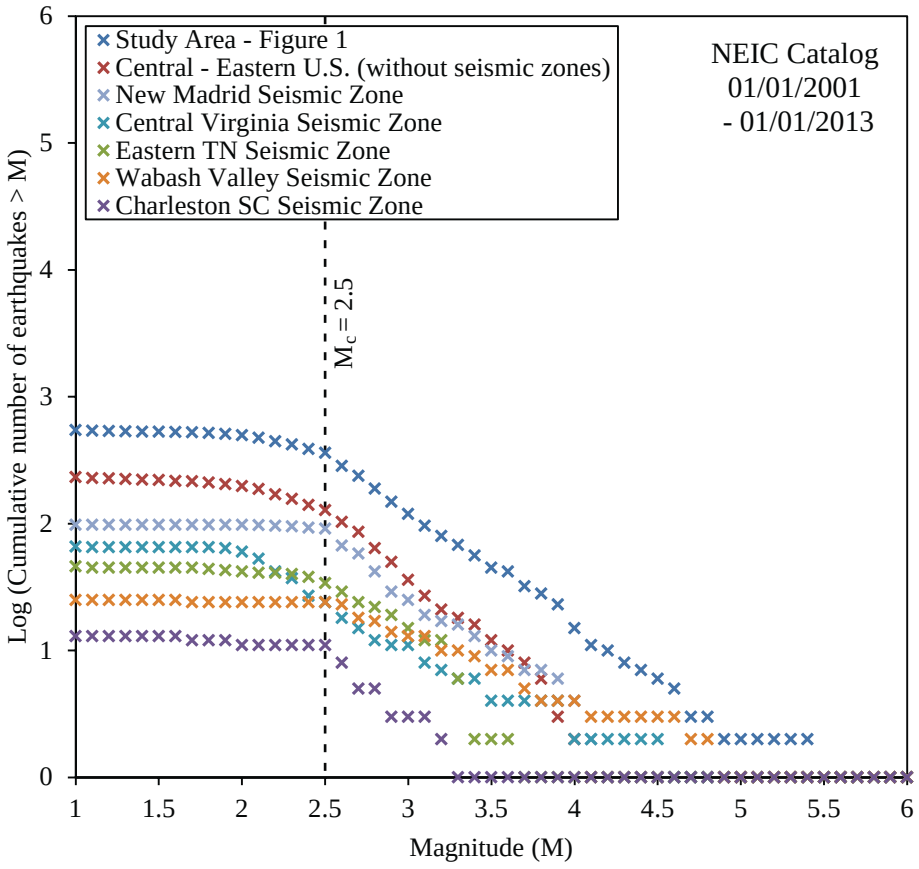

Figure 3-7. Magnitude of completeness for seismic zones in the central and eastern U.S. Cumulative number of events by magnitude (M) from the National Earthquake Information Center (NEIC) catalog within each specified region of interest. Events shown are in the time period between January 1, 2001 and January 1, 2013. I applied a common magnitude of completeness (M_c) threshold of 2.5 to the catalog before searching for signals of remote triggering.

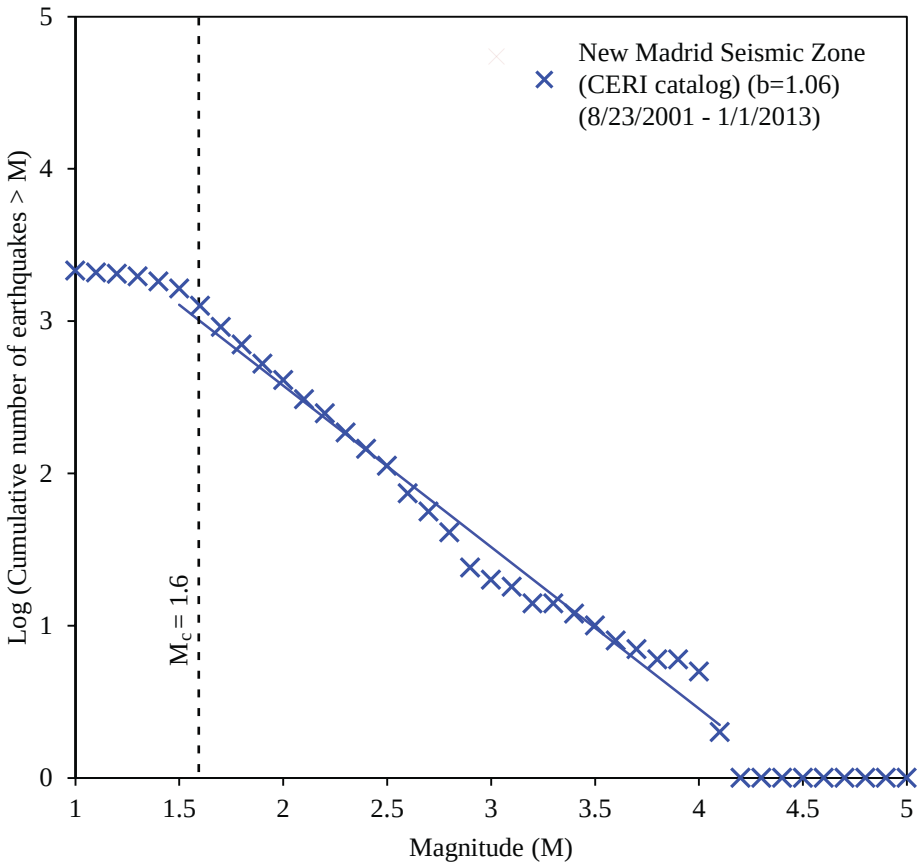

Figure 3-8. Magnitude of completeness for the New Madrid Seismic Zone (CERI catalog) Cumulative number of events by magnitude (M) from the Center for Earthquake Research and Information (CERI) catalog for the New Madrid Seismic Zone (NMSZ). Events shown are in the time period between August 23, 2001 and January 1, 2013. I applied a common magnitude of completeness (M_c) threshold of 1.6 to the catalog before analysis. Corresponding b-value was derived from a linear fit over the $1.5 \leq M \leq 4$ range.

Local catalogs, including the CERI catalog for the NMSZ, typically take great care to remove mining events from their catalog, therefore the mining issue was not an issue in this region (*Mitch Withers*, CERI, personal communication). I used the CERI catalog to re-evaluate changes in the seismicity rate in an ellipse encompassing the NMSZ for events ≥ 1.6. I also compared changes in seismicity rate in (1) the north, central, and south sub-regions of the NMSZ and (2) along sub-ellipses surrounding the Reelfoot fault (E1), Cottonwood Grove fault (E2), and North New Madrid fault (E3), and the earthquake cluster east of the Reelfoot fault (E4) (Figure 3-9).

3.3.2 Aftershock decay rate calculation

The rate of aftershocks, typically smaller magnitude events following the mainshock, tends to increase most rapidly immediately following the mainshock and less often over time. This decay of aftershocks over time follows a power law relationship known as Omori's Law [*Omori*, 1894]:

$$n(t) = \frac{K}{t + c'}$$

where $n(t)$ is the number of aftershocks per unit time above a given magnitude (M_c), t is the time measured from the mainshock, and K and c are constants [*Shearer*, 2009]. This relationship is often generalized to the modified Omori's law [*Utsu et al.*, 1995]:

$$n(t) = \frac{K}{(t + c)^{p'}}$$

which permits a more general power law relation where the exponent *p* is typically close to 1. The *p* value reflects the decay rate of the aftershock sequence, where values greater than 1 would have relatively rapid decay rates and values less than 1 would have relatively slower decay rates. *K* is the aftershock productivity and is

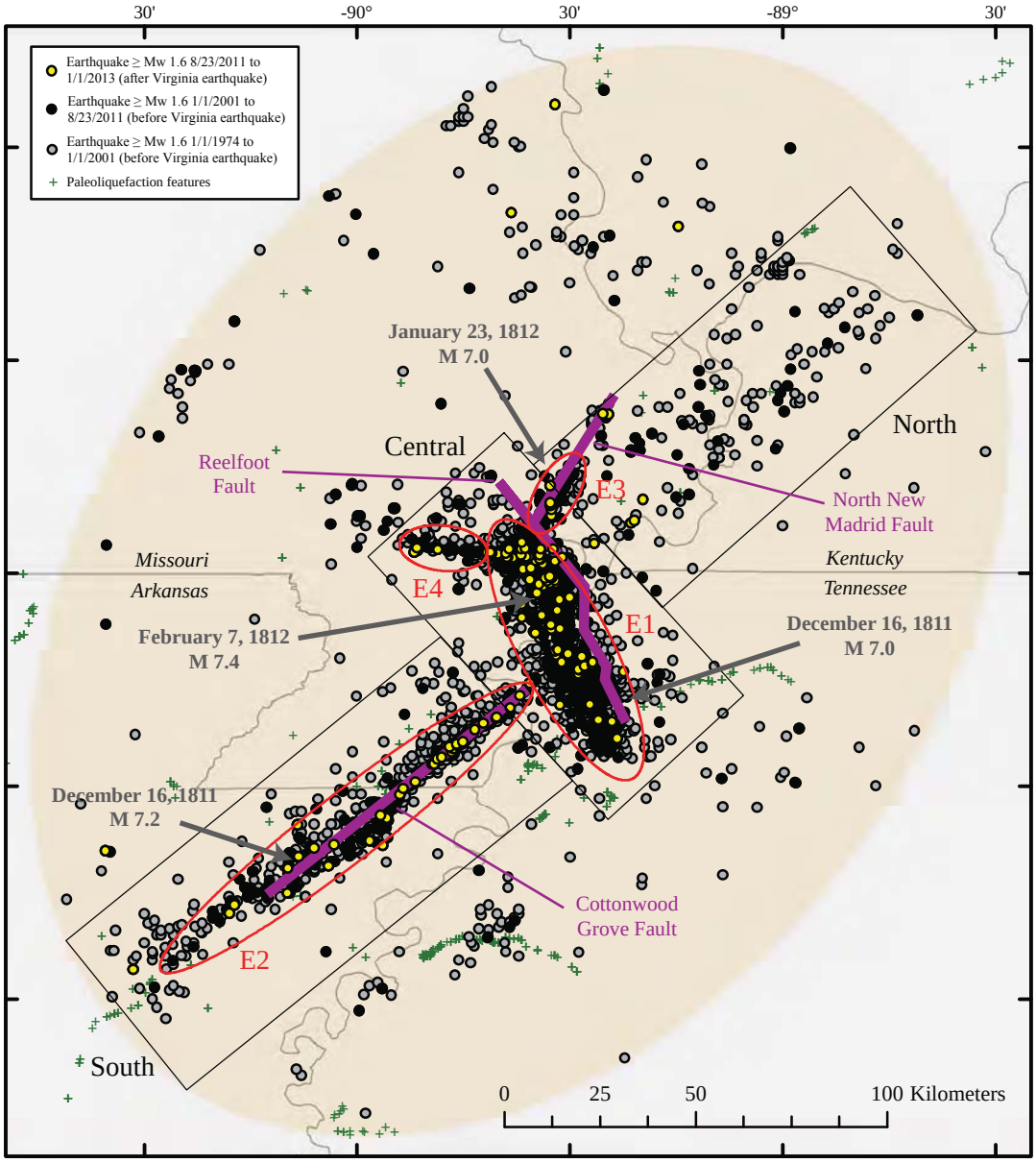

Figure 3-9. Map of seismicity in the New Madrid Seismic Zone
Spatial patterns of seismicity patterns in the New Madrid seismic zone (NMSZ). All events have magnitudes ≥ 1.6 and are from the CERI catalog. Ellipse encompassing the seismic zone defines region used in seismicity rate analysis (also shown in Figure 3-6). Locations, fault lengths, and magnitudes of the largest New Madrid earthquakes of 1811 and 1812 are from Hough [2004] and Figure 8.10 (page 114) in Stein [2010]. Paleoliquefaction features (+) are from the CEUS-SSC project [*Tuttle and Hartleb*, 2012]. Boundaries are from the North American Atlas - Political Boundaries jointly compiled by the Government of Canada, USGS, and Instituto Nacional de Estadistica y Geografia [2010].

dependent on the total number of events in the sequence and the parameter *c* relates to the rapid decrease in aftershocks immediately following the mainshock compared to a simple uniform power law decay. The *c* value marks the transition from the mainshock to the aftershock sequence and can thus provide information about the underlying mechanisms that control the aftershock occurrence [*Peng et al.*, 2006].

I used Matlab scripts based on the earthquake statistics program ZMAP [*Wiemer*, 2001] to fit modified Omori's law curves to the Mineral, Kettleman Hills, and Whittier Narrows aftershock sequences using a M_c of 2.2 and time elapse of 253 days after the mainshock. The script is designed to bootstrap a curve with the modified Omori's decay law constants for 1 day time intervals. ZMAP is freely available from the ETH Zurich Earthquake Statistics Group at http://www.earthquake.ethz.ch/software/zmap. The scripts used for this analysis were extracted from ZMAP and compiled by Brendan Sullivan, J. Luis, Zhigang Peng, and others in the Geophysics group at Georgia Institute of Technology and are available at http://geophysics.eas.gatech.edu/people/bsullivan/tutorial/StatisticalSeismology.htm. The scripts are accompanied by instructions, a tutorial, and explanations for their use on the website.

3.3.3 Identification of seismicity rate changes in the far-field

Time frame used and moving average windows

I examined a time frame from one decade before the Mineral earthquake (beginning on 8/22/2001) to ~1 year and 4 months after the mainshock (ending 1/1/2013). In order to remove the bias of the timing of an earthquake within each day

(for example, if one earthquake occurs at 11 PM and another occurs the next day at 2 AM), I applied varying moving average windows to each dataset. I calculated the average number of earthquakes per day over 3, 10, 30, and 100 days starting with the day of interest, added the seismicity rate for the number of specified days following the day of interest, and then divided by the number of days. This method of averaging enabled possible remotely triggered events to be identified in the days preceding the triggering. I also examined the seismicity rate per day with no averaging applied in conjunction with the averaged time series to identify the exact dates elevated rates of seismicity occurred and their associated geographic location.

Threshold for examining seismicity rate changes

I used a 98% threshold in order to assess increases in seismicity after the Mineral earthquake were larger than fluctuations due to random variation in the background seismicity rate. First, I first examined changes in seismicity that occurred in each region of interest over the last decade. I used the catalog of events for the decade preceding the Mineral earthquake to 1) determine the average number of events per day or background seismicity over the last decade, 2) average seismicity rate in days immediately preceding and following the Mineral earthquake, and 3) identified the rate of seismicity corresponding to the 98^{th} percentile to isolate time periods with the greatest seismicity rates. These time periods were characterized by seismicity rates falling within the 98^{th} to 100^{th} percentiles, thus encompassing 2% of the dataset, and allowed me to access the time periods in which the seismicity was especially elevated within the decade proceeding the earthquake as well as the time following the earthquake.

Dates in which the seismicity rate was greater than or equal to the seismicity rate corresponding to the 98th percentile were compared to with worldwide and local earthquake catalogs to test whether the increase in seismicity was triggered by a large magnitude global earthquake ($M \geq 7$) or a local moderate magnitude earthquake in the central and eastern U.S. ($M \geq 4$). I also explored if increases in seismicity were localized in a particular geographic location with similar magnitudes to assess the possibility that the increased rate was associated with swarm activity.

3.3.4 Frequency-Periodicity Analysis

In order to further characterize oscillations in the seismicity rate in the NMSZ, where the dense seismic network permits a lower M_c threshold (1.6), I transformed the seismicity rate time series with a 10 day moving average to the frequency-period domain via a Fourier Transform (Appendix 3-A). The purpose of this transformation is to assess if there is any significant periodicity in the seismicity rate in the NMSZ.

For this aspect of the analysis, the moving average was centered on the date of interest rather than calculated from the day of interest to the number of days in the window as in the long-distance triggering part of this study. The catalog was extended from January 1, 2001 to January 1, 2013. Ten days were removed from each end of the time series to remove any averaging affects from the database before the Fourier Transform. I present here only preliminary results and the significance of any peaks from the transform will not be evaluated.

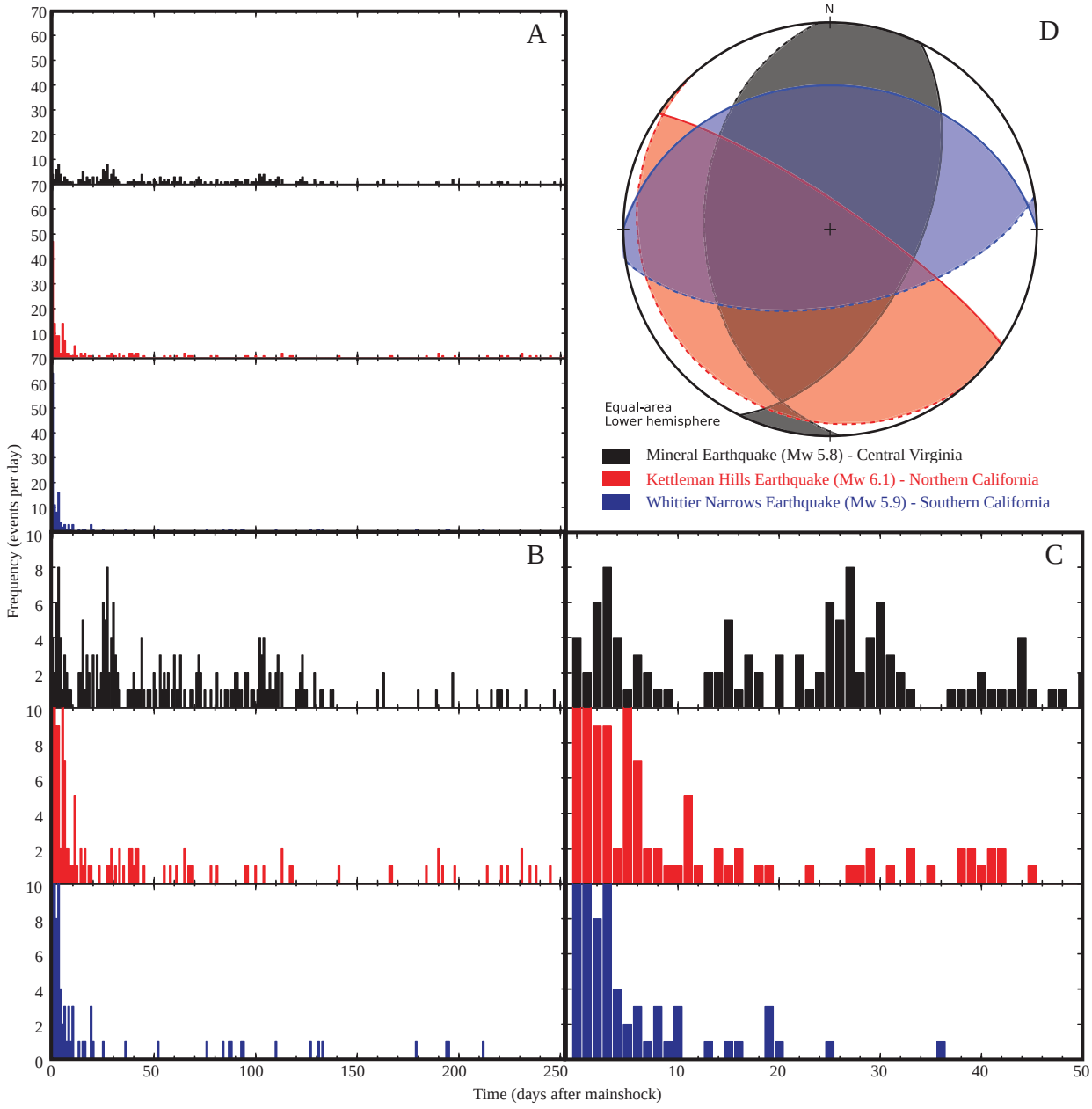

Figure 3-10. Aftershocks following the Mineral, Kettleman Hills, and Whittier Narrows earthquakes

Time series showing the number of aftershocks per day following the Mineral Virginia (black), Kettleman Hills (red), and Whittier Narrows (blue) mainshocks. The temporary seismic network in the Mineral region was not in place until ~3 days after the mainshock, therefore assumed large numbers of aftershocks immediately following the mainshock were not detected. Plot A shows each sequence with the y-axis scaled to 70 events per day. Plot B shows the same dataset with the y-axis scaled to 10 events per day. Plot C rescales the x-axis to zoom in on the first 50 days of the aftershock sequence. Plot D shows Global CMT focal mechanism solutions for each event which indicate thrust sense motion and similar dip magnitudes. Solid lines represent rupture planes associated with each earthquake and auxiliary planes are dashed (Table 3-1) [*Grohmann and Campanha*, 2010; *Grohmann et al*., 2011].

3.4 Results

3.4.1 Seismicity rate changes in the near-field (aftershock zone)

Figure 3-10 shows the number of aftershocks per day following the Mineral (Virginia) and Kettleman Hills (Northern California), and Whittier Narrows (Southern California) mainshocks [*Grohmann and Campanha*, 2010; *Grohmann et al.*, 2011]. The rate of aftershocks in the Californian aftershock sequences decrease to two or fewer aftershocks per day twenty days after the mainshock. In contrast, the rate of seismicity reflected in the aftershock sequence of the Mineral earthquake decreases in a power law decay fashion within 10 days after the mainshock, but then increases to more than two earthquakes per day ~25 and 100 days after the mainshock.

The modified Omori's law curves I fit to each observed aftershock sequence are shown in Figure 3-11. Each curve's defining parameters are Table 3-3. The p-value for the Mineral earthquake's sequence was significantly lower ($p = 0.76$) than the p-values for the California events (Kettleman Hills, $p = 1.13$; Whittier Narrows, $p = 1.25$). This is also visually apparent by comparing the shape of the decay curves in (Figure 3-11). The aftershock decay rate associated with the Mineral earthquake appears to have occurred at a much slower rate than demonstrated by the Californian events. There are also instances when the modeled aftershock decay rate for the Mineral earthquake does not closely match the observed number of aftershocks. For example, from ~6 to 28 days after the mainshock fewer aftershocks occurred than predicted. Conversely, from ~55 to 216 days after the mainshock there were significantly more aftershocks than predicted by the model. In particular, the

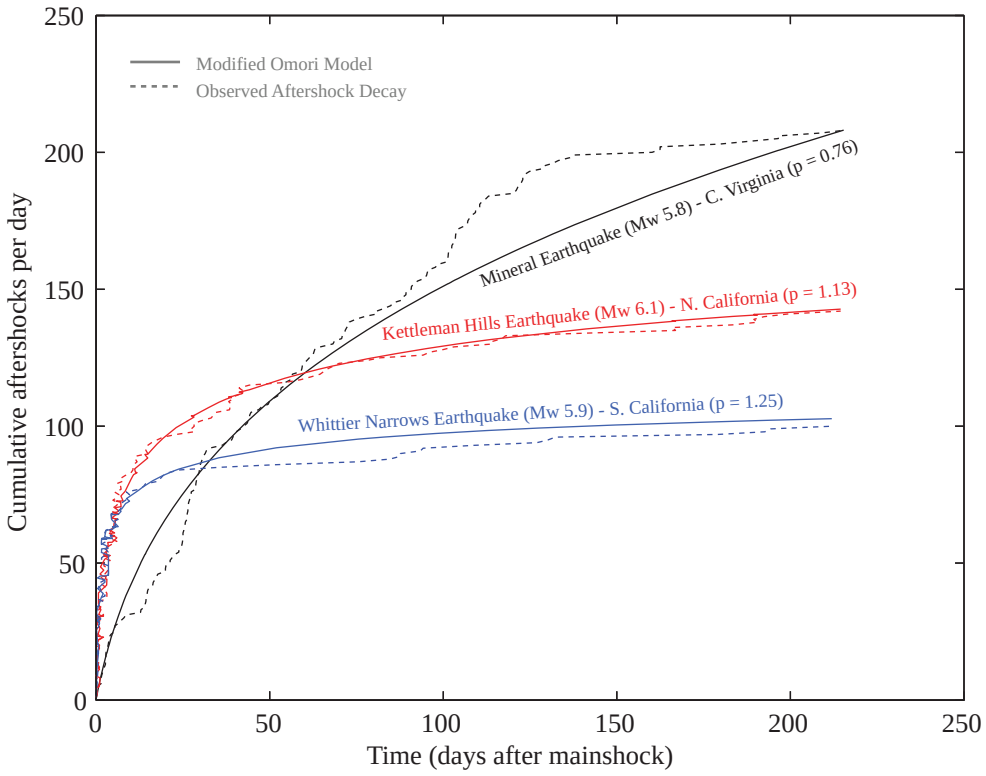

Figure 3-11. Omori's curve for aftershock decay rate of the Mineral, Kettleman Hills, and Whittier Narrows Earthquakes

Cumulative number of aftershocks versus time after the mainshock for the Mineral, Kettleman Hills, and Whittier Narrows events. Solid line is the predicted cumulative modified Omori's Law decay curve and the dashed lines show the actual observed aftershock decay.

observed rate of aftershocks 100 days or more after the Mineral earthquake far exceeded the predicted number of aftershocks by 15 to 30 events per day.

Figure 3-12 shows the number of aftershocks per day following each mainshock alongside the magnitude of each event and total moment release each day. Most events in each aftershock sequence have magnitudes close to two. There are instances during both the Virginian and Californian aftershock sequences when events with magnitudes greater than two occur causing a sharp, temporary, increase in the moment release rate. However, these spikes in moment release do not appear to correspond with any increases in the number of aftershocks per day other than the moment release from the mainshock (Figure 3-12).

The majority of recorded aftershocks that immediately followed the Mineral mainshock occurred on the Quail fault zone. Most seismicity in the Fredericks Hall fault zone, located to the east perpendicular to the mainshock, occurred ~25 days after the mainshock. Seismicity on the Late Steep fault zone, which is defined by a plane that dips more steeply than the rupture plane, occurred predominately ~100 days after the mainshock (Figures 3-4 and 3-13). Events in the North of Cuckoo fault zone and regions outside the delineated aftershock zones occurred approximately randomly throughout the time period examined.

3.4.2 Seismicity rate changes in the far-field (remote triggering zone)

Here I discuss changes in the seismicity rate observed at remote distances by examining time series (10 day moving average) for each seismic zone (Figure 3-14). The figures in Appendix B show the time series in each region of interest for all moving average windows. The only regions I examined in the far-field where there

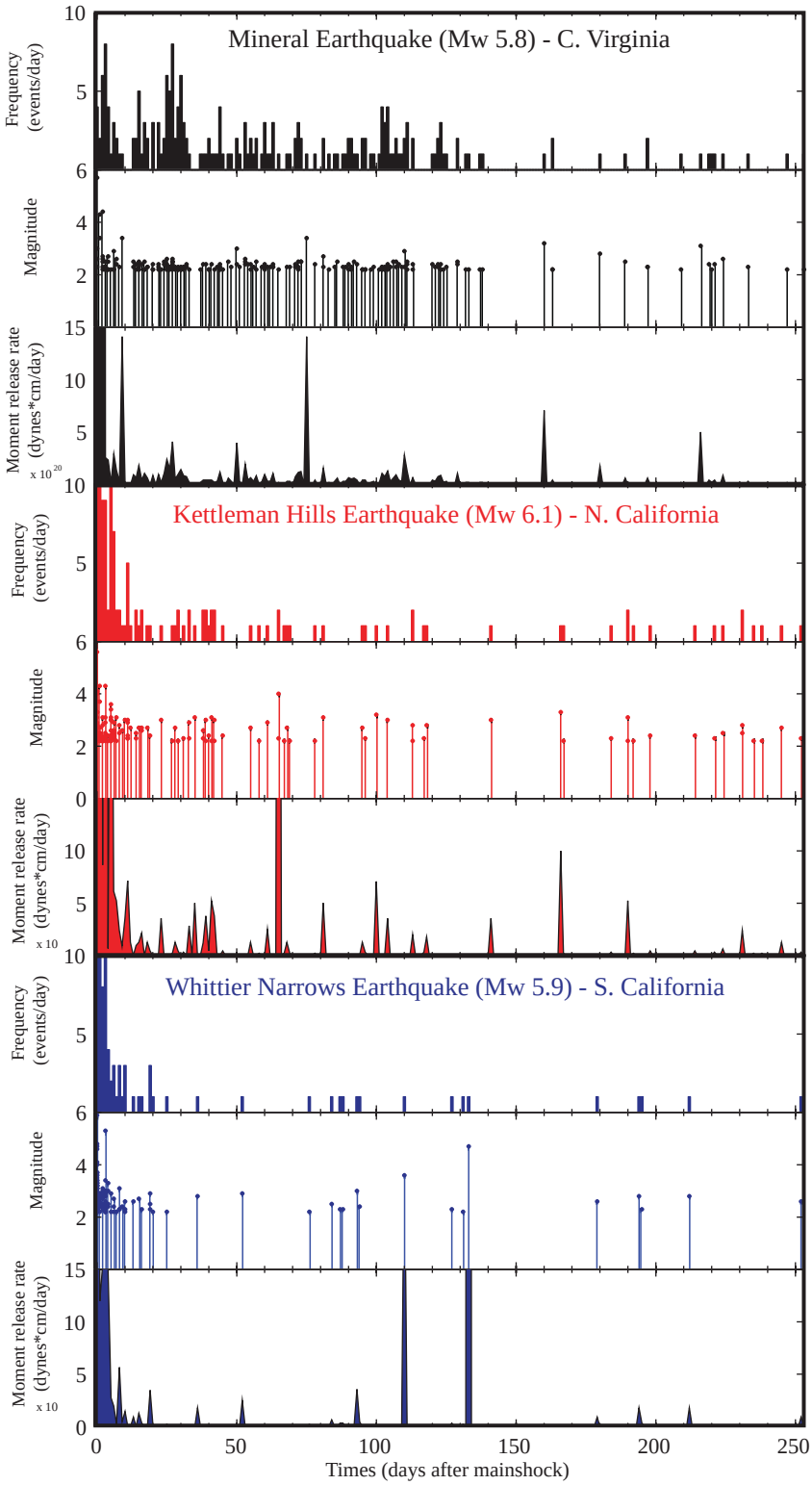

Figure 3-12. Aftershock frequency, magnitude, and moment release for Mineral versus California events

Aftershock frequency, magnitude, and moment release rate over time for the Mineral, Kettleman Hills, and Whittier Narrows aftershock sequences. Aftershocks ranging from magnitudes 3 to 4 occurring fifty or more days after the mainshock generated significant increases in the moment release rate. The change in moment release over time does not appear to explain major differences shown by the aftershock decay curves in Figure 3-11.

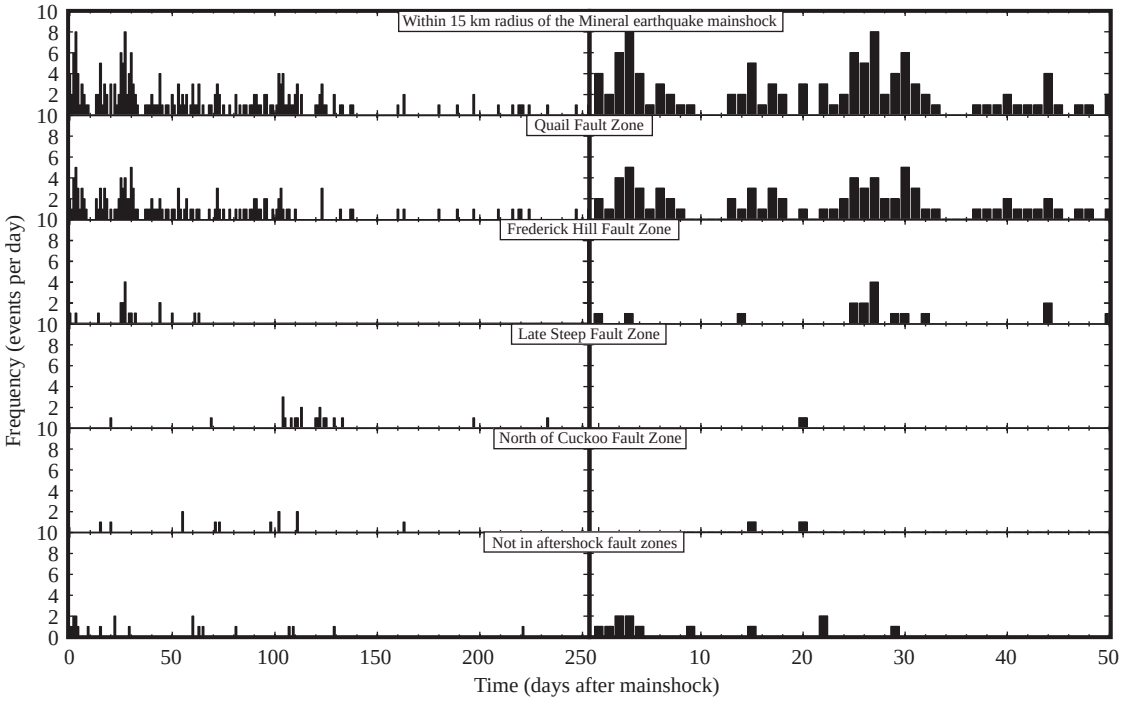

Figure 3-13. Number of events per day in each aftershock defined fault zone
Time series showing number of aftershocks per day in the aftershock zone and each named aftershock fault zone shown in Figure 3-4 [*Horton et al*., 2012]. The majority of recorded aftershocks occurred on the Quail Fault zone immediately following the mainshock, while the aftershocks that define the Fredericks Hall fault zone and Late Steep fault zone occurred ~25 and ~100 days, respectively, after the mainshock.

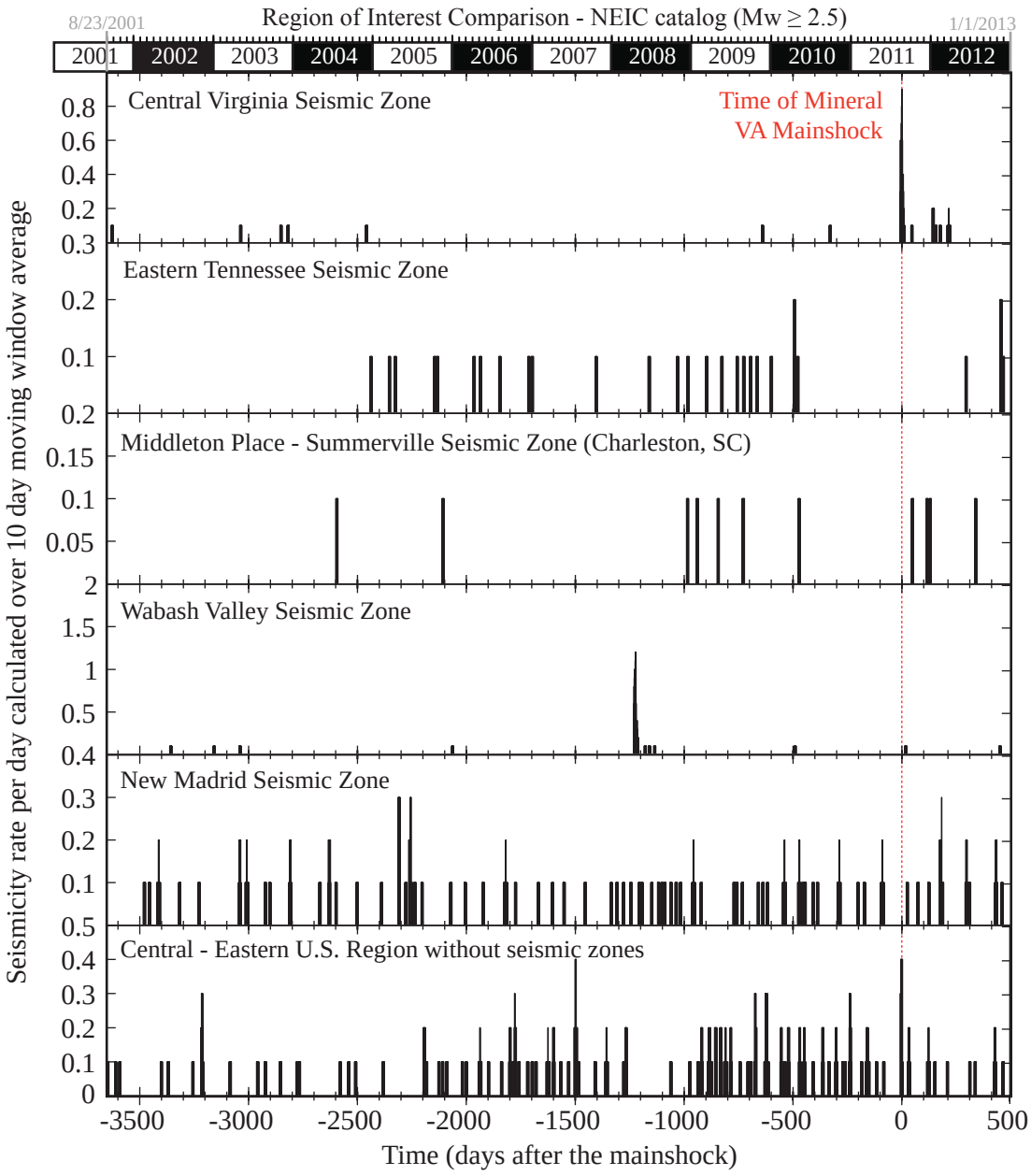

Figure 3-14. Decadal seismicity rate changes in specified regions
Seismicity rate per day (over a 10 day moving window average) for the decade before the Mineral earthquake through January 1, 2013 in specified regions of interest. The statistical significance of days with high seismicity rates occurring in the New Madrid Seismic Zones and Central – Eastern U.S. region (without seismic zones) after the Mineral earthquake are examined in Figure 3-16. Seismicity rate changes over time for no moving average and moving averages of 3, 30, 100, and 300 days for each region of interest are shown in the Figures in Appendix 3-B.

was an increase in the rate of seismicity within the 98th to 100th percentile after the occurrence of the Mineral earthquake on August 23, 2011 was in the Central – Eastern U.S. region (without seismic zones) and in the New Madrid Seismic Zone (Figures 3-14, 3-15, and 3-16). In the Central – Eastern U.S. region (without seismic zones) the seismicity rate exceeded 0.3 events per day on August 25, 2011 (two days after the mainshock) and in the New Madrid Seismic Zone the seismicity rate exceeded 0.9 events per day on February 21, 2012 (182 days after the mainshock) (Figure 3-17). This increase in seismicity was comprised of 4 events that all occurred on August 25th in West Virginia near the Virginia border and in eastern New York near Albany (Table 3-4, Figure 3-1B).

In the Central – Eastern U.S. region (without seismic zones) there was one other instance in the last decade in which the rate of seismicity exceeded 0.3 events per day. The seismicity rate exceeded 0.3 events per day on July 17, 2007, which coincides with the occurrence of two events on July 18, 2007 near Augusta, GA and Rochester, NY and two events July 24, 2007 near Albany, NY that are spaced only five days apart. In the NMSZ, the largest peak in seismicity in the last decade corresponds to 15 events that occurred between October 12th and 22nd in 2006.

No moderate events $\geq M_w$ 4 occurred in the central and eastern U.S. or large events $\geq M_w$ 7 occurred worldwide in the month preceding the events in the Central – Eastern U.S. region (without seismic zones). However, a M_w 3.4 event on October 18, 2006 and M_w 4.1 event on February 21, 2012 occurred in the NMSZ preceding the peaks in the seismicity rate in the NMSZ on October 12-22, 2006 and on February 21, 2012. The seismicity frequency time series for the north, central, and south

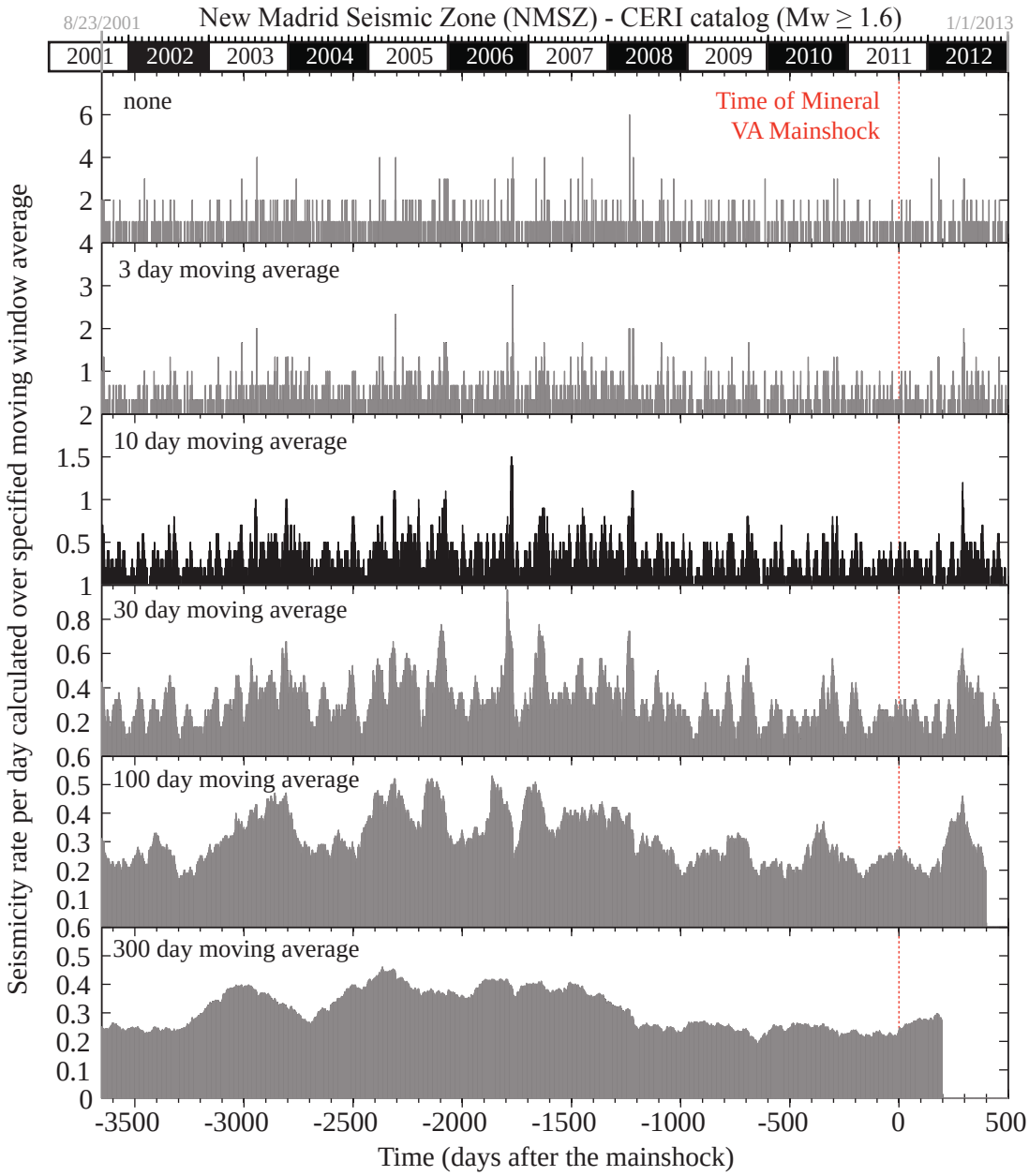

Figure 3-15. Decadal seismicity rate changes in the New Madrid seismic zone
Seismicity rate per day (over varying moving window averages) for the decade before the Mineral earthquake through January 1, 2013 in the New Madrid Seismic Zone. The time series shown in these plots use earthquake catalog data from the Center for Earthquake Research and Information (CERI) for events ≥ M 1.6). The time series with a moving average of 10 days is used to identify statistically significant events (see Figure 3-16).

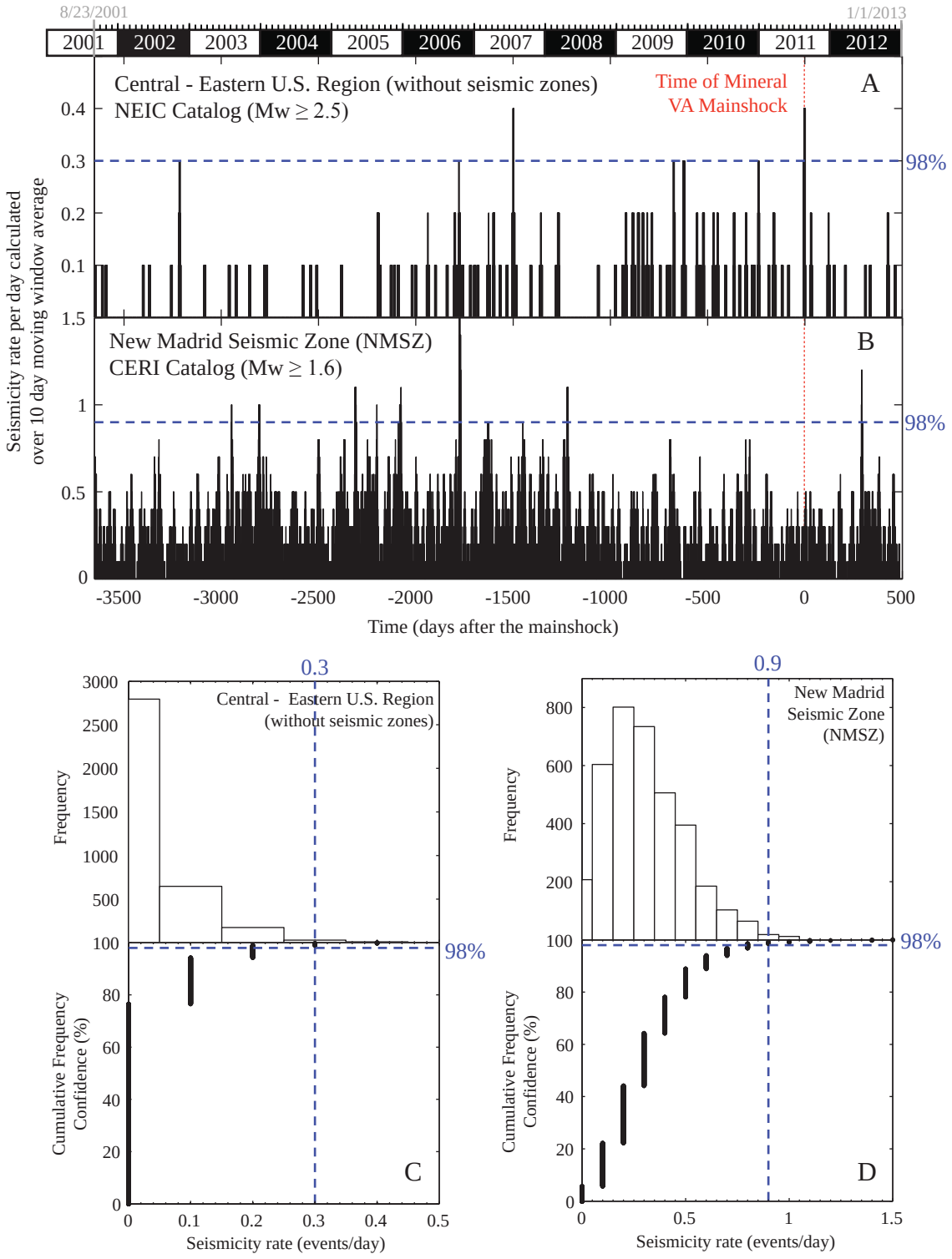

Figure 3-16. 98% threshold of seismicity rate changes
Seismicity rate over time in the Central – Eastern U.S. region (without seismic zones) (NEIC catalog) (A) and the New Madrid Seismic Zone (NMSZ) (CERI catalog) (B). Dates with seismicity rates greater than the 98% threshold, 0.3 events/day in the Central – Eastern U.S. region (without seismic zones) (C) and 0.9 events/day in the NMSZ (D), are considered to be periods of elevated seismicity in the time period spanning one decade before the Mineral earthquake through January 1, 2013.

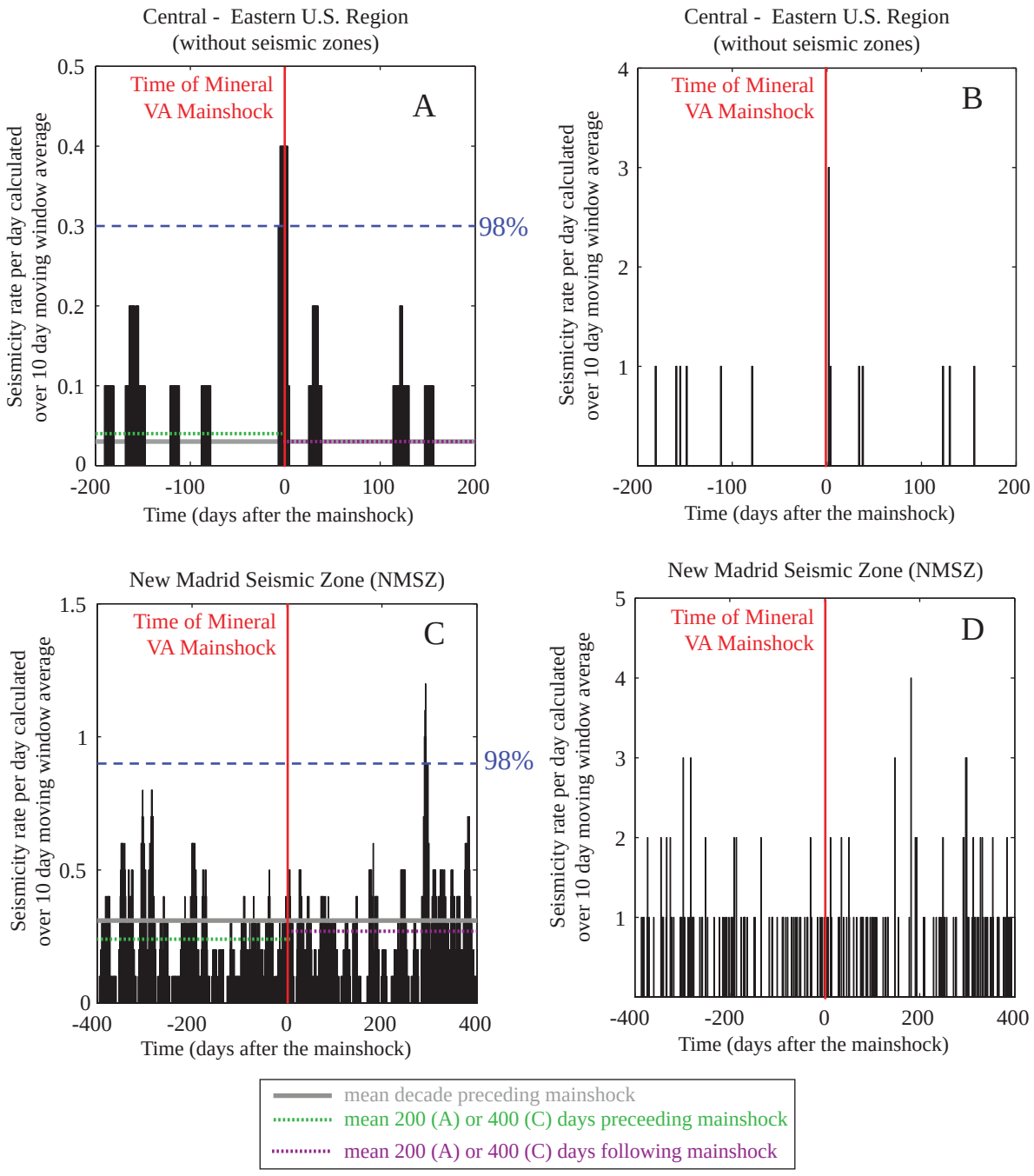

Figure 3-17. Zoom in to seismicity rate changes

Seismicity rate changes in the Central – Eastern U.S. region (without seismic zones) (A and B) and the New Madrid Seismic Zone (C and D) for 200 and 400 days, respectively, preceding and following the mainshock. Plots A and C show the number of events per day calculated over a 10 day moving window. The gray horizontal line shows the mean number of events per day over the last decade. The green dashed line shows the mean seismicity in the 200 or 400 days preceding the mainshock and the purple dashed line shows the mean seismicity in the 200 or 400 days following the mainshock. Plots B and D show the total number of earthquakes per day with no moving average applied. In the Central – Eastern U.S. region (without seismic zones), there was an elevated rate of seismicity on August 25, 2013 (2 days after the mainshock) located in West Virginia and near Albany, New York (Table 3-4). An increase in the rate of seismicity within the 98th to 100th percentiles is also present at ~182 days after the Mineral earthquake in the NMSZ.

Table 3-4. Events associated with elevated seismicity rate in the Central-Eastern U.S. following Mineral VA earthquake

Date	Origin Time (UTC)	Lat. (°)	Long. (°)	Depth (km)	M_w	Region
8/25/2011	5:59:13	37.92	-80.21	12	2.7	West Virginia
8/25/2011	13:32.2	42.68	-74.09	18	2.8	New York (Albany)
8/25/2011	20:55:53	42.69	-74.09	20	2.7	New York (Albany)
8/27/2011	14:38:40	42.69	-74.09	22	2.9	New York (Albany)

regions of the NMSZ indicate that the majority of the seismicity occurred in the central part of the seismic zone surrounding the Reelfoot Rift (Figure 3-18). There is a subtle increase in the rate of seismicity in the days immediately following the Mineral earthquake in the southern part of the seismic zone along the Cottonwood Grove fault, but this increase is not significant compared to the seismicity rate record for the decade preceding the Mineral earthquake. No other seismicity rates above the 98% threshold are apparent in any of the other sub-regions of the NMSZ after the occurrence of the Mineral earthquake.

The Fourier transform of the NMSZ seismicity rate time series does not reveal any significant periodicities; but the transform of the moment release reveals a possibly significant peak a periodicity of ~1 year (364 days) (Figure 3-19). However, other peaks from the Fourier transform at 19, 28, 38, 104, 230, 623, and 873 days (some with similar power magnitudes) indicate that the ~1 year periodicity isn't the only significant periodicity in the dataset. Further analyses including hypothesis testing by comparison to randomly generated earthquake catalogs would be needed to truly verify if there is any periodicity related to geologic processes present in the time series. I present these results here for completeness, but do not interpret them further in this chapter.

3.5 Numerical modeling

In order to further evaluate the significance of my results, I developed the models described in the subsequent sub-sections to evaluate the role of Coulomb stress transfer in the near-field (aftershock zone) and compared them to the

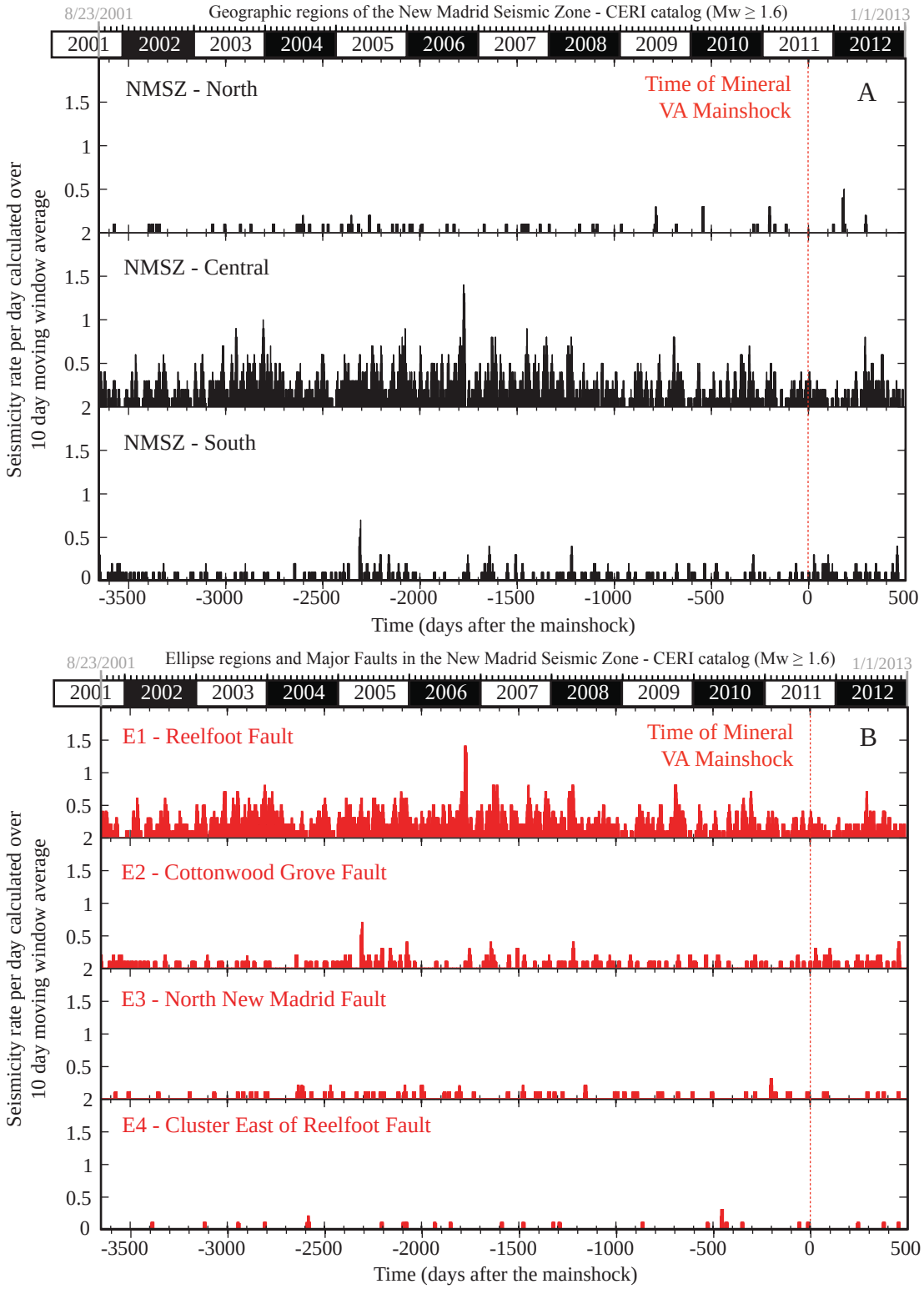

Figure 3-18. Seismicity rate changes in geographic regions and along faults in the New Madrid seismic zone

Seismicity rate changes in A) geographic regions (north, central, and south) and B) along major faults in the New Madrid Seismic Zone (E1 – Reelfoot fault, E2 – Cottonwood Grove fault, E3 – North New Madrid Fault, and E4 – Cluster east of Reelfoot fault) (Figure 3-9).

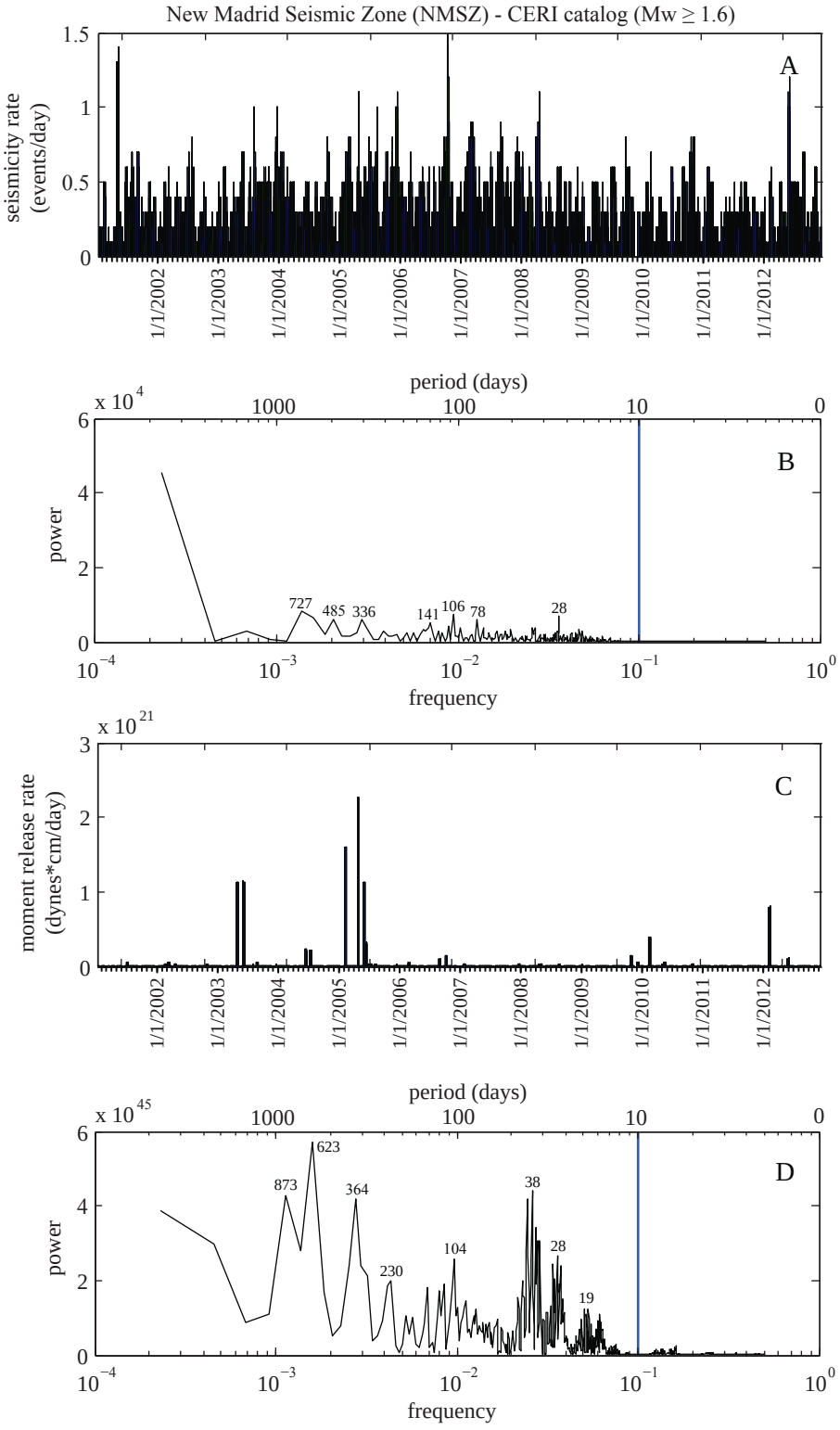

Figure 3-19. Fourier transform of seismicity rate changes and moment release in the New Madrid seismic zone

Time series of daily seismicity rate (A) and moment release rate (C) the ellipse defining the New Madrid Seismic Zone for the time period between January 1, 2001 and January 1, 2013. Rates are average values calculated using a 10 day moving window. Plots B and D show power spectra resulting from a Fourier transform of the seismicity rate (B) and moment release (D).

approximate amount of peak dynamic strain generated by the passage of seismic waves in the far-field (remote triggering zone) from the Mineral earthquake (*Pollitz*, 2013, personal communication).

3.5.1 Coulomb stress transfer in the aftershock zone

I identify regions where faults were brought closer to failure (stress trigger zones) and locations where faults were moved further from failure (stress shadows) by the mainshock in the aftershock zone by producing a model of changes in σ_{CF} using USGS Coulomb software [*Lin and Stein*, 2004; *Toda et al.*, 2005] software. Coulomb stress change, $\Delta\sigma_{CF}$, is given by:

$$\Delta\sigma_{CF} = \Delta\tau + \mu'\Delta\sigma_n$$

where Δ expresses the change in the associated stress component [*King et al.*, 1994; *Stein*, 1999; *Toda et al.*, 2005]. See Chapter 2 for more details on calculating the Coulomb stress change.

I use a coefficient of friction of μ'=0.8, which represents the high friction and stress drop expected in intraplate regions [*King et al.*, 1994; *Zoback*, 1992; *Li et al.*, 2007] in particular for the Mineral earthquake [*Ellsworth et al.*, 2011], a shear modulus of 3.2×10^5 bars and a Poisson's ratio of 0.25, which are similar to other $\Delta\sigma_{CF}$ calculations and representative of most rock types [*Toda et al.*, 2005]. In models of Coulomb failure stress change, the source fault slips and imparts stress to the surrounding crust and faults within it. Receiver faults do not slip, but receive stress transferred from the source fault. For this model, I use the rupture plane from the earthquake's focal mechanism as the source fault and the receiver fault. Therefore the model in Figure 3-20 shows the $\Delta\sigma_{CF}$ for faults in the aftershock zone with a

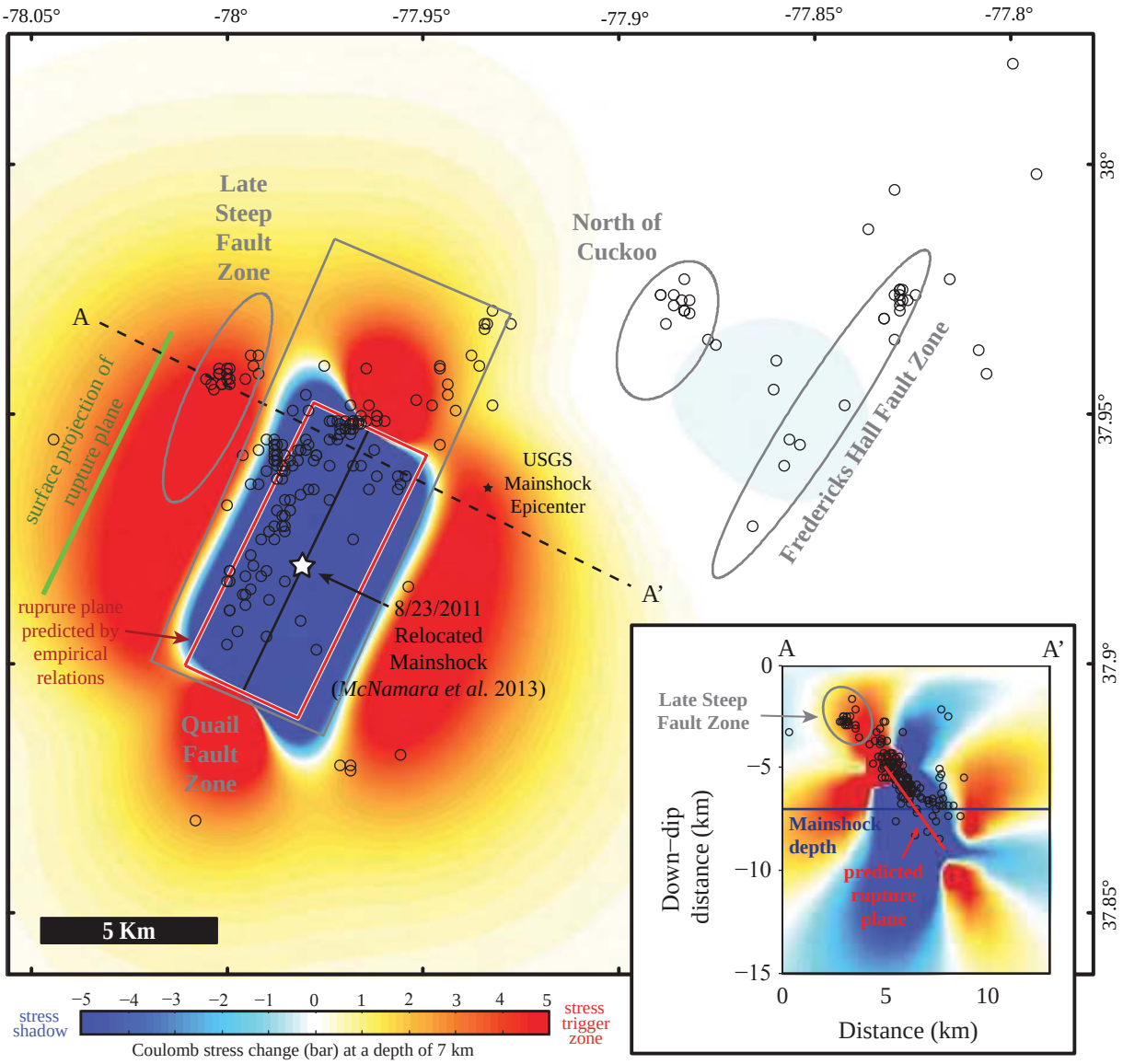

Figure 3-20. Coulomb stress transfer from the mainshock to aftershock clusters in the epicentral region

Regional Coulomb failure stress change ($\Delta\sigma_{CF}$) produced by the Mineral earthquakes mainshock. Stress is resolved for receiver faults oriented like the rupture plan of the Mineral Virginia mainshock in the local aftershock zone. Aftershocks that occurred ~100 days after the mainshock that define the Late Steep fault zone reside in a stress trigger zone produced by the mainshock. The large increase in Coulomb failure stress (5 – 6 bars) in the region of the Late Steep fault zone may explain the triggering of aftershocks in this location. Aftershocks that propagated from the rupture area towards the surface following the mainshock may also be explained by stress transfer.

similar strike and dip as the mainshock rupture plane with aftershocks relocated by McNamara et al. [2013] superimposed.

3.5.2 Strain from passage of seismic waves

Figure 3-1B shows the peak dynamic strain imparted by the Mineral earthquake's mainshock during seismic wave propagation at 600 seconds after the mainshock (well after the passage of seismic waves from the event). The seismic wavefields used to generate the peak dynamic strain grid were calculated by Fred Pollitz at the USGS - Menlo Park using the direct Green's function method of Friederich et al. [1995] on the Ibrahim and Nuttli [1967] layered Earth model. Regional seismic wavefields were calculated using a point source approximation of the August 23, 2011 mainshock from the source epicenter, depth, and moment tensor of the SLU moment tensor solution.

The actual rupture of the Mineral earthquake and structure of the lithosphere in the central and eastern U.S. is likely much more complex. However, this simplified model captures the first-order characteristics of the regional seismic wavefield produced by the Mineral earthquake, therefore enabling us to extract the approximate amount of peak dynamic strain generated by the passage of the seismic waves in each seismic zone of interest in this study. While triggering after the Mineral earthquake was not observed in many of the seismic zones, this model allows us to begin to characterize a possible minimum amount of dynamic strain required to promote remote triggering in these locations (Figure 3-21, Table 3-5). Since no signals of remote triggering were confirmed, the actual amount of dynamic strain

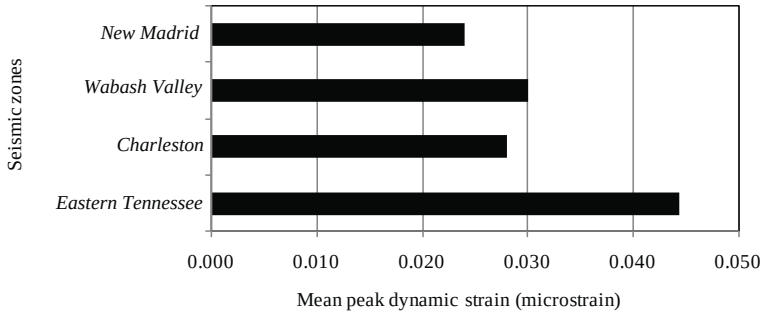

Figure 3-21. Mean peak dynamic strain in each seismic zone from the passage of seismic waves from the Mineral earthquake

Mean peak dynamic strain from the passage of seismic waves from the Mineral earthquake for seismic zones in the central and eastern U.S. Values are extracted from regions shown on map in Figure 3-1B. Table 3-5 shows all statistics for each region.

Table 3-5. Peak Dynamic Strain (microstrain) for seismic zones of interest

Seismic Zone	Minimum	1st quartile	Median	Mean	3rd Quartile	Maximum	Standard Deviation	number
Central Virginia	-0.142	0.215	0.268	0.553	0.050	13.676	1.386	166
Eastern Tennessee	0.032	0.039	0.042	0.044	0.350	0.063	0.007	310
Charleston	0.027	0.028	0.028	0.028	0.028	0.029	0.000	23
Wabash Valley	0.024	0.027	0.030	0.030	0.027	0.034	0.003	230
New Madrid	0.019	0.021	0.025	0.024	0.033	0.028	0.003	437

needed to spur long-distance triggering exceed these values possibly by several orders of magnitude.

3.6 Interpretations

3.6.1 Seismicity rate changes in the near-field (aftershock zone)

The Kettleman Hills and Whittier Narrows earthquakes have p-values that fall within a range of 0.85 to 1.3, the expected range of p-values for Californian earthquakes [*Reasenberg and Jones*, 1989; *Reasenberg and Matthews*, 1990]. Reasenberg and Jones [1989] compared the aftershock sequences from sixty-two mainshocks in California and give a p-value of 1.08 for a "generic California" aftershock sequence. Previous aftershock sequences from the following intraplate earthquakes have p-values ranging from 0.74 to 1.29: the 1982 magnitude 5.7 event near Miramichi, Canada, the 1983 magnitude 5.1 event near Goodnow, NY, the 1988 magnitude 6.8 event near Tennant Creek, Australia, the 1978 magnitude 5.7 event near Swabian Jura, Germany, the 1984 magnitude 5.4 event near Lleyn, Wales, and the 1994 magnitude 5.8 event near Roermond, Netherlands [*Ebel et al.*, 2000].

The p-values from these intraplate environments previously indicated that in general the p-values from intraplate environments overlap with the range expected from Californian aftershock sequences [*Ebel*, 2009; *Ebel et al.*, 2000]. The p-value from the Mineral earthquake's aftershock sequence ($p = 0.76$) falls on the minimum end of this p-value envelope. The aftershock sequence of the Goodnow, NY, earthquake is the only event in the preceding list that had a p-value less than 0.95 ($p = 0.74$), making it the aftershock sequence with the most similar p-value as that of the

Mineral earthquake. Figures 3-22 and 3-23 compare the p versus b-values for aftershocks sequences in intraplate regions from Ebel et al. [2000] and the Mineral earthquake to those in intraplate China and within convergent (Japan, Alaska, Taiwan) and transform (California, New Zealand, Turkey) boundary regions [*Ebertart*, 1998; *Wang*, 1994; *Wiermer et al*., 2002; *Bayrak and Osturk*, 2004; *Shcherbakov et al*., 2005]. Many aftershock sequences in intraplate China have relatively low p-values (~0.5 to 0.8), making them comparable to the decay rate of the Mineral earthquake [*Wang*, 1994].

The rate at which aftershocks decayed in response to the Mineral, Virginia, earthquake was much slower than the events from the Kettleman Hills and Whittier Narrows events in California, despite the similarity in their depths, magnitudes, and focal mechanisms. The delayed occurrences of aftershocks in the Fredericks Hall (~25 days after the mainshock) and Late Steep fault zones (~100 days after the mainshock) (Figures 3-4 and 3-13) appear to be the proximal causes for the slow decay rate of aftershocks from the Mineral earthquake. My modeling of Coulomb stress change indicates that the Late Steep fault zone falls in a stress trigger zone produced by the Mineral earthquake. The transfer of stress from the Mineral earthquake may have promoted failure in the region between the surface and the tip of the blind rupture from the mainshock, thus triggering the aftershocks that define the Late Steep fault zone (Figure 3-20). The dip of the Fredericks Hall fault zone is not well defined by aftershocks, therefore we do not know its orientation. The

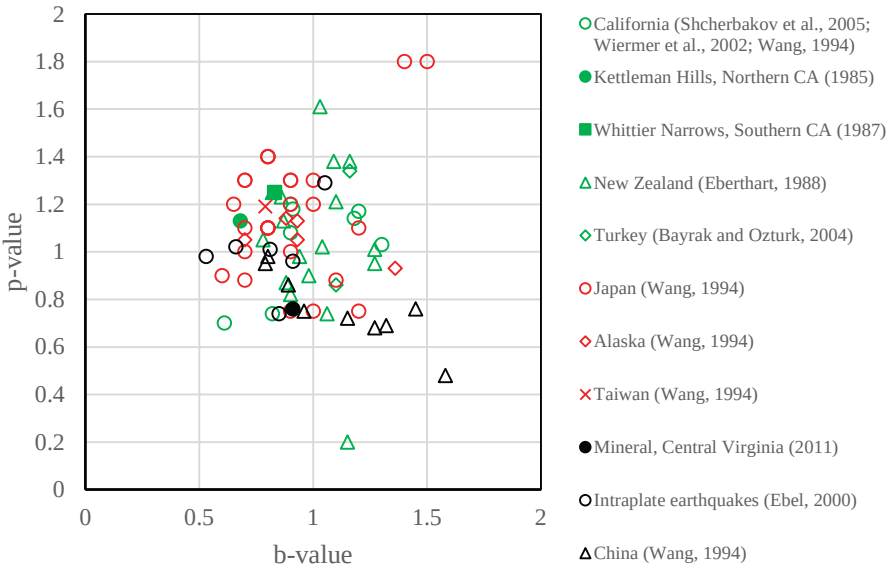

Figure 3-22. p-values versus b-values (aftershock decay parameters) for intraplate, convergent, and transform regions

Plot of p-value and b-value for aftershock decay sequences in intraplate, convergent, and transform regions [*Ebertart*, 1998; *Wang*, 1994; *Ebel et al*., 2000; *Wiermer et al*., 2002; *Bayrak and Osturk*, 2004; *Shcherbakov et al*., 2005]. Filled symbols represent the aftershock decay parameters associated with the Mineral (black circle) and Whittier Narrows (green square) events presented in Figure 3-11 or Table 3-3. The Mineral earthquake has a relatively average b-value, but a relatively low p-value compared to these populations.

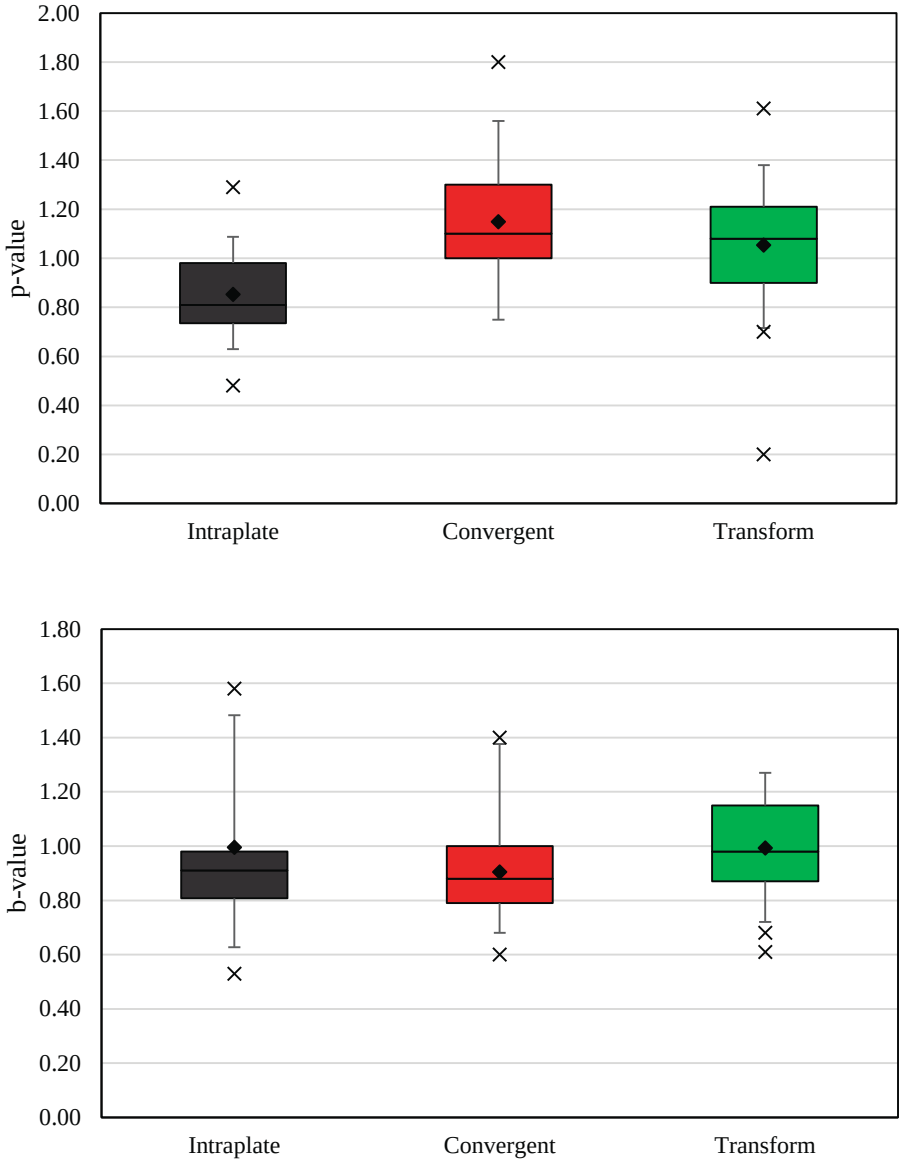

Figure 3-23. Box and whisker plots of p and b-values of aftershock decay sequences
Box and whisker plots showing the distributions of p-value (A) and b-value (B) parameters associated to aftershock decay sequences in intraplate, convergent, and transform regions [*Wang*, 1994; *Ebertart*, 1998; *Ebel et al*., 2000; *Wiermer et al*., 2002; *Bayrak and Osturk*, 2004; *Shcherbakov et al*., 2005]. The box represents the interquartile range (which represents the middle 50% of the data). The vertical ends of the box are the 25th and 75th percentiles, the whiskers extend to the 95% of the data, and the X symbols represent outliers. Mean values are shown as diamonds and the median values as horizontal lines. These distributions indicate that the majority of aftershock sequences in intraplate sequences have lower p-values, or slower aftershock decay rates, than those in convergent or transform boundary regions.

aftershocks defining the Fredericks Hall fault zone fall within the transition zone between positive and negative Coulomb stress for faults oriented like the mainshock's rupture, indicating that it is unlikely stress transfer from the mainshock alone triggered these aftershocks.

3.6.2 Seismicity rate changes in the far-field (remote triggering zone)

There are no apparent increases in the rate of seismicity after the occurrence of the Mineral earthquake in the Eastern Tennessee, Charleston South Carolina, or Wabash Valley seismic zones. The M_w 3.4 earthquake on October 18, 2006 and the M_w 4.1 earthquake on February 21, 2012 that occurred in the NMSZ could explain the increased rate of seismicity observed on October 12-22, 2006 (before the Mineral earthquake) and on February 21, 2012 (after the Mineral earthquake). Since the peak in the NMSZ was 182 days after the Mineral earthquake it is unlikely this event is related to long-distance triggering from the Mineral earthquake but is instead a local effect from seismicity in the seismic zone.

The increase in seismicity in the Central – Eastern U.S. region (without seismic zones) on August 25, 2011 (two days after the mainshock) may be related to dynamic triggering from the Mineral earthquake. The earthquake swarm that occurred near Albany, New York, on August 25th has previously been attributed to possibly being triggered from the passage of seismic waves from the Mineral earthquake [*Jacobi et al.*, 2012]. However, the occurrence of a high rate of seismicity (greater than 98% threshold) on July 17, 2007, before the Mineral earthquake, is unexplained. The two events associated with this peak occurred in Albany, NY. One of the events occurred in Augusta, GA, and the other north of Rochester, NY beneath

Lake Erie. It is possible that the four events that occurred on July 17th occurred on the same date by random chance.

The other issue with tying the earthquake swarm near Albany, NY, and West Virginia on August 25th to the Mineral earthquake is the two day delay. Many well documented cases of remote triggering occur instantaneously, or during the period in which seismic waves passed over an area [*Gomberg et al.*, 2004; *Antonioli et al.*, 2006]. However, the timing and physics of the earthquake nucleation process is not well understood [*van der Elst and Brodsky*, 2010], especially in intraplate environments. Tape et al. [2013] documented a case in which a M_w 3.9 earthquake was triggered in central Alaska from the passage of seismic waves from the April 2012 M_w 8.6 Sumatra earthquake and then followed by a slow, creep-like nucleation phase. A two day nucleation of seismicity in New York and West Virginia following the passage of seismic waves from the Mineral earthquake is plausible, therefore the possibility that these events were triggered by the Mineral earthquake cannot be ruled out.

The mean peak dynamic strain in each seismic zone from the passage of seismic waves is shown in Table 3-5 (Figure 3-1 and 3-21). The largest amount of strain, ~0.6 microstrain, associated by the passage of seismic waves was closest to the epicenter in the CVSZ. The mean peak dynamic strain in the ETSZ, CSSZ, NMSZ, and WVSZ range from 0.024 to 0.044 microstrain (Table 3-5). Remote triggering from the April 2011 Indian Ocean earthquake (M_w =8.6) required a peak dynamic strain of ~0.4 microstrain to trigger global remote events [*Pollitz et al.*, 2012] however, peak dynamic strain associated with remote triggering tend to range from

0.15 to 3 microstrain [*Hill et al.*, 1993; *Anderson et al.*, 1994; *Prejean et al.*, 2004; *Brodsky and Prejean*, 2005; *Hill and Prejean*, 2007], but has also been discerned at strain changes as small as 3 nanostrain (~0.003 microstrain) [*van der Elst and Brodsky*, 2010]. These values suggest that it is plausible to have remote triggering in these seismic zones. However, I observed no signals of long-distance triggering with seismicity rates greater than the 98% threshold from the Mineral earthquake in any of these seismic zones.

3.7 Discussion

3.7.1 Triggering in the aftershock zone

Triggering of the Late Steep fault zone by stress transfer is expected as slip on a surface-cutting thrust tends to drop stress in the adjacent crust whereas slip on blind thrusts can increase stress on nearby zones, particularly up dip of the source fault. In fact, the Kettleman Hills and Whittier Narrows events triggered aftershocks in a similar fashion in the region between the blind thrust and the surface [*Lin and Stein*, 2004]. While Coulomb stress transfer can explain the geographic location of the Late Steep zone, there is still no clear explanation for the delay of its occurrence. All aftershock clusters triggered by stress transfer from the Whittier Narrows and Kettleman Hills events occurred within 1 month (~30 days) of the mainshock, but the aftershock cluster that defines the Late Steep fault in the Mineral earthquake's epicentral region was triggered ~100 days later.

Structural heterogeneities, stress, and temperature in the crust have all been cited as factors responsible for causing variations in the p-value [*Kisslinger and*

Jones, 1991; *Utsu et al.*, 1995; *Enescu and Ito*, 2002]. The crust in the central and eastern U.S. has often been characterized as having older, colder, and drier crust than tectonically active regions [*Wu*, 1997; *Dixon et al.*, 2004]. Ellswoth et al. (2011) resolved a stress drop between 50 and 75 MPa (500 to 750 bars) for the Mineral earthquake's mainshock, which is over an order of magnitude higher than the normal range of 3-5 MPa commonly found in tectonically active areas. A high stress drop of this magnitude require a nearly complete stress drop for a crust in frictional equilibrium with a coefficient of friction of 0.6 [*Ellsworth et al.*, 2011]. The higher viscosity of the crust in the central and eastern U.S. compared to active tectonics regions such as California [*Dixon et al.*, 2004], may explain both the high stress drop and prolonged aftershock decay rate from the Mineral earthquake.

Delays in earthquake triggering from Coulomb stress transfer have been explained by considering the importance of viscoelastic processes in the triggering process [*Pollitz and Sacks*, 1995; 1997; *Freed and Lin*, 1998; 2001; *Deng et al.*, 1999; *Lin and Freed*, 2004]. For example, Coulomb stress transfer from the 1992 Landers M_w 7.3 earthquake is thought to have triggered the 1999 M_w 7.1 Hector Mine earthquake of southern California 7 years later [*Hauksson et al.*, 1993]. Three-dimensional viscoelastic modeling by Freed and Lin (2001) suggested that post-earthquake lower-crustal or upper mantle flow may have led to postseismic stress increases of 1 ± 2 bar at the location of the Hector Mine epicenter. It has been suggested that seismicity in intraplate regions is spatially migrating, so that no major earthquake ruptures the same fault segment twice [*Liu et al.*, 2011] and that recent earthquakes in these reflect long aftershock sequences from previous large magnitude

earthquakes [*Stein and Liu*, 2009]. The interaction between faults in intraplate environments as well as the characteristics of its crust may explain the delayed triggering of aftershock clusters in the epicentral region of the Mineral earthquake and thus the slow decay rate. Therefore, aftershocks might continue for a decade or more in the epicentral region of the Mineral earthquake [*Liu et al.*, 2011; *Stein and Liu*, 2009].

3.7.2 Lack of remote triggering in the far-field

It is possible that the energy release associated with the magnitude of the Mineral earthquake (M_w = 5.8) was too small to produce seismic waves with sufficient amounts of strain to generate remote-triggering from the passage of seismic waves. However, the phenomenon of long distance triggering has been observed before in southeastern Canada from similar, moderate magnitude earthquakes [*Hough*, 2007]. The lack of long-distance triggering from the Mineral earthquake is perhaps due to the poor density of seismic stations in the eastern U.S. If I were able to consistently detect earthquakes with magnitudes less than 2.5, perhaps I would have been able to observe a long-distance triggering affect. Another possibility is that faults in the central and eastern U.S. were not sufficiently close enough to failure for triggering to occur. Some researchers suggest that strain may be localized in pre-existing zones of weakness, such as pre-existing seismic zones [*Mazzotti and Townend*, 2010]. Perhaps known seismic zones were too far away from the Mineral earthquake's epicenter to generate large enough amounts of strain to bring faults in these zones to failure. Finally, I emphasize that the influence of mining blasts on the earthquake catalog for the central and eastern U.S. may significantly skew the rate of

seismicity before and after the Mineral earthquake. Even though I removed major mining regions from the catalog, it is impossible to remove all mining blasts. This will continue to be a challenge in searching for long-distance triggering affects and other analyses of the seismology in the central and eastern U.S.

The strain generated by the passage of seismic waves from the Mineral earthquake likely added to the overall stress field in the central and eastern U.S. The component of stress from the Mineral earthquake is a small addition to the overall stress field. Additional components of stress are be needed to bring faults to failure. The lack of observable remote triggering suggests that the Mineral earthquake did not generate any immediate increase in the seismicity rate in surrounding seismic zones, but I expect that the stress generated by the earthquake in the near-field and the far-field contributes to the magnitude and spatial distribution of stress in the central and eastern U.S. Liu and Stein [2011] suggest that earthquakes can cluster and migrate between faults. The Mineral earthquake occurred ~10 km northeast of the CVSZ (Chapter 2, Figure 2-2). If we expect earthquakes to migrate spatially over time, perhaps the next large magnitude earthquake in the central and eastern U.S. will occur outside the CVSZ.

3.7.3 Implications for seismic hazard evaluation

The triggering of the Late Steep fault zone by the Mineral earthquake provides additional evidence that aftershocks can be triggered by stress transfer in any tectonic environment, including both tectonic plate boundary and intraplate regions [*Lin and Stein*, 2004]. Stress triggering by Coulomb stress transfer in the aftershock zone of

the Mineral earthquake implies that building stress transfer into seismic hazard assessment in the central and eastern U.S. is crucial.

The lack of an observable signal of triggering in the far-field further highlights the possibility that remote triggering doesn't occur in intraplate regions, faults were not sufficiently close to failure to be triggered by a moderate magnitude earthquake, or that there is a need to add more stations to the seismic network in the central and eastern U.S. in order to detect the phenomenon of remote triggering. Continued study and observations of intraplate seismicity is essential for improving our understanding of the mechanisms responsible for triggering seismicity and thus our ability to mitigate the loss of life and property from large magnitude intraplate earthquakes.

3.8 Conclusions

Our examination of seismicity rate changes in the near-field and the far-field of the August 2011 Mineral earthquake reveals the following conclusions:

1. The decay of aftershocks from the Mineral earthquake was significantly slower than the decay rate of the Kettleman Hills and Whittier Narrows earthquakes in California.
2. The transfer of Coulomb stress from the Mineral earthquake's mainshock can explain the geographic location of the aftershocks that define the Late Steep fault zone.
3. There were no observable increases in the rates of seismicity above the 98% threshold at long distances associated with the passage of seismic waves from

the Mineral earthquake in the Eastern Tennessee, Charleston South Carolina, Wabash Valley, or New Madrid Seismic Zones.

4. The possibility that the earthquake swarm that occurred in Albany, New York, and in West Virginia near the Virginia border on August 25, 2011 (2 days after the mainshock) were triggered by the passage of seismic waves from the Mineral earthquake cannot be ruled out.

Chapter 4: Wrinkle ridges on Mercury and the Moon - Morphometric characterization, elastic dislocation modeling, and tectonic evaluation of planetary contraction

4.1 Abstract

Wrinkle ridges are structural anticlines formed by thrust faulting and folding resulting from crustal shortening and are found on all the terrestrial planets. MESSENGER has returned new high resolution imagery and altimetry data of the northern hemisphere of Mercury where there are large expanses of smooth plains deformed by wrinkle ridges. Recently obtained Lunar Reconnaissance Orbiter (LRO_ imagery and altimetry for lunar mare wrinkle ridges offer an excellent opportunity to compare their morphology and scale with newly imaged wrinkle ridges on Mercury. I evaluate the similarity and differences of wrinkle ridges on Mercury and the Moon by (1) locating and characterizing the morphology of 300 wrinkle ridges on Mercury (n = 150) and the Moon (n = 150), (2) producing statistical comparisons of maximum length and relief relations that define wrinkle ridge dimensions in different environments, and (3) estimate the depth of faulting of the largest wrinkle ridges using elastic dislocation modeling. Wrinkle ridges on Mercury are ~2.2 times higher and ~1.8 times longer in mean relief and length than wrinkle ridges on the Moon. Large relief wrinkle ridges in Mercury's northern smooth plains exceed ~600 m and may be attributed to a significant component of global contraction on Mercury (~1 to 2 km). Global contraction on the Moon is an order of magnitude smaller than on Mercury, therefore lunar wrinkle ridges were most likely formed primarily by flexure induced subsidence and contraction of mare basalts.

4.2 Introduction

On March 18, 2011 the MErcury Surface, Space Environment, Geochemistry, and Ranging (MESSENGER) spacecraft transitioned from orbiting the Sun to being the first spacecraft to orbit Mercury. Meanwhile, the Lunar Reconnaissance Orbiter (LRO) has been orbiting the Moon since June 2009. Crustal shortening on Mercury and the Moon is reflected by three tectonic landforms: lobate scarps, high-relief ridges, and wrinkle ridges [*Watters et al.*, 2009a; *Watters and Johnston*, 2010; *Watters and Nimmo*, 2010]. Recently obtained orbital imagery and altimetry data from both LRO and MESSENGER offer an unprecedented opportunity to characterize the morphology of these tectonic features. This study focuses on a morphometric characterization of wrinkle ridges, contractional tectonic features found in mare basalts on the Moon and smooth plains volcanic material on Mercury, formed from thrust faulting and folding [*Strom*, 1970; *Maxwell et al.*, 1975; *Strom et al.*, 1975; *Solomon and Head*, 1979; *Plescia and Golombek*, 1986; *Watters*, 1988; *Watters et al.*, 2009c; 2010].

Images obtained by Mariner 10 and from MESSENGER's three flybys [*Head et al.*, 2009; *McNutt et al.*, 2010; *Watters et al.*, 2009c] showed that a significant amount of Mercury's surface is covered by smooth plains. Global image mosaics generated from MESSENGER's orbital phase indicate that smooth plains cover almost 27% of Mercury's surface [*Solomon et al.*, 2008; *Denevi et al.*, 2009; *Watters et al.*, 2009c; *Denevi et al.*, 2012; *McNutt et al.*, 2010]. High spatial resolution (250 m/pixel), high-incidence angle (55 to 85°), mosaics enable us to more accurately

identify and characterize tectonic features. The greatest expanse of smooth plains material on Mercury is in the northern high-latitudes, covering ~6% of the surface (Figures 4-1 and 4-2A) [*Head et al.*, 2011]. In parallel, the Lunar Reconnaissance Orbiter (LRO) has been orbiting the Moon since 2009, compiling a database of high-resolution images and altimetry of the lunar surface covering lunar wrinkle ridges located in the mare basins. New data from the MESSENGER and LRO spacecrafts offer an excellent opportunity to quantitatively compare the morphology of wrinkle ridges on Mercury with previously detected wrinkle ridges on the Moon (Figure 4-3). In this chapter, I characterize the morphologies of wrinkle ridges on the Moon and Mercury though (1) statistical comparison of ridge dimensions, (2) the length-relief relations of underlying faults, and (3) elastic dislocation modeling of the fault depth and geometry. Examination of wrinkle ridges on Mercury and the Moon allows us to evaluate the influence of differences in tectonic setting and global radial contraction in the formation of these landforms.

4.3 Background on wrinkle ridges

Wrinkle ridges are one of the most ubiquitous tectonic features found on the terrestrial planets and are characterized as structural anticlines formed by folding and thrust faulting resulting from crustal shortening [*Plescia and Golombek*, 1986; *Watters*, 1988; *Golombek et al.*, 1991; *Watters and Schultz*, 2010]. A broad, low

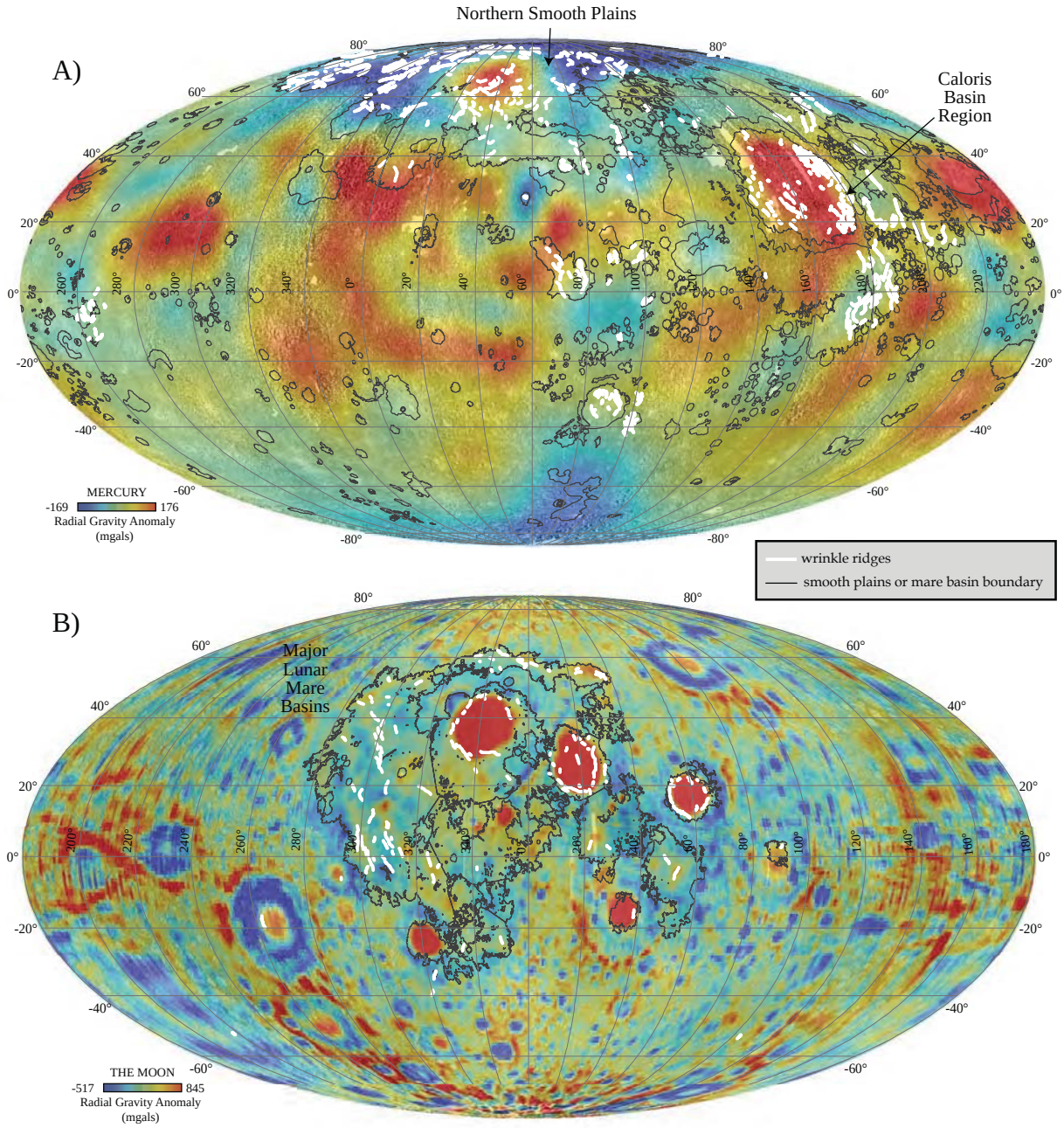

Figure 4-1. Tectonics and gravity on Mercury and the Moon

Free-air gravity and tectonics of Mercury (A) and the Moon (B) on a Mollweide equal area projection of a shaded relief map merged with a global MDIS or LROC WAC monochrome mosaic. Positive gravity anomalies correspond to mascon basin environments. The gravity model from Mercury is from radio tracking of the MESSENGER spacecraft [*Smith et al.*, 2012]. Lunar gravity model is from the Lunar Prospector LP150Q gravity model [*Konopliv et al.*, 2001] available from http://www.ipgp.fr/~wieczor/CrustalThicknessArchive/CrustalThickness.html. Tectonic features are wrinkle ridges (white) I digitized for this study, previously mapped features from the MESSENGER flybys [*Watters et al.*, 2009c], and newly mapped features from MESSENGER's orbital phase [*Watters et al.*, 2011]. Mercury smooth plains boundary from Denevi et al. [2012] and mare basins boundary digitized by Steven Koeber.

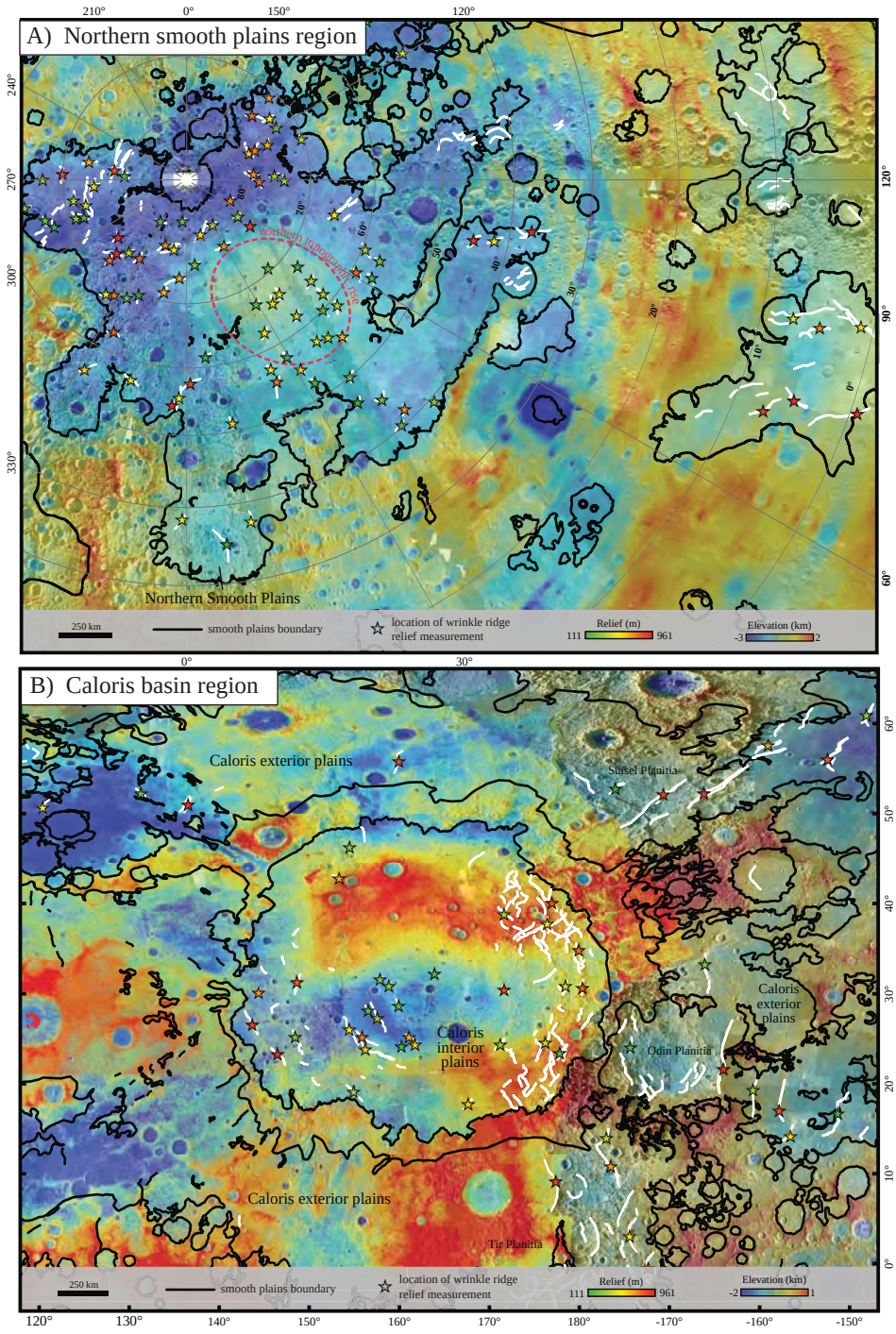

Figure 4-2. Locations of wrinkle ridges on Mercury

Locations of 97 wrinkle ridges in the northern smooth plains of Mercury (A) and 53 wrinkle ridges in the Caloris basin region (B) that I measured for this study (stars, see Table 4-B1). Stars are colored based on their measured relief. Smooth plains boundary from Denevi et al. [2012]. Wrinkle ridges (white lines) from both Watters et al. [2009c] and newly mapped wrinkle ridges from this analysis are shown on these maps. A) Wrinkle ridges are plotted on a north polar projection of a 250 m/pixel combined high-incidence angle and monochrome global mosaic of MDIS images overlaid with a DEM created from MLA tracks [*Zuber et al.*, 2012]. Northern topographic rise from Klimczak et al. [2012]. B) Wrinkle ridges are plotted on a Equirectangular projection of the MDIS mosaic overlaid with a stereo derived DEM created from M1 Flyby imagery (1 km^2) [*Oberst et al.*, 2010; *Preusker et al.*, 2011], a stereo derived DEM created from orbital imagery created by DLR (~500 m^2), and the USGS DEM (~2.7 km^2) [*Becker et al.*, 2012]. The transparency of the elevation DEMs is set to 50% in Map A and 70% in Map B. Brighter colors in Map B indicate locations where DEM sources overlap.

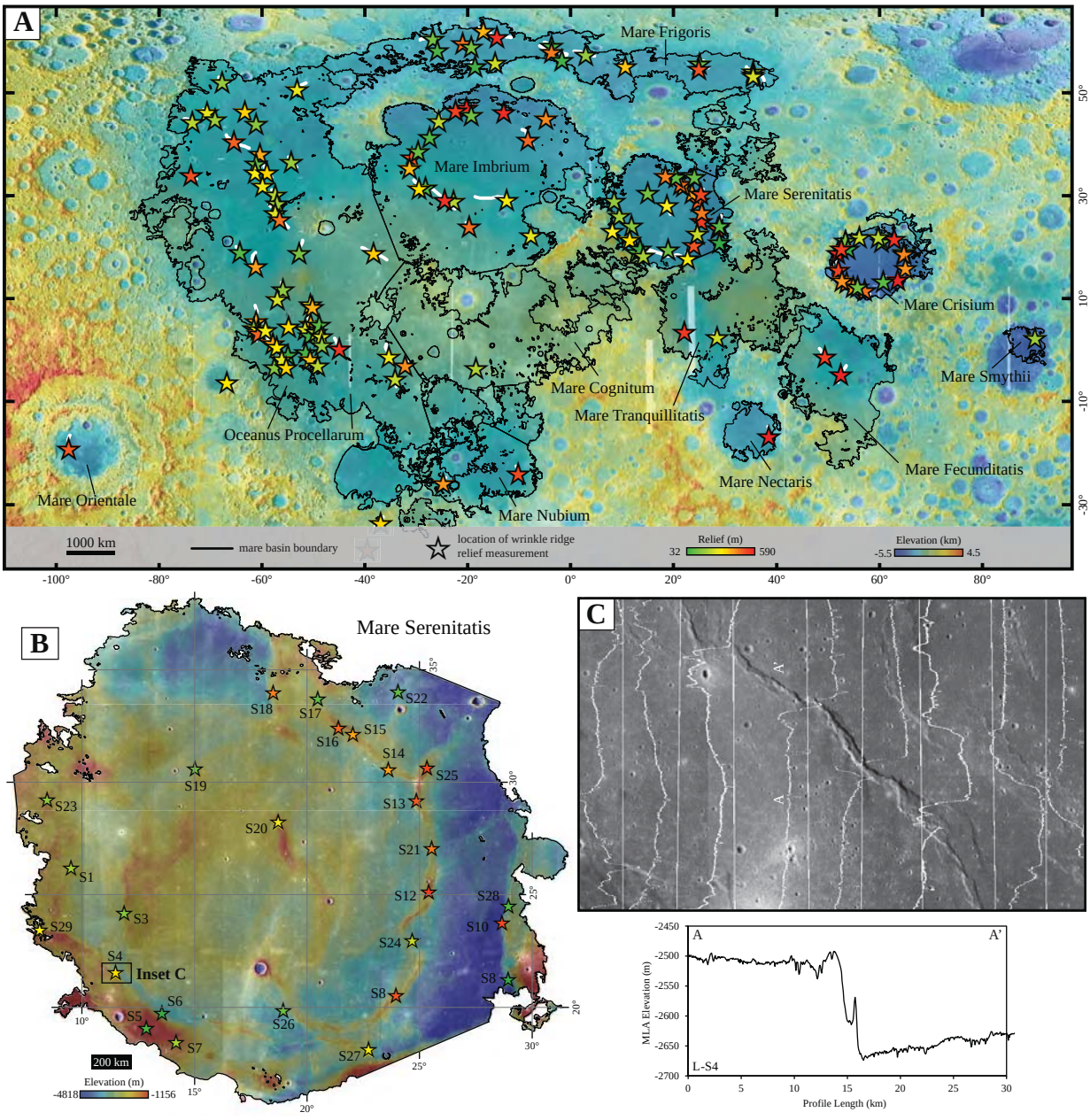

Figure 4-3. Locations of wrinkle ridges on the Moon
A) Locations of 150 wrinkle ridges in the mare basins of the Moon that I measured for this study (stars, see Table 4-B2) plotted on a 1:125,000,000 Equirectangular projection of a 100 m/pixel monochrome global mosaic of 400 m/pixel WAC images overlaid with a global LROC WAC stereo derived DEM [*Scholten et al*., 2012]. Stars are colored based on their measured relief. Mare basin boundaries were digitized by Steven Koeber. B) Concentric wrinkle ridges in Mare Serenitatis, a mascon-basin environment where wrinkle ridge formation is attributed to subsidence. The LROC WAC stereo DEM has been clipped to the basin boundary to highlight the topography within the basin. Map scale is 1:20,000,000. C) LOLA tracks and elevations overlaid on a WAC image of a wrinkle ridge in southwestern Mare Serenitatis.

relief arch and a superimposed ridge are typical morphologic elements of wrinkle ridges [*Watters*, 1988; *Schultz*, 2000] **(**Figure 4-4**).** Wrinkle ridges are typically found on topographically smooth material in two physiographic settings: (1) the interior of large impact basins, and (2) on broad expansive plains [*Watters*, 1988; *Watters and Johnston*, 2010; *Watters and Nimmo*, 2010]. Crustal shortening responsible for wrinkle ridge formation can be generated by a variety of processes, including load induced subsidence, regional or local contraction, and global contraction [*Maxwell and Gifford*, 1980; *Solomon and Head*, 1980; *Freed et al.*, 2001; *Watters et al.*, 2009c; 2010].

Wrinkle ridges were first recognized and mapped from Earth-based telescopic observations of the lunar maria [*Fielder*, 1961; *Baldwin*, 1965; 1970; *Gilbert*, 1893; *Watters and Johnston*, 2010]. On the Moon, wrinkle ridges are concentrated predominately on the nearside in basin-localized tectonic zones associated directly with the lunar maria (Figure 4-3). Wrinkle ridges are well mapped on the Moon from Apollo era and Lunar Reconnaissance Orbiter Camera (LROC) imagery and are confined to mare material known to be composed of basalt [*Watters*, 1988]. Wrinkle ridge rings and basin-concentric ridge patterns, such as those present in Mare Serenitatis (Figure 4-3B), have been cited as evidence that subsidence, cooling and contraction of the mare basalts played a key role in their formation [*Wilhelms and McCauley*, 1971; *Maxwell et al.*, 1975; *Wilhelms*, 1987]. Previous studies also tie the origin of the smooth plains on Mercury where wrinkle ridges occur to volcanism [*Melosh and McKinnon*, 1988; *Head et al.*, 2008; *Solomon et al.*, 2008]. Mercurian wrinkle ridges imaged by Mariner 10 occur in the interior smooth plains material of

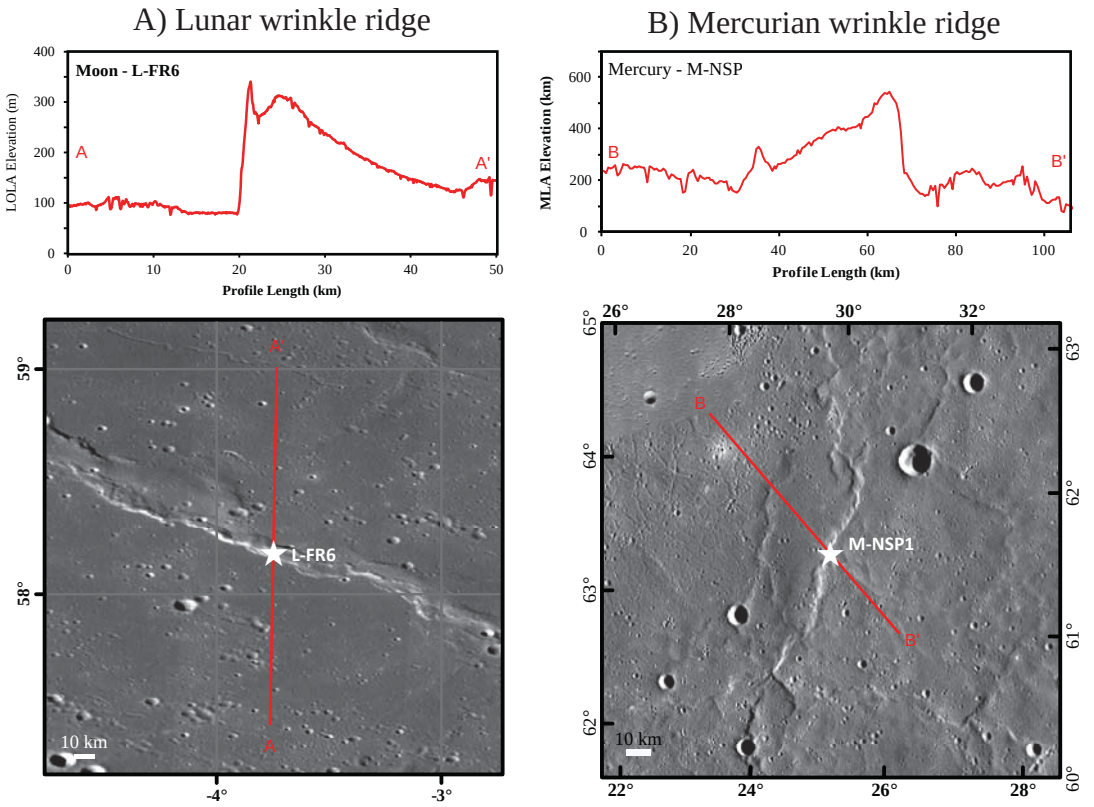

Figure 4-4. Example of a wrinkle ridge on the Moon and Mercury
Cross-section and imagery of wrinkle ridge in Mare Frigoris on the Moon (A) and in the northern smooth plains of Mercury (B) show the broad arch and superimposed ridge morphology typical of most wrinkle ridges. The 1:1 scale cross-section of the mercurian wrinkle ridge (C) demonstrates that in reality changes in topography across wrinkle ridges are subtle. The largest change in relief corresponds to a slope of only 10°. More examples of wrinkle ridges with the broad arch and superimposed ridge morphology, as well as the single ridge and complex morphologies, can be found in Appendix 4-A.

the Caloris basin and the exterior annulus of smooth plains [*Strom et al.*, 1975; *Melosh and McKinnon*, 1988; *Watters et al.*, 2005; *Fassett et al.*, 2009; *Watters et al.*, 2009a; 2009b; 2009c; *Watters and Nimmo*, 2010] (Figure 4-2B).

While imagery from Mariner 10 and the MESSENGER flybys returned imagery coverage for almost 98% of Mercury, very few observations existed in Mercury's north polar region until MESSENGER's orbital phase. The maximum reliefs of fourteen wrinkle ridges imaged by Mariner 10 were estimated using poorly constrained shadow measurements [*Watters*, 1988]. Earth based radar altimetry was used to measure the reliefs of seven wrinkle ridges in the smooth plains of Tir Planitia revealed arch-like structures with reliefs ranging 200 to 730 m and lengths up to 130 m long [*Harmon et al.*, 1986; *Watters*, 1988; *Watters and Nimmo*, 2010]. Wrinkle ridges also appear to occur in basalt plains on Mars and Venus, and on Earth in the continental flood basalts of the Columbia Plateau in the Pacific Northwest [*Plescia and Golombek*, 1986; *Watters*, 1988; *Watters*, 1991; *Watters and Nimmo*, 2010; *Watters and Schultz*, 2010]. Previous measurements of martian and mare wrinkle ridges indicate lower relief ridges and arches than wrinkle ridges on Mercury [*Watters*, 1988; *Golombek et al.*, 1991; *Watters*, 2004; *Watters and Nimmo*, 2010].

4.4 Methods – Morphometric comparison

I measured the length and maximum reliefs of 150 wrinkle ridges on Mercury and 150 wrinkle ridges on the Moon using imagery and altimetry data obtained by the MESSENGER and LRO spacecrafts. On Mercury, I measured the maximum length-relief dimensions of wrinkle ridges in the northern smooth plains and the smooth

plains interior and exterior to the Caloris basin (Figure 4-2, Table 4-B1). I sampled wrinkle ridge dimensions from all of the major mare basins on the Moon, including: Mare Serenitatis, Mare Crisium, Mare Imbrium, Mare Frigoris, and Oceanus Procellarum. I also extracted profiles across wrinkle ridges in Mare Fecunditatis, Mare Tranquillitatis, Mare Nubium, Mare Orientale, Mare Humorum, Mare Cognitum, Mare Nectaris, and Mare Smythii, Vitello Crater, Kugler Crater, Karrer Crater, and Grimaldi Crater (Figure 4-3, Table 4-B2). Ten profiles were extracted across wrinkle ridge – lobate scarp transitions. Wrinkle ridge – lobate scarp transitions are locations where the morphology changes from a wrinkle ridge in the mare basalts to a lobate scarp in highland materials reflecting a difference in mechanical properties (e.g. the presence or absence of layers). I excluded wrinkle ridges obviously influenced by the presence of ghost craters from the analysis [*Head et al.*, 2011; *Klimczak et al.*, 2012; *Watters et al.*, 2012a]. In the following sections, I describe in detail the data sources, data extraction procedures, and measurement techniques used in this analysis.

4.4.1 Length measurements from imagery

The locations and lengths of wrinkle ridges on Mercury and the Moon were digitized and measured from global mosaics in an ArcGIS environment. I used a 250 m/pixel mosaic of Wide-angle Camera (WAC) and Narrow-angle Camera (NAC) monochrome images obtained by the Mercury Dual Imaging System (MDIS) [*Hawkins et al.*, 2007] to digitize the lengths of wrinkle ridges on Mercury. Additional orbital imagery collected at large solar incidence angles ranging ~60° to 85°from nadir provided optimum lighting conditions for identifying and mapping

wrinkle ridges in Mercury's northern smooth plains [*Watters et al.*, 2013]. On the Moon, I digitized wrinkle ridges using primarily a WAC 100 m/pixel global mosaic from the Lunar Reconnaissance Orbiter Camera (LROC) on LRO. The LROC NACs provided additional very high-resolution imagery, up to 0.5 m-scale panchromatic images over a combined 5-km swath, for mapping wrinkle ridges [*Robinson et al.*, 2010]. On both Mercury and the Moon, I digitized wrinkle ridges continuously when their trend appeared to be unbroken in the imagery. In cases when the wrinkle ridge was segmented I digitized only the segment in which I measured the relief. Uncertainties of the lengths of digitized wrinkle ridges, determined by zooming into the 100 m/pixel LROC WAC and 250 m/pixel MDIS WAC mosaics and assessing possible digitization choices, are up to 2 km for lunar wrinkle ridges and 5 km for wrinkle ridges on Mercury. The uncertainty associated with using different resolution imagery for digitizing wrinkle ridges and then measuring and comparing their lengths is discussed in detail in Appendix 4-C.

4.4.2 Relief measurements from topographic profiles

I primarily used data from the Mercury Laser Altimeter (MLA) [*Smith et al.*, 2012; *Zuber et al.*, 2012] and the Lunar Orbiter Laser Altimeter (LOLA) [*Smith et al.*, 2010] to measure the maximum relief wrinkle ridges on Mercury and the Moon, respectively, where the altimeter tracks traverse the wrinkle ridges at orthogonal or near orthogonal angles (60° to 90° from strike). I preferred to extract elevation data directly from MLA and LOLA altimetry tracks when data was available because altimeter tracks 1) provided the densest and most accurate elevation profiles across

features and 2) allowed detailed viewing of the major morphologic elements of the wrinkle ridge (e.g. abroad arch with superimposed ridge) (Figure 4-4).

MLA illuminates surface areas averaging between 15 and 100 m in diameter, spaced ~400 m apart along the altimeter ground track, with radial precision of individual MLA ranging measurements less than 1 m [*Zuber et al.*, 2012]. Spacing between elevation data points is closer at the north pole and becomes more widely spaced approaching the equator due to MESSENGER's eccentric, near-polar orbit. Altimetry tracks were available for a variety of orientations over the smooth plains in Mercury's high northern latitudes, allowing us to measure reliefs of many wrinkle ridges (Figure 4-2A, Table 4-A1).

The LOLA instrument transmits 5 beams, returning the mean elevation of a 5-m spot from a 50-km altitude orbit. LOLA tracks are comprised of five parallel profiles, ~12 m apart, with individual observation points in each profile separated by ~56 m [*Smith et al.*, 2010]. LOLA ranging has a vertical precision of ±0.1 m. LRO's polar orbit enabled reliefs of only east-west trending wrinkle ridges, with sufficient coverage, in my study area on the Moon to be measured using LOLA (Figure 4-3A, Table 4-A2). LOLA elevation data were acquired using the Lunar Orbital Data Explorer (http://ode.rsl.wustl.edu).

Where altimetry tracks were not available, I extracted elevation profiles perpendicular to the structure from gridded digital elevation models (DEMs). For wrinkle ridges in Mercury's northern smooth plains (north of ~40°N), I used a ~500 m/pixel DEM derived by interpolating elevation points from MLA tracks (n = 46). For wrinkle ridges south of ~40°N in the Caloris interior and exterior smooth plains,

where MLA data points are widely spaced, I measured the relief from DEMs derived from stereo photogrammetry of MESSENGER orbital or flyby images with spatial resolutions from 500 m/pixel to ~2.7 km/pixel and with vertical precision ±135 m (n = 55) [*Oberst et al.*, 2010; *Preusker et al.*, 2011]. The USGS produced a 2.7 km/pixel global DEM by using camera pointing errors from the MDIS imagery metadata [*Becker et al.*, 2012]. Those data enabled a radius measurement at imagery control points to be constrained, and thus the global DEM to be produced. While the USGS DEM is coarser in resolution, it enabled me to make relief measurements at some wrinkle ridges that had no elevation data from MLA or the stereo-derived DEMs in the Caloris Basin region (Figure 4-C1).

I measured the relief across north–south-trending wrinkle ridges on the Moon by extracting elevations from a global 100 m/pixel DEM derived from stereo photogrammetric analysis of WAC images (n = 111). The LROC WAC stereo-derived DEM has a vertical precision of ± 10 m [*Scholten et al.*, 2012]. I compared DEMs available on Mercury and the Moon from a variety of sources to assess the most reliable data for elevation measurements (Figure 4-5). The details concerning variation in relief measurements depending on the chosen elevation data source are discussed in detail in Appendix 4-C.

The lateral limits of the ridges were identified using major inflection points in the profiles and checked by comparison with rectified images [*Watters*, 1988]. Relief was measured by taking the difference between the maximum elevation on the profile and the elevation at the major inflection point on the vergent side of the ridge. For wrinkle ridges located on regional slopes, relief was measured using detrended

elevation profiles. Profiles were detrended by subtracting a least squares linear fit from the elevation data across the wrinkle ridge. I report the greatest relief measured for each wrinkle ridge, however, note that this is not necessarily the maximum relief as MLA and LOLA profiles do not always provide continuous coverage across the entire length of each wrinkle ridge. When measuring relief from DEMs, it is possible to extract profiles across the entire length of the wrinkle ridge, which allowed the maximum relief to be determined. Therefore, relief measured from MLA or LOLA profiles is described as "greatest measured relief" while relief measured from DEMs is described as "maximum relief" [*Banks et al.*, 2012] (See Tables 4-B1 and 4-B2).

4.4.3 Statistical sub-sampling

I sub-sampled the total population of wrinkle ridges on Mercury and the Moon to examine the statistical difference between wrinkle ridges located in basin environments with mascons, dense concentrations of mass identifiable by positive gravity anomalies, to wrinkle ridges in regions with no mascon-like gravity anomalies [*Maxwell et al.*, 1975; *Solomon and Head*, 1980; *Konopliv et al.*, 2001; *Watters et al.*, 2005; *Smith et al.*, 2012] (Figure 4-1). Lunar mascons tend to correlate with major impact basins (e.g. Mare Serenitatis, Imbrium, and Crisum) and are interpreted to be regions of thickened crust due to flood volcanism associated with the impact [*Konopliv et al.*, 2001; *Watters and Johnson*, 2010]. Basins with mascon signatures generally exhibit basin-concentric and basin-radial wrinkle ridges that are interpreted to have formed in response to localized contraction driven by flexure of the lithosphere and subsidence from the superisostatic loading of thick sequences of mare basalt [*Solomon and Head*, 1979; *Freed et al.*, 2001] (Figure 4-3B).

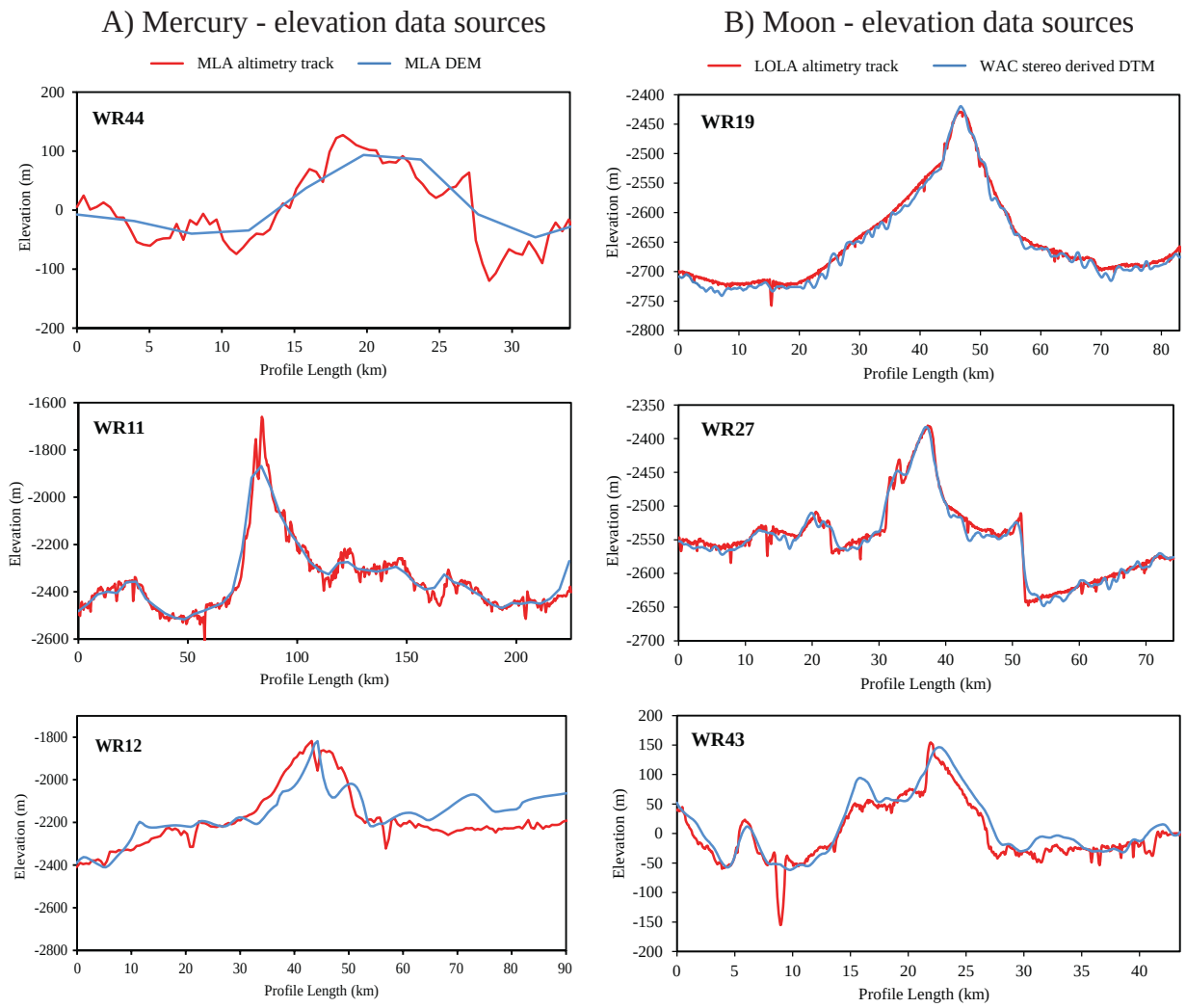

Figure 4-5. Elevation profile comparison
Comparison of elevation profiles extracted across wrinkle ridges from different elevation data sources for Mercury (A) and the Moon (B). I selected the elevation data source for wrinkle ridges on Mercury depending on the highest resolution and coverage available for its location. I used LOLA tracks to measure the relief of nearly east-west trending lunar wrinkle ridges and the WAC stereo derived DEM to measure all other lunar wrinkle ridges.

On the Moon, I compared the dimensions of wrinkle ridges in mascon environments (Mare Serenitatis, Mare Crisium, and Mare Imbrium) to wrinkle ridges in non-mascon like environments (Oceanus Procellarum and Mare Frigoris). Wrinkle ridges in Oceanus Procellarum and Mare Frigoris generally are not concentric, but instead traverse each basin in a variety of orientations implying a complex history of deformation [*Schultz et al.*, 2010; *Watters et al.*, 2010; 2012; *Banks et al.*, 2011; *Williams et al.*, 2012]. The Caloris basin interior plains and northern smooth plains and Caloris basin exterior plains on Mercury provide analogs for comparison to mascon and non-mascon environments on the Moon, respectively [*Smith et al.*, 2012] (Figure 4-1).

These populations of wrinkle ridges are further subdivided to examine differences in the relief and length of wrinkle ridges by lunar basin. On Mercury, we subdivide wrinkle ridges into (1) the Caloris basin interior and (2) the Caloris exterior plains (Figure 4-2B). Near the center of Mercury's northern smooth plains there is a topographic rise, termed here as the northern rise [*Klimczak et al.*, 2012; *Zuber et al.*, 2012] that coincides with a positive gravity anomaly [*Smith et al.*, 2012]. I also subdivided the wrinkle ridges in the northern smooth plains into wrinkle ridges on the rise and outside the rise to search for any statistical differences in measured relief and length.

4.5 Results – Relief and length statistics

The tables in Appendix 4-B list the relief and length for each wrinkle ridge measured for this analysis. The relief - length measurements for each wrinkle ridge

population are plotted as box and whisker plots, where the box represents the interquartile range (which represents the middle 50% of the data). The vertical ends of the box represent the 25th and 75th percentiles, the line through the box represents the median of the data, the whiskers extend to 95% of the data and X symbols represent outliers (Figure 4-6). Plotting the data in this manner enables the distribution of the data, whether it is normal or non-normal to be visualized. Box and whisker plots showing the aspect ratio (length/relief) for each population are shown in Appendix 4-D.

4.5.1 Comparison of dimensions of wrinkle ridges on Mercury and the Moon

The relief of wrinkle ridges measured on Mercury ranges from ~112 to 961 m with a mean relief of ~404 m (median = ~353 m, *n* = 150) and the lengths of these wrinkle ridges range from ~27 to 362 km with a mean length of ~94 km (median = ~80, *n* = 150) (Figure 4-6A, Table 4-1). Wrinkle ridges on the Moon range in relief from ~33 to 590 m with a mean relief of ~187 m (median = ~157 m, *n* = 150) and in length from ~10 to 241 km with a mean length of ~53 km (median = ~45 km, *n* = 150).

The mean relief of wrinkle ridges on Mercury is ~2.2 times higher than the mean relief of wrinkle ridges on the Moon (Table 4-1, Figures 4-6A and 4-7). The mean length of wrinkle ridges on Mercury is ~1.8 times longer than the mean length of wrinkle ridges on the Moon. There is a population of wrinkle ridges on Mercury that are taller (> 600 m) than any lunar wrinkle ridges and a population of wrinkle ridges on the Moon that are shorter (< 100 m) than any mercurian wrinkle ridges (Figure 4-7).

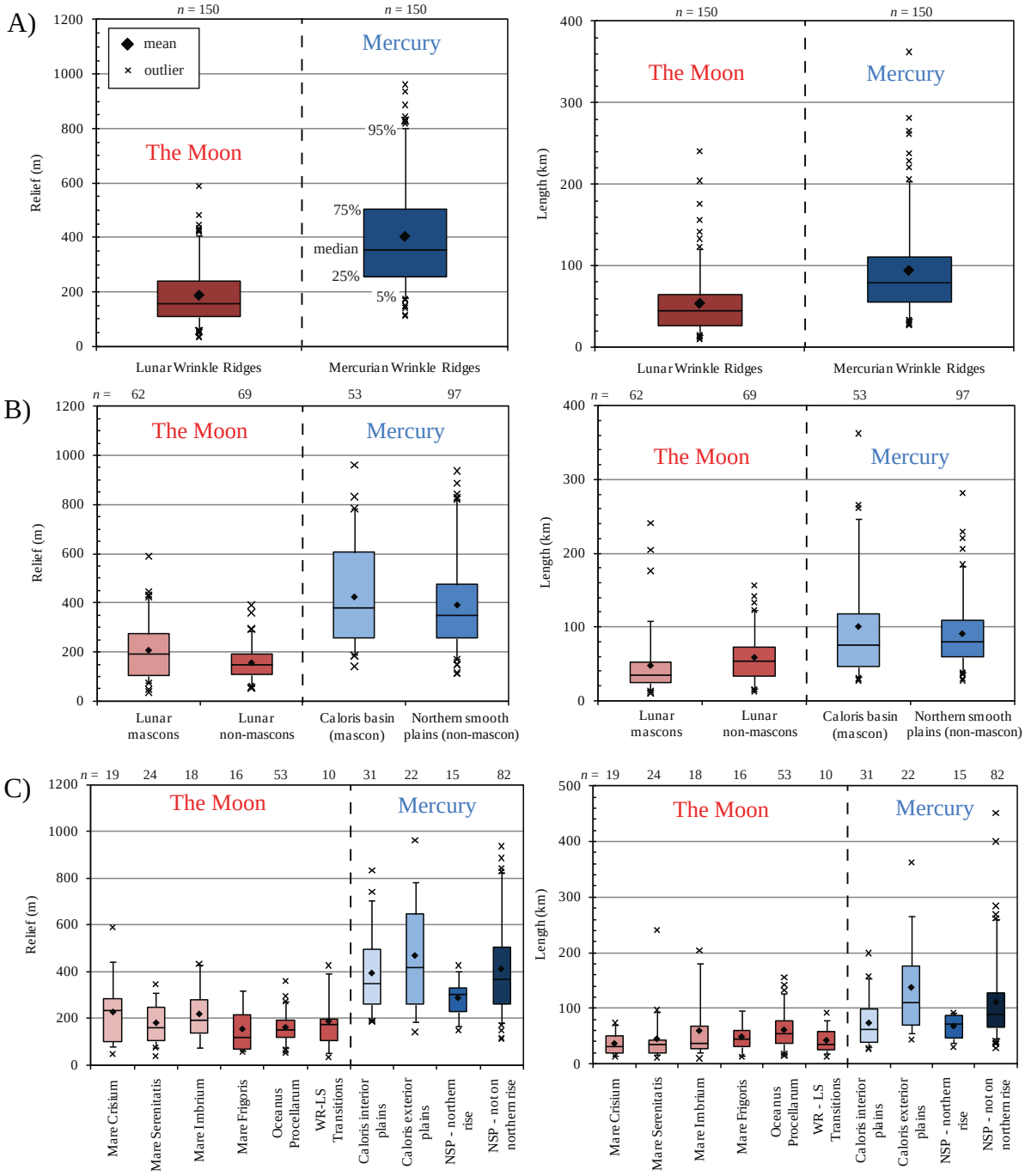

Figure 4-6. Box and whisker plots of wrinkle ridge relief-length on Mercury and the Moon
Box and whisker plots showing the relief and length of wrinkle ridge populations in the following regions: A) the Moon and Mercury, B) mascon and non-mascon basin environments, C) specified location. The box represents the interquartile range (which represents the middle 50% of the data). The vertical ends of the box are the 25th and 75th percentiles, the whiskers extend to the 95% of the data, and the X symbols represent outliers. Mean values are shown as diamonds and the median values as horizontal lines. The aspect ratio (length/relief) for each population is shown in Appendix 4-D (Figure 4-D1).

Table 4-1. Comparison of wrinkle ridge statistics on Mercury and the Moon

Location	Minimum	5%	25%	Median	Mean	75%	95%	Maximum	*n* (#)
All wrinkle ridges on Mercury									
Relief (m)	112	179	257	353	404	503	802	961	150
Length (km)	27	35	56	80	94	111	203	362	150
L/R aspect ratio	55	86	145	228	266	326	487	1434	150
All wrinkle ridges on the Moon									
Relief (m)	33	63	109	157	187	241	408	590	150
Length (km)	10	15	27	45	53	65	121	241	150
L/R aspect ratio	33	97	152	269	371	453	798	6616	150
Dimensions of mercurian divided by lunar wrinkle ridge measurements									
Relief (m)	3.39	2.84	2.36	2.25	2.16	2.09	1.97	1.63	1
Length (km)	2.70	2.33	2.07	1.78	1.77	1.71	1.68	1.50	1
L/R aspect ratio	1.7	0.9	1.0	0.8	0.7	0.7	0.6	0.2	1

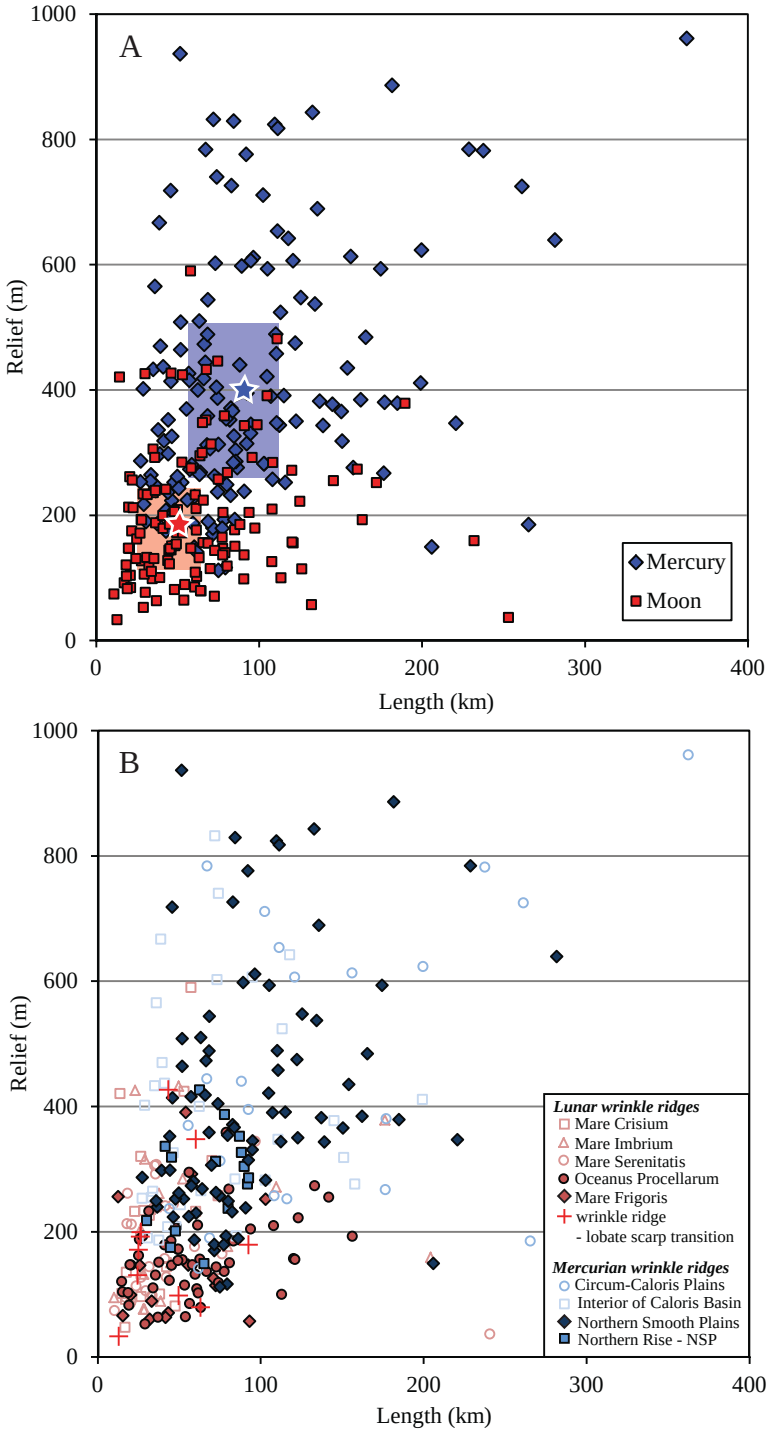

Figure 4-7. Relief – length relationships of wrinkle ridges on Mercury and the Moon
A) Plot of relief and length of 300 wrinkle ridges on Mercury and the Moon. The dimensions of wrinkle ridges on Mercury are ~2.2 times and ~1.8 times larger in mean relief and length than wrinkle ridges on the Moon (stars). Boxes extend from the 25th to 75th percentiles of each population, representing 50% of the dataset, and indicate that the reliefs of wrinkle ridges on Mercury and the Moon are statistically significantly different. B) Wrinkle ridge dimensions on Mercury and the Moon subdivided by location. Mascon basin environments are indicated by open symbols.

Wrinkle ridges on Mercury fall within an interquartile envelope ranging from ~257 to 503 m in relief and ~56 to ~111 km in length. On the Moon, wrinkle ridges fall within an interquartile envelope ranging from ~109 to 241 m in relief and ~27 to 65 km in length (Figure 4-7). The relief ranges defining these interquartile envelopes do not overlap, indicating that the majority of the wrinkle ridges on Mercury have are taller than most wrinkle ridges on the Moon. Clearly, there is some overlap in length for the interquartile range defining wrinkle ridges on Mercury and the Moon. However there is a population of wrinkle ridges on Mercury with relatively longer lengths than those on the Moon.

4.5.2 Mascon and non-mascon environments

Mercurian wrinkle ridge sub-populations

Wrinkle ridges in the interior and exterior plains of the Caloris basin range in relief from ~141 to 961 m with a mean relief of ~425 m (median = ~380 m, n = 53) and in length from ~27 to 362 km with a mean length of ~100 km (median = ~75 km, n = 53). In the northern smooth plains, wrinkle ridges range in relief from ~112 to 937 m with a mean relief of ~392 m (median = ~350 m, n = 97) and in length from ~27 to 282 km with a mean length of ~90 km (median = ~80 km, n = 97) (Figure 4-6B, Table 4-2). The variation on the length-relief relations of wrinkle ridges in the Caloris basin region extend over a larger interquartile range than those in the northern smooth plains, indicating that there is a more diverse range of wrinkle ridge dimensions in the Caloris basin region.

Table 4-2. Relief and length statistics for wrinkle ridges in the Caloris basin region and northern smooth plains of Mercury

Location	Minimum	5%	25%	Median	Mean	75%	95%	Maximum	*n* (#)
Wrinkle ridges located in the Caloris basin region (interior plains = mascon)									
Relief (m)	141	188	257	380	425	606	783	961	53
Length (km)	27	32	46	75	100	118	247	362	53
L/R aspect ratio	58	77	142	207	268	362	520	1434	53
Wrinkle ridges in northern smooth plains (non-mascon)									
Relief (m)	112	174	257	350	392	475	819	937	97
Length (km)	27	39	59	80	90	110	182	282	97
L/R aspect ratio	55	109	149	229	264	318	463	1380	97

Lunar wrinkle ridge sub-populations

The population of wrinkle ridges on the Moon were sub-sampled into mascon and non-mascon tectonic environments. Wrinkle ridges in lunar mascons (Mare Crisium, Mare Serenitatis, and Mare Imbrium), range in relief from ~36 to 590 m with a mean relief of ~208 m (median = ~190 m, *n* = 62) and in length from ~10 to 241 km with a mean length of ~47 km (median = ~35 km, *n* = 62). In non-mascon environments on the Moon (Oceanus Procellarum and Mare Frigoris), wrinkle ridges range in relief from ~52 to 391 m with a mean relief of ~158 m (median = ~147 m, *n* = 69) and in length from ~13 to 156 km with a mean length of ~58 km (median = ~53 km, *n* = 69) (Figure 4-6B, Table 4-3). Wrinkle ridges in mascon basin environments have a larger range of reliefs and relatively shorter lengths than those in non-mascons.

4.5.3 Comparison of statistics by region

Caloris basin interior and exterior plains

Caloris basin wrinkle ridges were sub-divided into basin interior and exterior plains ridges. The wrinkle ridges in the Caloris basin interior range from ~186 to 832 m in relief with a mean relief of ~394 m (median = ~374 m, *n* = 31) and in length from ~27 to 199 km with a mean length of ~73 km (median = ~62 km, *n* = 31) (Figure 4-3, Table 4-4). Wrinkle ridges in the northern and eastern Caloris exterior plains range from ~141 to 961 m in relief with a mean relief of ~470 m (median = ~418 m, *n* = 22) and ~44 to 362 km in length with a mean length of ~137 km (median= ~110 km, *n* = 22). Wrinkle ridges in the interior plains of Caloris have a narrower range of reliefs and shorter lengths than those in the exterior plains.

Table 4-3. Lunar wrinkle ridge relief and length statistics (mascons versus non-mascon regions)

Location	Minimum	5%	25%	Median	Mean	75%	95%	Maximum	*n* (#)
Wrinkle ridges located in lunar mascons									
Relief (m)	36	15	102	190	208	274	425	590	62
Length (km)	10	76	24	35	47	53	109	241	62
L/R aspect ratio	33	83	126	209	346	323	528	6616	62
Wrinkle ridges located in lunar non-mascons									
Relief (m)	52	17	109	147	158	193	284	391	69
Length (km)	13	63	34	53	58	73	122	156	69
L/R aspect ratio	49	136	232	372	418	557	809	1640	69

Table 4-4. Mercurian wrinkle ridge relief and length statistics by location

Location	Minimum	5%	25%	Median	Mean	75%	95%	Maximum	*n* (#)
Northern Smooth Plains (NSP) (non-mascon)									
Wrinkle ridges located in NSP (on northern rise)									
Relief (m)	149	167	227	304	287	331	399	426	15
Length (km)	30	338	47	72	68	88	92	93	15
L/R aspect ratio	123	134	174	247	249	310	369	439	15
Wrinkle ridges located in NSP (not on northern rise)									
Relief (m)	112	179	262	366	412	503	167	937	82
Length (km)	28	46	65	90	110	127	38	451	82
L/R aspect ratio	61	104	163	249	308	364	689	1755	82
Wrinkle ridges located in Caloris basin region (mascon)									
Wrinkle ridges located in Circum-Caloris Plains (NCCP, ECCP-OP, and SCCP)									
Relief (m)	141	185	260	418	470	646	784	961	22
Length (km)	44	56	70	110	137	177	265	362	22
L/R aspect ratio	86	145	189	279	346	410	652	1434	22
Wrinkle ridges located in the Caloris Basin's interior (CB)									
Relief (m)	186	191	259	374	394	497	704	832	31
Length (km)	27	30	38	62	73	99	154	199	31
L/R aspect ratio	58	68	104	162	212	268	480	573	31

Wrinkle ridges on Mercury's northern topographic rise

In order to evaluate any differences in length and relief, wrinkle ridges on the northern topographic rise are compared to wrinkle ridges beyond the rise. Wrinkle ridges on the northern rise range from ~112 to 937 m in relief with a mean relief of ~413 m (median = ~367 m, *n* = 15) and in length from ~28 to 451 km with a mean length of ~111 km (median = ~91 km, *n* = 15). Wrinkle ridges surrounding the rise range from ~149 to 426 m in relief with a maximum mean of ~287 m (median = ~304 m) and in length from ~30 to 93 km with a mean length of ~68 km (median = ~72 km) (Figure 4-3A and 4-6C, Table 4-4). Wrinkle ridges on the northern rise have relatively smaller reliefs and lengths than those beyond the rise.

Lunar wrinkle ridges by location

Wrinkle ridges in Oceanus Procellarum have the narrowest range of reliefs out of all of the lunar wrinkle ridges, ranging ~99 to 220 m (*n* = 53) . Lengths of wrinkle ridges in Oceanus Procellarum range from ~15 to 156 km with a mean length of ~61 km (median = ~54 m, *n* = 53). Wrinkle ridges in Mare Frigoris range in relief from ~56 to 248 m (*n* = 16) and lengths from ~23 to 74 km (*n* = 16). Wrinkle ridges in Oceanus Procellarum have relatively shorter relief ridges with longer length than those in Frigoris.

Wrinkle ridges in Oceanus Procellarum have the largest mean length on the Moon and in non-mascon regions at ~61 km (median = ~54 km) (Figure 4-6C, Table 4-5). The longest wrinkle ridges in a mascon basin are in Mare Imbrium with mean lengths of ~60 km (median = ~38 km, *n* = 18). The interquartile range for the relief of wrinkle ridges in Mare Serenitatis and Mare Frigoris are similar, differing by less

than ~30 m. Wrinkle ridges in Mare Serenitatis have a mean relief of ~178 and range in relief from ~92 to 265 km (n = 24), while wrinkle ridges in Mare Frigoris cover a similar, but slightly wider range of reliefs (n = 16). Wrinkle ridges in Mare Crisium and Mare Imbrium have the largest mean relief (~225 (n = 19) and 217 m (n = 18) respectively). Wrinkle ridges located in mascon basin regions tend to have slightly wider ranges in relief, including some of the largest relief wrinkle ridges on the Moon, than those in non-mascon regions and are slightly shorter in length (Figure 4-6C). However, overall the dimensions of wrinkle ridges on the Moon are fairly similar.

4.6 Interpretation – Relief and length comparison

4.6.1 Wrinkle ridges on Mercury and the Moon

A population of wrinkle ridges on Mercury and the Moon are similar in length and relief. The aspect ratios indicates a similar scaling relationship for wrinkle ridges in the mascon and non-mascon environments on Mercury and the Moon, suggesting similar processes are generating wrinkle ridges on both bodies (Figure 4-D1). Most of the wrinkle ridges on Mercury taller and longer than wrinkle ridges on the Moon. This is true especially in the northern smooth plains and Caloris exterior plains where wrinkle ridge relief exceeds 400 m. There are ~20 lunar wrinkle ridges that have slightly lower relief (only a few tens of meters) than wrinkle ridges on Mercury. A few lunar wrinkle ridges are very slightly shorter in length than those on Mercury, by

Table 4-5. Lunar wrinkle ridge relief and length statistics by location

Location	Minimum	5%	25%	Median	Mean	75%	95%	Maximum	*n* (#)
Wrinkle ridges located in lunar mascons									
Mare Crisium									
Relief (m)	47	78	101	232	225	285	440	590	19
Length (km)	14	15	20	32	37	50	71	74	19
L/R aspect ratio	33	78	124	150	210	283	401	587	19
Mare Serenitatis									
Relief (m)	36	75	104	161	178	248	307	344	24
Length (km)	10	17	21	34	45	43	94	241	24
L/R aspect ratio	70	87	137	210	480	280	446	6616	24
Mare Imbrium									
Relief (m)	76	76	134	190	217	281	427	432	18
Length (km)	10	21	28	38	60	69	180	204	18
L/R aspect ratio	54	86	131	255	321	425	644	1286	18
Wrinkle ridges located in lunar non-mascons									
Oceanus Procellarum									
Relief (m)	52	73	119	151	159	193	270	358	53
Length (km)	15	19	37	54	61	78	127	156	53
L/R aspect ratio	123	136	234	362	411	556	807	1133	53
Mare Frigoris									
Relief (m)	57	59	69	120	152	216	317	391	16
Length (km)	13	15	30	45	49	61	96	103	16
L/R aspect ratio	49	116	203	376	440	578	907	1640	16
Wrinkle ridge - Lobate scarp transitions									
Relief (m)	33	54	106	175	186	197	391	426	10
Length (km)	13	18	25	35	42	58	79	93	10
L/R aspect ratio	102	116	139	180	309	478	671	798	10

only a few meters; however this determination approaches the uncertainty level associated with the length measurements.

I suggest that the larger dimensions of wrinkle ridges on Mercury is due to a more significant component of global contraction. In the following sections, I analyze the dimensions of wrinkle ridges more closely by examining wrinkle ridges in mascon and non-mascon environments and by region on Mercury or the Moon.

4.6.2 Mascon and non-mascon environments

Mascon-basin environments are associated with large impact events. Large impacts are expected to reset regional and global background stress fields [*Freed et al.*, 2009; *Watters et al.*, 2009b]. Therefore, it is likely that contractional strain accommodated by wrinkle ridges in the mascon-basins (i.e. the Caloris basin, Mare Crisium, Mare Serenitatis, and Mare Imbrium) were dominated by basin-localized, load induced subsidence generated infilling of basalt and basalt-like volcanic plains.

Wrinkle ridges in the interior plains of the Caloris basin, centered on a positive free-air gravity anomaly, had generally smaller reliefs and lengths than those in the Caloris basin exterior plains and northern smooth plains (with the exception of wrinkle ridges located on the topographic rise in the northern smooth plains (Figure 4-6C). Wrinkle ridges in the northern smooth plains, which lacks any positive free-air gravity anolamies, have generally greater mean relief and length than ridges confined to the interior plains of Caloris. The great dimensions of the non-mascon wrinkle ridges in the northern smooth plains, in some cases extending to over 600 m in relief, are likely due to the combination of compressional stresses from flexural induced subsidence and global contraction.

Oceanus Procellarum and Mare Frigoris on the Moon lack positive free-air gravity anomalies, typical of mascons [*Konopliv et al.*, 2001; *Watters and Johnston*, 2010; *Zuber et al.*, 2013] yet maintain similar wrinkle ridge dimensions to those in mascon basins. In particular, the distribution of length-relief relationships of wrinkle ridges in Mare Frigoris are similar to those in Mare Serenitatis. Since the amount of global contraction on the Moon is small, it is most likely that the majority of wrinkle ridges on the Moon are generated primarily by subsidence.

4.6.3 Comparison of statistics by region

Mercurian wrinkle ridges

The relief of wrinkle ridges in the northern smooth plains and Caloris exterior plains are larger than those in the interior plains of the Caloris basin. This difference in relief may be explained predominately by the amount of contraction contributed by either basin-localized subsidence or global contraction. The majority of wrinkle ridges in the Caloris exterior plains are greater in relief than those in the Caloris basin interior. The smallest relief wrinkle ridges occur near the center of the Caloris basin (Figure 4-2B). In contrast, ~75% of wrinkle ridges in the interior and exterior plains have similar lengths. The small relief and basin concentric orientation of wrinkle ridges in the interior of the Caloris basin suggest they were most likely generated by solely subsidence related contraction [*Maxwell et al.*, 1975; *Maxwell and Gifford*, 1980; *Watters et al.*, 2009b]. I suggest that the existence of larger relief ridges in the Caloris exterior plains reflect components of both global contraction and subsidence associated with loading of volcanic lavas.

The interquartile range of wrinkle ridge relief in the northern smooth plains overlaps that of wrinkle ridges in the Caloris basin interior. This means that wrinkle ridges with similar relief to those in the Caloris basin interior can also be found in the northern smooth plains. However, many wrinkle ridges in the northern smooth plains have a larger relief. More than half the population of wrinkle ridges in the Caloris exterior plains have a similar relief to wrinkle ridges in the northern smooth plains and a few ridges in the exterior plains have greater relief than those in the northern smooth plains. Wrinkle ridges on the northern topographic rise in Mercury's northern smooth plains range in relief from ~112 to 937 m (n = 15). This range of relief falls within a broader range of reliefs (~149 to 426 m, n = 31) for wrinkle ridges measured outside the rise. Wrinkle ridges located near the boundary of the northern smooth plains tend to have larger reliefs (Figure 4-2A).

Lunar wrinkle ridges

The positive free-air gravity anomalies associated with Mare Serenitatis, Crisium, and Imbrium indicates the existence of thick layers of mare basalt [*Konopliv et al.*, 2001]. The loading of these dense basalts on the lithosphere cause the flexural bending and subsidence responsible for the formation of the basin concentric and radial wrinkle ridges that correlate with the shape of these basins (Figure 4-3B) [*Solomon and Head*, 1980]. No major mascon-like gravity anomalies have been observed in Mare Frigoris or Oceanus Procellarum, however wrinkle ridges deform the mare basalts in this region [*Williams et al.*, 2012].

The relief of lunar wrinkle ridges in Mare Frigoris, a non-mascon, is very similar in average relief to those in Mare Serenitatis, a mascon basin [*Maxwell et al.*,

1975; *Solomon and Head*, 1980] (Figure 4-6C). Yet the length of wrinkle ridges in Mare Frigoris are ~1.8 times longer than those in Mare Serenitatis. Similarly, the standard deviation envelopes for the relief of wrinkle ridges in Mare Crisium and Mare Imbrium also overlap with the relief of wrinkle ridges in Mare Frigoris but the mean relief is ~70 m higher. Approximately 56% of lunar wrinkle ridges in Mare Imbrium and Mare Crisium are larger in relief than wrinkle ridges in the non-mascon basins on the Moon. However, wrinkle ridges with the largest mean relief are located in Mare Crisium (~261 m), followed by Mare Imbrium (~239 m), and then Mare Serenitatis (~184 m). While variations in the dimensions of wrinkle ridges for each mare basin exist, overall there are no statistically significant differences between those in mascon and non-mascon environments. The existence of wrinkle ridges with comparable dimensions in both mascon and non-mascon settings indicates that significant subsidence and contraction occurred without superisostatic loading.

4.7 Elastic dislocation modeling

To evaluate how differences in relief on wrinkle ridges correspond to the amount of displacement on associated faults in the subsurface, I used the elastic dislocation modeling software Coulomb [*Lin and Stein*, 2004; *Toda et al.*, 2005] to predict the expected topographic expression associated with wrinkle ridges resulting from displacement on a listric thrust in the subsurface. Elastic dislocation modeling has been used to successfully model the subsurface geometry, amount of slip, and depth of faulting responsible for creating wrinkle ridges on Mars [*Watters*, 2004], lobate scarps on Mars, Mercury, and the asteroid 433 Eros [*Schultz and Watters*,

2001; *Watters et al.*, 2002; *Egea-Gonzalez et al.*, 2012; *Watters et al.*, 2011b], and terrestrial faults [*Stein and King*, 1984; *King et al.*, 1988; *Stein et al.*, 1988; *Bilham and King*, 1989; *King and Ellis*, 1990; *Taboada et al.*, 1993; *King et al.*, 1994]. I constrained the maximum depth of faulting and amount of cumulative slip required to produce the topographic expressions of one of the largest scale wrinkle ridges on Mercury (M-NSP5, relief = ~843 m) and the Moon (L-FR4, relief = ~391 m) (Figure 4-8).

Although there is consensus that wrinkle ridges are compressional tectonic features formed by folding and thrust faulting, several specific kinematic models have been proposed for their formation [*Schultz*, 2000; *Watters*, 2004]. The proposed geometry of faults in the subsurface include: fault-bend folding and fault-propagation models [*Suppe and Connors*, 1992], multiple-fault models that involve deformation over a blind thrust and development of a backthrust [*Schultz*, 2000; *Golombek et al.*, 2001], or an array of thrust faults that intersect a mechanically weak décollement [*Okubo and Schultz*, 2003]. However, the broad low relief arch and superimposed ridge typical of wrinkle ridge morphologies can be obtained simply by contraction on a blind listric fault that flattens into a décollement [*Watters*, 2004]. For simplicity, I chose the listric geometry for these models.

Following Watters [2004], I approximate a listric geometry by connecting planar fault segments of varying lengths with dip angles θ of 30°, 10°, and 5° with a nearly flat (0.01°) final segment. Since I observed no obvious surface breaks associated with the wrinkle ridges, the thrusts are assumed to be blind with the upper tip 0.1 km below the surface [*Schultz*, 2000]. I fixed the upper tip of the near-surface

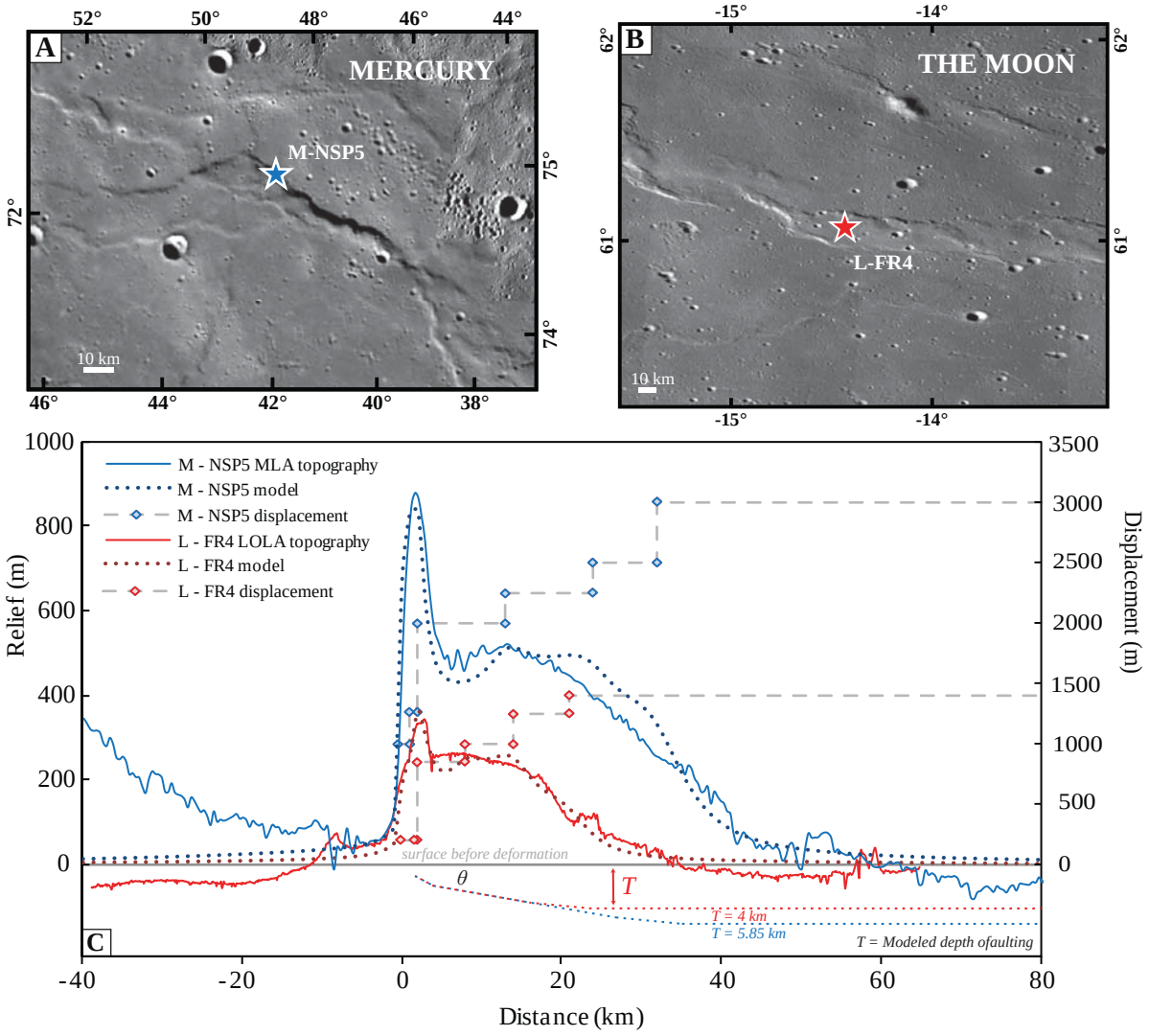

Figure 4-8. Numerical models of one of the largest wrinkle ridges on Mercury and the Moon
A) One of the largest wrinkle ridges on Mercury, M-NSP5 (relief = ~843 m; 250 m/pixel MDIS WAC monochrome mosaic; north polar projection), and B) the Moon, L-FR4 (relief = ~391 m; ~100 m/pixel LROC WAC monochrome mosaic; Equirectangular projection). C) Detrended topographic profile across these wrinkle ridges shown with corresponding best-fit listric thrust fault models. The listric geometry for these wrinkle ridges is approximated by fault segments with fault-plane dip angles (θ) ranging from 30° to 0° where the final fault segment flattens into a décollement at a maximum depth of faulting *T* [*Watters*, 2004] (Tables 4-6 and 4-7). I varied the amount of displacement D on each fault segment until the permanent vertical surface displacement predicted by the model (dotted line) best fits the topography. The depth of faulting is not to scale. Vertical exaggeration of the topography is ~ 50:1.

thrust fault segment under the edge of the vergent side of the wrinkle ridge and the lower tip is placed near the inner edge of the arch where the fault flattens into the décollement (Figure 4-8). The length L, depth T, dip θ, and amount of slip D on the fault segments are free parameters. I used a Young's modulus E of 80 GPa, a Poisson's ratio n of 0.25, and a coefficient of friction of 0.4, which are comparable to parameters used to model deformation associated with fault offset in terrestrial continental crust and on Mercury [*Burgmann et al.*, 1994; *King et al.*, 1994; *Freed and Lin*, 1998; *Watters et al.*, 2002].

I used a tapered slip distribution, by accommodating smaller amounts of slip on the uppermost segments and larger amounts of slip on lower segments that form the listric geometry, which allows modeling of the broad arch and superimposed ridge (major morphologic elements) of wrinkle ridges and avoids unrealistically large concentrations of stress near fault tips predicted by uniform slip [*Toda et al.*, 1998; *Watters*, 2004]. I iteratively adjusted the amount of slip and length of the fault segments until the modeled topographic expression of the surface best fit the measured relief across each wrinkle ridge. All models are two-dimensional and designed to reflect the maximum surface displacement expected along the ridge.

My best fit model for one of the largest wrinkle ridges in Mercury's northern smooth plains (M-NSP5), incorporated a cumulative slip of ~12 km (sum of slip on individual fault segments) on a listric fault with a maximum depth of ~5.85 km (depth of décollement) (Figure 4-8, Table 4-6). I used a similar fault geometry to model one of the largest wrinkle ridges on the Moon in Mare Frigoris (L-FR4). The best fit model I obtained for this lunar wrinkle ridge included cumulative slip of ~4.9 km on a

Table 4-6. Parameters for the listric thrust beneath mercurian wrinkle ridge M-NSP5

Segment number	*L* (km)	*θ*°	*T* (km)	*D* (m)
1	1	30	0.677	1000
2	1	30	1.250	1300
3	11	10	3.190	2000
4	11	10	5.130	2250
5	8	5	5.830	2500
6	85.9	0.01	5.85	3000

Table 4-7. Parameters for the listric thrust beneath lunar wrinkle ridge L-FR4

Segment number	*L* (km)	*θ*°	*T* (km)	*D* (m)
1	1.5	30	0.98	200
2	0.5	30	1.255	200
3	6	10	2.315	850
4	6	10	3.375	1000
5	7	5	3.981	1250
6	85.9	0.01	4	1400

listric fault with a maximum depth of faulting of ~4 km (Figure 4-8, Table 4-7). Iterative modeling indicated that the large differences in relief between wrinkle ridges on the Moon and Mercury could be accounted for using listric faults with the same overall geometry but with proportionally smaller fault segments [*Watters*, 2004]. Subtle differences in morphology, or the overall shape of the wrinkle ridges, are controlled by a combination of the amount of slip and length of each fault segment. Note that the resolved cumulative slip represents the total accumulation of slip on the fault segments as the structure developed over time.

My models indicated that the cumulative slip on the fault underlying the largest wrinkle ridge on Mercury is up to ~2.5 times greater than the largest wrinkle ridge on the Moon. The depth of faulting I constrained in these models indicated that the maximum depth of faulting for the mercurian wrinkle ridge is ~1.5 times greater than the lunar wrinkle ridge. The ratio of the cumulative slip to the maximum depth of faulting is ~2 for the wrinkle ridge on Mercury and ~1.2 for the wrinkle ridge on the Moon. Therefore, the ratio of the cumulative slip to depth of faulting is ~1.7 times greater for the largest wrinkle ridge on Mercury compared to the largest wrinkle ridge on the Moon.

In order for faults beneath these wrinkle ridges to form, a preexisting horizontal weakness or discontinuity must exist at the depth of the décollement [*Watters*, 2004]. A likely candidate for a discontinuity for the wrinkle ridge in Mercury's northern smooth plains (M-NSP5) is the interface between the smooth plains material and the underlying crust.

Previous estimates of the thickness of the plains unit from the size of buried impact craters indicated that the plains thickness locally exceeded 1 to 2 km in Mercury's northern smooth plains [*Head et al.*, 2011]. My modeling constrains the thickness of Mercury's northern smooth plains to at least ~5.85 km, the maximum depth of faulting at the depth of the décollement. Similarly, I constrain the thickness of the mare basalt in Mare Frigoris on the Moon to ~4 km, the depth of the décollement for my elastic dislocation model of L-FR4. Note however that these models are non-unique and different geometries and amounts of slip could also explain the topographic expression we observe across these wrinkle ridges.

4.8 Discussion

Wrinkle ridges that deform volcanic rocks on Mercury and the Moon, both relatively small one-plate planetary bodies, reflect similar processes of tectonic deformation [*Maxwell and Gifford*, 1980; *Watters*, 1988; *Schultz et al.*, 2006; *Head et al.*, 2009]. In general, the populations of wrinkle ridges on Mercury and the Moon are similar in morphology but there are statistically significant differences in length and relief (Figure 4-6 and Figure 4-7) that reflect differences in the tectonic evolution of each body.

The radius of Mercury is 2440 km, ~1.4 times larger than the Moon (radius = 1737.4 km). Differences in gravity or the volume of Mercury or the Moon may account in part for these difference in wrinkle ridge dimension [*Schultz et al.*, 2006]. Globally distributed lobate scarps on Mercury and the Moon are believed to have formed primarily from horizontally isotropic compressional stresses resulting from

global radial contraction [*Strom et al.*, 1975; *Solomon and Head*, 1979; *Watters et al.*, 1998; *Watters et al.*, 2004; *Solomon et al.*, 2008; *Watters et al.*, 2009c; *Watters and Nimmo*, 2010; *Watters et al.*, 2010]. The distribution of small scale lunar lobate scarps, with maximum reliefs <100 m and proportionally smaller lengths (less than tens of kilometers), indicate only ~100 m radial global contraction of the Moon [*Watters and Johnston*, 2010; *Watters et al.*, 2010; *Watters et al.*, 2012a]. Conservative estimates for the amount of global contraction from thrust faults on Mercury suggest a decrease in radius of no more than ~1 to 2 km [*Strom et al.*, 1975; *Watters*, 1988; *Watters et al.*, 1998; 2009c; 2013], although some estimate the radius change to be as high as ~2.4-3.6 km [*Di Achille et al.*, 2012]. Regardless, these estimates indicate that global contraction was at least an order of magnitude greater on Mercury than on the Moon.

My statistical analysis indicates that wrinkle ridges in the interior of the Caloris basin are smaller in relief and length than those in the northern smooth plains or Caloris exterior plains. However, wrinkle ridges in the northern smooth plains and Caloris exterior plains have similar dimensions. It is likely that the impact event that formed the Caloris basin modified the pre-existing surface deformation, especially in the interior of the basin [*Freed et al.*, 2009], temporarily resetting the stress field and isolating the basin from background global compressional stresses. Thus, the compressional stresses that formed the wrinkle ridges in the interior plains of Caloris were probably dominated by flexure induced subsidence [*Freed et al.*, 2009; *Watters et al.*, 2009b].

The depth and extent of the impact damage zone diminishes with increasing radial distance from the impact center [*Freed et al.*, 2009]. Much of the Caloris exterior plains are probably too far away from the impact damage zone for pre-existing deformation to have been completely reset. Wrinkle ridges in the northern smooth plains and Caloris exterior plains are larger than those in the Caloris interior plains because they are likely the result of a combination of compressional stresses due to subsidence and global contraction.

The small amount of global contraction on the Moon (<100 m indicate that compressional stresses due to flexure induced subsidence predominately formed the lunar wrinkle ridges. Wrinkle ridges located in mascon basins, including Mare Serenitatis, Mare Crisium, and Mare Imbrium, although slightly larger in dimension than wrinkle ridges in non-mascon regions, Oceanus Procellarum and Mare Frigoris, are not statistically significantly different. Although the similarity of lunar wrinkle ridges, particularly in Mare Frigoris, to the relief of wrinkle ridges in the mascon basins environments is puzzling, it suggests comparable compressional stresses due to flexure induced subsidence in both mascon and non-mascon environments.

4.9 Conclusions

I reach the following main conclusions from my morphometric analysis and numerical modeling:

1. Wrinkle ridges on Mercury are ~2.2 times higher and ~1.8 times longer in mean relief and length than wrinkle ridges on the Moon.

2. Wrinkle ridges on Mercury fall within an envelope ranging from ~112 to 961 m in relief and ~27 to ~362 km in length. On the Moon, wrinkle ridges fall within an envelope ranging from ~33 to 590 m in relief and ~10 to 241 km in length.
3. Wrinkle ridges in the northern smooth plains and the Caloris exterior plains are larger than those in the Caloris interior.
4. Elastic dislocation modeling indicates that the amount of cumulative slip on underlying thrust faults is ~2.5 times greater on Mercury than on the Moon for the largest wrinkle ridges.

I suggest that varying combinations of global contraction and subsidence on Mercury and the Moon likely explain these differences in wrinkle ridge dimension and that the largest relief wrinkle ridges located in the northern smooth plains and Caloris exterior plains on Mercury were generated by a combination of compressional stresses due to subsidence and global contraction.

Chapter 5: Synthesis and future work

5.1 Synthesis

My comparison of relief-length relationships of wrinkle ridges on Mercury and the Moon indicated that there is a larger component of global contraction on Mercury (Chapter 4). Tectonic deformation on Mercury and the Moon dates back as far as ~3.5 to 4 billion years [*Boyce*, 1976; *Solomon et al.*, 2008; *Watters et al.*, 2004; 2009c; *Watters and Johnston*, 2010; *Watters and Nimmo*, 2010], while the current eastern U.S. has only been an intraplate region since the end of the early Jurassic rifting following the Paleozoic Appalachian orogeny [*Manspeizer et al*., 1989; *Poag and Sevon*, 1989; *Williams*, 1995; *Weems and Olson*, 1997; *Kunk et al.*, 2004; 2005; *Southworth et al.*, 2006; *Blackburn et al*., 2013].

New imagery and altimetry data returned from the MESSENGER and LRO spacecraft offer a unique opportunity to view an intraplate environment that has been deforming over a longer period of time than in the central and eastern U.S. The surfaces of Mercury and the Moon may reflect several generations of faulting, revealing varying time periods in which the stress field changed orientation, imprinting on top of pre-existing features. If the processes that drive tectonic deformation in intraplate regions manifest themselves on the surface more clearly as longer periods of time elapse, or if there is no vegetation, weathering, and erosion, perhaps the pattern of faulting on Mercury and the Moon can provide insight into the mechanisms driving tectonic deformation in the central and eastern U.S. on Earth.

5.1.1 Zones of pre-existing weakness in the crust

The largest relief wrinkle ridges in the northern smooth plains imply large amounts of stress were accommodated at these locations. The faults associated with the largest relief wrinkle ridges could be characterized as pre-existing weaknesses in the crust where stress is most easily accommodated. Seismicity in the central and eastern U.S. appears to concentrate in zones where previous large magnitude earthquakes have occurred (e.g. the site of the 1811 – 1812 New Madrid earthquakes or the 1886 Charleston earthquake). In some cases, the sites of previous large magnitude earthquakes or concentrations of low to moderate magnitude seismicity in the central and eastern U.S. (i.e. the Central Virginia Seismic Zone) coincide with Iapetus rift structures [*Mazzotti and Townend,* 2010]. This suggests that the occurrence of the Mineral earthquake in the Central Virginia seismic zone, a pre-existing zone of weakness, is not unexpected. In fact, the slow aftershock decay rate associated with the Mineral earthquake implies that earthquakes in the epicentral region of the Mineral earthquake might continue for a decade or longer.

5.1.2 Seismicity and patterns of faulting in intraplate regions

The presence of young lunar graben, contractional lobate scarps, and wrinkle ridge – lobate scarp transitions (perhaps 50 Myr old) could be related to shallow moonquakes (<100 km depth) recorded during the Apollo era passive seismic experiment between 1969 and 1977 (28 shallow moonquakes recorded), indicating that significant tectonic activity has occurred on the Moon relatively recently [*Nakamura et al*., 1979; *Nakamura et al*., 1981; *Watters et al*., 2010; *Watters and Johnson,* 2010; *Watters et al.,* 2012b]. Similarly, the presence of tectonic features on

Mercury's surface suggests that Mercury might have experienced recent shallow seismicity. While seismicity on Mercury and the Moon may be tied to relatively young tectonic features, earthquakes in the central and eastern U.S. are often difficult to tie to previously identified faults. This poses the question: are we not able to identify active faults in the central and eastern U.S. because they are difficult to detect due to vegetation and human infrastructure, or do seismic events in intraplate regions tend to activate new faults rather than re-activating previously active faults?

The random distribution and orientations of cross-cutting wrinkle ridges in the northern smooth plains of Mercury are quite similar to patterns of faulting observed in the Mid-Atlantic region of the central and eastern U.S. (Figure 5-1 and 5-2). The Mid-Atlantic region of the central and eastern U.S. shows evidence of cases in which pre-existing faults were reactivated (e.g. the Stafford fault zone) as well as cases in which new faults formed in order to adapt to the current stress field (e.g. the DC fault zone). It is probable that the preference to either re-activate a pre-existing fault or form a new fault depended on the orientation of the stress field at the time in which the fault formed. Reactivated faults in the central and eastern U.S. may be similar to the largest relief wrinkle ridges on Mercury and the Moon, where underlying faults are pre-existing weaknesses in the crust that act as conduits allowing stress to be relieved. Conversely, if stress is acting on the crust in a direction in which there is no pre-existing fault, eventually a new fault may form with a different orientation than these faults in order to accommodate stress.

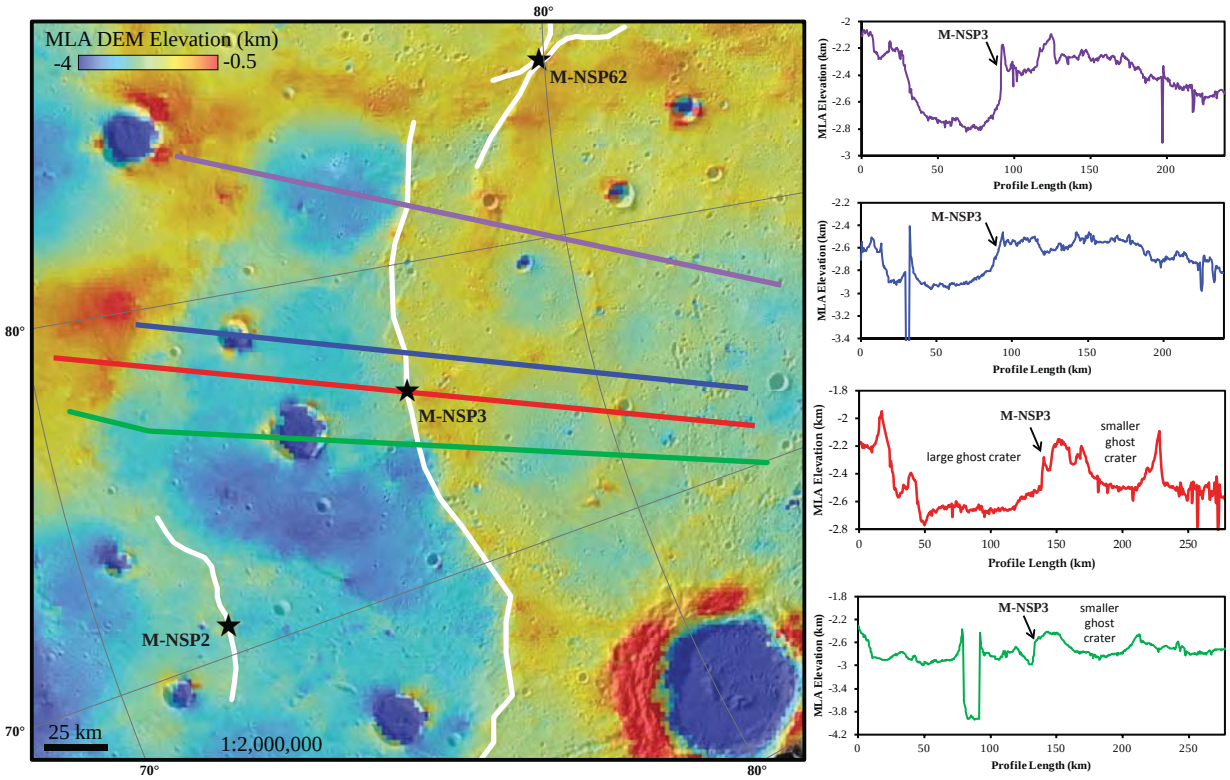

Figure 5-1. Complex patterns of faulting in Mercury's northern smooth plains
Example of a complex tectonic environment surrounding wrinkle ridge M-NSP3 (73.26°N, 76.07°W) in Mercury's northern smooth plains. MLA DEM overlaid on the MDIS WAC 250 m/pixel mosaic illuminates the presence of a line of east-west trending large diameter ghost craters (~60 km) to the south and a line of smaller diameter ghost craters (~40 m) to the north. The presence of ghost craters near the wrinkle ridge produce complex topographic profiles that in some cases make it difficult to distinguish the topographic expression of the wrinkle ridge from the ghost craters.

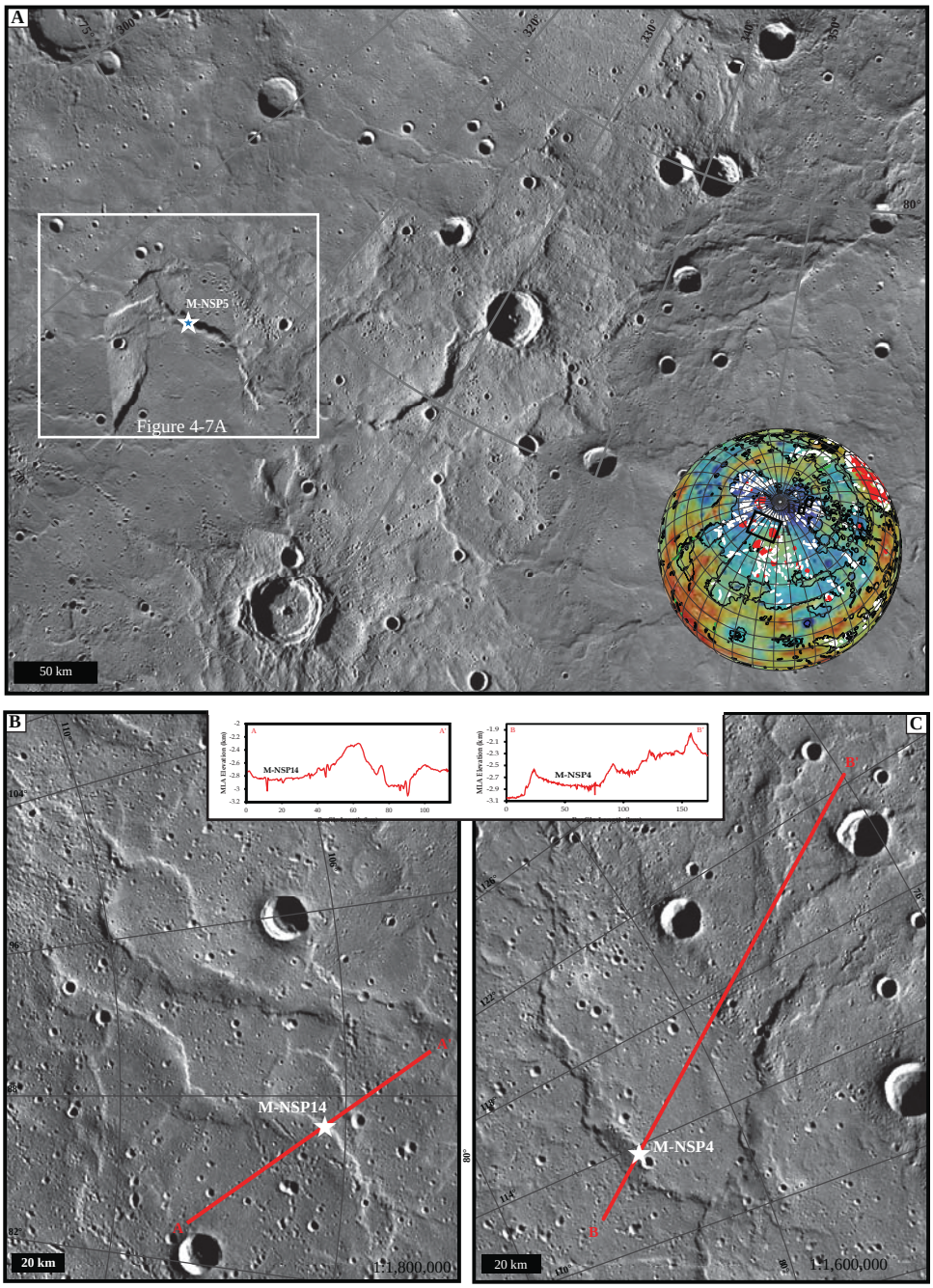

Figure 5-2. Cross-cutting wrinkle ridges in the northern smooth plains
The density of wrinkle ridges alone may explain the complexity revealed by topographic profiles crossing wrinkle ridges in Mercury's northern smooth plains. However, cross-cutting relations visible in the 250 m/pixel global monochrome mosaic (A, B, and C: north polar projection) and what appear to be stacks of wrinkle ridges (B) may indicate multiple episodes of deformation have occurred in the northern smooth plains. Locations of maps are shown on an orthographic projection (center latitude = 66.87°N, center longitude = 43°E) of the MLA DEM overlaying the 500 m/pixel global monochrome mosaic. Inset in image A is one of the largest wrinkle ridges on Mercury modeled in Chapter 4. Transects and topographic A to A' and B to B' are from MLA tracks.

On the Moon, the majority of wrinkle ridges form concentric rings parallel to basin borders, suggesting they were created due to subsidence (Figure 4-3B). However, in some locations wrinkle ridges transition into lobate scarps cutting across rocks in both the mare basins and in the highlands. These wrinkle ridge – lobate scarp transitions are attributed to global contraction and are good examples of cases when the pattern of faulting diverges from the regional pattern in order to accommodate the current, dominant stresses. Initial analysis shows that the rupture plane of the Mineral earthquake dips in a similar direction as pre-existing faults and the regional foliation, but appears to have a steeper dip than any pre-existing features. We await modern reprocessing of geophysical data collected in the epicentral region to see if any small scale pre-existing structure existed before the Mineral earthquake, but it is possible that the earthquake ruptured on a new fault in order to adjust to the current day stress field.

5.1.3 Contributions to the regional stress field

By their nature, many of the components driving intraplate seismicity deform the surface over large regions, or spatially broad zones, that span hundreds to thousands of kilometers. Instead of concentrating stress in a narrow zone like at tectonic plate boundaries, rocks within intraplate regions must adjust to stress over wide, spatially diffuse, regions. A variety of mechanisms could be responsible for triggering intraplate seismicity in the Mid- Atlantic region of the central and eastern U.S. [*Stein et al.*, 1989]: topographic relaxation of the Appalachians [*Ghosh et al.*, 2009], loading of water and sediments in the Chesapeake Bay and on the Atlantic margin [*Calais et al.*, 2010], isostatic uplift from melting of the Laurentide ice sheet

from the last glacial maximum (12,000 years ago) [*Calais et al.*, 2006; *Sella et al.*, 2007; *Stewart et al.*, 2000], or ridge push generated by the cooling of the oceanic portion of the North American plate [*Zoback*, 1992]. On other planets, subsidence due to loading from thick sequences of lava and global contraction generated by interior cooling are the largest contributors to the stresses that generate tectonic features on the surface [*Strom*, 1970; *Maxwell et al.*, 1975; *Solomon et al.*, 2008].

5.1.4 Spatially migrating seismicity and Coulomb stress transfer

The regional extent in which stresses can act within intraplate regions may explain why many events in the CEUS seem to occur randomly in locations far away from any pre-existing seismic zone or known fault (e.g. the July 2010 Germantown earthquake). Some researchers suggest that seismicity in intraplate regions is spatially migrating, so that the same fault never ruptures twice [*Liu et al.*, 2011]. Although I concluded that the magnitude of stress transferred from the Mineral and Germantown earthquakes was small, static stress transfer may play a role in the geospatial distribution of tectonic features in intraplate regions. Stress transfer from previous earthquakes could drive spatially migrating seismicity. For example, the stress transferred from the 2003 earthquakes in the Central Virginia Seismic Zone may have triggered the Mineral earthquake to the northeast (Figure 2-2). Therefore, the next earthquake may occur in a seismic gap or regions that have not yet experienced seismicity rather than in locations were previous earthquakes have occurred.

5.1.5 Overall conclusions

By comparing patterns of tectonic deformation on Mercury and the Moon to the central and eastern U.S., I can make the following conclusions about the characteristics of intraplate regions:

1. Pre-existing zones of weakness in the crust can concentrate seismicity and deformation for long periods of time.
2. The orientation of the stress field in intraplate regions fluctuates over time due to the timing and duration of various factors contributing stress. The complex patterns of faulting in intraplate regions are due, in part, to faults accommodating changes in the stress field over time.
3. The transfer of stress from earthquakes over time may drive spatially migrating seismicity.

5.2 Future directions of research and closing remarks

5.2.1 Coulomb stress accumulation and monitoring

Since earthquakes in intraplate regions tend to have low to moderate magnitudes, only small amounts of stress are transferred from individual events to nearby faults. While alone these changes in stress may seem negligible, mapping migration of stress over time and documenting its accumulation in the crust is vital to understanding seismicity in passive margins. Although the absolute state of stress in intraplate North America (including the amount of stress contributed by each component to the stress field over time) is largely unknown, we can use existing geologic and seismic data as a starting point. Continued monitoring of stress transfer

after moderate magnitude events occur may enable us to track the migration of stress over time, and thus the timing and location of future intraplate earthquakes.

5.2.2 The potential of LIDAR as a tool for understanding patterns of faulting

One of the challenges of deciphering patterns of faulting in the central and eastern U.S. is that many tectonic features are obscured by vegetation and human-modification to the topography (e.g. city development). The emergence of high-resolution digital elevation models produced from Light Detection and Ranging (LIDAR) offer a new tool for finding and characterizing recently active scarps in densely forested and metropolitan regions [*Harding and Berghoff*, 2000; *Engelkemeir and Khan*, 2007; *Sherrod et al.*, 2004]. High resolution LIDAR elevation data collected in the epicentral region of the Mineral earthquake (Figure 3-4) offer an opportunity to map and characterize active faults in the CVSZ. These new data combined with continued geologic field mapping of pre-existing faults in the central and eastern U.S. will enable us to improve our knowledge of periods of tectonic deformation that shaped the landscape in the past and thus our ability to identify regions of active deformation and possible zones of pre-existing structural weakness in intraplate North America.

Comparison of the pattern of faulting in the central and eastern U.S. to southeast Australia, which is located in an intraplate environment, may yield promising results. Low erosion rates and sparse vegetation have enabled the development of a new dataset of intraplate Quaternary active structures in Australia, developed by Geoscience Australia [*Clark*, 2010; *Clark et al.*, 2011; *Quigley et al.*, 2010]. This database includes information on large, surface-rupturing earthquakes,

spanning tens of thousands of years, based on the preservation of recently active fault scarps in the landscape [*McPherson et al.*, 2012]. The Southeast seismic zone exists in a tectonic domain similar to the Appalachians, Piedmont, and Coastal Plain of the central and eastern U.S. and offers an analog for understanding intraplate seismicity in the Central Virginia seismic zone (site of the Mineral earthquake) in particular [*Leonard*, 2008]. This domain is comprised of Phanerozoic crust, including arcs and mobile belts, which was accreted to the eastern margin of Australia during the Paleozoic and is reminiscent of the Paleozoic contraction and Mesozoic extension that formed the Appalachians [*Williams*, 1995; *Clark et al.*, 2011].

Geoscience Australia plans to collect a high-resolution LIDAR-derived elevation model of quaternary-active scarps in southeastern Australia (e.g. the Avonmore scarp), which will offer the opportunity to compare the LIDAR data collected in the region of the Mineral earthquake to another intraplate region. Further, examination of the patterns of faulting in Australia may enable us to work out the importance of different components to the stress field in the central and eastern U.S., as our comparison of Mercury to the Moon helped us work out relative contributions of global contraction and subsidence.

5.2.3 Arrival of EarthScope and need for more dense seismic network

The role of remote triggering due to the passage of seismic waves in intraplate environments is yet to be confirmed. The arrival of EarthScope to the eastern U.S. in 2013 will temporarily improve our ability to detect smaller magnitude earthquakes that may be associated with long-distance triggering and provide an opportunity to characterize the regional crustal structure. Installation of more permanent seismic

stations in the central and eastern U.S. to increase the density of the detection network is needed to more robustly monitor seismicity rate changes, which in addition to evaluating if the phenomena of remote triggering exists in intraplate region, may be key to deciphering the recurrence interval of earthquakes in passive margins.

5.2.4 Opportunity to advance our understanding of tectonics on other planets

The MESSENGER and LRO spacecraft are still in orbit and continue to provide high-resolution imagery and altimetry data of tectonic features on the surfaces of Mercury and the Moon. Continued mapping of wrinkle ridges and other tectonic features will enable us to more accurately estimate the amount of global contraction on Mercury and the Moon, recount their tectonic histories, and thus advance our understanding of tectonic deformation on other planets. Continued morphometric characterization of wrinkle ridges on each planet and conversion of reliefs to displacement would allow us to more accurately estimate the amount of contraction on the faults underlying each ridge, thus enabling us to possibly resolve the thickness of smooth plains material in which wrinkle ridges reside and estimate the amount of regional subsidence. In particular, the effort to decipher patterns of faults on Mercury's surface may lead to an opportunity to understand patterns of faulting in intraplate regions on Earth, and thus our ability to improve seismic hazard mitigation procedures in these environments.

New measurements of wrinkle ridge relief from MESSENGER and LRO orbital data indicate that there are larger relief wrinkle ridges on Mercury and the Moon than recognized previously [*Watters*, 1988] (Figure 5-3). The range of ridge reliefs for lunar wrinkle ridges is most similar to those on Mars. Wrinkle ridges

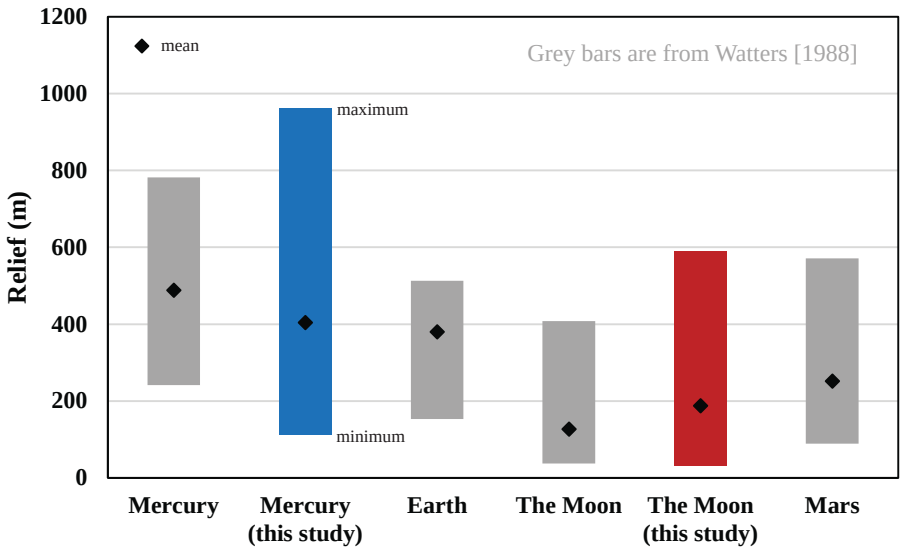

Figure 5-3. Comparison of wrinkle ridges on the terrestrial planets and the Moon

Range of relief for wrinkle ridges on Mercury, Earth, the Moon, and Mars. Grey bars are from Watters [1988] and blue (Mercury) and red (the Moon) bars are from this study. Notice larger relief wrinkle ridges than previously measured were found on Mercury and the Moon using new orbital data from the MESSENGER and LRO spacecraft. All bodies contain a population of wrinkle ridges ranging from ~190 to 460 m in relief. Differences in wrinkle ridge relief are likely caused by varying contributions of load induced subsidence and global contraction due to interior cooling.

located in the basalts of the Columbia River Plateau in the Pacific Northwest on Earth have the narrowest range of reliefs. While there are subtle differences in the dimensions of wrinkle ridges on an each body, notice that there is a population of wrinkle ridges ranging from ~190 to ~460 m in relief on all the terrestrial planets and the Moon.

I suggest that the subtle differences in relief exist due to varying contributions of load induced subsidence and global contraction. The amount of subsidence due to loading on the lithosphere is most likely controlled by the basin size, as well as the thickness of smooth plains material and their composition. Similarly, the contribution of global radial contraction due to interior cooling is probably caused by a combination of planet radius, internal structure, and composition. Comparing the dimensions of wrinkle ridges on Mercury and the Moon allowed the dominant components of the stress field to be resolved. Therefore, perhaps a similar comparison of tectonic features in the central and eastern U.S. to those in southeastern intraplate Australia would enable components of the stress field in intraplate environments on Earth to be constrained.

5.2.5 Seismic hazard re-evaluations for the central and eastern U.S.

The occurrence of the Mineral earthquake has spurred the need for seismic hazard re-evaluation in the central and eastern U.S. The next step would be to integrate the results of this research into the new ongoing seismic hazard re-evaluations for the central and eastern U.S. led by government agencies, particularly the Nuclear Regulatory Commission, and ongoing research in the geologic consulting

industry regarding safe siting and operation of nuclear reactors and construction of new critical facilities including bridges, dams, tunnels, and hospitals.

My analysis of stress transfer in the aftershock zone demonstrates that stress transfer plays a role in the triggering of earthquakes in intraplate environments and should therefore be incorporated in the seismic hazard evaluations. The recent release of the databases in the CEUS-SSC project (http://www.ceus-ssc.com/) is a good starting place for re-evaluating seismic hazard in the central and eastern U.S. However, the influence of the Mineral earthquake, which occurred after the release of this project, needs to be incorporated into seismic hazard re-evaluation. Continued monitoring and analysis of earthquakes in the central and eastern U.S. will advance our understanding of the mechanisms that trigger seismicity in intraplate regions, as well as in tectonic plate boundary zones, and thus our ability to mitigate the effects of the next large magnitude earthquake.

Appendices

Appendix 2-A: Data and Resources for Chapter 2

- The Aftershock data for the region of the Mineral earthquake are available from Saint Louis University Earthquake Center who deployed a temporary seismic network in the region between 23 August 2011 and 2 May 2012 at http://www.eas.slu.edu/eqc/eqc_significant/2011_Virginia/aftershock.html (last accessed September 2012).
- The location of the 23 August 2011 Mineral earthquake's mainshock is available from the USGS at http://earthquake.usgs.gov/earthquakes/recenteqsww/Quakes/se082311a.php. The USGS/SLU Moment Tensor Solution for the Mineral earthquake is available at http://earthquake.usgs.gov/earthquakes/eqarchives/fm/se082311a_rmt.php (last accessed September 2012).
- The location of the Germantown earthquake and its aftershock were acquired from the USGS at http://earthquake.usgs.gov/earthquakes/recenteqsww/Quakes/us2010yua6.php and the IRIS earthquake browser at http://www.iris.edu/servlet/eventserver/map.do. The relocated location of the Germantown mainshock was provided by Lamont-Doherty Earth Observatory at Columbia University at http://www.ldeo.columbia.edu/LCSN/recenteqs/Quakes/ld60020503.html. The USGS/SLU Moment Tensor Solution for the Germantown earthquake is available at

http://earthquake.usgs.gov/earthquakes/eqinthenews/2010/us2010yua6/neic_yua6_rmt.php (last accessed September 2012).

- The location and magnitude of earthquakes that occurred between 1973 and 2011 shown in figure 2 were obtained for each state from the USGS National Earthquake Information Center (NEIC) significant earthquake database at http://earthquake.usgs.gov/earthquakes/states/state_largest.php. The location of historic earthquakes that occurred between 1774 and 1984 were obtained from http://earthquake.usgs.gov/earthquakes/states/historical_state.php (last accessed December 2011).
- Intensity derived from USGS "Did you feel it?" surveys and USGS/SLU focal mechanism information are from the USGS pages for these earthquakes: Mineral earthquake: http://earthquake.usgs.gov/earthquakes/recenteqsww/Quakes/se082311a.php; Trinidad earthquake: http://earthquake.usgs.gov/earthquakes/recenteqsww/Quakes/usc0005idz.php (last accessed September 2012).
- GIS data and a digital representation of the 1993 Geologic Map of Virginia is available at http://mrdata.usgs.gov/geology/state/state.php?state=VA (last accessed September 2012).
- The location and orientation of the Everona fault was measured by Andrew Bobyarchick at the University of North Carolina at Charlotte (personal communication, July 2012).

- The map of the DC fault zone was provided by David Prowell of the USGS (personal communication, January 2012).
- The photographic of the crack in the Washington Monument is available from the National Park Service at http://www.nps.gov/wamo/photosmultimedia/washington-monument-earthquake-damage-photos.htm (last accessed September 2012).
- The software Coulomb version 3.3 used in our analysis is publically available at http://earthquake.usgs.gov/research/modeling/coulomb/ (last accessed September 2012).
- Report from Dominion Power (2011) titled “Dominion Power Wants to Restart Nuclear Reactors Shut Down During Quake” is available at http://www.nbcwashington.com/news/local/Dominion-Wants-to-Restart-Nuclear-Reactors-Shut-Down-During-Quake-132314903.html (accessed October 24, 2011).
- All other data used in this paper came from published sources listed in the references

Appendix 2-B: Location of the Germantown earthquake

This appendix includes a map (Figure 2-B1) showing the location of the July 16, 2010 Germantown, Maryland, earthquake and its aftershock and a table with the location, depth, magnitude, and time of the mainshock and aftershock.

Table 2-B1: Information for the Germantown earthquake and aftershock

Earthquake	Date	Time (UTC)	Latitude (°)	Longitude (°)	Depth (km)	Magnitude
Mainshock	7/16/2010	9:04:48	39.261	-77.41	7	3.4
Aftershock	7/16/2010	9:16:08	39.204	-77.299	5	2.1

(from LCSN - Lamont-Doherty Earth Observatory)

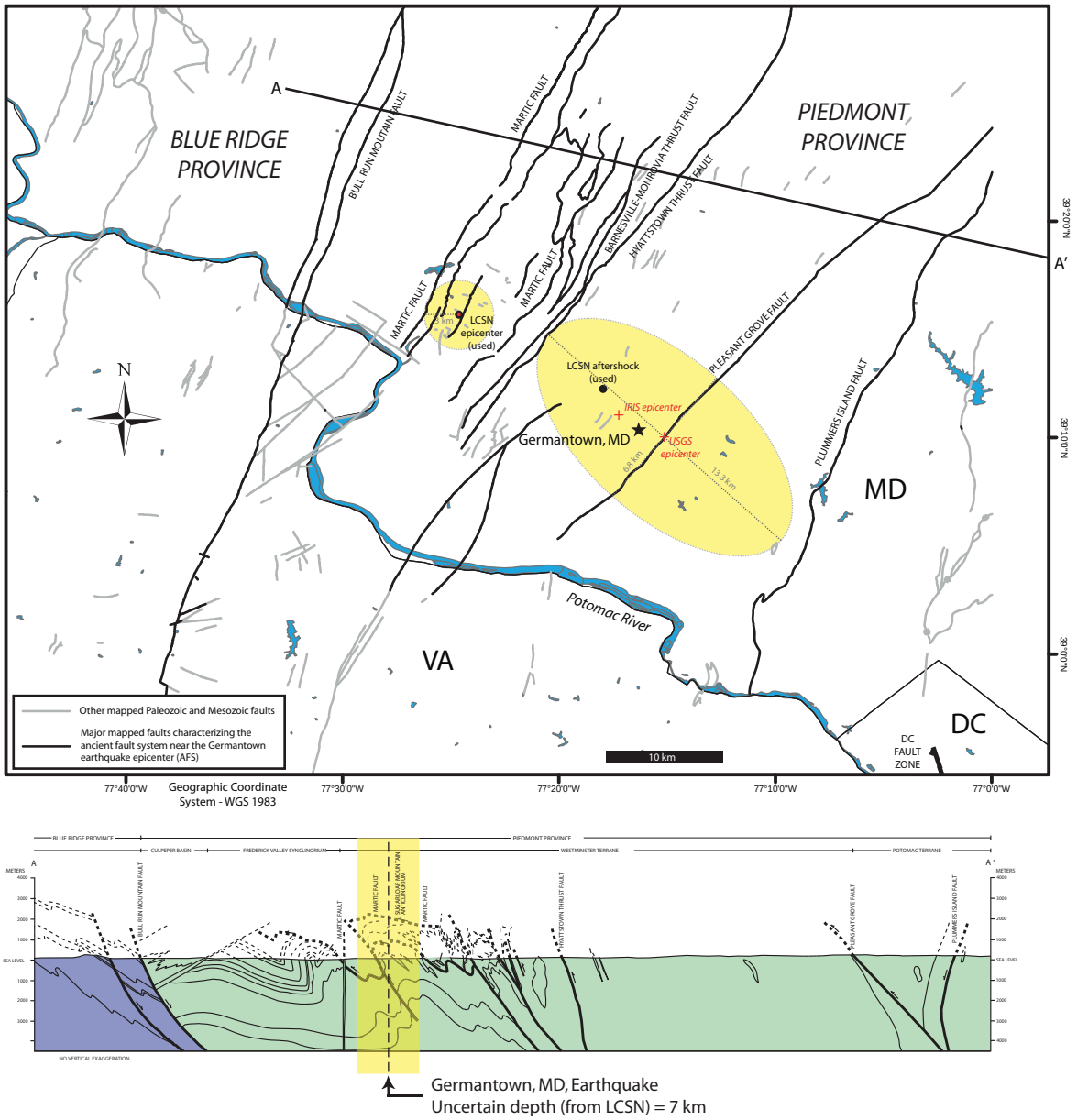

Figure 2-B1. Germantown earthquake location

Earthquake epicenters and uncertainty ellipses from Lamont-Doherty Earth Observatory (LCSN) and the U.S. Geological Survey (USGS) for the Germantown earthquake and its aftershock superimposed on local modified geologic map [*Mixon and Newell*, 1977; *Prowell*, 1988; *Davis et al.*, 2001; *Southworth et al.*, 2002; *Southworth et al.*, 2007]. The error circle for the LCSN solution has a radius of approximately 3 km. The USGS earthquake location was prominently used in media releases after the earthquake's occurrence. The error ellipse for the USGS location has axes of 13.3 km and 6.8 km. USGS and Lamont mainshock epicenters are ~ 17 km apart. Note also the location of the aftershock on the map (Table 2-B1). The depth of the earthquake is not well constrained. Important ancient faults near the earthquakes epicenter are shown on the map. Faults in the vicinity of the earthquake epicenter generally strike N25°E to N40°E.

Appendix 2-C: Coulomb stress change ($\Delta\sigma_{CFS}$) parameter input tests

Description of a variety of input parameters tests I performed to gauge the uncertainty of my $\Delta\sigma_{CFS}$ calculations. Plan view maps are made at 7 km depth in all figures except Figure 2-C7.

1. Source fault

I selected NP1 from the Germantown earthquake's focal mechanism to use as the source fault in my $\Delta\sigma_{CFS}$ calculation. Here I used the orientation of the DCFZ (163°, 68°, 93°) as the receiver fault for this test to compare $\Delta\sigma_{CFS}$ results for NP1 versus NP2. Using either rupture plane as the source fault does not change the pattern of $\Delta\sigma_{CFS}$ (Figure 2-C1). The nodal planes from the earthquake's focal mechanism have an uncertainty of ±10° (Bob Herrmann, personal communication). I tested the effect of A) using the preferred orientation of NP1 - 195°, 57°, 123°, B) adding 10° to the strike of NP1 - 205˚, 57˚, 123˚, and C) adding 10° to the dip of NP1 - 195°, 67°, 123°. The uncertainty of the nodal plane orientation produces only minor changes in the $\Delta\sigma_{CFS}$ patterns produced in this analysis (Figure 2-C1).

2. Receiver fault

The orientation of the receiver fault determines the pattern of $\Delta\sigma_{CFS}$. Rake can vary due to uncertainties associated with calculating the P, N, and T axes. Strike and dip can vary due to uncertainty from field measurements. Strike and dip values for fault systems were extracted from the geologic maps for the SFS and AFS,

whereas the orientation for the DCFZ was recognized and measured in the field. Uncertainties for strike, dip, and rake can vary up to at least 10°, therefore I tested these variations by changing each of these variables and examine how each parameter affects the pattern of $\Delta\sigma_{CFS}$. I used NP1 as the source fault.

2.1 Strike

For simplicity, for the receiver fault I used the orientation of a hypothetical thrust fault striking north (0°) and dipping 45°E. I compared differences in the $\Delta\sigma_{CFS}$ pattern for thrust faults dipping 45° and with a strike ranging from 0° to 360° in increments of 45° (Figure 2-C2). I also examined smaller variations in strike, on the order of ±10°, which might be expected from error in measurements of strike in the field or measurements from a geologic map. For this test, I used the DCFZ (163°, 68°, 93°) as the receiver fault and varied the strike of the DCFZ from 1° to 10° in increments of 2° (Figure 2-C3). I found no noticeable variation in the pattern of $\Delta\sigma_{CFS}$ for a strike variance ±10°. Variations greater than ±15° started to show minor changes in the $\Delta\sigma_{CFS}$ pattern. More noticeable changes started to appear with variations ±20° (e.g. strike = 183°). Variations in strike greater than 45° change the location and size of stress trigger zones and stress shadows in the $\Delta\sigma_{CFS}$ pattern.

2.2 Dip

I used the hypothetical thrust fault striking 0° from the previous test again to compare differences in the $\Delta\sigma_{CFS}$ pattern created when dips vary from 10° to 90° in increments of 10° (Figure 2-C4). Dip has a much greater influence than strike on the pattern of $\Delta\sigma_{CFS}$ in plan view. Variations in dip ±10° change the location and size of the stress shadows and trigger zones more than ±45° changes in strike. Similarly,

smaller variations in strike affect the pattern of $\Delta\sigma_{CFS}$ in cross-section view. I also examined smaller variations in dip, on the order of ±10°, which might be expected from error in measurements of strike in the field or measurements from a geologic map. Here I present differences in $\Delta\sigma_{CFS}$ created by small variations in the dip of the receiver fault. We again use the DCFZ (163°, 68°, 93°) as the receiver fault for this test to allow comparison to my analysis. I varied the dip of the DCFZ from 1° to 10° in increments of 2° (Figure 2-C5). Minor variations in dip make only subtle differences in the pattern of ΔCFS.

2.3. Rake

I computed $\Delta\sigma_{CFS}$ for each of the end-members of slip (thrust: rake = 90°, normal: rake = -90°, left-lateral: rake = 0°, and right-lateral: rake =180°). I also examined smaller variations in rake, on the order of ±10°, which might be expected from error in calculating the expected slip vector. I used the DCFZ (163°, 68°, 93°) as the receiver fault for this test to allow comparison to my analysis. I varied the rake in increments of 2° from ±1 to 10°. Note there is significant variation in the $\Delta\sigma_{CFS}$ pattern created for rakes varying by ±90°), however there is only minor variation created by small changes in rake (Figure 2-C6).

2.4 Summary

Dip has a much greater influence than strike on the pattern of $\Delta\sigma_{CFS}$ in plan view. Variations in strike produce a greater effect on the pattern of $\Delta\sigma_{CFS}$ in cross-section view. The orientations of strike, dip, and rake control the pattern of $\Delta\sigma_{CFS}$. However, these tests show that small variations in strike, dip, and rake (on the order of ±10° for strike, ±5° for dip, and ±5° for rake), as expected from measurement

uncertainty in the field or on a geologic map, have little effect on patterns of $\Delta\sigma_{CFS}$. Strikes, dips, and rakes ranging -1° to -10° from preferred dip produce a similar variation as strikes, dips, and rakes ranging +1° to +10°.

3. Earthquake rupture depth

The hypocenter depth, 7 km, is not well constrained. Here I explore the influence of using different proposed depths for the Germantown earthquake (3, 5, 7, and 18 km) on patterns of $\Delta\sigma_{CFS}$ (Figure 2-C7). The depth of the earthquake has a moderate effect on the expression of $\Delta\sigma_{CFS}$ near the surface where there are known mapped faults.

4. Coefficient of friction (μ')

Different coefficients of friction (μ') produce noticeable differences in patterns of $\Delta\sigma_{CFS}$ in both plan view and cross-section view. I suggest $\Delta\sigma_{CFS}$ calculations that use a μ' = 0.8 are more representative of static stress transfer occurring in intraplate regions [*Zoback*, 1992; *King et al.*, 1994; *Li et al.*, 2007; *Viegas*, 2012]. However, we include $\Delta\sigma_{CFS}$ results for μ' = 0.4, which an average coefficient of friction for comparison (Figure 2-C8).

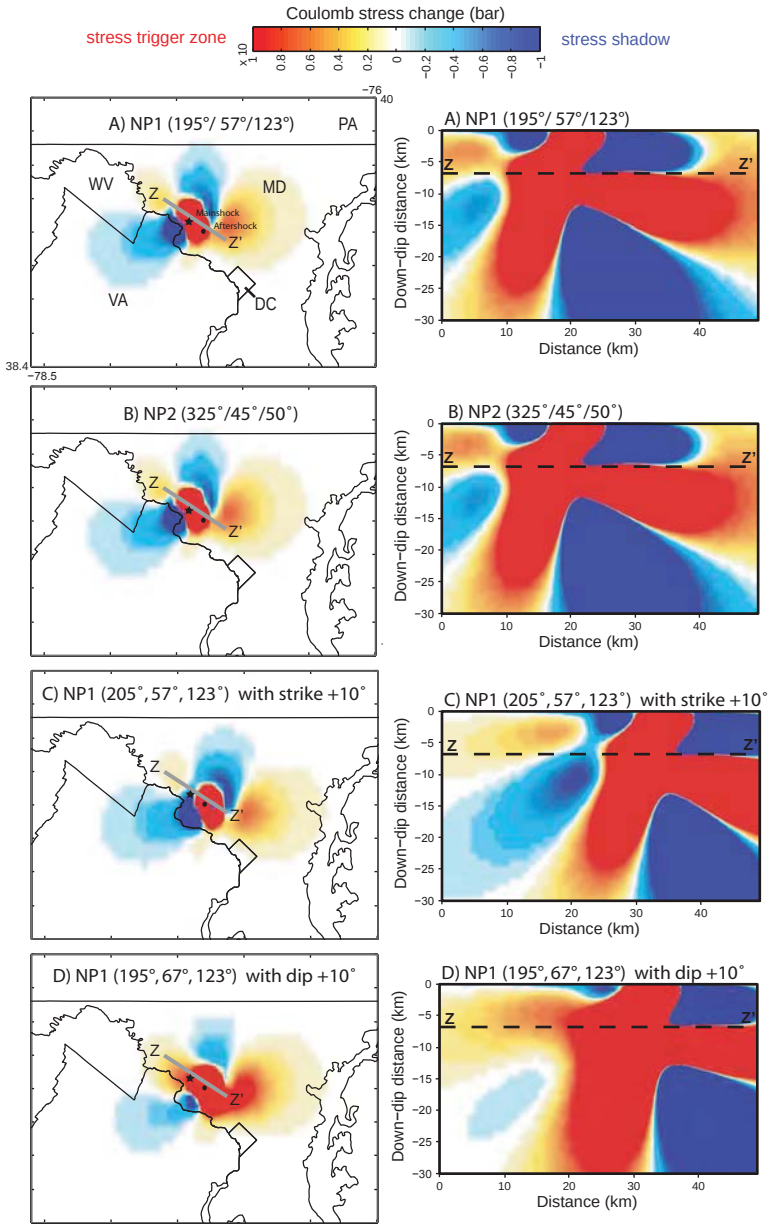

Figure 2-C1. Changes in patterns of σ_{CFS} for different rupture planes from focal mechanism Comparison of $\Delta\sigma_{CFS}$ patterns calculated using A) NP1 and B) NP2 for the earthquake's focal mechanism for the source fault. $\Delta\sigma_{CFS}$ generated by ±10° variation of NP1. C) adding 10° to the strike of NP1, and D) adding 10° to the dip of NP1. The pattern of $\Delta\sigma_{CFS}$ is the same regardless whether NP1 or NP2 is selected as the source fault. Similar results are produced when subtracting 10°. The DCFZ is used as the receiver fault.

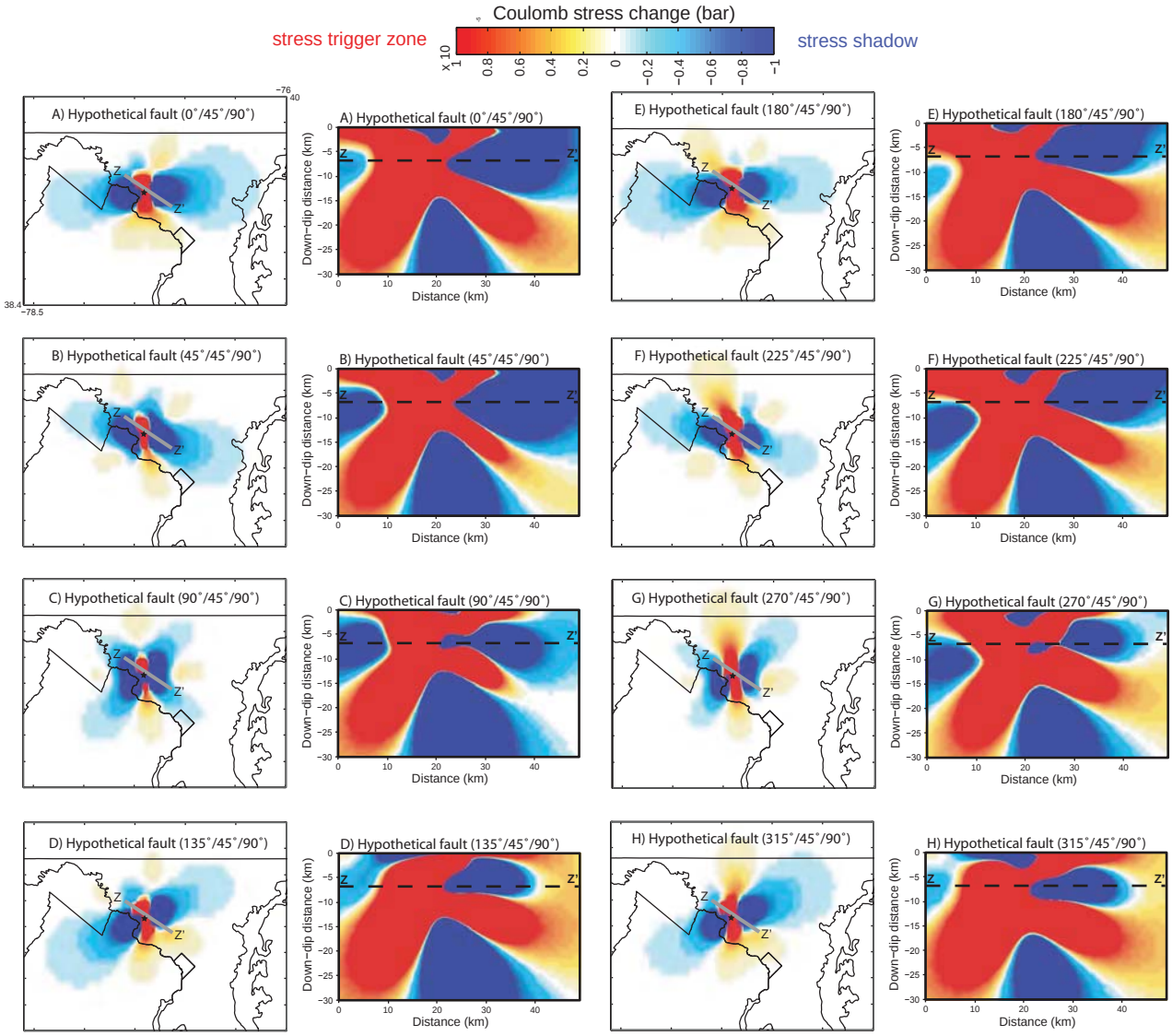

Figure 2-C2. Effect of varying strike on $\Delta\sigma_{CFS}$ result – fault dipping 45°
$\Delta\sigma_{CFS}$ generated for a hypothetical receiver thrust fault dipping 45° with strikes ranging from 0° to 360°.

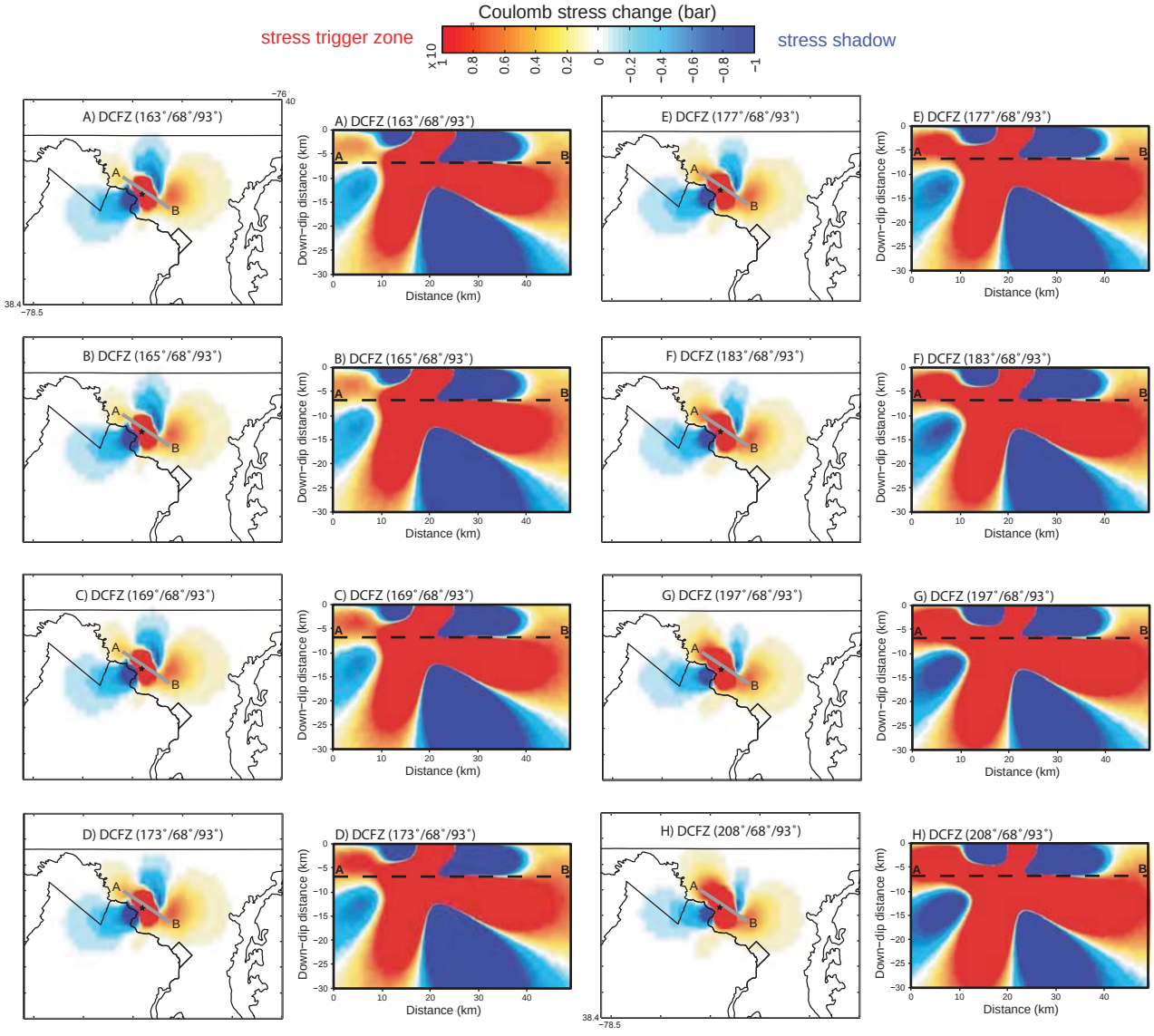

Figure 2-C3. Effect of small variations in strike on $\Delta\sigma_{CFS}$ result
Effect of small variations in the receiver fault's strike (ranging 2° to 45° from preferred strike - A) on the $\Delta\sigma_{CFS}$ pattern. Strikes ranging -1° to -10° from the preferred strike produce a similar variation.

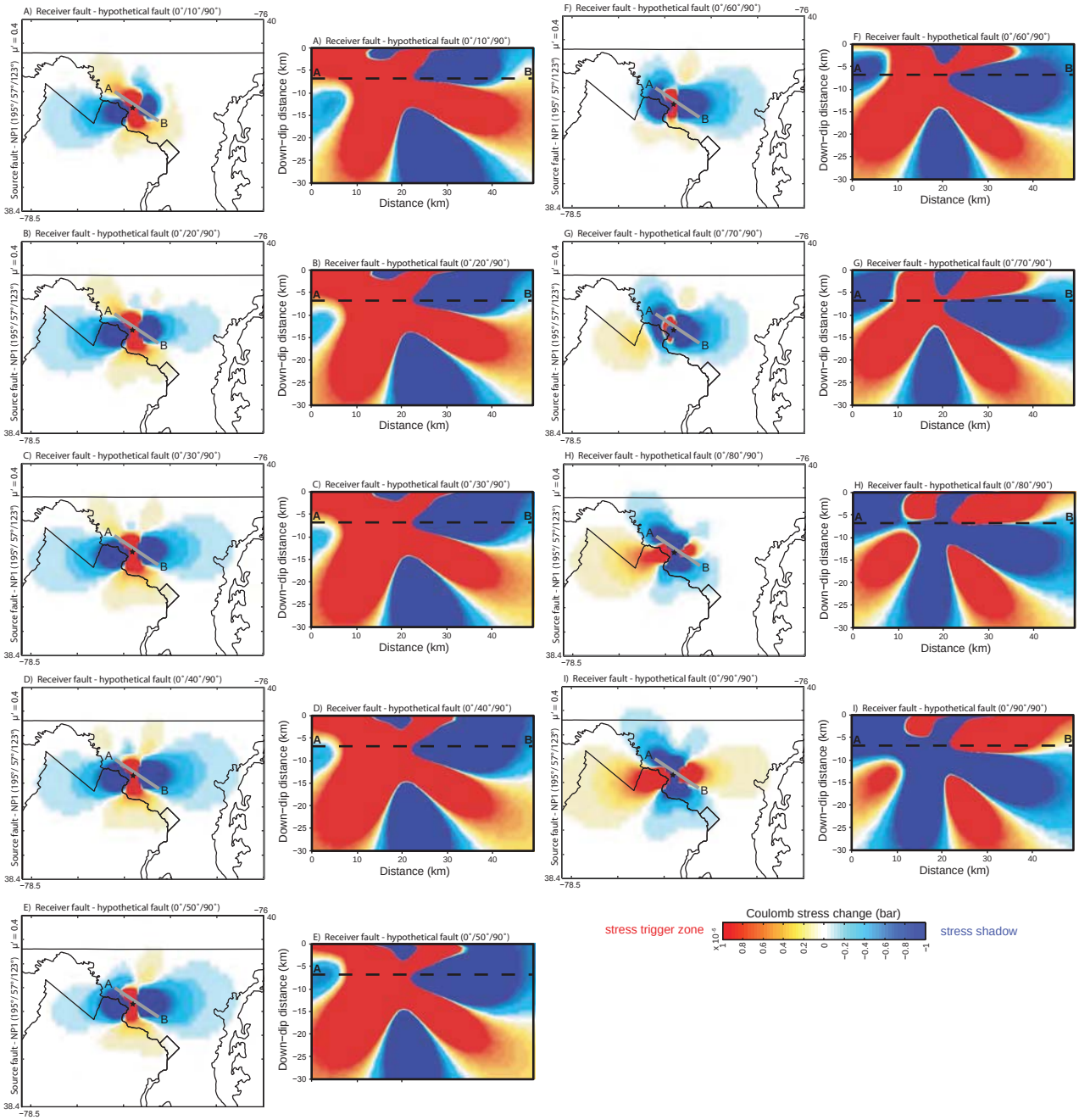

Figure 2-C4. Effect of varying dip on $\Delta\sigma_{CFS}$ result – fault striking 0°

$\Delta\sigma_{CFS}$ generated for a hypothetical thrust fault striking 0° with dips ranging from 10° to 90°.

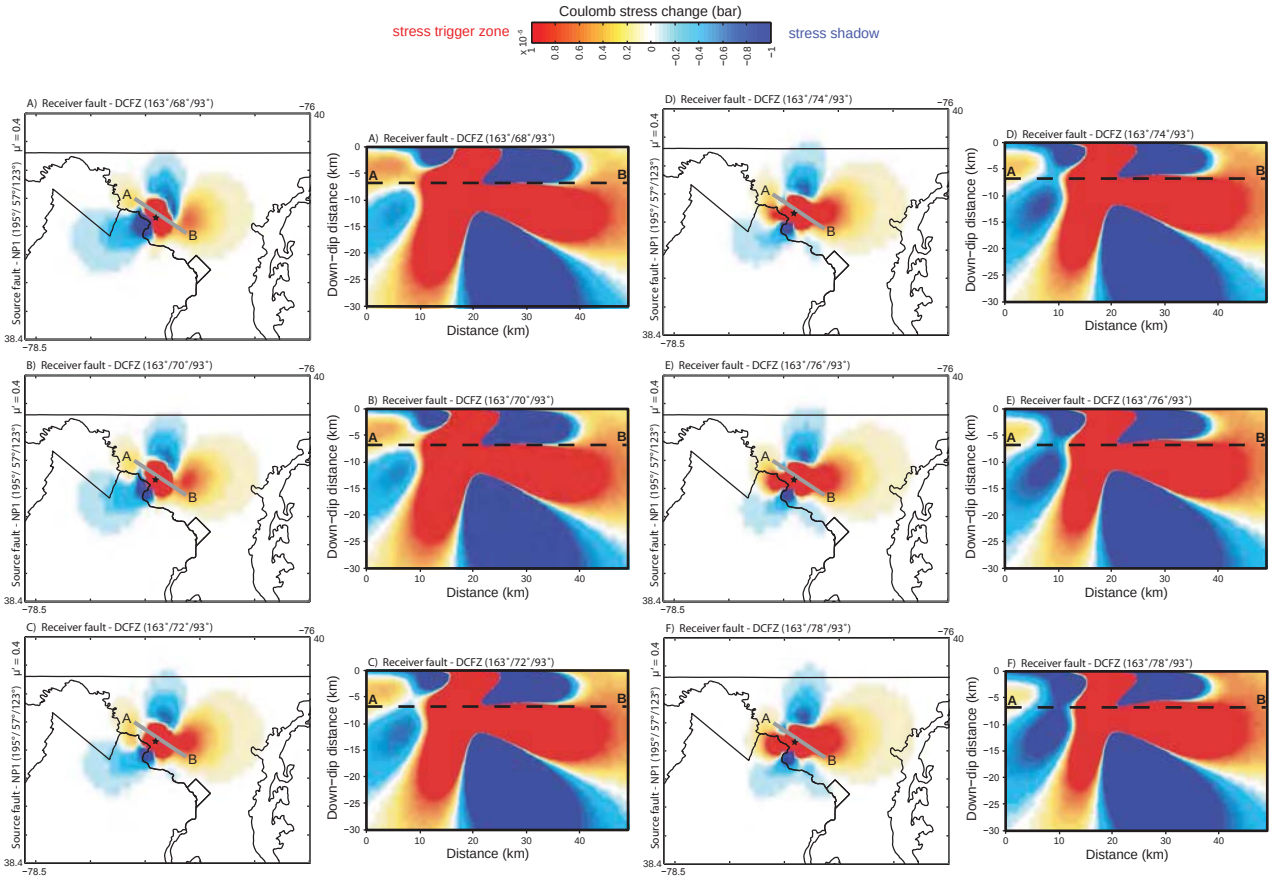

Figure 2-C5. Effect of small variations in dip on $\Delta\sigma_{CFS}$ result
Effect of small variations in the receiver fault's dip (ranging from 1° to 10° from preferred dip - A) on the $\Delta\sigma_{CFS}$ pattern. Dips ranging -1° to -10° from the preferred dip produce a similar variation.

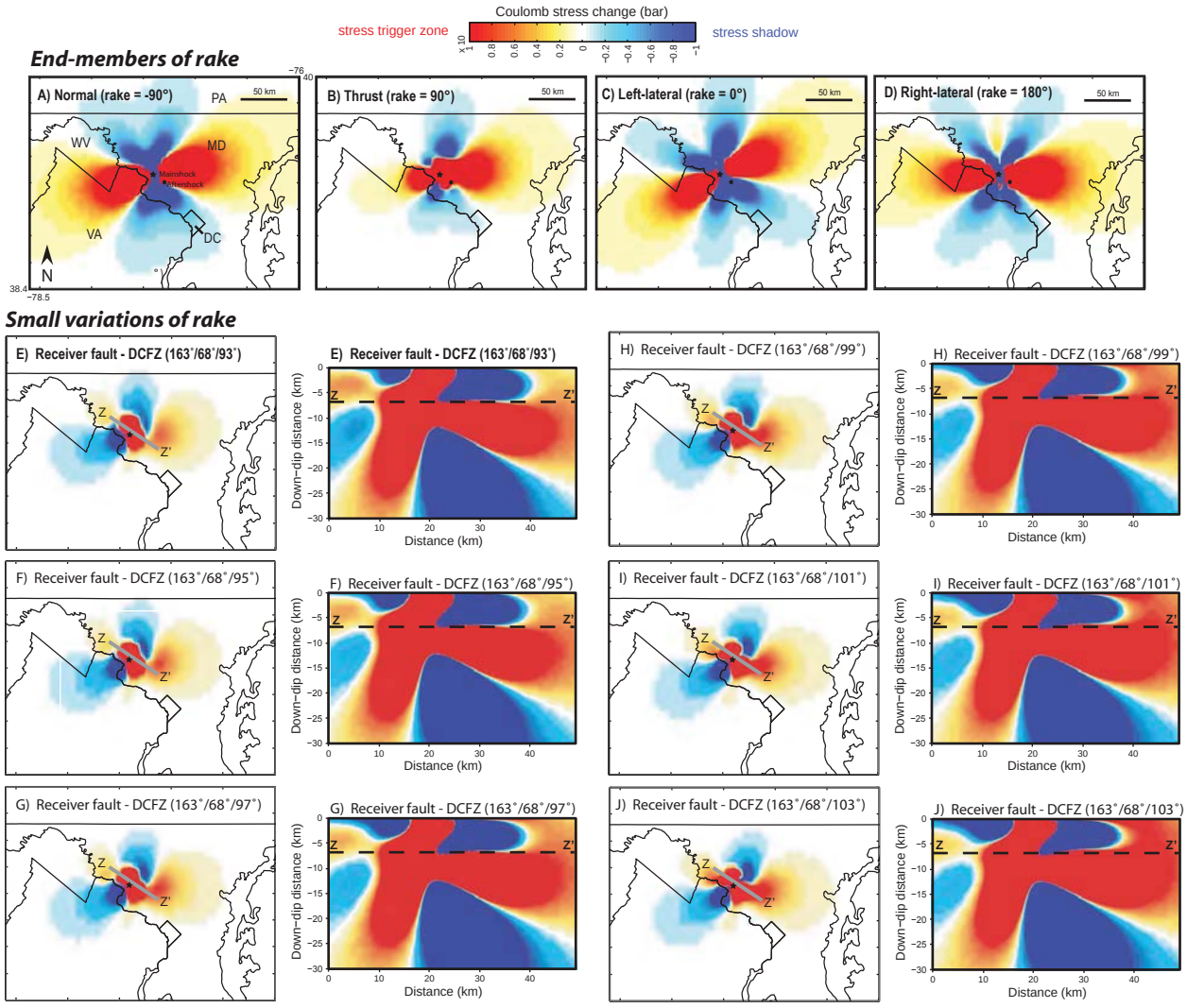

Figure 2-C6. Effect of different rakes on $\Delta\sigma_{CFS}$ result

$\Delta\sigma_{CFS}$ for rake end-members: A) normal (rake = -90°), B) thrust (rake = 90°), C) left-lateral (rake = 0°), and D) right-lateral (rake = 180°). E - J) Effect of small variations in the receiver fault's rake (ranging 1° to 10° from preferred rake - E) on $\Delta\sigma_{CFS}$ pattern. Rakes ranging -1° to -10° from preferred dip produce a similar variation.

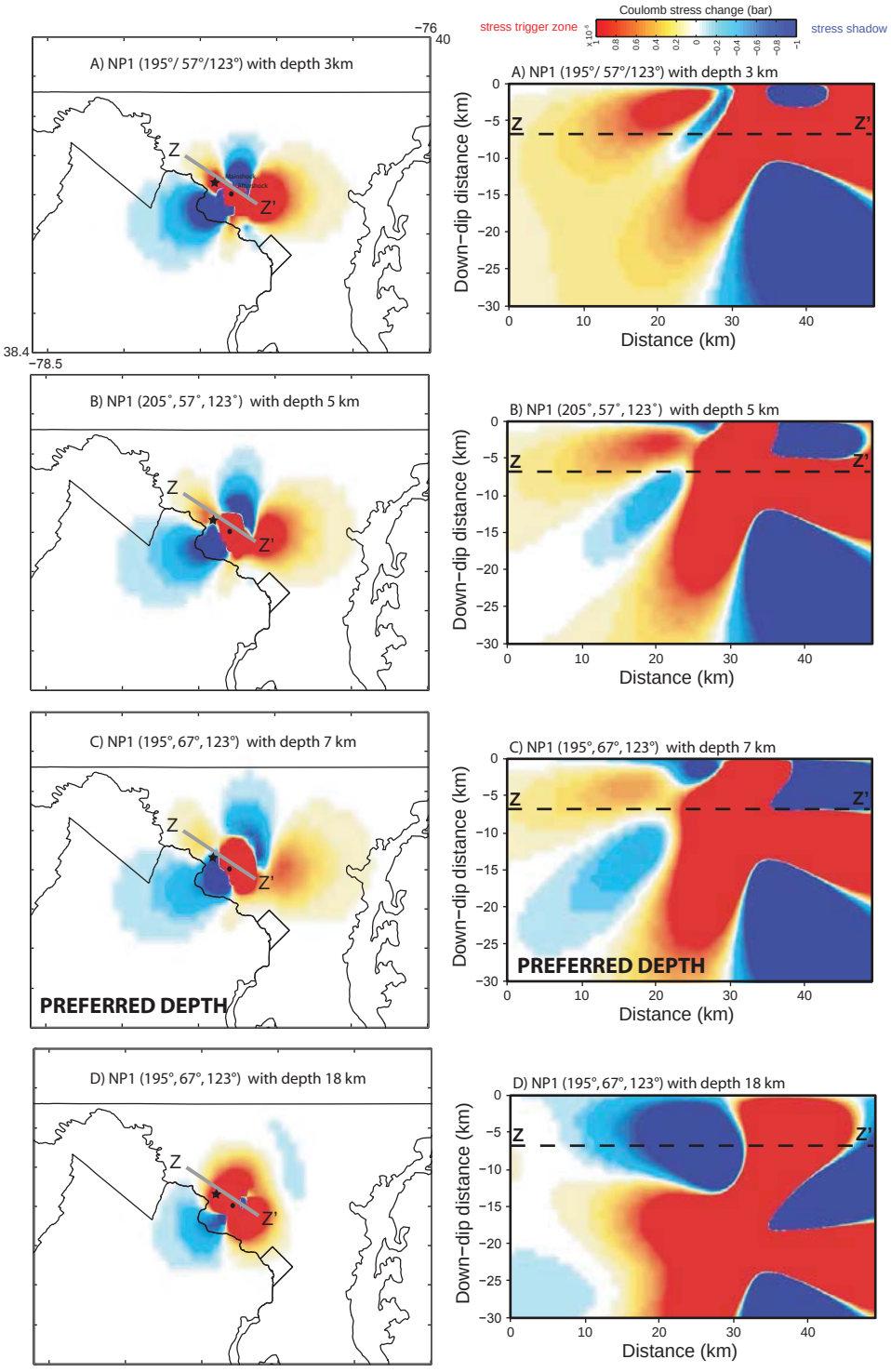

Figure 2-C7. Effect of earthquake depth $\Delta\sigma_{CFS}$ result
Effect of earthquake depth on $\Delta\sigma_{CFS}$ patterns for DCFZ as receiver fault. A) depth = 3 km (shallower), B) depth = 5 km (USGS), C) depth = 7 km (LCSN), and D) depth = 18 km (Bob Herrmann's focal mechanism solution). $\mu' = 0.8$

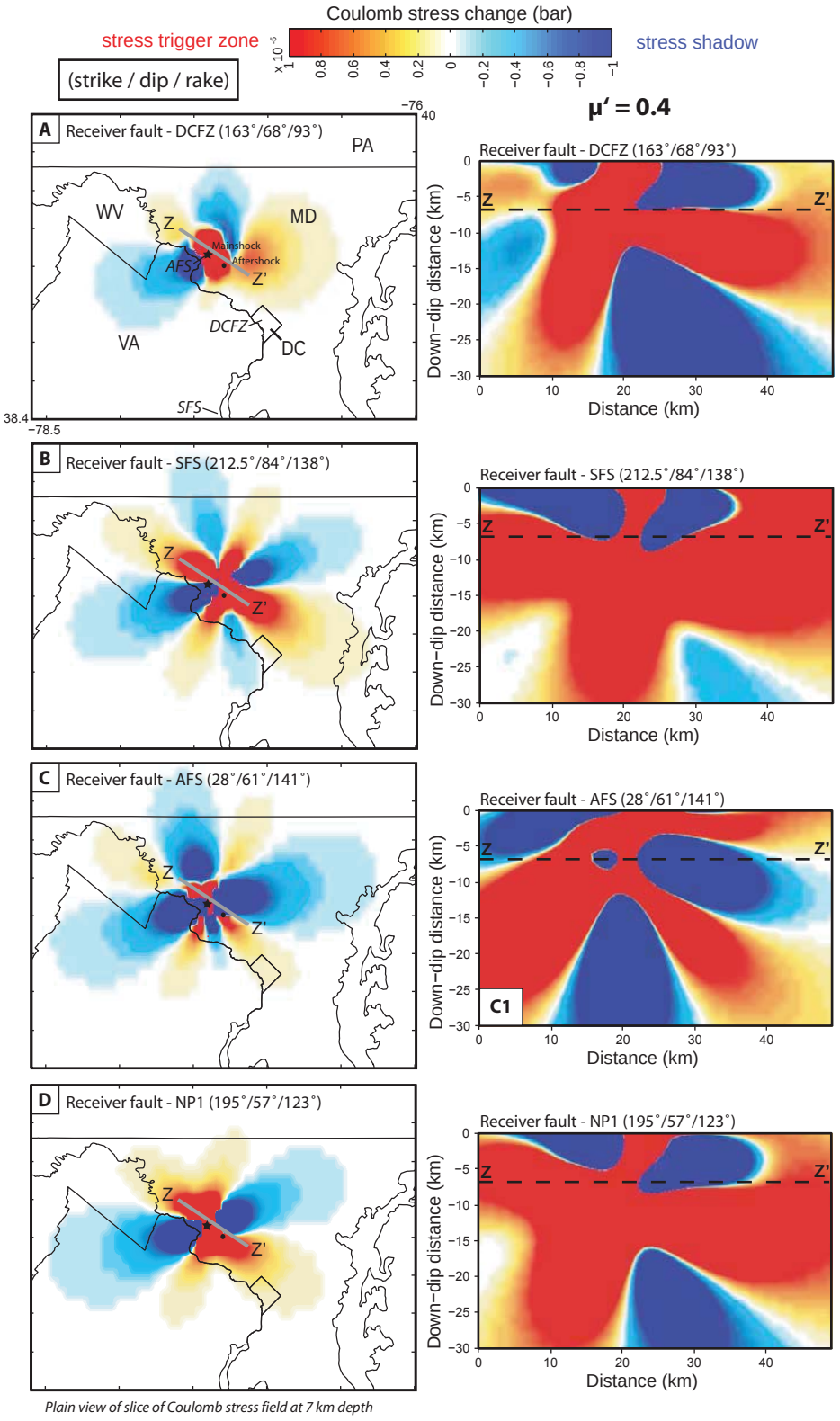

Figure 2-C8. $\Delta\sigma_{CFS}$ result in plan view and cross-section
Plan view (left column) and vertical cross-section (right column) of Coulomb stress change ($\Delta\sigma_{CFS}$) on specified faults A) DCFZ, B) SFS, C) AFS, and D) NP1.

Appendix 2-D: Example of calculation of slip vector on a fault surface

I resolved the slip vector consistent with the Mineral and Germantown earthquakes focal mechanisms on each receiver fault. using the strike A_f and dip δ_f of the fault plane of interest (e.g. DCFZ, SFS, MRFZ, or AFS) to define the normal vector N_f and the trace N_s of the fault plane

$$N_f = \begin{bmatrix} \cos A_f \sin\delta_f \\ -\sin A_f \sin\delta_f \\ \cos\delta_f \end{bmatrix}$$

$$N_s = \begin{bmatrix} \cos A_f \\ -\sin A_f \\ 0 \end{bmatrix}$$

The orientation of the P, N, and T axes are taken from the focal mechanism and gathered in a rotation matrix R.

$$R = \begin{bmatrix} \cos A_P \cos\delta_P & \cos A_N \cos\delta_N & \cos A_T \cos\delta_T \\ -\sin A_P \cos\delta_P & -\sin A_N \cos\delta_N & -\sin A_T \cos\delta_T \\ \sin\delta_P & \sin\delta_N & \sin\delta_T \end{bmatrix}$$

Where A and δ stand for azimuth and dip and the subscript P, N, and T refers to the associated stress axis for either the Mineral or Germantown earthquake. If the stress tensor in the principal reference frame is defined as

$$\sigma_p = \frac{\Delta\sigma}{2}\begin{bmatrix} -1 & 0 & 0 \\ 0 & 0 & 0 \\ 0 & 0 & 1 \end{bmatrix}$$

with $\Delta\sigma$ an arbitrary stress amplitude, the stress tensor in the geographic reference frame is given by

$$\sigma_g = R\sigma_g R'$$

Slip is then assumed to be collinear with the traction T from this stress tensor resolved on the fault plane

$$T = \sigma_g \cdot N_f$$

The normal traction T_n and the vectorial shear traction T_s defined as

$$T_n = N_f{}' \cdot T$$

and

$$T_s = T - T_n N_f$$

Fault slip is assumed to be collinear to the shear traction vector. The rake of the slip vector, following the convention of Aki and Richards (1980), is given by

$$rake = \arccos \frac{N_s \cdot T_s}{||N_s||\ ||T_s||} \sin[T_s(3)]$$

Appendix 2-E: Matlab script for rake calculation

```
% Example calculation – resolving expected slip vector (rake)
expected for DC fault zone (DCFZ) receiver fault

% definitions of fault plane
df=deg2rad(68);
af=deg2rad(163);
% Normal to the fault
nf=[cos(af)*sin(df);-sin(af)*sin(df);cos(df)];
nf'*nf; %check its norm is 1.
% Trace of the fault
ns=[sin(af);cos(af);0];

% definitions of P-axis
dp=deg2rad(7);
ap=deg2rad(262);
np=[sin(ap)*cos(dp);cos(ap)*cos(dp);-sin(dp)];
np'*np; %check its norm is 1.
% definitions of N-axis
dn=deg2rad(27);
an=deg2rad(356);
nn=[sin(an)*cos(dn);cos(an)*cos(dn);-sin(dn)];
nn'*nn; %check its norm is 1.
% definitions of T-axis
dt=deg2rad(62);
at=deg2rad(159);
nt=[sin(at)*cos(dt);cos(at)*cos(dt);-sin(dt)];
nt'*nt; %check its norm is 1.

% Rotation matrix
A=[np nn nt];
% Stress tensor
s=A*[-1,0,0;0,0,0;0,0,1]*A';

T=s*nf;
Tn=nf'*T;
Ts=T-Tn*nf;

rake=acos(dot(ns,Ts)/(norm(ns)*norm(Ts)))*sign(Ts(3));

disp(sprintf('Rake is %g degrees',rad2deg(rake)))
disp(sprintf('Normal stress coefficient is %g',Tn))
%%
figure(1);clf;
nd=cross(ns,nf);
L=5;D=-3;
plot3(L*[1,1,-1,-1,1],L*[1,-1,-
1,1,1],0*[1,1,1,1,1],'k','linewidth',2);hold on;
plot3(L*[1,1,-1,-1,1],L*[1,-1,-
1,1,1],D*[1,1,1,1,1],'k','linewidth',2);hold on;
plot3(L*[1,1],L*[1,1],[-D,D],'k','linewidth',2);
plot3(L*[1,1],L*[-1,-1],[0,D],'k','linewidth',2)
plot3(L*[-1,-1],L*[-1,-1],[0,D],'k','linewidth',2)
plot3(L*[-1,-1],L*[1,1],[0,D],'k','linewidth',2);
```

```
axis equal;
%
Lf=5;Ld=2;
F=[Lf*ns,Lf*ns+Ld*nd,-Lf*ns+Ld*nd,-Lf*ns,Lf*ns];
fill3(F(1,:),F(2,:),F(3,:),'y');

quiver3(0,0,0,nf(1),nf(2),nf(3),'k','linewidth',4);
quiver3(0,0,0,ns(1),ns(2),ns(3),'k','linewidth',4);

% Plot principal stress directions
quiver3(-2,-2,0,np(1),np(2),np(3),'b','linewidth',2);
quiver3(-2,-2,0,-np(1),-np(2),-np(3),'b','linewidth',2);
quiver3(-2,-2,0,nt(1),nt(2),nt(3),'r','linewidth',2);
quiver3(-2,-2,0,-nt(1),-nt(2),-nt(3),'r','linewidth',2);
quiver3(-2,-2,0,nn(1),nn(2),nn(3),'g','linewidth',2);
quiver3(-2,-2,0,-nn(1),-nn(2),-nn(3),'g','linewidth',2);

quiver3(nd(1),nd(2),nd(3)+0.2,T(1),T(2),T(3),'b','linewidth',4);
quiver3(nd(1),nd(2),nd(3)+0.2,Ts(1),Ts(2),Ts(3),'g','linewidth',2);
quiver3(nd(1)+Ts(1),nd(2)+Ts(2),nd(3)+0.2+Ts(3),Tn*nf(1),Tn*nf(2),Tn
*nf(3),'b','linewidth',2);

quiver3(nd(1),nd(2),nd(3)+0.2,ns(1),ns(2),ns(3),'k','linewidth',2);
quiver3(nd(1),nd(2),nd(3)+0.2,nd(1),nd(2),nd(3),'k','linewidth',2);
```

Appendix 3-A: Fourier Transform Matlab script

```
%Import .csv file with julian date in first column and seismicity
rate or
%moment release in second column to the matrix M in Matlab.
M = csvread('Your_file_name_here.csv');

%Reassign julian date to matlab date
for j = 1:size(M,1)
    if(M(j,1)>2012000) % We are in 2012
        startdate = datenum(2012,1,1) - 1;
        M(j,1) = M(j,1) - 2012000 + startdate;
    elseif(M(j,1)>2011000) % We are in 2011
        startdate = datenum(2011,1,1) - 1;
        M(j,1) = M(j,1) - 2011000 + startdate;
    elseif(M(j,1)>2010000) % We are in 2010
        startdate = datenum(2010,1,1) - 1;
        M(j,1) = M(j,1) - 2010000 + startdate;
    elseif(M(j,1)>2009000) % We are in 2009
        startdate = datenum(2009,1,1) - 1;
        M(j,1) = M(j,1) - 2009000 + startdate;
    elseif(M(j,1)>2008000) % We are in 2010
        startdate = datenum(2008,1,1) - 1;
        M(j,1) = M(j,1) - 2008000 + startdate;
    elseif(M(j,1)>2007000) % We are in 2007
        startdate = datenum(2007,1,1) - 1;
        M(j,1) = M(j,1) - 2007000 + startdate;
    elseif(M(j,1)>2006000) % We are in 2006
        startdate = datenum(2006,1,1) - 1;
        M(j,1) = M(j,1) - 2006000 + startdate;
    elseif(M(j,1)>2005000) % We are in 2005
        startdate = datenum(2005,1,1) - 1;
        M(j,1) = M(j,1) - 2005000 + startdate;
    elseif(M(j,1)>2004000) % We are in 2004
        startdate = datenum(2004,1,1) - 1;
        M(j,1) = M(j,1) - 2004000 + startdate;
    elseif(M(j,1)>2003000) % We are in 2003
        startdate = datenum(2003,1,1) - 1;
        M(j,1) = M(j,1) - 2003000 + startdate;
    elseif(M(j,1)>2002000) % We are in 2002
        startdate = datenum(2002,1,1) - 1;
        M(j,1) = M(j,1) - 2002000 + startdate;
    elseif(M(j,1)>2001000) % We are in 2001
        startdate = datenum(2001,1,1) - 1;
        M(j,1) = M(j,1) - 2001000 + startdate;
    end
end

%Commands for Fourier Transform
% Create windowing function
Frac = 0.1; % Fraction of all points that will have taper applied to
them
b = tukeywin(size(M,1),Frac);

% Calculate Fourier Transform
ftM = fft((M(:,2)).*b);
```

```
% Sampling frequency
f_sample = M(2,1)-M(1,1); % 1 sample per day

% Increment in frequency
df = 1/(f_sample*size(M,1)); % 1 / total length of time series

% Maximum frequency
fmax = f_sample/2; % Nyquist Frequency

frequencies = 0:df:fmax;

power = conj(ftM).*ftM;

%Plot time series versus seismicity frequency
figure;
bar((M(:,1)),(M(:,2)));
set(gca,'yscale','linear','xscale','linear');
YLABEL('moment release rate (dynes*cm/day)');
XLABEL('day');

% Plot frequency versus power
figure;
plot(frequencies,power(1:length(frequencies)));
set(gca,'yscale','linear','xscale','log');
YLABEL('power');
XLABEL('frequency');
```

Appendix 3-B: Time series with moving average windows for each seismic zone

Figures 3-B1 through 3-B6 show time series from the NEIC catalog with the following moving average windows: none, 3 days, 10 days, 30 days, 100 days, and 300 days. Figures 3-B7 through 3-B9 show the moving average windows above for the north, central, and south segments of the New Madrid Seismic Zone (NMSZ) using the CERI catalog. Figures 3-B10 through 3-B13 show the moving average windows for major fault zones in the NMSZ.

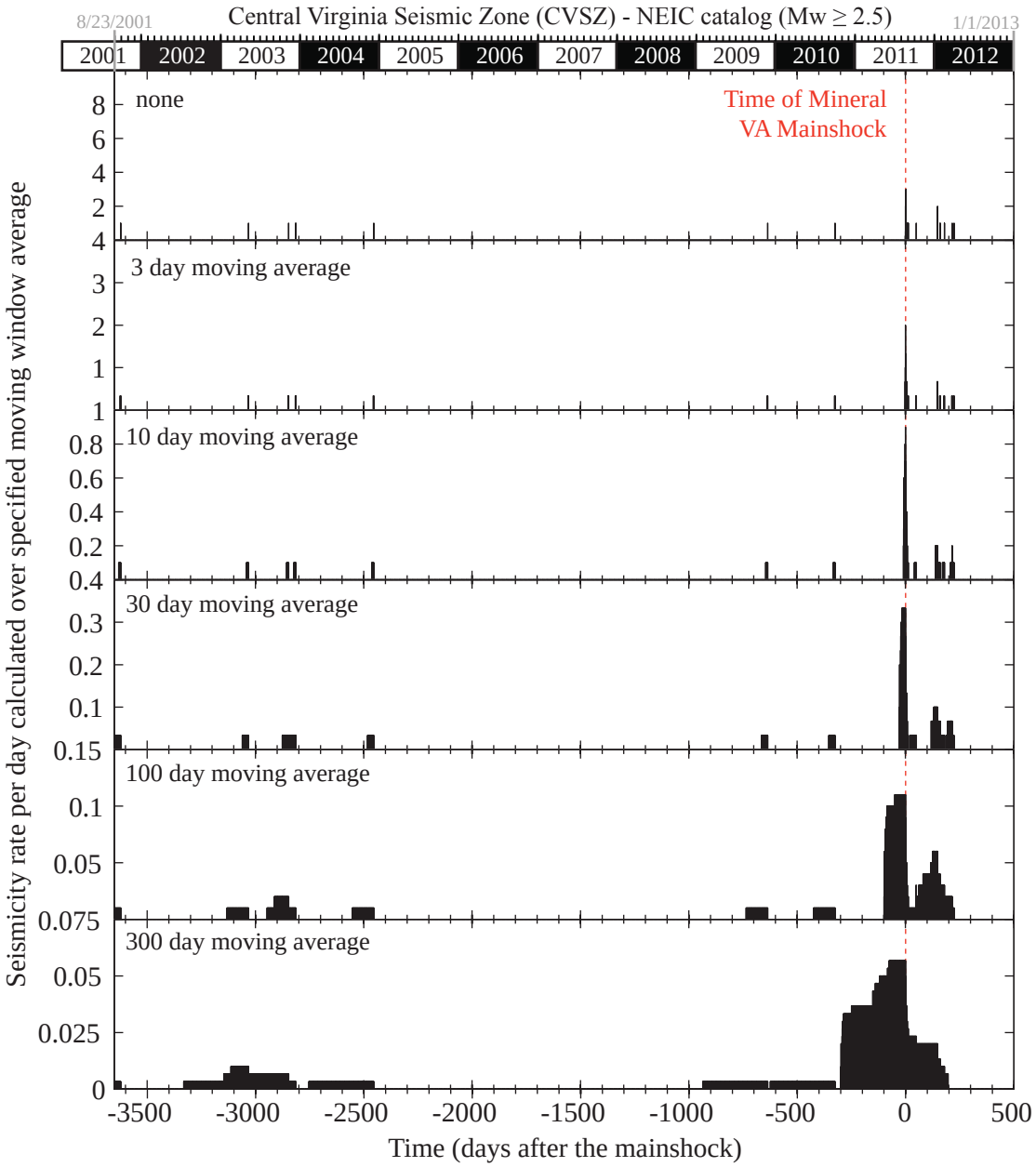

Figure 3-B1. Time series of seismicity rate in the Central Virginia Seismic Zone (CVSZ), site of the Mineral, Virginia earthquake, for a variety of moving window averages.

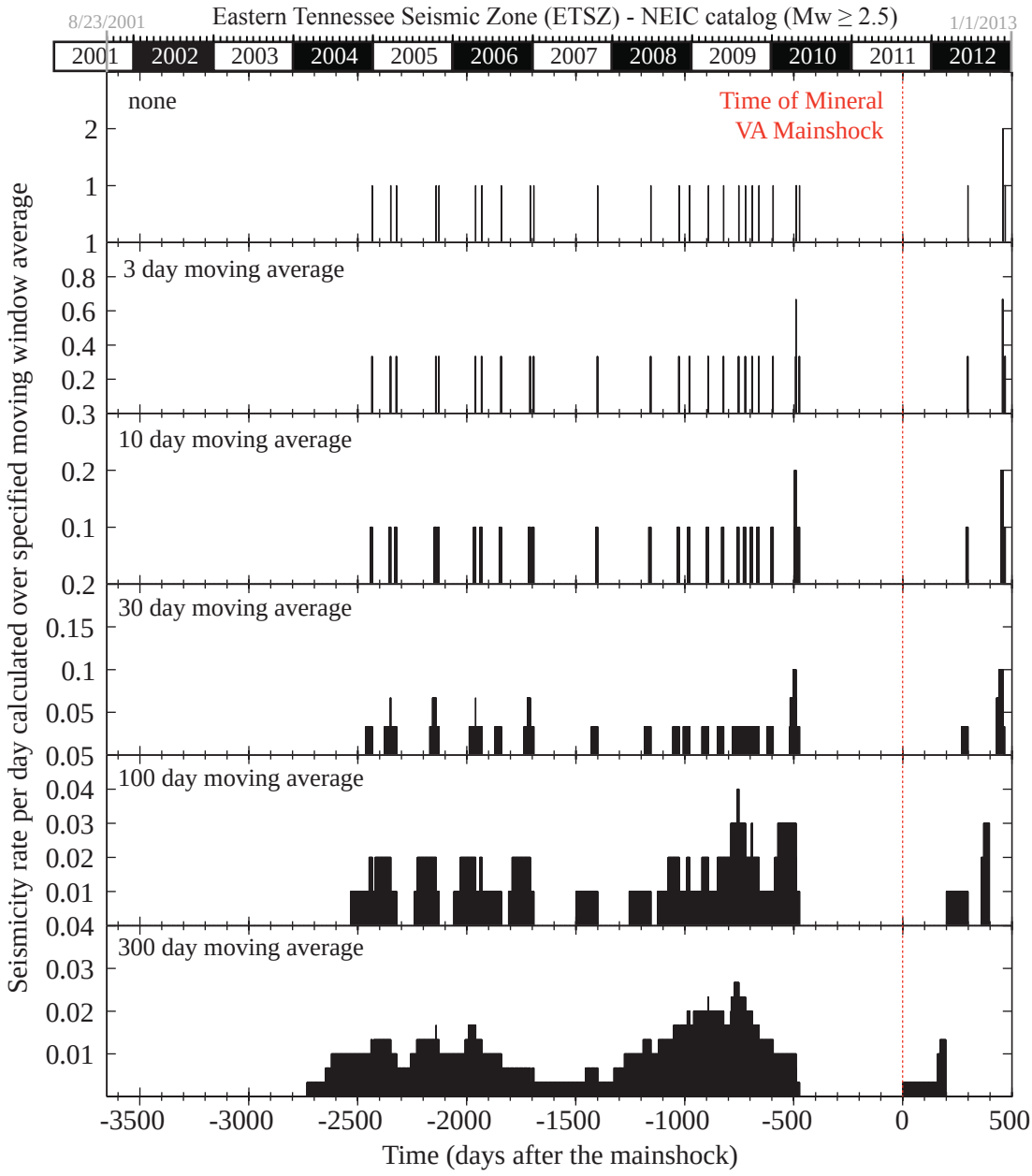

Figure 3-B2. Time series of seismicity rate in the Eastern Tennessee Seismic Zone (ETSZ) for a variety of moving window averages.

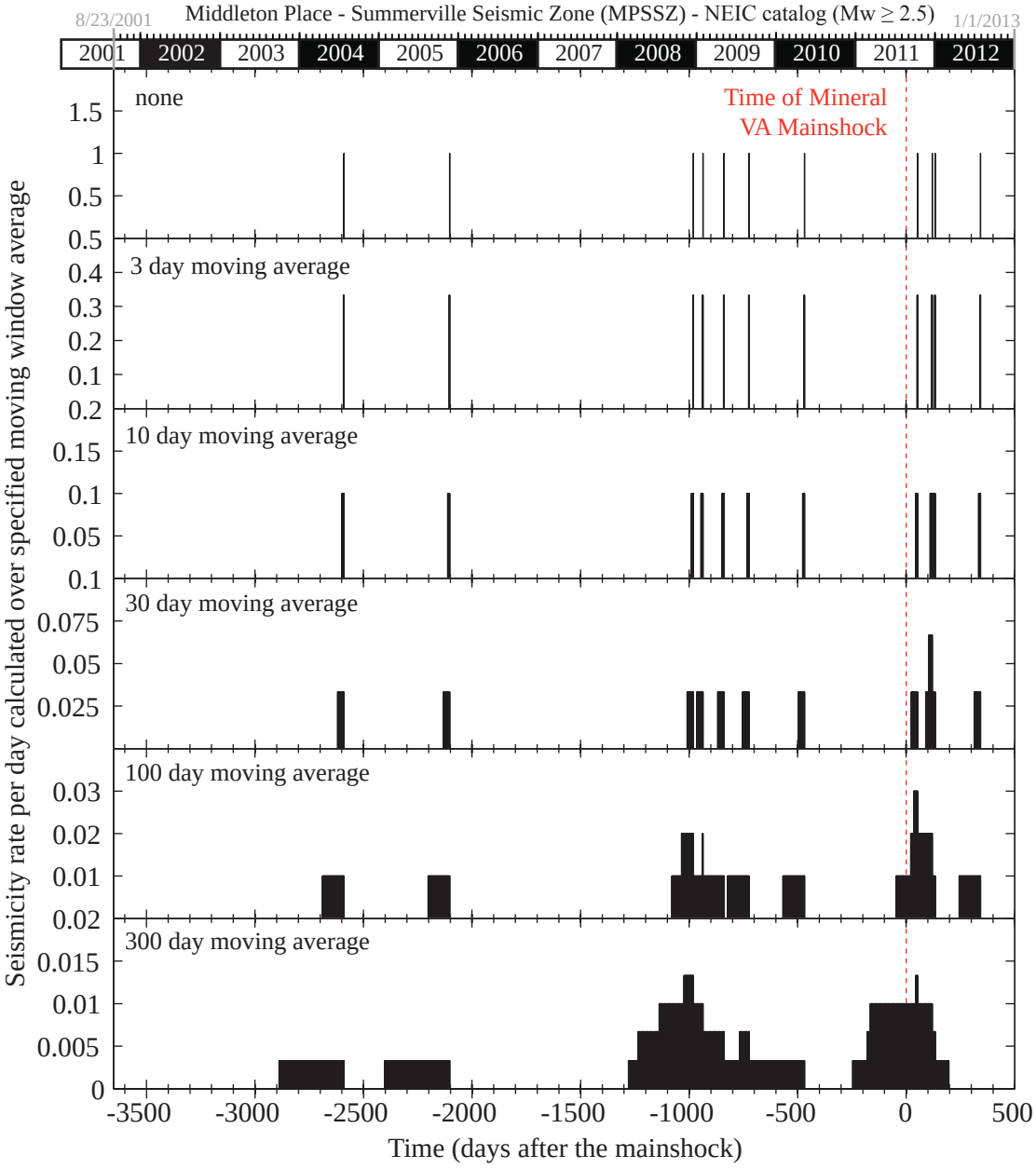

Figure 3-B3. Time series of seismicity rate in the Middleton Place - Summerville Seismic Zone near Charleston, SC (MPSSZ) for a variety of moving window averages.

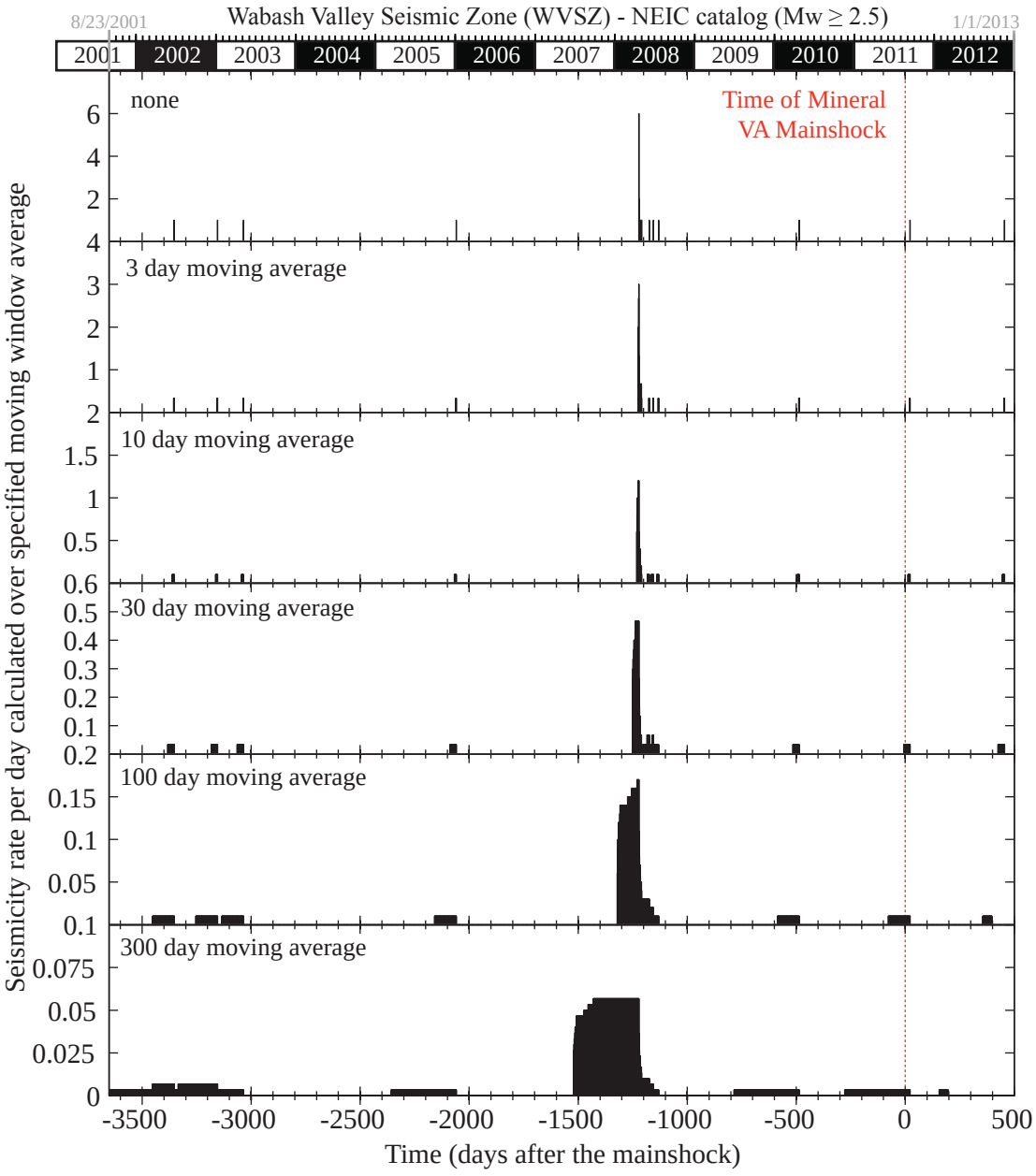

Figure 3-B4. Time series of seismicity rate in the Wabash Valley Seismic Zone (WVSZ) for a variety of moving window averages.

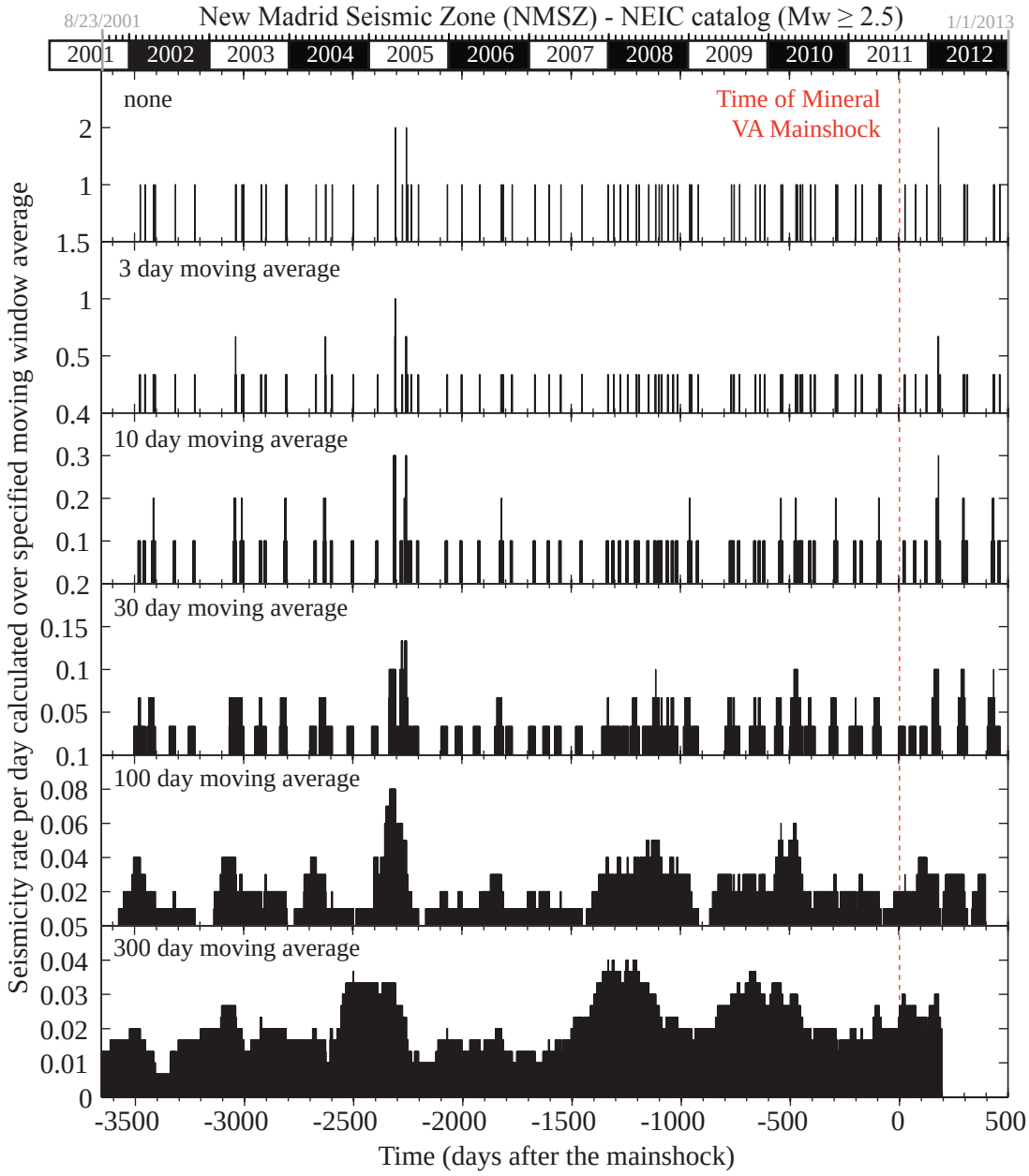

Figure 3-B5. Time series of seismicity rate in the New Madrid Seismic Zone (NMSZ) for a variety of moving window averages.

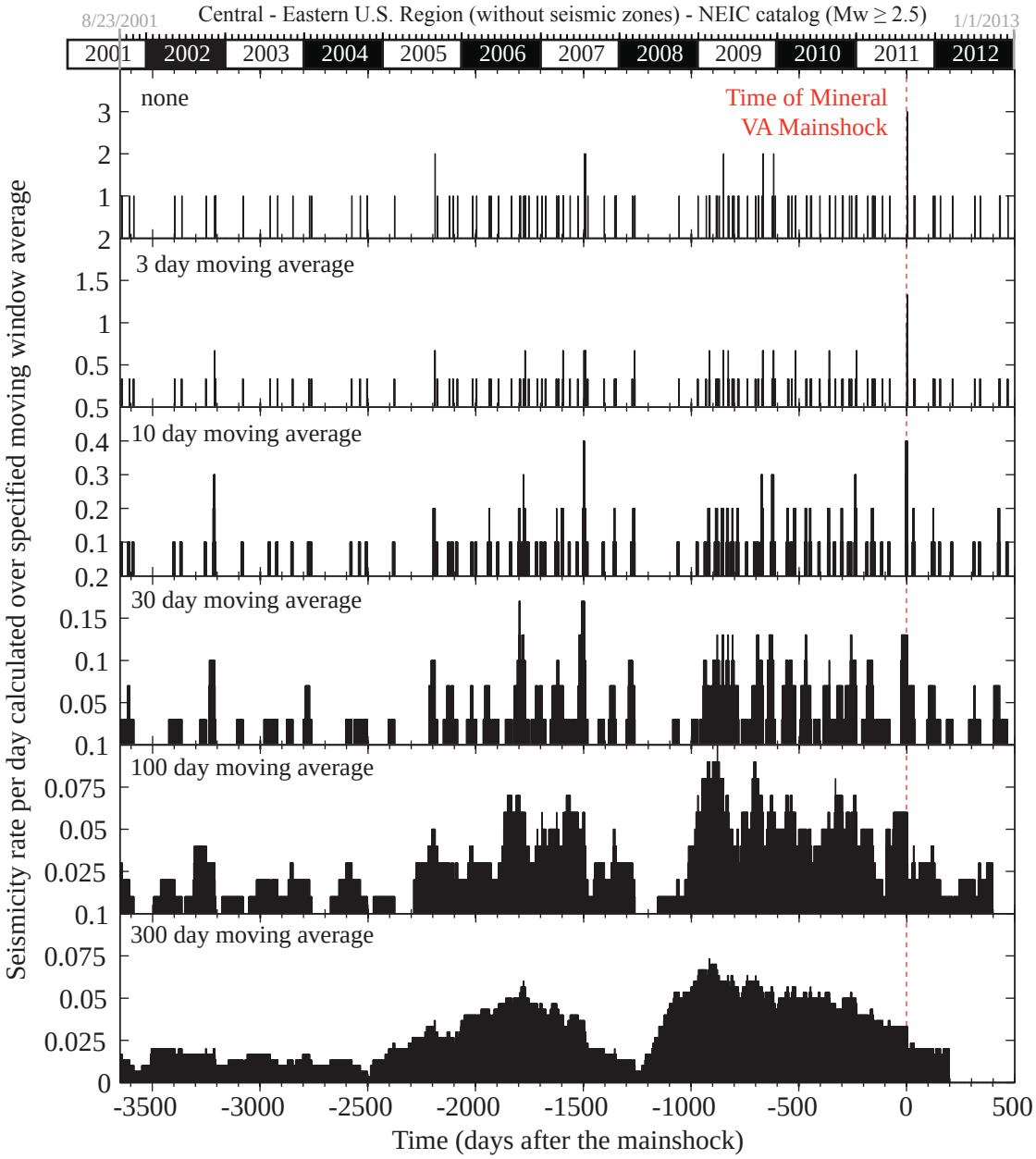

Figure 3-B6. Time series of seismicity rate in the Central – Eastern U.S. region (without seismic zones) for a variety of moving window averages.

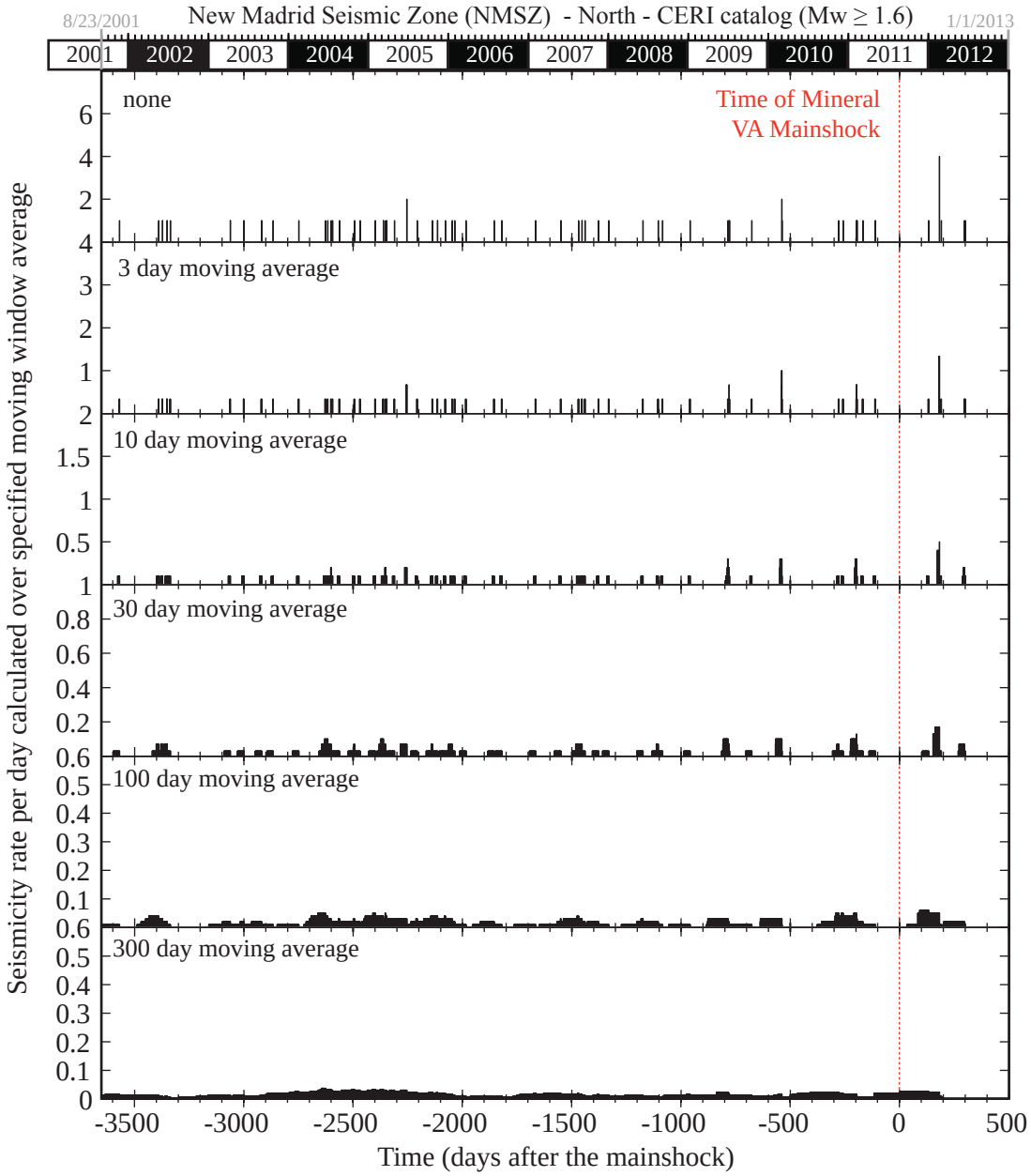

Figure 3-B7. Time series of seismicity rate in the northern region of the New Madrid Seismic Zone (NMSZ) for a variety of moving window averages.

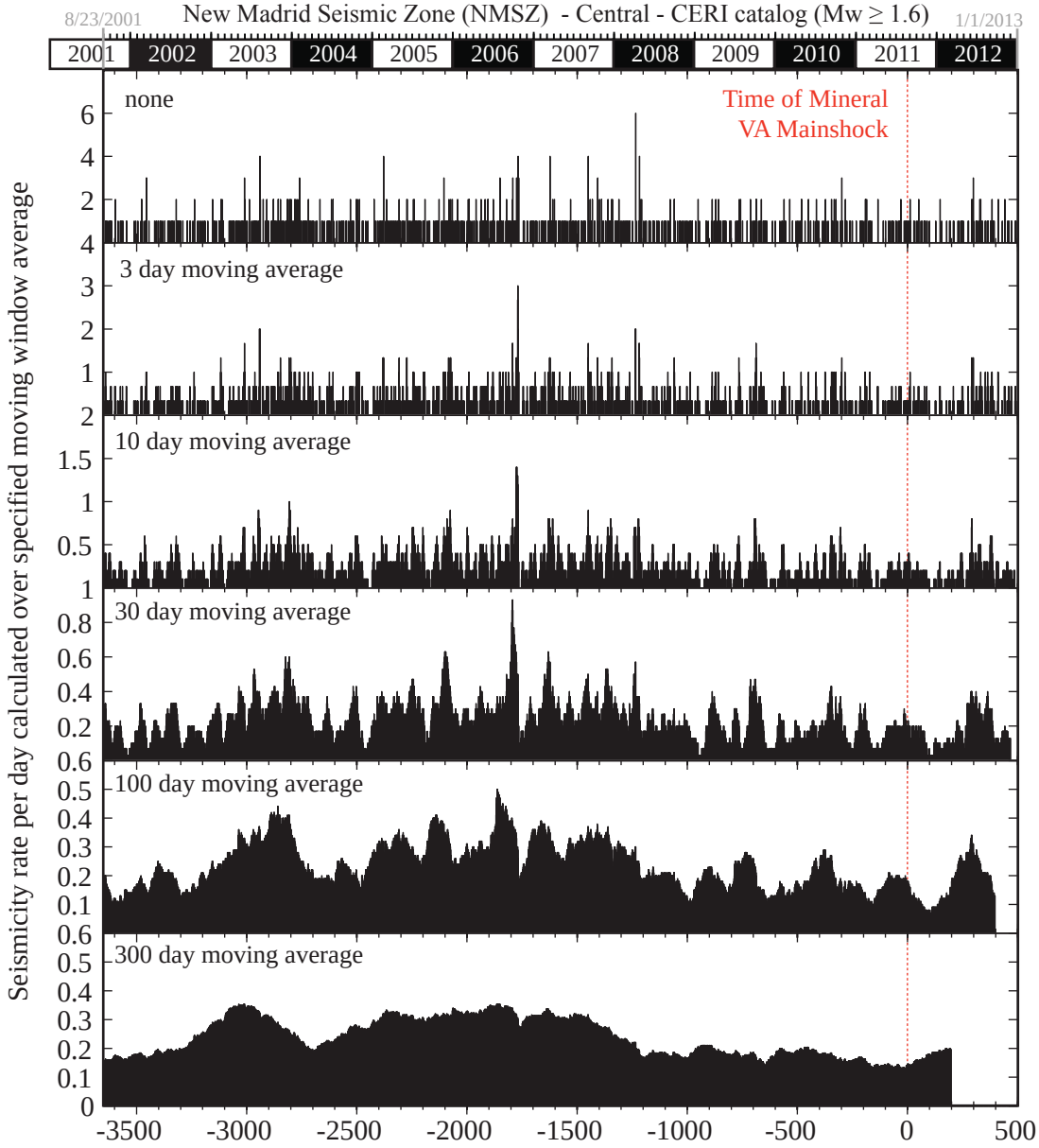

Figure 3-B8. Time series of seismicity rate in the central region of the New Madrid Seismic Zone (NMSZ) for a variety of moving window averages.

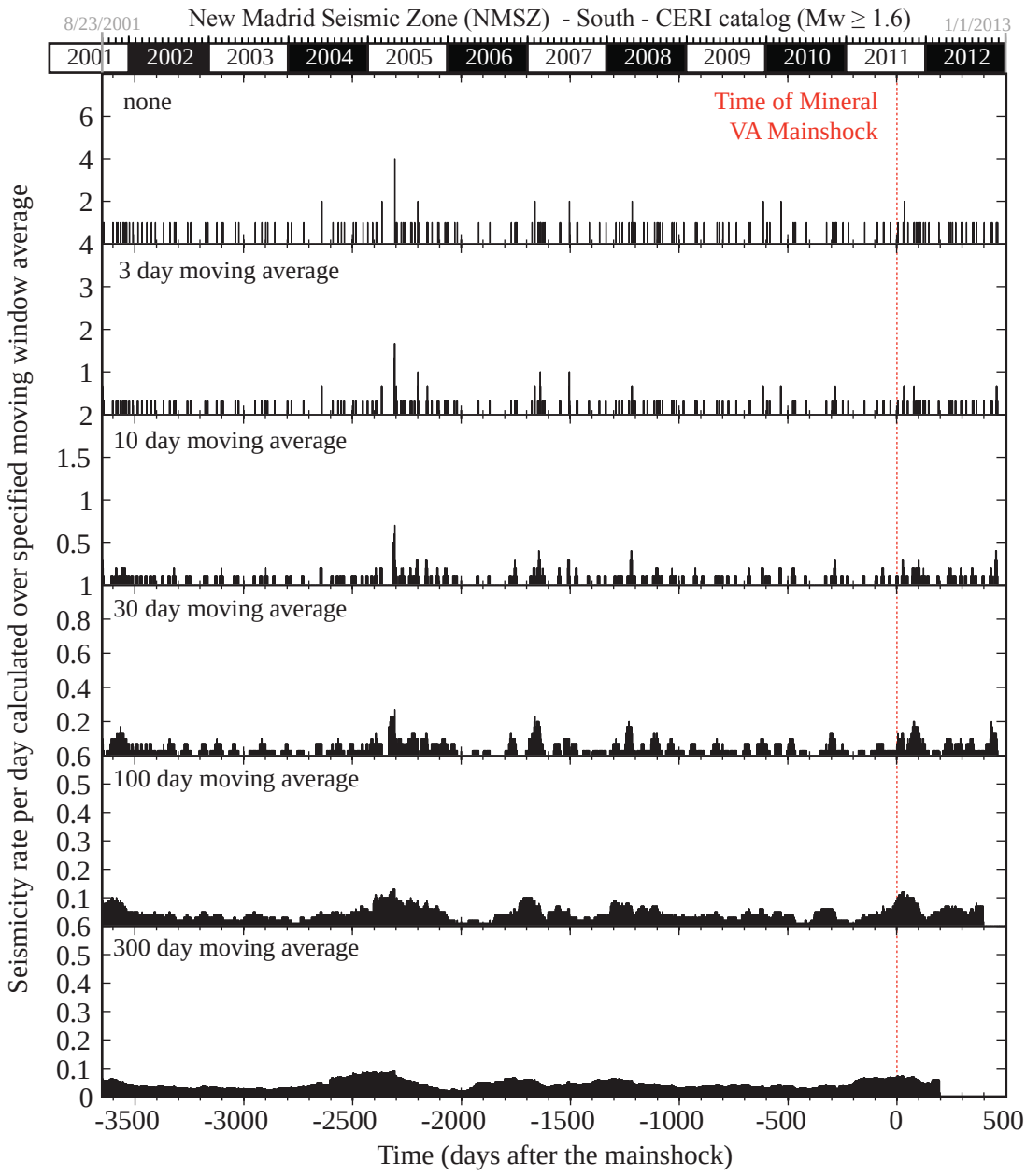

Figure 3-B9. Time series of seismicity rate in the southern region of the New Madrid Seismic Zone (NMSZ) for a variety of moving window averages.

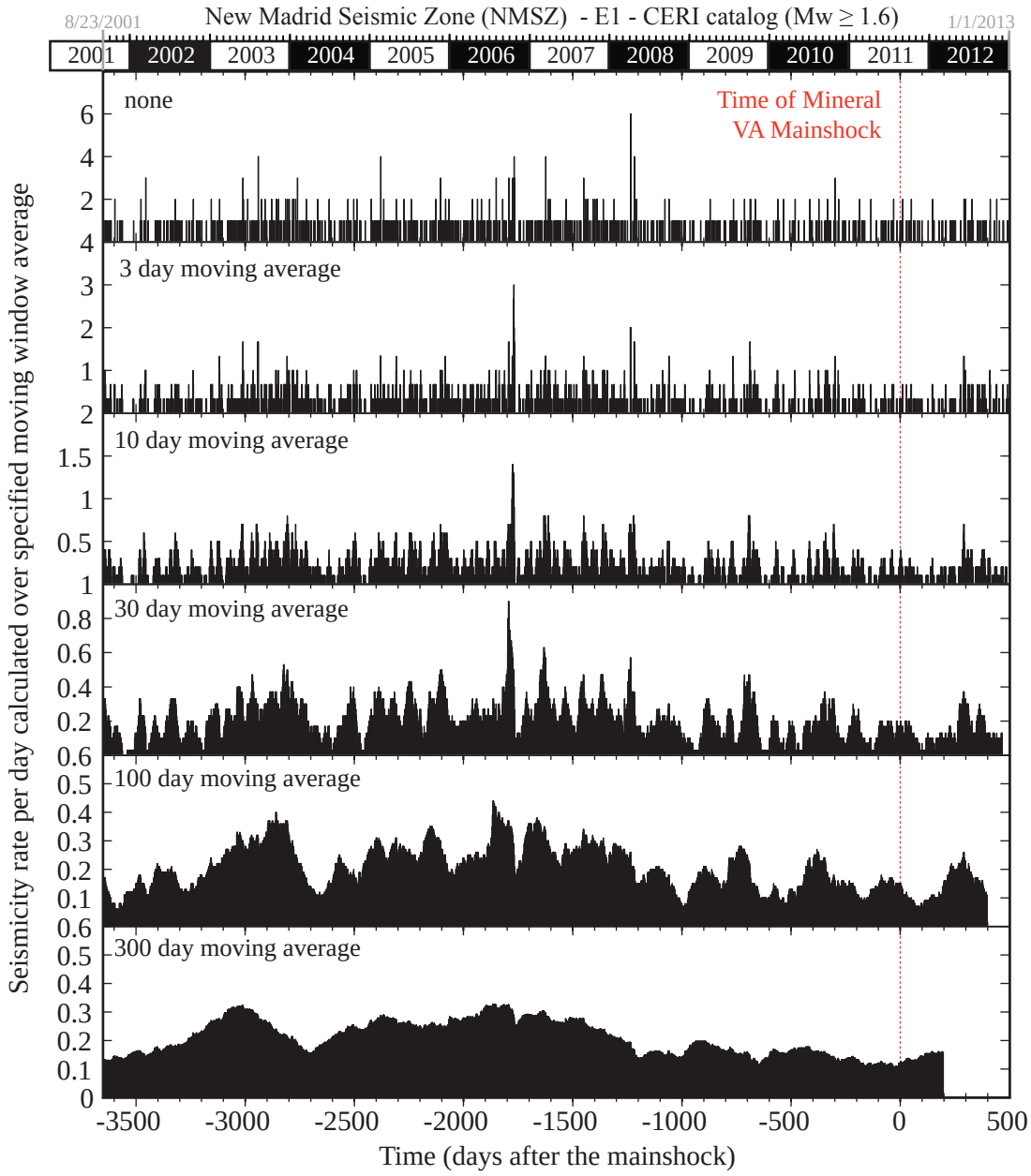

Figure 3-B10. Time series of seismicity rate along the Reelfoot fault (E1) of the New Madrid Seismic Zone (NMSZ) for a variety of moving window averages.

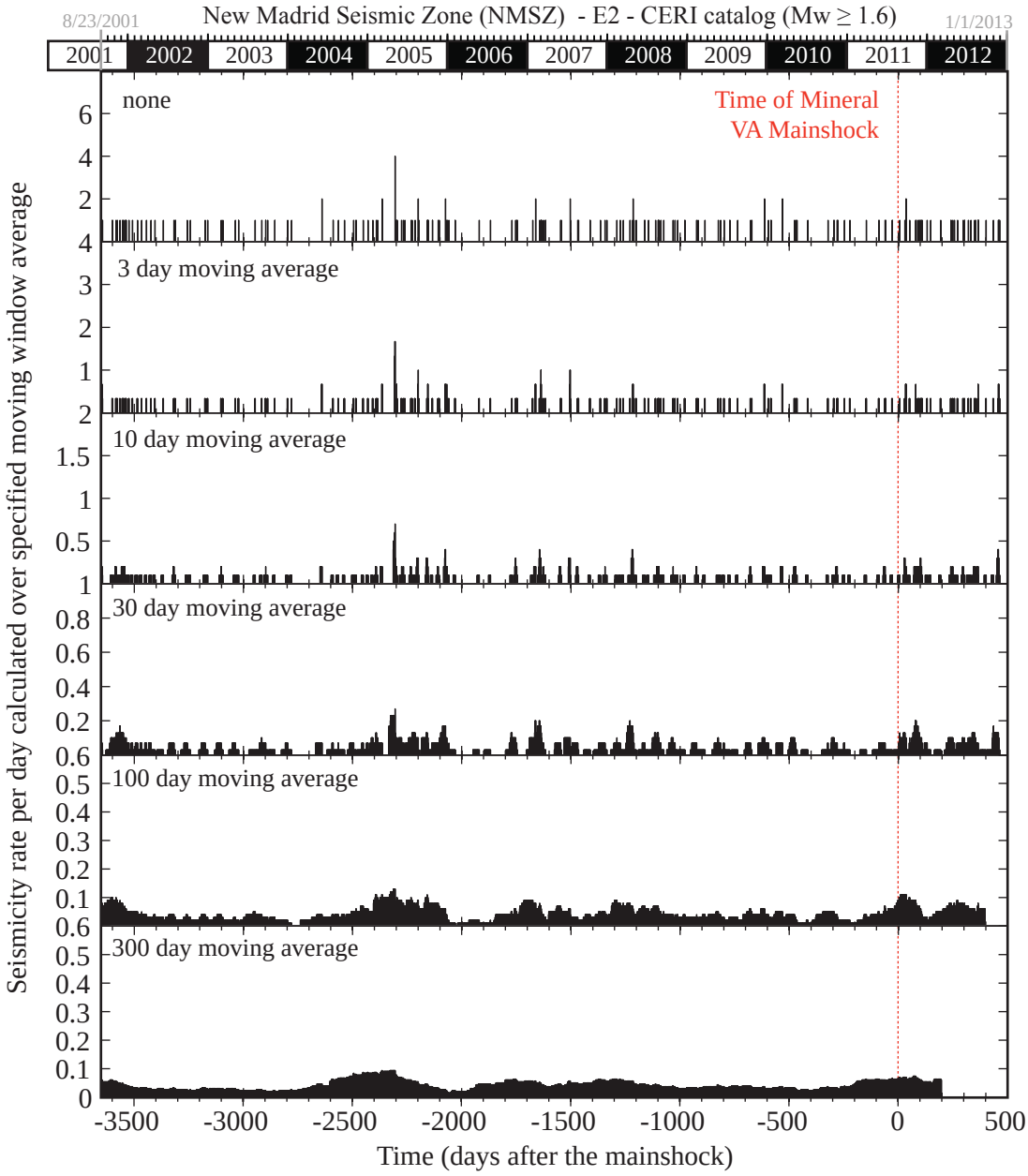

Figure 3-B11. Time series of seismicity rate along the Cottonwood Grove fault (E2) of the New Madrid Seismic Zone (NMSZ) for a variety of moving window averages.

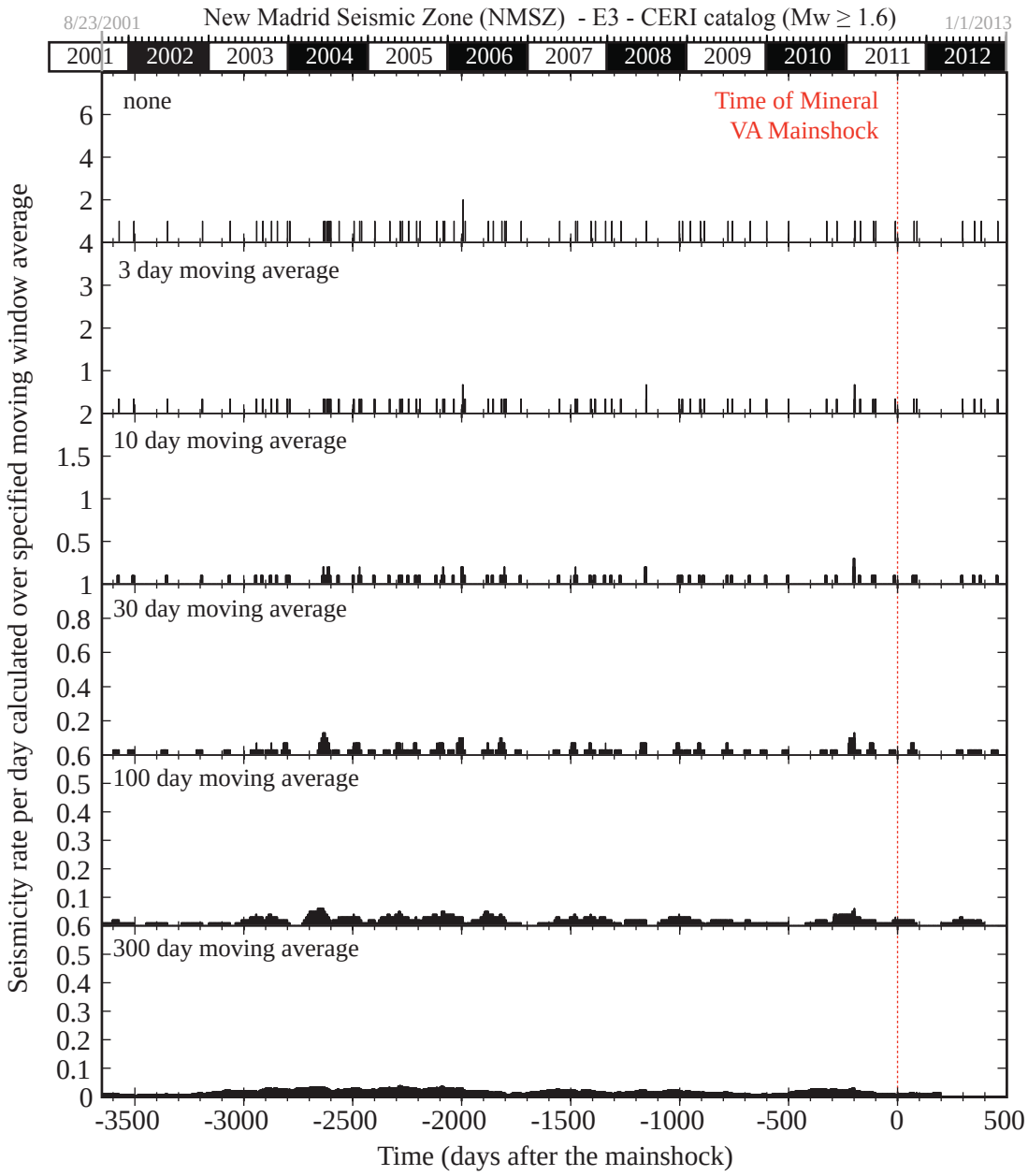

Figure 3-B12. Time series of seismicity rate along the North New Madrid fault (E3) of the New Madrid Seismic Zone (NMSZ) for a variety of moving window averages.

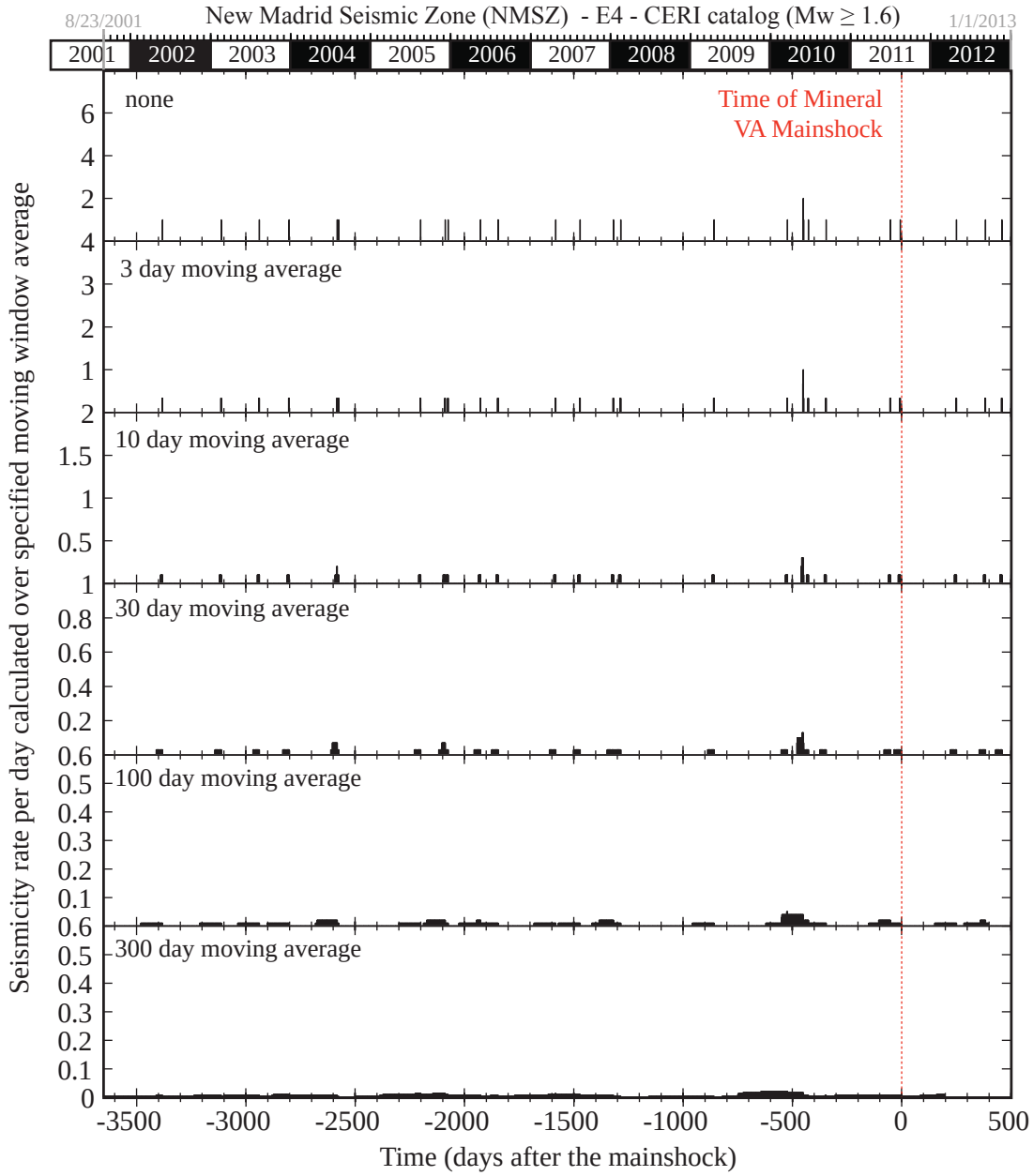

Figure 3-B13. Time series of seismicity rate along the Cluster east of the Reelfoot fault (E4) of the New Madrid Seismic Zone (NMSZ) for a variety of moving window averages.

Appendix 4-A. Additional examples of wrinkle ridge MLA and LOLA profiles

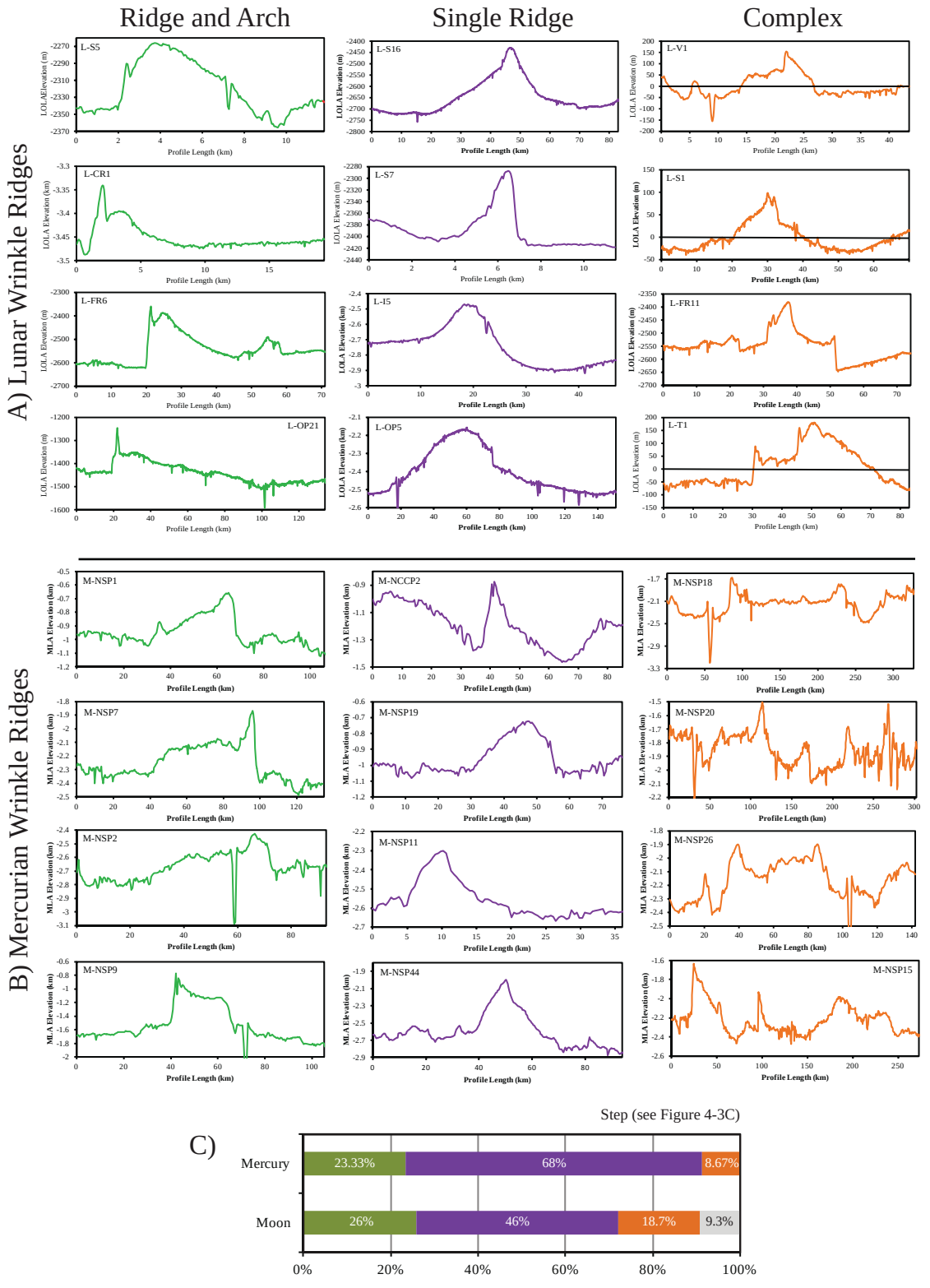

Figure 4-A1. Topographic profiles across a selection of wrinkle ridges on the Moon (A) and Mercury (B) with the following morphology classifications: broad arch and superimposed ridge (classic), single arch, and complex. C) Bar graph showing a comparison of the percentage of wrinkle ridges in each morphology class.

Appendix 4-B: Wrinkle ridge locations and relief and length measurements

Table 4-B1. Mercurian wrinkle ridge locations and relief and length measurements

Mercurian wrinkle ridge ID (informal)[a]	Longitude (°E)	Latitude (°N)	Relief (m)	Length (km)	Topographic data source
Wrinkle ridges located in the northern smooth plains (NSP)					
M-NSP1	27.15	62.54	352	82	MLA altimetry track
M-NSP2	-70.84	71.12	257	75	MLA altimetry track
M-NSP3	-76.07	73.26	343	139	MLA altimetry track
M-NSP4	113.18	78.95	390	107	MLA altimetry track
M-NSP5[†]	-43.49	73.59	843	133	MLA altimetry track
M-NSP6	134.45	75.10	547	126	MLA altimetry track
M-NSP7	-32.20	68.14	510	63	MLA altimetry track
M-NSP8	64.84	82.11	508	52	MLA altimetry track
M-NSP9	1.08	57.71	689	136	MLA altimetry track
M-NSP10	24.09	55.03	537	134	MLA altimetry track
M-NSP11	89.74	74.13	280	59	MLA altimetry track
M-NSP12	-92.91	70.00	776	92	MLA altimetry track
M-NSP13	14.38	80.76	384	162	MLA altimetry track
M-NSP14	88.74	78.18	593	175	MLA altimetry track
M-NSP15	76.73	65.57	379	185	MLA altimetry track
M-NSP16	35.12	65.86	387	75	MLA altimetry track
M-NSP17	-4.13	74.04	435	154	MLA altimetry track
M-NSP18	-25.64	63.13	611	97	MLA altimetry track
M-NSP19	51.15	64.33	304	86	MLA altimetry track
M-NSP20	68.91	59.48	282	103	MLA altimetry track
M-NSP21	-97.61	78.22	639	282	MLA altimetry track
M-NSP22	-15.59	57.16	344	112	MLA altimetry track
M-NSP23	39.04	62.04	312	68	MLA altimetry track
M-NSP24	24.06	57.13	352	44	MLA DEM
M-NSP25	-30.86	75.21	598	89	MLA DEM
M-NSP26	-17.84	78.87	484	166	MLA altimetry track
M-NSP27	-31.84	82.01	193	79	MLA DEM
M-NSP28	-74.11	66.39	458	60	MLA altimetry track
M-NSP29	29.53	77.62	371	111	MLA altimetry track
M-NSP30	-90.00	66.89	276	39	MLA DEM
M-NSP31	126.35	73.27	273	83	MLA altimetry track
M-NSP32	50.21	61.64	718	87	MLA altimetry track
M-NSP33	54.63	79.74	217	57	MLA altimetry track
M-NSP34	53.99	77.24	175	46	MLA altimetry track
M-NSP35	42.61	70.53	314	29	MLA DEM
M-NSP36	51.99	67.31	223	43	MLA altimetry track
M-NSP37	30.16	81.49	230	92	MLA DEM

M-NSP38	-5.35	83.28	298	46	MLA altimetry track
M-NSP39	32.36	52.28	187	59	MLA DEM
M-NSP40	-28.17	55.93	391	115	MLA DEM
M-NSP41	41.95	56.49	318	42	MLA DEM
M-NSP42	44.87	55.11	426	57	MLA DEM
M-NSP43	-38.54	75.01	306	70	MLA DEM
M-NSP44	-50.15	75.62	829	84	MLA altimetry track
M-NSP45	6.31	34.97	149	206	M2 DEM flyby
M-NSP46	10.71	37.41	367	84	M2 DEM flyby
M-NSP47	-0.75	38.41	345	95	M2 DEM flyby
M-NSP48	10.74	51.24	404	74	MLA DEM
M-NSP49	-1.98	55.51	366	151	MLA DEM
M-NSP50	6.20	61.55	116	79	MLA DEM
M-NSP51	-3.66	54.45	937	52	MLA DEM
M-NSP52	77.70	1.05	382	137	M3 DEM flyby
M-NSP53	77.18	6.98	347	221	M3 DEM flyby
M-NSP54	76.88	4.49	475	122	M3 DEM flyby
M-NSP55	68.16	7.09	726	83	M3 DEM flyby
M-NSP56	70.79	-0.57	784	229	M3 DEM flyby
M-NSP57	113.49	77.89	489	110	MLA altimetry track
M-NSP58	113.76	75.65	415	57	MLA altimetry track
M-NSP59	-93.82	79.92	224	56	MLA altimetry track
M-NSP60	-100.81	73.94	421	105	MLA DEM
M-NSP61	-70.34	67.44	170	72	MLA altimetry track
M-NSP62	-86.17	74.99	331	95	MLA altimetry track
M-NSP63	37.70	46.53	180	72	MLA DEM
M-NSP64	43.57	41.48	473	66	MLA DEM
M-NSP65	41.27	40.23	232	83	MLA altimetry track
M-NSP66	41.70	44.68	238	91	MLA altimetry track
M-NSP67	39.79	50.06	249	80	MLA DEM
M-NSP68	46.39	60.05	237	75	MLA altimetry track
M-NSP69	-69.99	72.35	189	86	MLA altimetry track
M-NSP70	-79.77	71.47	287	27	MLA altimetry track
M-NSP71	29.33	67.13	201	46	MLA altimetry track
M-NSP72	134.89	71.18	464	52	MLA DEM
M-NSP73	39.32	66.44	326	85	MLA DEM
M-NSP74	5.70	76.27	252	53	MLA DEM
M-NSP75	-10.29	78.60	350	123	MLA altimetry track
M-NSP76	-26.94	68.82	239	37	MLA DEM
M-NSP77	-22.64	70.00	112	75	MLA DEM
M-NSP78	-11.40	71.57	418	66	MLA DEM
M-NSP79	-43.96	72.12	544	69	MLA DEM
M-NSP80	-35.15	67.52	358	68	MLA DEM

M-NSP81	50.36	58.85	285	86	MLA DEM
M-NSP82	61.59	59.32	593	105	MLA DEM
M-NSP83	92.68	75.75	268	64	MLA DEM
M-NSP84	95.54	79.02	488	68	MLA DEM
M-NSP85	120.08	73.18	249	36	MLA DEM
M-NSP86	109.79	70.29	298	44	MLA DEM
M-NSP87	67.27	56.83	252	48	MLA DEM
M-NSP88	62.11	56.79	179	77	MLA DEM
M-NSP89	48.18	39.42	262	50	MLA DEM
M-NSP90	-80.17	63.67	262	73	MLA DEM
M-NSP91	39.04	57.21	336	38	MLA DEM
M-NSP92	29.62	57.71	149	60	MLA DEM
M-NSP93	31.05	54.98	413	46	MLA DEM
M-NSP94	70.05	4.82	824	110	M3 DEM flyby
M-NSP95	81.49	37.18	886	182	M3 DEM flyby
M-NSP96	78.16	44.70	817	111	M3 DEM flyby
M-NSP97	78.78	41.86	354	80	M3 DEM flyby
Wrinkle ridges located in northern Caloris exterior plains (NCCP)					
M-NCCP1	-166.15	52.32	782	238	MLA altimetry track
M-NCCP2	-159.05	57.65	444	67	MLA altimetry track
M-NCCP3	-152.39	56.11	606	121	MLA altimetry track
M-NCCP4	136.52	51.07	784	67	MLA altimetry track
M-NCCP5	-148.11	60.99	257	108	MLA DEM
M-NCCP6	-175.96	52.84	141	62	MLA DEM
M-NCCP7	131.31	52.32	237	44	MLA DEM
M-NCCP8	120.42	50.74	369	56	MLA DEM
M-NCCP9	159.99	55.89	653	111	MLA DEM
M-NCCP10	176.95	60.33	767	103	MLA DEM
M-ECCP-OP1*	-164.02	21.64	961	362	USGS DEM
M-ECCP-OP2*	-157.81	17.03	623	200	USGS DEM
M-ECCP-OP3*	-151.29	16.70	185	265	USGS DEM
M-ECCP-OP4*	-156.55	14.28	395	93	USGS DEM
M-ECCP-OP5*	-174.34	24.08	190	69	USGS DEM
M-ECCP-OP6*	-166.05	33.36	252	116	USGS DEM
M-ECCP-OP7*	-160.71	19.38	267	177	USGS DEM
Wrinkle ridges located in southern Caloris exterior plains - (SCCP)					
M-SCCP1*	-176.51	10.91	440	88	USGS DEM
M-SCCP2*	177.38	9.18	725	261	USGS DEM
M-SCCP3*	-174.42	3.16	380	177	USGS DEM
M-SCCP4*	-172.32	-0.39	613	156	USGS DEM
M-SCCP5*	-176.98	14.00	313	75	USGS DEM
Wrinkle ridges located in Mercury's Caloris basin interior (CB)					
M-WR-CB1	157.56	27.27	276	158	DLR Orbital DEM

M-WR-CB2	156.57	28.11	208	43	DLR Orbital DEM
M-WR-CB3	155.88	25.20	524	113	DLR Orbital DEM
M-WR-CB4	156.25	23.87	411	199	DLR Orbital DEM
M-WR-CB5	154.44	26.04	377	145	DLR Orbital DEM
M-WR-CB6	160.26	24.20	186	38	DLR Orbital DEM
M-WR-CB7	161.09	25.23	433	35	DLR Orbital DEM
M-WR-CB8	161.76	24.36	402	29	DLR Orbital DEM
M-WR-CB9	159.95	28.66	207	48	DLR Orbital DEM
M-WR-CB10	158.85	30.92	264	34	DLR Orbital DEM
M-WR-CB11	157.86	31.64	254	33	DLR Orbital DEM
M-WR-CB12	163.92	32.21	190	31	DLR Orbital DEM
M-WR-CB13	148.62	31.31	606	95	M1 DEM flyby
M-WR-CB14	144.40	30.18	470	40	M1 DEM flyby
M-WR-CB15	143.70	26.62	740	74	M1 DEM flyby
M-WR-CB16	146.50	23.28	832	72	M1 DEM flyby
M-WR-CB17	148.44	25.23	243	51	M1 DEM flyby
M-WR-CB18	154.95	19.10	282	103	M1 DEM flyby
M-WR-CB19	167.65	17.80	400	62	M1 DEM flyby
M-WR-CB20	171.22	24.34	265	64	M1 DEM flyby
M-WR-CB21	176.23	24.60	318	151	M1 DEM flyby
M-WR-CB22	177.84	23.45	193	85	M1 DEM flyby
M-WR-CB23	-179.67	30.65	602	73	M1 DEM flyby
M-WR-CB24	178.46	30.89	326	46	M1 DEM flyby
M-WR-CB25	179.93	34.89	565	36	M1 DEM flyby
M-WR-CB26	171.64	30.47	667	39	M1 DEM flyby
M-WR-CB27	176.94	40.14	642	118	M1 DEM flyby
M-WR-CB28	176.44	37.81	347	111	M1 DEM flyby
M-WR-CB29	171.63	38.86	284	84	M1 DEM flyby
M-WR-CB30	154.47	46.27	253	27	M1 DEM flyby
M-WR-CB31	153.31	42.80	437	41	M1 DEM flyby

[a]Wrinkle ridges are unofficially named for the purposes of this study using abbreviations based on their locations in basin or smooth plains material.

[†]Cumulative slip and depth of faulting constrained with elastic dislocation modeling

*Wrinkle ridges previously identified from Mariner 10 and MESSENGER flyby imagery [*T R Watters et al.*, 2009c]

Table 4-B2. Lunar wrinkle ridge locations and relief and length measurements

Lunar wrinkle ridge ID (informal)[a]	Longitude (°E)	Latitude (°N)	Relief (m)	Length (km)	Topographic data source
Mare Crisium (CR)					
L-CR1	56.20	21.96	144	45	LOLA
L-CR2	60.45	21.11	100	39	WACDEM
L-CR3	62.96	21.62	420	14	WACDEM
L-CR4	64.85	19.15	92	17	LOLA
L-CR5	64.86	18.71	233	29	LOLA
L-CR6	65.11	15.93	232	61	WACDEM
L-CR7	63.65	13.86	590	58	WACDEM
L-CR8	60.87	13.32	81	48	WACDEM
L-CR9	57.20	11.68	257	75	LOLA
L-CR10	53.75	13.21	239	36	WACDEM
L-CR11	52.04	15.74	313	71	WACDEM
L-CR12	52.03	18.87	424	53	WACDEM
L-CR13	54.96	12.73	226	32	WACDEM
L-CR14	55.77	12.57	96	27	WACDEM
L-CR15	52.79	13.96	232	23	WACDEM
L-CR16	59.77	22.31	135	18	WACDEM
L-CR17	53.40	21.54	101	15	WACDEM
L-CR18	53.95	19.98	47	17	WACDEM
L-CR19	52.69	20.14	320	26	WACDEM
Mare Serenitatis (S)					
L-S1	9.52	26.18	127	28	LOLA
L-S3	11.88	24.19	106	30	WACDEM
L-S4	11.50	21.53	176	62	LOLA
L-S5	12.85	19.06	74	11	LOLA
L-S6	13.56	19.73	36	253	LOLA
L-S7	14.18	18.46	127	44	LOLA
L-S8	23.95	20.52	292	36	WACDEM
L-S10	28.65	23.73	305	35	WACDEM
L-S12	25.40	25.15	344	99	WACDEM
L-S13	24.85	29.19	275	58	WACDEM
L-S14	23.61	30.55	212	20	LOLA
L-S15	22.03	32.14	212	23	WACDEM
L-S16	21.39	32.43	261	21	LOLA
L-S17	20.47	33.71	84	21	WACDEM
L-S18	18.49	33.98	241	43	WACDEM
L-S19	15.01	30.59	98	35	WACDEM
L-S20	18.72	28.21	165	77	WACDEM
L-S21	25.54	27.04	244	46.65	WACDEM

L-S22	24.04	34.01	88	20.6	WACDEM
L-S23	8.46	29.22	113	23.59	WACDEM
L-S24	24.67	22.95	144	31.6	WACDEM
L-S25	25.33	30.64	307	36.04	WACDEM
L-S26	18.95	19.87	95	17.21	WACDEM
L-S27	22.74	18.10	157	41.19	WACDEM
L-I1	-25.58	44.70	140	79	WACDEM
L-I2	-20.15	47.27	432	68	LOLA
L-I3	-12.93	46.29	426	30	LOLA
L-I4	-4.73	45.15	236	35	WACDEM
L-I5	-8.25	40.97	271	120	WACDEM
L-I6	-7.67	22.42	151	46	WACDEM
L-I7	-12.43	29.23	159	232	LOLA
L-I8	-22.77	29.15	132	31	LOLA
L-I9	-24.51	29.22	378	190	LOLA
L-I10	-28.19	31.77	76	30	WACDEM
L-I11	-29.45	31.64	176	85	WACDEM
L-I12	-30.85	37.54	284	53	WACDEM
L-I13	-22.38	46.92	316	29	WACDEM
L-I14	-19.29	46.11	95	10	WACDEM
L-I15	-27.46	41.77	76	29	WACDEM
L-I16	-29.58	39.11	89	39	WACDEM
L-I17	-31.29	35.82	204	26	WACDEM
L-I18	-19.76	24.26	261	38	WACDEM
L-NE1	38.54	-16.65	446	75	WACDEM
Oceanus Procellarum (OP)					
L-OP1	-53.18	50.89	155	69	WACDEM
L-OP2	-67.70	52.28	114	70	LOLA
L-OP3	-70.67	46.39	151	48	LOLA
L-OP4	-63.31	46.59	188	37	LOLA
L-OP5	-69.11	45.10	120	19	LOLA
L-OP6	-73.49	44.53	136	91	LOLA
L-OP7	-61.16	44.17	104	21	LOLA
L-OP8	-65.43	40.75	273	160	WACDEM
L-OP9	-60.38	38.23	208	50	WACDEM
L-OP10	-54.33	36.77	119	80	WACDEM
L-OP11	-61.15	36.38	85	61	WACDEM
L-OP12	-73.85	34.10	295	64	WACDEM
L-OP13	-61.37	34.65	172	53	WACDEM
L-OP14	-59.06	34.66	185	88	WACDEM
L-OP15	-59.91	32.16	156	66	WACDEM
L-OP16	-57.44	30.40	132	63	WACDEM
L-OP17	-57.01	28.62	122	45	WACDEM

L-OP18	-57.43	26.76	150	85	WACDEM
L-OP19	-56.61	25.57	255	146	WACDEM
L-OP20	-52.76	19.05	100	114	WACDEM
L-OP21	-38.33	18.93	193	163	LOLA
L-OP22	-64.33	19.20	79	64	WACDEM
L-OP23	-61.20	16.44	222	125	LOLA
L-OP24	-55.89	11.94	109	61	WACDEM
L-OP25	-57.05	10.14	146	45	WACDEM
L-OP26	-50.60	9.09	154	49	WACDEM
L-OP27	-50.19	8.52	205	48	WACDEM
L-OP28	-61.15	5.85	210	108	WACDEM
L-OP29	-61.66	4.46	102	19	WACDEM
L-OP30	-60.79	4.34	162	25	WACDEM
L-OP31	-60.69	3.49	268	81	WACDEM
L-OP32	-59.33	4.00	157	120	WACDEM
L-OP33	-57.90	1.52	210	61	WACDEM
L-OP34	-57.13	0.76	172	50	WACDEM
L-OP35	-54.99	-0.61	52	29	WACDEM
L-OP36	-56.23	-1.53	147	58	WACDEM
L-OP37	-57.58	-3.24	102	62	WACDEM
L-OP38	-55.35	-3.18	186	45	WACDEM
L-OP39	-50.62	5.36	204	94	WACDEM
L-OP40	-51.59	4.19	146	21	WACDEM
L-OP41	-50.77	3.06	64	54	WACDEM
L-OP42	-49.52	3.75	130	35	WACDEM
L-OP43	-48.82	5.13	82	19	WACDEM
L-OP44	-48.52	2.89	147	20	WACDEM
L-OP45	-48.43	1.25	110	34	WACDEM
L-OP46	-44.93	0.48	358	79	WACDEM
L-OP47	-51.54	-0.30	63	37	WACDEM
L-OP48	-50.71	-1.52	193	28	WACDEM
L-OP49	-49.17	-2.81	136	78	WACDEM
L-OP50	-35.32	-1.07	156	121	WACDEM
L-OP51	-32.17	-2.79	232	31	WACDEM
L-OP52	-34.06	-5.38	143	73	WACDEM
L-OP53	-54.86	4.80	178	41	WACDEM
Mare Frigoris (FR)					
L-FR2	-20.92	59.81	256	22	LOLA
L-FR3	-16.99	62.28	204	78	LOLA
L-FR4[†]	-14.33	61.10	391	105	LOLA
L-FR5	-3.74	59.42	70	73	LOLA
L-FR6	-3.75	58.18	252	172	LOLA
L-FR7	2.99	57.61	114	126	LOLA

L-FR9	25.03	56.02	89	55	LOLA
L-FR10	24.99	54.83	292	96	LOLA
L-FR11	35.53	54.46	126	108	LOLA
L-FR12	35.54	53.87	57	132	LOLA
L-FR13	35.54	53.54	146	78	LOLA
L-FR14	-1.73	56.77	63	41.72	WACDEM
L-FR15	-18.60	55.50	60	32	WACDEM
L-FR16	-14.64	56.22	146	25.84	WACDEM
L-FR17	-25.94	58.60	66	15.45	WACDEM
L-FR18	-19.32	59.34	99	20.24	WACDEM
L-FE1	49.43	-1.04	343	91	LOLA
L-FE2	52.58	-4.41	481	111	WACDEM
L-GC1	-66.88	-6.12	175	22	WACDEM
L-NU1	-10.19	-23.79	300	65	WACDEM
L-NU2	-24.75	-25.56	224	66	WACDEM
L-O2	-97.65	-18.88	284	108	WACDEM
L-SM1	90.25	2.70	117	32	LOLA
L-T1	28.44	2.78	144	46	LOLA
L-T2	22.08	3.79	351	68	WACDEM
Wrinkle ridge - Lobate scarp transitions					
L-CO1	-18.36	-3.24	131	24	WACDEM
L-FR01	-26.77	60.86	98	91	WACDEM
L-FR08	10.64	55.45	199	41	WACDEM
L-H1	-39.54	-38.57	348	65	WACDEM
L-KAC1	-142.41	-52.19	192	28	WACDEM
L-KUC1	103.66	-53.33	426	46	WACDEM
L-S1	8.12	23.43	171	27	WACDEM
L-S8	28.94	21.22	33	13	WACDEM
L-S10	28.95	24.51	79	64	WACDEM
L-V1	-36.96	-33.28	179	98	LOLA

[a]Wrinkle ridges are unofficially named for the purposes of this study using abbreviations based on their basin location or nearby craters.

[†]Cumulative slip and depth of faulting constrained with elastic dislocation modeling

Appendix 4-C. Resolution of imagery and elevation data sources and resulting uncertainty on length and relief measurements

The varying imagery and elevation data sources available from MESSENGER (Figure 4-C1) and LRO for Mercury and the Moon solicit concern for any influence these different data sources may have on the relief and length measurements and ultimately the comparison of wrinkle ridge dimensions presented in this analysis (Tables 4-C1 and 4-C2). Therefore, in this appendix I detail the influence of imagery resolution on my length measurements as well as use of varying elevation data sources on my relief measurements. Figure 4-C2A shows the relief – length relationships of all measured wrinkle ridges colored by the elevation data source used to measure the relief.

Table 4-C1. Length measurement uncertainties from different imagery data sources

Location	Imagery	Length uncertainty (horizontal precision)
Mercury	250 m/pixel MDIS mosaic	5 km
The Moon	100 m/pixel LROC WAC mosaic	2 km

Table 4-C2. Relief measurement uncertainties from different elevation data sources

Location	Elevation data source	Number of measurements (*n*)	Relief uncertainty (vertical precision)
Mercury	MLA altimetry tracks	46	< 1 m (<2 m relief)
Mercury	MLA DEM	49	< 1 m (<2 m relief)
Mercury	Flyby and orbital stereo-derived DEMs	43	± 135 m (± 270 m relief)
Mercury	USGS DEM	12	± 276 m (± 552 m relief)
The Moon	LOLA altimetry tracks	39	± 10 cm (± 20 cm relief)
The Moon	WAC stereo-derived DEM	111	± 10 m (± 20 m relief)

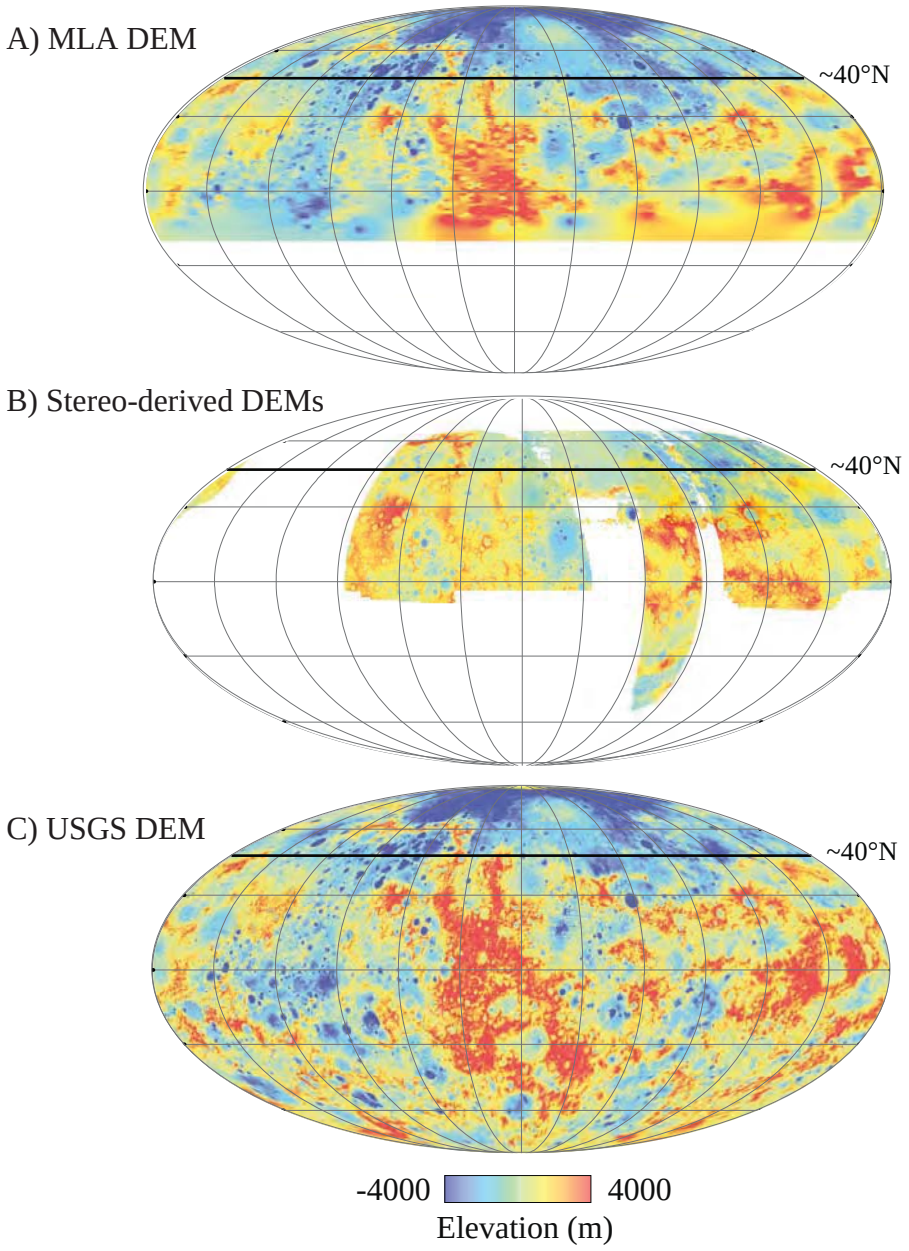

Figure 4-C1. Visual comparison of DEM sources available for Mercury
A) When MLA tracks were not available, the relief of wrinkle ridges located north of ~40°N (primarily in the northern smooth plains on Mercury) were measured from a ~500 m/pixel DEM interpolated from MLA tracks [*Zuber et al*., 2012]. B) Relief across wrinkle ridges located south of ~40°N (primarily in the Caloris Basin region) was measured using ~500 m/pixel DEMs produced from stereo photogrammetry of images from MESSENGER flyby and orbital imagery [*Oberst et al*., 2010; *Preusker et al*., 2011]. C) In cases when MLA tracks, the MLA DEM, or stereo-derived DEMs from the MESSENGER flyby or orbital imagery were not available, the relief across wrinkle ridges was measured using a ~2.7 km/pixel global DEM produced by the USGS using imagery metadata [*Becker et al*., 2012]. All DEMs are shown on a Mollweide equal area projection of Mercury centered at 0° longitude.

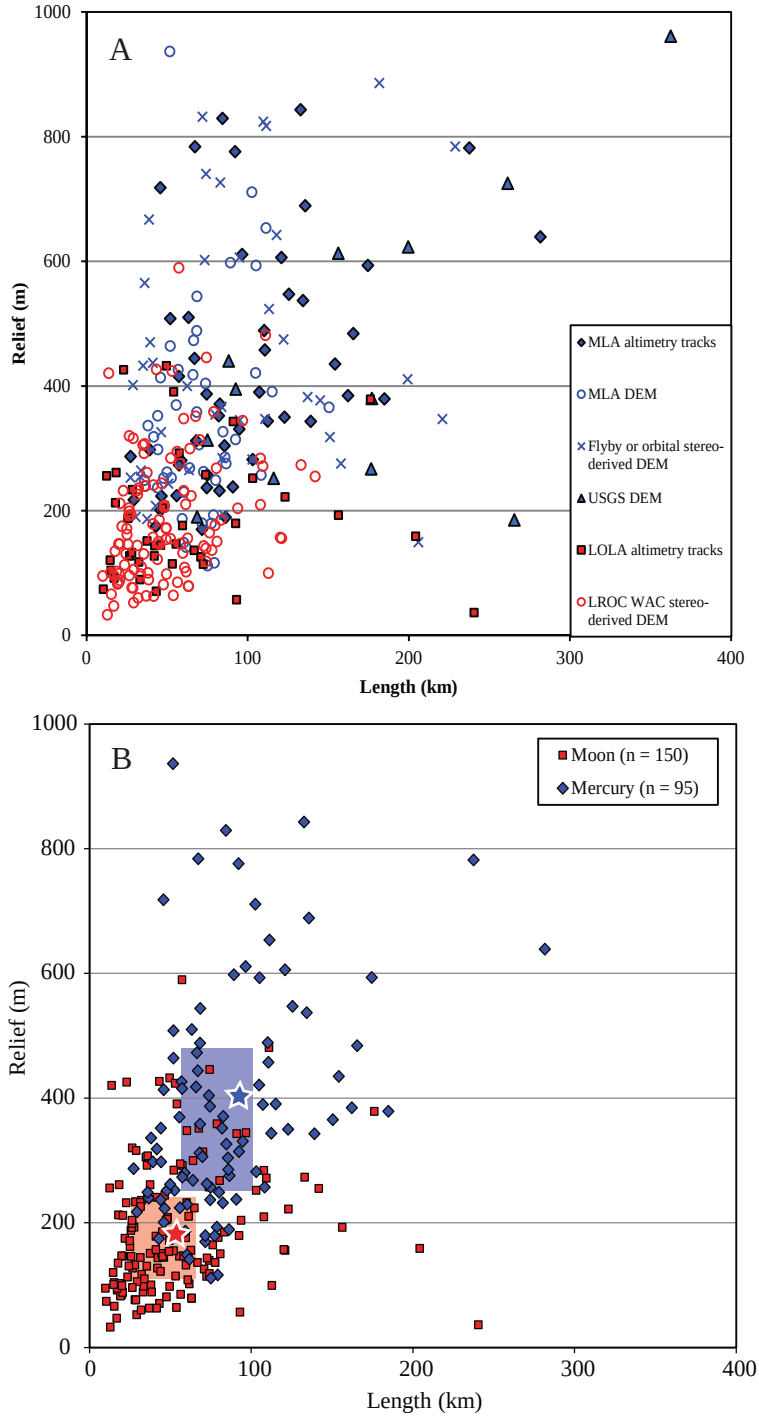

Figure 4-C2. Relief – length relationships of wrinkle ridges on Mercury and the Moon colored by elevation data source used to measure relief

A) Plot of relief and length of 300 wrinkle ridges on Mercury (shades of blue) and the Moon (shades of red). The dimensions of wrinkle ridges on Mercury are ~2.2 times and ~1.8 times larger in mean relief and length than wrinkle ridges on the Moon (stars). Boxes extend from the 25th to 75th percentiles of each population, representing 50% of the dataset. Symbols are colored by the elevation data source used to measure the relief measurement. B) Plot of relief and length of 95 wrinkle ridges on Mercury and 150 wrinkle ridges on the Moon (excluding wrinkle ridges measured using MESSENGER flyby and orbital stereo-derived DEM and USGS DEM shown in A and Figure 4-7. The dimensions of wrinkle ridges on Mercury are ~2.1 times and ~1.6 times larger in mean relief and length than wrinkle ridges on the Moon (stars). Notice that the overall interpretation that most of the wrinkle ridges on Mercury are taller than those on the Moon still stands without the inclusion of these data.

1. Length measurement from different resolution global mosaics

Wrinkle ridges were digitized in an ArcGIS environment from either the 100 m/pixel LROC WAC for wrinkle ridges on the Moon or the 250 m/pixel MDIS imagery mosaic for wrinkle ridges on Mercury. By assessing possible digitization choices from the imagery, I found that the length could vary by up to 2 km for lunar wrinkle ridges and up to 5 km for wrinkle ridges on Mercury. Because the global mosaic for the Moon is ~2.5 times higher in resolution than the global mosaic for Mercury, some very small scale wrinkle ridges (<1 km) can be observed on the Moon and not on Mercury.

I used a 500 m/pixel LROC WAC global mosaic in addition to the 100 m/pixel LROC WAC global mosaic when identifying and then digitizing digitize wrinkle ridges on the Moon. The majority of wrinkle ridges I digitized on the Moon are visible in both the 500 m/pixel and 100 m/pixel LROC WAC global mosaics. The 100 m/pixel global mosaic allowed the shape of the wrinkle ridge in map view to be more accurately mapped and whether the wrinkle ridge was continuous or segmented to be discerned. In addition, Figure 4-C2A shows that there is only a very limited range (<30 km) of wrinkle ridges on the Moon with shorter lengths than any of the wrinkle ridges on Mercury. The lack of very short length wrinkle ridges on the Moon indicates that the difference in resolution between the global mosaic used for Mercury and the Moon did not influence my length measurements and thus the comparison of lengths presented in this analysis.

2. Relief measurements from different elevation data sources

The relief of wrinkle ridges on Mercury were measured from MLA altimetry tracks (n = 46), MLA DEM (n = 49), Flyby and orbital stereo-derived DEMs (n = 43), and the USGS DEM (n = 12). Relief across lunar wrinkle ridges was measured using either LOLA altimetry tracks (n = 39) or the WAC stereo-derived DEM (n = 111) (Figure 4-C2A). The uncertainty associated with elevation measurements that comprise these elevation data sources is shown in Table 4-C2. Since measuring the relief requires subtraction of two elevation data points, uncertainty associated with the elevation measurements is doubled. Therefore, the uncertainty associated with relief measurements is twice that of the elevation data used. For example, elevation data points comprising LOLA altimetry tracks have a vertical precision of ±10 cm. Therefore, the uncertainty associated with measuring the relief of a wrinkle ridge doubles to ±20 cm.

Altimetry tracks (LOLA or MLA) provided the most detailed view of wrinkle ridges in cross-section (Figure 4-A1) and the smallest uncertainty in vertical precision. Since the vertical precision is ±10 cm for LOLA and ±1 m for MLA, the uncertainty associated with relief measurements for wrinkle ridges measured using LOLA or MLA altimetry tracks or the MLA DEM is smaller than the symbol size (~25 m in the relief dimension) on the relief-length plot (Figure 4-7). The vertical precision of the WAC stereo-derived DEM is also quite small, only ±10 m. Therefore the uncertainty accompanying relief measurements from the WAC stereo derived DEM (± 20 m) is also smaller than the symbol size.

Elevation data comprising the MESSENGER flyby and orbital stereo-derived DEMs and the USGS DEM respectively have a vertical precision of ±135 m (±270 m in relief) and ±276 m (±552 m in relief). Note however, that these are the worst case uncertainties and that in some cases profiles extracted across wrinkle ridges visible in the imagery did not exhibit any measureable reliefs. The stereo-derived DEMs and USGS DEM use MLA elevation data as control points when possible to help reduce the uncertainty associated with these elevation datasets. Since I cannot avoid these large uncertainties, I chose to regard measurements from the MESSENGER stereo-derived DEMs and USGS DEM with caution when making my interpretations.

Figure 4-C2B demonstrates that excluding wrinkle ridges where relief was measured from the MESSENGER stereo-derived DEMs and USGS DEM from my dataset does not change the core interpretation presented in this analysis, that wrinkle ridges on Mercury are taller than those on the Moon. When excluding the MESSENGER stereo-derived DEMs and USGS DEM relief measurements, wrinkle ridges on Mercury are ~2.1 times taller and ~1.6 times longer in mean relief and mean length (compared to ~2.2 times taller and ~1.8 times longer in mean relief and mean length with entire dataset). Also, the interquartile ranges still do not overlap in the relief dimension indicating that the majority of wrinkle ridges on Mercury are larger in relief than most wrinkle ridges on the Moon.

Appendix 4-D. Aspect ratio graphs

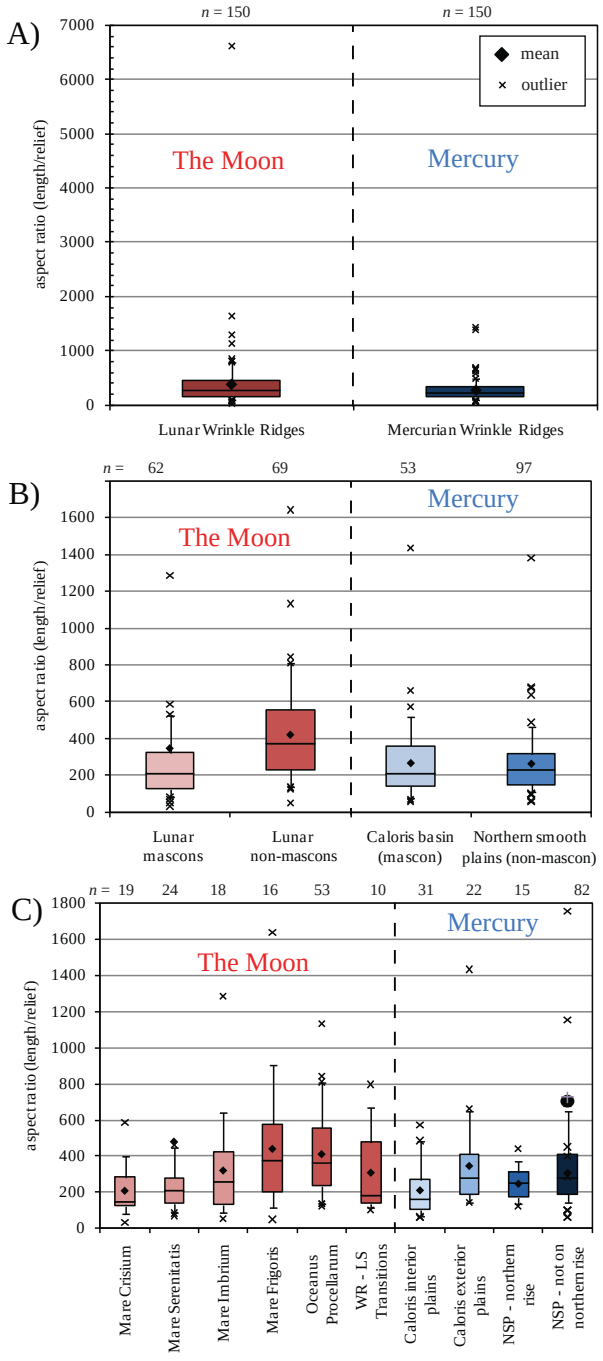

Figure 4-D1. Box and whisker plots of aspect ratio (length/relief) of wrinkle ridges
Box and whisker plots showing the aspect ratio (length/relief) of wrinkle ridge populations in the following regions: A) the Moon and Mercury, B) mascon and non-mascon basin environments, C) specified location. The box represents the interquartile range (which represents the middle 50% of the data). The vertical ends of the box are the 25th and 75th percentiles, the whiskers extend to the 95% of the data, and the X symbols represent outliers. Mean values are shown as diamonds and the median values as horizontal lines. There is an outlier in the lunar non-mascon population has an aspect ratio of 1132 and in Mare Serenitatis that has an aspect ratio of 6616, however these plots are scaled from 0 to 1800 to show variation in the rest of the dataset.

Bibliography

Adams, J.Q. (1828), John Quincy Adams diary 37, 11 November 1825 - 24 June 1828, edited.

Aleinikoff, J.N., J.W. Horton, and M. Walter (1996), Middle Proterozoic age for the Montpelier Anorthosite, Goochland terrane, eastern Piedmont,Virginia, *Geological Society of America Bulletin*, *108*(11), 1481-1491, doi: 10.1130/0016-7606(1996)108<1481:MPAFTM>2.3.CO;2.

Amante, C., and B.W. Eakins (2009), ETOPO1 1 Arc-Minute Global Relief Model: Procedures, Data Sources and Analysis. NOAA Technical Memorandum NESDIS NGDC-24., edited, p. 19, http://www.ngdc.noaa.gov/mgg/global/global.html.

Anderson, J.G., J.N. Brune, J.N. Louie, Y.H. Zeng, M. Savage, G. Yu, Q.B. Chen, and D. Depolo (1994), Seismicity in the western great-basin apparently triggered by the Landers, California, Earthquake, 28 June 1992, *Bulletin of the Seismological Society of America*, *84*(3), 863-891.

Antonioli, A., M.E. Belardinelli, A.Bizzarri, and K. S. Vogfjord (2006), Evidence of instantaneous dynamic triggering during the seismic sequence of year 2000 in south Iceland, *Journal of Geophysical Research-Solid Earth*, *111*(B3), doi:10.1029/2005jb003935.

Assumpcao, M., J.C. Dourado, L.C. Ribotta, W.U. Mohriak, F.L. Dias, and J.R. Barbosa (2011), The Sao Vicente earthquake of 2008 April and seismicity in the continental shelf off SE Brazil: further evidence for flexural stresses, *Geophysical Journal International*, *187*(3), 1076-1088, doi:10.1111/j.1365-246X.2011.05198.x.

Bailey, C.M., B.E. Francis, and E.E. Fahrney (2004), Strain and vorticity analysis of transpressional high-strain zones from the Virginia Piedmont, USA, *Geological Society, London, Special Publications*, *224*(1), 249-264, doi:10.1144/gsl.sp.2004.224.01.16.

Bailey, C.M., S.E. Peters, J. Morton, and N. L. Shotwell (2007), The Mechum River Formation, Virginia Blue Ridge: A Record of Neoproterozoic and Paleozoic Tectonics in Southeastern Laurentia, *American Journal of Science*, *307*(1), 1-22, doi:10.2475/01.2007.01.

Bailey, C.M., C.E. Webber, B.E. Francis, and J. Felis (2003), Structural geometry and kinematics of the Spotsylvania zone, central Virginia Piedmont [abs.], paper presented at Geological Society of America Abstracts with Programs.

Baldwin, R.B. (1965), *A fundamental survey of the Moon*, McGraw-Hill, New York, NY.

Baldwin, R.B. (1970), A new method of determining the depth of lave in lunar maria, *Astronomical Society Pacific Publication*, *82*, 857-864.

Banks, M.E., T.R. Watters, M.S. Robinson, J.F. Bell III, M.E. Pritchard, N.R. Williams, and K. Daud (2011), The search for lunar lobate scarps using images from the Lunar Reconnaissance Orbiter, in *Lunar and Planetary Science Conference XLII*, edited, p. Abstract 2736.

Banks, M.E., T.R. Watters, M.S. Robinson, L.L. Tornabene, T. Tran, L. Ojha, and N.R. Williams (2012), Morphometric analysis of small-scale lobate scarps on the Moon using data from the Lunar Reconnaissance Orbiter, *Journal of Geophysical Research-Planets*, *117*, 11, doi:10.1029/2011je003907.

Bayrak, Y., and S. Osturk (2004), Spatial and temporal variations of the aftershock sequences of the 1999 Izmit and Duzce earthquakes, Earth Planets Space, 56, 933-944.

Becker, K.J., L.A. Weller, K. Edmundson, T.L. Becker, M.S. Robinson, A.C. Enns, and S.C. Solomon (2012), Global Controlled Mosaic of Mercury from MESSENGER Orbital Images, paper presented at 43rd Lunar and Planetary Science Conference.

Bent, A.L. (1994), The 1989 Ms 6.3 Ungava, Quebec, Earthquake - A complex intraplate event, *Bulletin of the Seismological Society of America*, *84*(4), 1075-1088.

Bilham, R., and G. King (1989), The morphology of strike-slip faults: examples from the San Andreas Fault, California, *Journal of Geophysical Research-Solid Earth and Planets*, *94*(B8), 10204-10216, doi:10.1029/JB094iB08p10204.

Bisrat, S., H.R. DeShon, and C. Rowe (2012), Microseismic Swarm Activity in the New Madrid Seismic Zone, *Bulletin of the Seismological Society of America*, *102*(3), 1167-1178, doi:10.1785/0120100315.

Blackburn, T.J., Olsen, P.E., Bowring, S.A., McLean, N.M., Kent, D.V., Puffer, J., McHone, G., Rasbury, E.T., and Et-Touhami, M. (2013), Zircon U-Pb Geochronology links the end-Triassic extinction with the central Atlantic magmatic province, *Science*, doi: 10.1126/science.1234204.

Bobyarchick, A.R. (1988), Location and geometry of Alleghanian dispersal-related strike-slip faults in the southern Appalachians, *Geology*, *16*(10), 915-919, doi:10.1130/0091-7613(1988)016<0915:lagoad>2.3.co;2.

Bobyarchick, A.R. (1999), Continuity of late Paleozoic orogen-parallel shear zones in the western Piedmont of the Southern Appalachian Mountains, paper presented at Geological Society of America annual meeting.

Bodin, P., R. Bilham, J. Behr, J. Gomberg, and K.W. Hudnut (1994), Slip triggered on southern California faults by the 1992 Joshua-tree, Landers, and Big-Beak earthquakes, *Bulletin of the Seismological Society of America*, *84*(3), 806-816.

Bollinger, G.A., and M.G. Hopper (1971), Virginia's two largest earthquakes - December 22, 1875 and May 31, 1897, *Bulletin of the Seismological Society of America*, *61*(4), 1033-1039.

Bowman, J.R., G. Gibson, and T. Jones (1990), Aftershocks of the 1988 January 22 Tennant-Creek, Australia intraplate earthquakes - Evidence for a complex thrust-fault geometry, *Geophysical Journal International*, *100*(1), 87-97, doi:10.1111/j.1365-246X.1990.tb04570.x.

Boyce, J.M. (1976), Ages of flow units in the lunar nearside maria based on Lunar Orbiter IV photographs, paper presented at Proceedings of the Lunar and Planetary Science Conference, 7.

Braile, L.W., W.J. Hinze, G.R. Keller, E.G. Lidiak, and J.L. Sexton (1986), Tectonic development of the New Madrid rift complex, Mississippi embayment, North America, *Tectonophysics*, *131*(1-2), 1-21.

Braile, L.W., G.R. Keller, W.J. Hinze, and E.G. Lidiak (1982), An ancient rift complex and its relations to contemporary seismicity in the New Madrid Seismic Zone, *Tectonics*, *1*(2), 225-237, doi:10.1029/TC001i002p00225.

British Oceanographic Data Centre (BODC) (2008), General Bathymetric Chart of the Oceans (GEBCO), edited, CEUS-SSC Project GIS Database, http://www.ceus-ssc.com.

Brodsky, E.E., and S.G. Prejean (2005), New constraints on mechanisms of remotely triggered seismicity at Long Valley Caldera, *Journal of Geophysical Research-Solid Earth*, *110*(B4), doi:10.1029/2004jb003211.

Brown, L.D., and J.E. Oliver (1976), Vertical crustal movements from leveling data and their relation to geologic structure in the eastern United States, *Review in Geophysics*, *14*(1), 13-35.

Burgmann, R., D.D. Pollard, and S.J. Martel (1994), Slip distributions on faults - effects of stress gradients, inelastic deformation, heterogeneous host-rock stiffness, and fault interaction, *Journal of Structural Geology*, *16*(12), 1675-1690, doi:10.1016/0191-8141(94)90134-1.

Calais, E., A.M. Freed, R. Van Arsdale, and S. Stein (2010), Triggering of New Madrid seismicity by late-Pleistocene erosion, *Nature*, *466*(7306), 608-611.

Calais, E., J.Y. Han, C. DeMets, and J.M. Nocquet (2006), Deformation of the North American plate interior from a decade of continuous GPS measurements, *Journal of Geophysical Research-Solid Earth*, *111*(B6), doi:10.1029/2005jb004253.

Chapman, M.C., S. Huang, and J.A. Snoke (1993), Single-station backazimuth estimation from P- and Rg- waves at regional distance in the central Appalachians: PL-TR-93-2228, Phillips Laboratory, 43 pp., edited.

Clark, D. (2010), Identification of Quaternary scarps in southwest and central west Western Australia using DEM-based hill shading: application to seismic hazard assessment and neotectonics, *International Journal of Remote Sensing*, *31*(23), 6297-6325, doi:10.1080/01431161003631592.

Clark, D., A. McPherson, and C.D.N. Collins (2011), Australia's seismogenice neotectonic record, edited, Geoscience Australia, GeoCat #70288.

Coffin, M.F., L.M. Gahagan, and L.A. Lawver (1998), Present-day Plate Boundary Digital Data Compilation, in *University of Texas Institute for Geophysics Technical Report No. 174*, edited, p. 5, http://www.ig.utexas.edu/research/projects/plates/data.htm.

Coler, D.G., G.L. Wortman, S.D. Samson, J.P. Hibbard, and R. Stern (2000), U-Pb geochronology, Nd isotopic, and geochemical evidence for the correlation of the Chopawamsic and Milton terranes, Piedmont zone, Southern Appalachian orogen, *The Journal of Geology*, *108*, 363–380, doi:10.1086/314411.

Cramer, C.H., J. Kutliroff, and D. Dangkua (2011), The 2011 Mineral, VA M5.8 Earthquake Ground Motions and Stress Drop: An Important Contribution to the NGA East Ground Motion Database, paper presented at Abstract S11B-2239 presented at 2011 Fall Meeting, AGU, San Francisco, Calif., 5–9 Dec.

Crone, A.J., and R.L. Wheeler (2000), Data for Quaternary faults, liquefaction features, and possible tectonic features in the Central and Eastern United States, east of the Rocky Mountain front, U.S. Geological Survey, Open-File Report 00-260.

Csontos, R., and R. Van Arsdale (2008), New Madrid seismic zone fault geometry, *Geosphere*, *4*(5), 802-813, doi:10.1130/ges00141.1.

Darton, N.H. (1891), Mesozoic and Cenozoic formations of eastern Virginia and western Maryland, *Geological Society of America Bulletin*, *2*, 431-450.

Darton, N.H. (1950), *Configuration of the bedrock surface of the District of Columbia and vicinity*, Department of the Interior, United States Government Printing Office.

Davis, A.M., C.S. Southworth, J.E. Reddy, and J.S. Schindler (2001), Geologic Map Database of the Washington DC Area featuring data from three 30 x 60 minute quadrangles: Frederick, Washington West, and Fredericksburg, edited, U.S. Geological Survey.

Denevi, B.W., C.E. Ernst, H.M. Meyer, M.S. Robinson, S.L. Murchie, J.L. Whitten, J.W. Head, T.R. Watters, S.C. Solomon, L.R. Ostrach, C.R. Chapman, P.K. Byrne, C. Klimczak, and P.N. Peplowski (2012), The Distribution and Origin of Smooth Plains on Mercury, *Journal of Geophysical Research - Planets*.

Denevi, B.W., M.S. Robinson, S.C. Solomon, S.L. Murchie, D.T. Blewett, D.L. Domingue, T.J. McCoy, C.M. Ernst, J.W. Head, T.R. Watters, and N.L. Chabot (2009), The Evolution of Mercury's Crust: A Global Perspective from MESSENGER, *Science*, *324*(5927), 613-618, doi:10.1126/science.1172226.

Deng, J. S., K. Hudnut, M. Gurnis, and E. Hauksson (1999), Stress loading from viscous flow in the lower crust and triggering of aftershocks following the 1994 Northridge California, earthquake, *Geophysical Research Letters*, *26*(21), 3209-3212, doi:10.1029/1999gl010496.

Dewey, J.W., and D.W. Gordon (1984), Map showing recomputed hypocenters of earthquakes in the eastern and central United States and adjacent Canada,

1925-1980, *U.S. Geological Survey*(Miscellaneous Field Studies Map MF-1699).

Di Achille, G., C. Popa, M. Massironi, E.M. Epifani, M. Zusi, G. Cremonese, and P. Palumbo (2012), Mercury's radius change estimates revisited using MESSENGER data, *Icarus*, *221*(1), 456-460, doi:10.1016/j.icarus.2012.07.005.

Dixon, J.E., T.H. Dixon, D.R. Bell, and R. Malservisi (2004), Lateral variation in upper mantle viscosity: role of water, *Earth and Planetary Science Letters*, *222*(2), 451-467, doi:10.1016/j.epsl.2004.03.022.

Dominion Nuclear North Anna, L.L.C. (2006), North Anna Early Site Application, Part 2 – Site Safety Analysis Report, Sections 2.5.1 & 2.5.3, Rev. 9, September 2006, http://pbadupws.nrc.gov/docs/ML0625/ML062580103.pdf.

Dominion Power (2011), Dominion Power Wants to Restart Nuclear Reactors Shut Down During Quake, http://www.nbcwashington.com/news/local/Dominion-Wants-to-Restart-Nuclear-Reactors-Shut-Down-During-Quake-132314903.html, accessed October 24, 2011.

Drake, A.A., and L. Pavlides (1993), Stratigraphic Notes, *U.S. Geological Survey Bulletin*, *2076*, 27-28, ISBN 1071-7102.

Dunn, M.M., and M.C. Chapman (2006), Fault orientation in the eastern Tennessee seismic zone: A study using the double-difference earthquake location algorithm, *Seismological Research Letters*, *77*(4), 494-504, doi:10.1785/gssrl.77.4.494.

Dutton, C.E. (1889), The Charleston earthquake of August 31, 1866, edited by G. S. United States Department of the Interior, 203-528.

Eagar, K.C., G.L. Pavlis, and M.W. Hamburger (2006), Evidence of possible induced seismicity in the Wabash Valley seismic zone from improved microearthquake locations, *Bulletin of the Seismological Society of America*, *96*(5), 1718-1728, doi:10.1785/0120050190.

Ebel, J.E., and P.G. Somerville, J.D. (1986), A Study of the Source Parameters of Some Large Earthquakes of Northeastern North America, *Journal of Geophysical Research*, *91*, doi:10.1029/JB091iB08p08231.

Ebel, J.E. (2009), Analysis of Aftershock and Foreshock Activity in Stable Continental Regions: Implications for Aftershock Forecasting and the Hazard of Strong Earthquakes, *Seismological Research Letters*, *80*(6), 1062-1068, doi:10.1785/gssrl.80.6.1062.

Ebel, J.E., K.P. Bonjer, and M.C. Oncescu (2000), Paleoseismicity: Seismicity Evidence for Past Large Earthquakes, *Seismological Research Letters*, *71*(2), 283-294, doi:10.1785/gssrl.71.2.283.

Ebertart (1988), Aftershock sequence parameters in New Zealand, Bulletin of the Seismological Society of America, 85(4), 1095-1097.

Egea-Gonzalez, I., J. Ruiz, C. Fernandez, J.P. Williams, A. Marquez, and L.M. Lara (2012), Depth of faulting and ancient heat flows in the Kuiper region of Mercury from lobate scarp topography, *Planetary and Space Science*, *60*(1), 193-198, doi:10.1016/j.pss.2011.08.003.

Ekstrom, G., R.S. Stein, J.P. Eaton, and D. Eberhartphillips (1992), Seismicity and geometry of a 110-km-long blind thrust-fault: The 1985 Kettleman Hills, California, earthquake, *Journal of Geophysical Research-Solid Earth*, *97*(B4), 4843-4864, doi:10.1029/91jb02925.

Ellsworth, W.L., S.H. Hickman, A.L. Lleons, A. McGarr, A.J. Michael, and J.L. Rubinstein (2012), Are seismicity rate changes in the midcontinent natural or manmade?, in *Seismological Society of America Annual Meeting*, edited, San Diego, California.

Ellsworth, W.L., K. Imanishi, J.H. Luetgert, J. Kruger, and J. Hamilton (2011), The Mw 5.8 Virginia earthquake of August 23, 2011 and its aftershocks: A shallow high stress drop event, in *American Geophysical Union, 2011 Fall Meeting*, edited, San Francisco.

Enescu, B., and K. Ito (2002), Spatial analysis of the frequency-magnitude distribution and decay rate of aftershock activity of the 2000 Western Tottori earthquake, *Earth Planets and Space*, *54*(8), 847-859.

Engelkemeir, R.E., and S.D. Khan (2007), Near surface geophysical studies of Houston faults, *The Leading Edge*, *26*(8), 1004-1008, doi: 10.1190/1.2769557.

Fassett, C. I., J.W. Head, D.T. Blewett, C.R. Chapman, J.L. Dickson, S.L. Murchie, S.C. Solomon, and T.R. Watters (2009), Caloris impact basin: Exterior geomorphology, stratigraphy, morphometry, radial sculpture, and smooth plains deposits, *Earth and Planetary Science Letters*, *285*(3-4), 297-308, doi:10.1016/j.epsl.2009.05.022.

Fenneman, N.M., and D.W. Johnson (1946), Physiographic divisions of the conterminous U. S, *U.S. Geological Survey*, doi:http://water.usgs.gov/GIS/metadata/usgswrd/XML/physio.xml.

Fenster, D.F., and L.S. Walsh (2012), Preliminary Information on the Mw 5.8 August 23, 2011 Mineral, VA, Earthquake, *Association of Environmental and Engineering Geologists News*, *54*(4), 26-30.

Fielder, G. (1961), *Structure of the Moon's suface*, Pergamon, New York, NY.

Freed, A. (2005), Earthquake, triggering by static, dynamic, and postseismic stress transfer, *Annual Review of Earth and Planetary Sciences*, *33*, 335-367, doi:10.1146/annurev.earth.33.092203.122505.

Freed, A.M., and J. Lin (1998), Time-dependent changes in failure stress following thrust earthquakes, *Journal of Geophysical Research-Solid Earth*, *103*(B10), 24393-24409, doi:10.1029/98jb01764.

Freed, A.M., and J. Lin (2001), Delayed triggering of the 1999 Hector Mine earthquake by viscoelastic stress transfer, *Nature*, *411*(6834), 180-183, doi:10.1038/35075548.

Freed, A.M., H.J. Melosh, and S.C. Solomon (2001), Tectonics of mascon loading: Resolution of the strike-slip faulting paradox, *Journal of Geophysical Research-Planets*, *106*(E9), 20603-20620, doi:10.1029/2000je001347.

Freed, A.M., S.C. Solomon, T.R. Watters, R.J. Phillips, and M.T. Zuber (2009), Could Pantheon Fossae be the result of the Apollodorus crater-forming impact within the Caloris basin, Mercury?, *Earth and Planetary Science Letters*, *285*(3-4), 320-327, doi:10.1016/j.epsl.2009.02.038.

Friederich, W., and J. Dalkolmo (1995), Complete synthetic seismograms for a spherically symmetrical Earth by numerical computation of the Greens-Function in the frequency-domain, *Geophysical Journal International*, *122*(2), 537-550, doi:10.1111/j.1365-246X.1995.tb07012.x.

Geller, R.J. (2011), Shake-up time for Japanese seismology, *Nature*, *472*, 407–409, doi:doi:10.1038/nature10105.

Ghosh, A., W.E. Holt, and L. M. Flesch (2009), Contribution of gravitational potential energy differences to the global stress field, *Geophysical Journal International*, *179*(2), 787-812.

Gilbert, G.K. (1893), The Moon's face, a study of the origin and its features, *Philosophy Society of Washington Bulletin*, *12*, 241 - 292.

Glowacka, E., F.A. Nava, G.D. de Cossio, V. Wong, and F. Farfan (2002), Fault slip, seismicity, and deformation in Mexicali Valley, Baja California, Mexico, after the M 7.1 1999 Hector Mine earthquake, *Bulletin of the Seismological Society of America*, *92*(4), 1290-1299, doi:10.1785/0120000911.

Golombek, M.P., F.S. Anderson, and M.T. Zuber (2001), Martian wrinkle ridge topography: Evidence for subsurface faults from MOLA, *J. Geophys. Res.*, *106*(E10), 23811-23821, doi:10.1029/2000JE001308.

Golombek, M.P., J.B. Plescia, and B.J. Franklin (1991), Faulting and folding in the formation of planetary wrinkle ridges, *Proceedings of Lunar and Planetary Science*, *21*, 679-693.

Gomberg, J. (2001), The failure of earthquake failure models, *Journal of Geophysical Research-Solid Earth*, *106*(B8), 16253-16263, doi:10.1029/2000jb000003.

Gomberg, J., P. Bodin, K. Larson, and H. Dragert (2004), Earthquake nucleation by transient deformations caused by the M=7.9 Denali, Alaska, earthquake, *Nature*, *427*(6975), 621-624, doi:10.1038/nature02335.

Gomberg, J., and S. Davis (1996), Stress strain changes and triggered seismicity at The Geysers, California, *Journal of Geophysical Research-Solid Earth*, *101*(B1), 733-749, doi:10.1029/95jb03250.

Government of Canada, N.R.C., Mapping Information Branch, The Atlas of Canada, I. N. d. E. y. Geografia, and U. S. G. S. United States Department of the

Interior, National Atlas of the United States (2010), North American Atlas - Political Boundaries, edited, http://geogratis.gc.ca/download/frameworkdata/North_America_Atlas10M/boundaries/.

Grohmann, C.H., and G.A.C. Campanha (2010), OpenStereo: open source, cross-platform software for structural geology analysis, in *American Geophysical Union Fall Meeting*, edited, San Francisco, CA.

Grohmann, C.H., G.A.C. Campanha, and A. V. Soares Jr. (2011), OpenStereo: um programa Livre e multiplataforma para análise de dados estruturais., *In: XIII Simpósio Nacional de Estudos Tectônicos. (In Potuguese)*.

Hack, T.J. (1973), Stream-profile analysis and stream-gradient index, *U.S. Geological Survey Journal of Research*, *1*(4), 421-429.

Harding, D.J., and G.S. Berghoff (2000), Fault scarp detection beneath dense vegetation cover: airborne LIDAR mapping of the Seattle Fault Zone, Brainbridge Island, Washington State, paper presented at Proceedings of the American Society of Photogrammetry and Remote Sensing Annual Conference, Washington, DC.

Harmon, J.K., D.B. Campbell, D.L. Bindschadler, J.W. Head, and Shapiro, II (1986), Radar altimetry of Mercury - a preliminary analysis, *Journal of Geophysical Research-Solid Earth and Planets*, *91*(B1), 385-401, doi:10.1029/JB091iB01p00385.

Harris, L.D., W. deWitt, Jr., and K.C. Bayer (1986), Interpretive seismic profile along Interstate I-64 in central Virginia from the Valley and Ridge to the Coastal Plain, Virginia Department of Mines, Minerals, and Energy, Publication 66, https://www.dmme.virginia.gov/commerce/ProductDetails.aspx?productID=2419.

Hauksson, E., L.M. Jones, K. Hutton, and D. Eberhart-Phillips (1993), The 1992 Landers Earthquake Sequence: Seismological Observations, *J. Geophys. Res.*, *98*(B11), 19835-19858, doi: 10.1029/93JB02384.

Hawkins, S.E., J.D. Boldt, Darlington, E.H., Espiritu, R.E. Gold, B. Gotwols, M.P. Grey, C.D. Hash, J.R. Hayes, S.E. Jaskulek, C.J. Kardian Jr., M.R. Keller, E.R. Malaret, S.L. Murchie, P.K. Murphy, K. Peacock, L.M. Prockter, R.A. Reiter, M.S. Robinson, E.D. Schaefer, R.G. Shelton, R.E. Sterner II, H.W. Taylor, T.R. Watters, and B.D. Williams, The Mercury Dual Imaging System on the MESSENGER spacecraft, *Space Science Reviews*, *131*(1-4), 247-338, doi:10.1007/s11214-007-9266-3.

Head, J.W., C.R. Chapman, R.G. Strom, C.I. Fassett, B.W. Denevi, D.T. Blewett, C.M. Ernst, T.R. Watters, S.C. Solomon, S.L. Murchie, L.M. Procketer, N.L. Chabot, J.J. Gillis-Davis, J.L. Whitten, T.A. Goudge, D.M.H. Baker, D.M. Hurwitz, L.R.Ostrach, Z. Xiao, W.J. Merline, L. Kerber, J.L. Dickson, J. Oberst, P.K. Byrne, C. Klimczak, and L.R. Nittler (2011), Flood Volcanism in the Northern High Latitudes of Mercury Revealed by MESSENGER, *Science*, *333*(6051), 1853-1856, doi:10.1126/science.1211997.

Head, J.W., S.L. Murchie, L.M. Procker, M.S. Robinson, S.C. Solomon, R.G. Strom, C.R. Chapman, T.R. Watters, W.E. McClintock, D.T. Blewett, and J.J. Gillis-Davis (2008), Volcanism on Mercury: Evidence from the first MESSENGER flyby, *Science*, *321*(5885), 69-72, doi:10.1126/science.1159256.

Head, J.W., S.L. Murchie, L.M. Prockter, M.S. Robinson, S.C. Solomon, R.G. Strom, C.R. Chapman, T.R. Watters, W.E. McClintock, D.T. Blewett, and J.J. Gillis-Davis (2009), Volcanism on Mercury: Evidence from the first MESSENGER flyby for extrusive and explosive activity and the volcanic origin of plains, *Earth and Planetary Science Letters*, *285*(3-4), 227-242, doi:10.1016/j.epsl.2009.03.007.

Hildenbrand, T.G., and D. Ravat (1997), Geophysical Setting of the Wabash Valley Fault System, *Seismological Research Letters*, *68*(4), 567-585, doi:10.1785/gssrl.68.4.567.

Hill, D.P. (2008), Dynamic stresses, Coulomb failure, and remote triggering, *Bulletin of the Seismological Society of America*, *98*(1), 66-92, doi:10.1785/0120070049.

Hill, D.P., and S.G. Prejean (2007), *Dynamic triggering*, 257 - 292 pp., Elsevier, New York.

Hill, D.P., P.A. Reasenberg, A. Michael, W.J. Arabaz, G. Beroza, D. Brumbaugh, J.N. Brune, R. Castro, S. Davis, D. dePolo, W.L. Ellsworth, J. Gomberg, S. Harmsen, L. House, S.M. Jackson, M.J.S. Johnson, L. Jones, R. Keller, S. Malone, L. Munguia, S. Nava, J.C. Pechmann, A. Sanford, R.W. Simpson, R.B. Smith, M. Stark, M. Stickney, A. Vidal, S. Walter, V. Wong, and J. Zollweg (1993), Seismicity remotely triggered by the magnitude 7.3 Landers, California, earthquake, *Science*, *260*(5114), 1617-1623, doi:10.1126/science.260.5114.1617.

Holford, S.P., R.R. Hillis, M. Hand, and M. Sandiford (2011), Thermal weakening localizes intraplate deformation along the southern Australian continental margin, *Earth and Planetary Science Letters*, *305*(1-2), 207-214, doi:10.1016/j.epsl.2011.02.056.

Horton (2012), Faults delineated by aftershocks associated with the 2011 central Virginia earthquake and their tectonic setting, paper presented at Geological Society of America Southeastern Section Meeting, Asheville, NC, April 1st.

Horton, J.W., J.N. Aleinikoff, A.A. Drake, and C.M. Fanning (2010), Ordovician volcanic-arc terrane in the Central Appalachian Piedmont of Maryland and Virginia: SHRIMP U-Pb geochronology, field relations, and tectonic significance, *Geological Society of America Memoirs*, *206*, 621-660, doi:doi:10.1130/2010.1206(25).

Horton, J.W., D.E. McNamara, A.K. Shah, A.K. Gilmer, A.M. Carter, W.C. Burton, R.W. Harrison, M.W. Carter, R.B. Herrmann, and S.L. Snyder (2012), Preliminary analysis of magnitude 5.8 Virginia earthquake causative fault and subsidary faults illuminated by aftershocks, in *Geological Society of America Annual Meeting*, edited, Charlotte, NC.

Horton, J.W., and R.A. Williams (2012), The 2011 Virginia Earthquake: What are Scientists Learning, *EOS, Transactions, American Geophysical Union*, *93*(33), 317-318.

Hough, S.E. (2004), Scientific overview and historical context of the 1811-1812 New Madrid earthquake sequence, *Annals of Geophysics*, *47*, 523-537.

Hough, S.E. (2001), Triggered earthquakes and the 1811-1812 New Madrid, central United States, earthquake sequence, *Bulletin of the Seismological Society of America*, *91*(6), 1574-1581, doi:10.1785/0120000259.

Hough, S.E. (2007), Remotely triggered earthquakes following moderate main shocks, in *Continental Intraplate Earthquakes: Science, Hazard, and Policy Issues: Geological Society of America Special Paper 425*, edited by S. Stein and S. Mazzotti, pp. 73-86, doi:10.1130/2007.2425(06).

Hough, S.E. (2012), Initial Assessment of the Intensity Distribution of the 2011 Mw 5.8 Mineral, Virginia, Earthquake, *Seismological Research Letters*, *83*(4), 649-657, doi:10.1785/0220110140.

Hough, S. E., and H. Kanamori (2002), Source properties of earthquakes near the Salton Sea triggered by the 16 October 1999 M 7.1 Hector Mine, California, earthquake, *Bulletin of the Seismological Society of America*, *92*(4), 1281-1289, doi:10.1785/0120000910.

Hough, S.E., L. Seeber, and J.G. Armbruster (2003), Intraplate triggered earthquakes: Observations and interpretation, *Bulletin of the Seismological Society of America*, *93*(5), 2212-2221, doi:10.1785/0120020055.

Hughes, S., A. Terblanche, D. Nance, J. Hibbard, and B. Miller (2012), New observations on the chopawamsic fault, an early paleozoic terrane boundary in the western piedmont of virginia, *Geological Society of America Abstracts with Programs*, *44*(4), 29, doi:https://gsa.confex.com/gsa/2012SE/finalprogram/abstract_201910.htm.

Ibrahim, A.B.K., and O.W. Nuttli (1967), Travel-time curves and upper-mantle structure from long period S waves, *Bulletin of the Seismological Society of America*, *57*(5), 1063-1092.

Iverson, W.P., and S.B. Smithson (1983), Reprocessing and reinterpretation of COCORP southern Appalachian profiles, *Earth and Planetary Science Letters*, *62*(1), 75-90, doi:10.1016/0012-821X(83)90072-9.

Jacobi, R.D., J.E. Ebel, and A. O'Hara (2012), Earthquake swarm near Albany, NY, at the time of the Mineral, VA, seismic event, in *Geological Society of America Annual Meeting*, edited, p. 593, Charlotte, NC.

Jibson, R.W., and E.L. Harp (2012), Extraordinary Distance Limits of Landslides Triggered by the 2011 Mineral, Virginia, Earthquake, *Bulletin of the Seismological Society of America*, *102*(6), 2368-2377, doi:10.1785/0120120055.

Johnson, D.W. (1999), The Culpeper Basin, *Virginia Minerals, Commonwealth of Virginia, Department of Mines, Minerals and Energy, Richmond, Virginia*, *45*(5).

Kanamori, H. (1977), Energy-release in great earthquakes, *Journal of Geophysical Research*, *82*(20), 2981-2987, doi:10.1029/JB082i020p02981.

Kelson, K.I., G.D. Simpson, R.B. VanArsdale, C.C. Haraden, and W.R. Lettis (1996), Multiple late Holocene earthquakes along the Reelfoot fault, central New Madrid seismic zone, *Journal of Geophysical Research-Solid Earth*, *101*(B3), 6151-6170, doi:10.1029/95jb01815.

Kerr, R. (2011), Seismic crystal ball proving mostly cloudy around the world, *Science*, *332*, 912–913.

Kim, W.Y., M. Gold, C. Scharnberger, J. Jones, and H. Delano (2009), The 2008-2009 earthquake swarm near Dillsburg, Pennsylvania, *Pennsylvania Geological Survey, Open-File Report OFMI 09–01.0*, *4*, , 20.

Kim, W.Y., and M. Chapman (2005), The 9 December 2003 central Virginia earthquake sequence: A compound earthquake in the central Virginia seismic zone, *Bulletin of the Seismological Society of America*, *95*(6), 2428-2445, doi:10.1785/0120040207.

King, G., and M. Ellis (1990), The origin of large local uplift in extensional regions, *Nature*, *348*(6303), 689-692, doi:10.1038/348689a0.

King, G.C.P., R.S. Stein, and J. Lin (1994), Static stress changes and the triggering of earthquakes, *Bulletin of the Seismological Society of America*, *84*(3), 935-953.

King, G.C. P., R.S. Stein, and J.B. Rundle (1988), The growth of geological structures by repeated earthquakes. 1. Conceptual-Framework, *Journal of Geophysical Research-Solid Earth and Planets*, *93*(B11), 13307-13318, doi:10.1029/JB093iB11p13307.

Kisslinger, C., and L.M. Jones (1991), Properties of aftershock sequences in southern California, *Journal of Geophysical Research-Solid Earth and Planets*, *96*(B7), 11947-11958, doi:10.1029/91jb01200.

Klimczak, C., T.R. Watters, C.M. Ernst, A.M. Freed, P.K. Byrne, S.C. Solomon, D. M. Blair, and J.W. Head (2012), Deformation associated with ghost craters and basins in volcanic smooth plains on Mercury: Strain analysis and implications for plains evolution, *Journal of Geophysical Research-Planets*, *117*, 15, doi:10.1029/2012je004100.

Konopliv, A.S., S.W. Asmar, E. Carranza, W.L. Sjogren, and D.N. Yuan (2001), Recent gravity models as a result of the lunar prospector mission, *Icarus*, *150*(1), 1-18, doi:10.1006/icar.2000.6573.

Kunk, M.J., R.P. Wintsch, C.W. Naeser, N.D. Naeser, C.S. Southworth, A.A. Drake, and J.L. Becker (2005), Contrasting tectonothermal domains and faulting in the Potomac terrane, Virginia-Maryland-discrimination by Ar-40/Ar-39 and

fission-track thermochronology, *Geological Society of America Bulletin, 117*(9-10), 1347-1366, doi:10.1130/b25599.1.

Kunk, M.J., R.P. Wintsch, C.S. Southworth, B.K. Mulvey, C.W. Naeser, and N.D. Naeser (2004), Multiple Paleozoic Metamorphic Histories, Fabrics, and Faulting in the Westmister and Potomac Terranes, Central Appalachian Piedmont, Northern Virginia and Southern Maryland, in *Geology of the National Capitol Region - Field Trip Guidebook*, edited by C. S. Southworth and W. Burton, 163-188.

Lampshire, L.D., C. Coruh, and J.K. Costain (1994), Crustal structures and the eastern extent of lower Paleozoic shelf strata within the central Appalachians - A seismic-reflection interpretation, *Geological Society of America Bulletin, 106*(1), 1-18, doi:10.1130/0016-7606(1994)106<0001:csatee>2.3.co;2.

Leonard, M. (2008), One hundred years of earthquake recording in Australia, *Bulletin of the Seismological Society of America*, *98*(3), 1458-1470, doi:10.1785/0120050193.

Li, Q., M. Liu, Q. Zhang, and E. Sandvol (2007), Stress evolution and seismicity in the central-eastern United States: Insights from geodynamic modeling, *Geological Society of America Special Papers, 425,* 149-166, doi:10.1130/2007.2425(11).

Lin, J., and A.M. Freed (2004), *Time-Dependent Viscoelastic Stress Transfer and Earthquake Triggering*, 21-38 pp., Higher Education Press, Beijing.

Lin, J., and R.S. Stein (2004), Stress triggering in thrust and subduction earthquakes and stress interaction between the southern San Andreas and nearby thrust and strike-slip faults, *J. Geophys. Res.*, *109*(B2), B02303, doi:10.1029/2003JB002607.

Linde, A. T., and M.J.S. Johnston (1989), Source parameters of the October 1, 1987 Whittier-Narrows earthquake from crustal deformation data, *Journal of Geophysical Research-Solid Earth and Planets*, *94*(B7), 9633-9643, doi:10.1029/JB094iB07p09633.

Liu, M., S. Stein, and H. Wang (2011), 2000 years of migrating earthquakes in North China: How earthquakes in midcontinents differ from those at plate boundaries, *Lithosphere*, doi:10.1130/l129.1.

Madabhushi, S., and Talwani, P. (1993), Fault plane solutions and relocations of recent earthquakes in Middleton Place Summerville seismic zone near Charleston, South Carolina, *Bulletin of the Seismological Society of America*, *83*(5), 1442-1466.

Manspeizer, W., DeBoer, J., Costain, J.K., Froelich, A.J., Coruh, C., Olsen, P.E., McHone, G.J., Puffer, J.H., and Prowell, D.C. (1989), Post-Paleozoic activity, in Hatcher, R. D., Jr., Thomas, W. A., and Viele, G. W., eds., The Appalachian-Ouachita orogen in the United States: Boulder, Colorado, Geological Society of America, *The Geology of North America*, F-2, 319-374.

Martin, A.J. (2012), Implications of the C. 550 MA crystallization of the Sabot amphibolite protolith in the Goochland Terrane of the central Virginia Piedmont, Geological Society of America Abstracts with Programs.

Maxwell, T.A., F. El-Baz, and S.H. Ward (1975), Distribution, Morphology, and Origin of Ridges and Arches in Mare Serenitatis, *Geological Society of America Bulletin*, *86*(9), 1273-1278.

Maxwell, T.A., and A.W. Gifford (1980), Ridge systems of Caloris: Comparison with lunar basins, paper presented at Lunar and Planetary Science Conference.

Mazzotti, S., and J. Townend (2010), State of stress in central and eastern North American seismic zones, *Lithosphere*, *2*(2), 76-83, doi:10.1130/l65.1.

McNamara, D.E., R. Herrmann, H. Benz, A. Leeds, M. Chapman, and L. Gee (2013), The M_w 5.8 Mineral, Virginia earthquake of August 23, 2011 and aftershock sequence: Constraints on earthquake source parameters and fault geometry, edited, *Bulletin of the Seismological Society of America*, in review.

McNutt, R.L., S.C. Solomon, P.D. Bedini, E.J. Finnegan, D.G. Grant, and M. Team (2010), The MESSENGER mission: Results from the first two Mercury flybys, *Acta Astronautica*, *67*(7-8), 681-687, doi:10.1016/j.actaastro.2010.05.020.

McPherson, A., D. Clark, M. Cupper, C.D.N. Collins, and G. Nelson (2012), The Cadell Fault: A record of long-term fault behavior in south-eastern Australia, Extended Abstract, in *Second Australian Regolith Geoscientists Association Conference and the 22nd Australian Clay Minerals Society Conference*, edited, Mildura, Victoria.

Melosh, H.J., and W.B. McKinnon (1988), The Tectonics of Mercury, in *Mercury*, edited, pp. 374-400, University of Arizona Press.

Mixon, R.B., and W.L. Newell (1977), Stafford fault system: Structures documenting Cretaceous and Tertiary deformation along the Fall Line in northeastern Virginia, *Geology*, *5*(7), 437-440, doi:10.1130/0091-7613(1977)5<437:sfssdc>2.0.co;2.

Mixon, R.B., L. Pavlides, J.W. Horton, D.S. Powars, and S.J. Schindler (2005), Geologic Map of the Stafford Quadrangle, Stafford County, Virginia, U.S. Geological Survey.

Mueser, R. (1967), Washington Metropolitan Area Rapid Transit Authorized Basic System, Final Report, *Subsurface Investigation*, 1 p., prepared for National Capital Transportation.

Nakamura, Y., G.V. Latham, H.J. Dorman, A.B.K. Ibrahim, J. Koyama, and P. Horvath (1979), Shallow moonquakes: Depth, distribution and implications as to the present state of the lunar interior, *Proceedings of the Lunar Science Conference*, 10, 2299-2309.

Nakamura, Y., G.V. Latham, H.J. Dorman, and J. Harris (1981), Passive sismic experiment long-period event catalog: Final version, *Technical Report* No. 18, Galveston Geophysics Laboratory, University of Texas at Austin.

National Park Service (2011), Washington Monument Post-Earthquake Assessment, Wiss, Janney, Elstner Associates, Inc and Tipping Mar Structural Engineering, http://www.nps.gov/wamo/upload/Post-Earthquake-assessment12_22_logo.pdf.

Nishenko, S.P. and G.A. Bollinger (1990), Forecasting damaging earthquakes in the Central and Eastern United States, *Science, 249*, 1412-1416.

Nuttli, O. (1987), The effects of earthquakes in the central United States: Report for Central U.S. Earthquake Consortium: Memphis, TN, *Federal Emergency Management Agency*, 33 pages.

Obermeier, S.F., and W.E. McNulty (1998), Paleoliquefaction evidence for seismic quiescence in central Virginia during the late to middle Holocene time, *EOS Transactions of the American Geophysical Union*, *79*(17).

Oberst, J., F. Preusker, R.J. Phillips, T.R. Watters, J.W. Head, M.T. Zuber, and S.C. Solomon (2010), The morphology of Mercury's Caloris basin as seen in MESSENGER stereo topographic models, *Icarus*, *209*(1), 230-238, doi:10.1016/j.icarus.2010.03.009.

Okubo, C.H., and R.A. Schultz (2003), Two-dimensional wrinkle ridge strain & energy release based on numerical modeling of MOLA topography, paper presented at Proceedings of the Lunar and Planetary Science Conference.

Omori, R. (1894), On the aftershocks of earthquakes, *J. Coll. Sci. Imp. Univ. Tokyo*, *7*, 111-200.

Owens, B.E., and R.D. Tucker (2003), Geochronology of the Mesoproterozoic State Farm gneiss and associated Neoproterozoic granitoids, Goochland terrane, Virginia, *Geological Society of America Bulletin*, *115*, 972-982, doi: 10.1130/B25258.1.

Owens, B.E., R. Buchwaldt, and C.R. Shirvell (2010), Geochemical and geochronological evidence for Devonian magmatism revealed in the Maidens gneiss, Goochland terrane, Virginia, in Tollo, R.P., Bartholomew, M.J., Hibbard, J.P., and Karabinos, P.M., eds., From Rodinia to Pangea: The Lithotectonic Record of the Appalachian Region, *The Geological Society of America Memoir 206*, 1-14, doi:10.1130/2010.1206(28).

Parsons, T., and D.S. Dreger (2000), Static-stress impact of the 1992 Landers earthquake sequence on nucleation and slip at the site of the 1999 M=7.1 Hector Mine earthquake, southern California, *Geophysical Research Letters*, *27*(13), 1949-1952, doi:10.1029/1999GL011272.

Parsons, T., J.O. Kaven, A.A. Velasco, and H. Gonzalez-Huizar (2012), Unraveling the apparent magnitude threshold of remote earthquake triggering using full wavefield surface wave simulation, *Geochemistry Geophysics Geosystems*, *13*, Q06016, doi:10.1029/2012GC004164.

Pavlides, L. (1986), Mountain Run Fault zone of Virginia, in Jacobsen, M.L., and Rodriguez, T.R., comp., National earthquake hazards reduction program, summaries of technical reports, *U.S. Geological Survey Open-File Report, 23,* 93-94.

Pavlides, L. (1989), Early Paleozoic composite melange terrane, central Appalachian Piedmont, Virginia and Maryland: Its origin and tectonic history, in *Melanges and olistostromes of the U.S. Appalachians*, edited by J. W. Horton and N. Rast, pp. 135-193, Geological Society of America Special Paper.

Pavlides, L. (1990), Geology of part of the northern Virginia Piedmont: U.S. Geological Survey Open-File Report 90–548, 1 sheet, scale 1:100,000.

Pavlides, L. (1995), Piedmont geology of the Stafford, Storck, Salem Church, and Fredericksburg quadrangles, Stafford, Fauquier, and Spotsylvania Counties, Virginia: U.S. Geological Survey Open-File Report 95–577, 2 sheets, scale 1:24,000.

Pavlides, L., J.D. Arth, J.F. Sutler, T.W. Stern, and H. Cortesini Jr (1994), Early Paleozoic alkalic and calc-alkalic plutonism and associated contact metamorphism, central Virginia Piedmont, *U.S. Geological Survey Professional Paper, 1529*.

Pazzaglia, F.J., and T.W. Gardner (1993), Fluvial terraces of the lower Susquehanna River, *Geomorphology*, *8*(2-3), 83-113, doi:10.1016/0169-555X(93)90031-V.

Peng, Z.G., J.E. Vidale, and H. Houston (2006), Anomalous early aftershock decay rate of the 2004 Mw6.0 Parkfield, California, earthquake, *Geophysical Research Letters*, *33*(17), 5, doi:10.1029/2006gl026744.

Petersen, M.D., A.D. Frankel, S.C. Harmsen, C.S. Mueller, K.M. Haller, R.L. Wheeler, R.L. Wesson, Y. Zeng, O.S. Boyd, D.M. Perkins, N. Luco, E.H. Field, C.J. Willis, and K.S. Rukstales (2008), Documentation for the 2008 Update of the United States National Seismic Hazard Maps, *U.S. Geological Survey Open-File Report 2008–1128.*, 61 pages.

Plescia, J.B., and M.P. Golombek (1986), Origin of planetary wrinkle ridges based on the study of terrestrial analogs, *Geological Society of America Bulletin*, *97*(11), 1289-1299.

Poag, C.W., and W.D. Sevon (1989), A record of Appalachian denundation in post rift Mesozoic and Cenozoic sedimentary deposits in the U.S. Middle Atlantic continental margin, *Geomorphology*, *2*(1-3), 119-157, doi:10.1016/0169-555X(89)90009-3.

Pollitz, F.F., and I.S. Sacks (1995), Consequences of stress changes following the 1891 Nobi earthquake, Japan, *Bulletin of the Seismological Society of America, 85*(3), 796-807.

Pollitz, F.F., and I.S. Sacks (1997), The 1995 Kobe, Japan, earthquake: A long-delayed aftershock of the offshore 1944 Tonankai and 1946 Nankaido earthquakes, *Bulletin of the Seismological Society of America, 87*(1), 1-10.

Pollitz, F.F., R.S. Stein, V. Sevilgen, and R. Burgmann (2012), The 11 April 2012 east Indian Ocean earthquake triggered large aftershocks worldwide, *Nature*, *490*(7419), 250, doi:10.1038/nature11504.

Prejean, S.G., D.P. Hill, E.E. Brodsky, S.E. Hough, M.J.S. Johnston, S.D. Malone, D.H. Oppenheimer, A.M. Pitt, and K.B. Richards-Dinger (2004), Remotely triggered seismicity on the United States west coast following the M-W 7.9 Denali fault earthquake, *Bulletin of the Seismological Society of America*, *94*(6), S348-S359, doi:10.1785/0120040610.

Preusker, F., J. Oberst, J.W. Head, T.R. Watters, M.S. Robinson, M.T. Zuber, and S.C. Solomon (2011), Stereo topographic models of Mercury after three MESSENGER flybys, *Planetary and Space Science*, *59*(15), 1910-1917, doi:10.1016/j.pss.2011.07.005.

Prowell, D.C. (1983), Index of faults of Cretaceous and Cenozoic age in the eastern United States.

Prowell, D.C. (Ed.) (1988), *Cretaceous and Cenozoic tectonism on the Atlantic Coastal Margin*, 557-564 pp., The Geology of North America.

Prowell, D.C. (2010), The fault with the White House: A study of late Cenozoic tectonism in Washington, DC, paper presented at Geological Society of America Northeastern and Southeastern Section Joint Meeting, Geological Society of America, Baltimore, MD, 15 March 2010.

Prowell, D.C., and R.A. Christopher (2004), Data Collected from USGS Drilling in Lafayette Park, Washington, D.C. in November-December, 1976, *USGS Open-File Report 2004-1343*.

Quigley, M., D. Clark, and M. Sandiford (2010), Late Cenozoic tectonic geomorphology of Australia, *Geological Society of London Special Publication*, *346*, 243-265.

Rastogi, B.K., S.K. Aggrawal, N. Rao, and P. Choudhury (2013a), Triggered/migrated seismicity due to the 2001 M (w)7.7 Bhuj earthquake, Western India, *Natural Hazards*, *65*(2), 1085-1107, doi:10.1007/s11069-011-0083-3.

Rastogi, B.K., S. Kumar, S.K. Aggrawal, K. Mohan, N. Rao, N.P. Rao, and G.C. Kothyari (2013b), The October 20, 2011 M-w 5.1 Talala earthquake in the stable continental region of India, *Natural Hazards*, *65*(2), 1197-1216, doi:10.1007/s11069-012-0226-1.

Reasenberg, P.A., and L.M. Jones (1989), Earthquake hazard after a mainshock in California, *Science*, *243*(4895), 1173-1176, doi:10.1126/science.243.4895.1173.

Reasenberg, P.A., and M.V. Matthews (1990), Response, *Science*, *247*, 343-345.

Robinson, M.S., S.M. Brylow, M. Tschimmel, D. Humm, S.J. Lawrence, P.C. Thomas, B.W. Denevi, E. Bowman-Cisneros, J. Zerr, M.A. Ravine, M.A. Caplinger, F.T. Ghaemi, J.A. Schaffner, M.C. Malin, P. Mahanti, A. Bartels,

J. Anderson, T.N. Tran, E.M. Eliason, A.S. McEwen, E. Turtle, B.L. Jolliff, and H. Hiesinger (2010), Lunar Reconnaissance Orbiter Camera (LROC) Instrument Overview, *Space Science Reviews*, *150*(1-4), 81-124, doi:10.1007/s11214-010-9634-2.

Roeloffs, E. (2012), Groundwater-level changes caused by the 2011 Mw 5.8 Mineral Virginia Earthquake, in *Geological Society of America Annual Meeting*, edited, Charlotte, NC.

Schmidtlein, M.C., J.M. Shafer, M. Berry, and S.L. Cutter (2011), Modeled earthquake losses and social vulnerability in Charleston, South Carolina, *Applied Geography*, *31*(1), 269-281, doi:doi:10.1016/j.apgeog.2010.06.001.

Scholten, F., J. Oberst, K.D. Matz, T. Roatsch, M. Wahlisch, E.J. Speyerer, and M.S. Robinson (2012), GLD100: The near-global lunar 100 m raster DTM from LROC WAC stereo image data, *Journal of Geophysical Research-Planets*, *117*, doi:10.1029/2011je003926.

Schulte, S.M., and W.D. Mooney (2005), An updated global earthquake catalogue for stable continental regions: reassessing the correlation with ancient rifts, *Geophysical Journal International*, *161*(3), 707-721, doi:10.1111/j.1365-246X.2005.02554.x.

Schultz, R.A. (2000), Localization of bedding plane slip and backthrust faults above blind thrust faults: Keys to wrinkle ridge structure, *J. Geophys. Res.*, *105*(E5), 12035-12052, doi:10.1029/1999JE001212.

Schultz, R.A., E. Hauber, S.A. Kattenhorn, C.H. Okubo, and T.R. Watters (2010), Interpretation and analysis of planetary structures, *Journal of Structural Geology*, *32*(6), 855-875, doi:10.1016/j.jsg.2009.09.005.

Schultz, R.A., C.H. Okubo, and S.J. Wilkins (2006), Displacement-length scaling relations for faults on the terrestrial planets, *Journal of Structural Geology*, *28*(12), 2182-2193, doi:10.1016/j.jsg.2006.03.034.

Schultz, R.A., and T.R. Watters (2001), Forward mechanical modeling of the Amenthes Rupes thrust fault on Mars, *Geophysical Research Letters*, *28*(24), 4659-4662, doi:10.1029/2001gl013468.

Sella, G.F., S. Stein, T.H. Dixon, M. Craymer, T.S. James, S. Mazzotti, and R.K. Dokka (2007), Observation of glacial isostatic adjustment in "stable" North America with GPS, *Geophysical Research Letters*, *34*(2), doi:10.1029/2006gl027081.

Shchervakov, R., D.L. Turcotte, and J.B. Rundle (2005), Aftershock statistics, Pure Applied Geophysics, 162(6-7), 1051-1076, doi: 10.1007/s00024-004-2661-8.

Shearer, P.M. (2009), *Introduction to Seismology*, Cambridge University Press, New York.

Sherrod, B.L., T.M. Brocher, C.S. Weaver, R.C. Bucknam, R.J. Blakely, H.M. Kelsey, A.R. Nelson, and R. Haugerud (2004), Holocene fault scarps near Tacoma, Washington, *Geology*, *32*(1), 9-12, doi:10.1130/G19914.

Simpson, D.W. (1986), Triggered Earthquakes, *Annual Review of Earth and Planetary Sciences*, *14*, 21-42, doi:10.1146/annurev.earth.14.1.21.

Smith, D.E., M.T. Zuber, G.B. Jackson, H. Riris, G.A. Neumann, X. Sun, J.F. McGarry, J.F. Cavanaugh, L.A. Ramos-Izquierdo, R. Zellar, M.H. Torrence, E. Mazarico, J. Connelly, A. Matuszeski, M. Ott, D.D. Rowlands, T. Zagwodzki, M.H. Torrence, R. Katz, I. Kleyner, C. Peters, P. Liiva, C. Coltharp, S. Schmidt, L. Ramsey, V.S. Scott, G. Unger, D.C. Krebs, A.D. Novo-Gradac, G.B. Shaw, and A.W. Yu (2010), The Lunar Orbiter Laser Altimeter Investigation on the Lunar Reconnaissance Orbiter Mission, *Space Science Reviews*, *150*(1-4), 209-241, doi:10.1007/s11214-009-9512-y.

Smith, D.E., M.T. Zuber, R.J. Phillips, S.C. Solomon, S.A. Hauck II, F.G. Lemoine, E. Mazarico, G.A. Neumann, S.J. Peale, J. Margot, C.L. Johnson, M.H. Torrence, M.E. Perry, D.D. Rowlands, S. Goossens, J.W. Head, and A.H. Taylor (2012), Gravity Field and Internal Structure of Mercury from MESSENGER, *Science*, *336*(6078), 214-217, doi:10.1126/science.1218809.

Solomon, S.C., and J.W. Head (1979), Vertical movement in mare basins - relation to mare emplacement, basin tectonics, and lunar thermal history, *Journal of Geophysical Research*, *84*(NB4), 1667-1682, doi:10.1029/JB084iB04p01667.

Solomon, S.C., and J.W. Head (1980), Lunar mascon basins: Lava filling, tectonics, and evolution of the lithosphere, *Reviews of Geophysics*, *18*(1), 107-141, doi:10.1029/RG018i001p00107.

Solomon, S.C., R.L. McNutt Jr., T.R. Watters, D.J. Lawrence, W.C. Feldman, J.W. Head, S.M. Krimigis, S.L. Murchie, R.J. Phillips, J.A. Slavin, and M.T. Zuber (2008), Return to Mercury: A global perspective on MESSENGER's first mercury flyby, *Science*, *321*(5885), 59-62, doi:10.1126/science.1159706.

Southworth, C.S., D.K. Brezinski, A.A. Drake, W. Burton, R.C. Orndorff, and A.J. Froelich (2002), Digital geologic map and database of the Fredrick 30' x 60' Quadrangle, Maryland, Virginia, and West Virginia, *Open-file Report 02-437*, *1.0*.

Southworth, C.S., D.K. Brezinski, A.A. Drake, W.C. Burton, R.C. Orndorff, A.J. Froelich, J.E. Reddy, D. Denenny, and D.L. Daniels (2007), Geologic Map of the Frederick 30' x 60' Quadrangle, Maryland, Virginia, and West Virginia.

Southworth, C.S., A.A. Drake, D.K. Brezinski, R.P. Wintsch, M.J. Kunk, C. Aleinikoff, W. Naeser, and N.D. Naeser (2006), Central Appalachian Piedmont and Blue Ridge tectonic transect, Potomac River corridor, in *Excursions in Geology and History: Field Trips in the Middle Atlantic States: Geological Society of America Field Guide 8*, edited by F. J. Pazzaglia, 135-167.

Spears, D.B., B.E. Owens, and C.M. Bailey (2004), *The Goochland-Chopawamsic Terrane Boundary, Central Virginia Piedmont: in Geology of the National Capital Region - Field Trip Guidebook, eds. Scott Southworth and William Burton*, *Curcular 1264*(Chapter 7), 223-245.

Stark, M.A., and S.D. Davis (1996), Remotely triggered microearthquakes at The Geysers geothermal field, California, *Geophysical Research Letters*, *23*(9), 945-948, doi:10.1029/96gl00011.

Stein, R.S. (1999), The role of stress transfer in earthquake occurrence, *Nature*, *402*(6762), 605-609, doi:10.1038/45144.

Stein, R.S., A.A. Barka, and J.H. Dieterich (1997), Progressive failure on the North Anatolian fault since 1939 by earthquake stress triggering, *Geophysical Journal International*, *128*(3), 594-604, doi:10.1111/j.1365-246X.1997.tb05321.x.

Stein, R.S., and G.C.P. King (1984), Seismic potential revealed by surface folding - 1983 Coalinga, California, Earthquake, *Science*, *224*(4651), 869-872, doi:10.1126/science.224.4651.869.

Stein, R.S., G.C.P. King, and J. Lin (1992), Change in Failure Stress on the Southern San Andreas Fault System Caused by the 1992 Magnitude = 7.4 Landers Earthquake, *Science*, *258*(5086), 1328-1332, doi:10.1126/science.258.5086.1328.

Stein, R.S., G.C.P. King, and J.B. Rundle (1988), The growth of geological structures by repeated earthquakes. 2. Field examples of continental dip-slip faults, *Journal of Geophysical Research-Solid Earth and Planets*, *93*(B11), 13319-13331, doi:10.1029/JB093iB11p13319.

Stein, S. (2010), *Disaster deferred: How new science is changing our view of earthquakes hazards in the Midwest*, 282 pp., Columbia University Press, New York, NY.

Stein, S., S. Cloetingh, N.H. Sleep, and R. Wortel (1989), Passive margin earthuqakes, stresses, and rheology, in *Earthquakes at North-Atlantic Passive Margin: Neotectonics and postglacial rebound*, edited by S. Gregersen and P. W. Bashan, pp. 231-259, Kluwer Academic Publishers.

Stein, S., R.J. Geller, and M. Liu (2011), Bad Assumptions or Bad Luck: Why Earthquake Hazard Maps Need Objective Testing, *SRL Opinion*, *2011*, doi:10.1785/gssrl.82.5.623.

Stein, S., and M. Liu (2009), Long aftershock sequences within continents and implications for earthquake hazard assessment, *Nature*, *462*(7269), 87-89, doi:10.1038/nature08502.

Stein, S., and E. Okal (2011), The size of the 2011 Tohoku earthquake needn't have been a surprise, *Eos*, *92*, 227–228.

Stein, S., N.H. Sleep, R.J. Geller, S. Wang, Chen, and G.C. Kroeger (1979), Earthquakes along the passive margin of eastern Canada, *Geophysical Research Letters*, *6*(7), 537-540, doi:doi:10.1029/GL006i007p00537.

Stewart, I.S., J. Sauber, and J. Rose (2000), Glacio-seismotectonics: ice sheets, crustal deformation and seismicity, *Quaternary Science Reviews*, *19*(14-15), 1367-1389, doi:10.1016/s0277-3791(00)00094-9.

Strom, R.G. (1970), Lunar mare ridges, rings, and volcanic ring complexes, *Transactions-American Geophysical Union*, *51*(11), 773-&.

Strom, R.G., N.J. Trask, and J.E. Guest (1975), Tectonism and Volcanism on Mercury, *J. Geophys. Res.*, *80*(17), 2478-2507, doi:10.1029/JB080i017p02478.

Suppe, J., and C. Connors (1992), Critial taper erdge mechanics of fold-and-thrust belts on Venus - initial results from MAGELLAN, *Journal of Geophysical Research-Planets*, *97*(E8), 13545-13561.

Taboada, A., J.C. Bousquet, and H. Philip (1993), Coseismic elastic models of folds above blind thrusts in the Betic Cordilleras (Spain) and evaluation of seismic hazard, *Tectonophysics*, *220*(1-4), 223-241, doi:10.1016/0040-1951(93)90233-a.

Talwani, P., and J. Cox (1985), Paleoseismic evidence for recurrence of earthquakes near Charleston, South-Carolina, *Science*, *229*, 1412-1416, doi:10.1126/science.229.4711.379.

Tanaka, S. (2010), Tidal triggering of earthquakes precursory to the recent Sumatra megathrust earthquakes of 26 December 2004 (Mw 9.0), 28 March 2005 (Mw 8.6), and 12 September 2007 (Mw 8.5), *Geophysical Research Letters*, *37*(2), L02301, doi:10.1029/2009GL041581.

Tanaka, S. (2012), Tidal triggering of earthquakes prior to the 2011 Tohoku-Oki earthquake (Mw 9.1), *Geophysical Research Letters*, *39*, L00G26, doi:10.1029/2012GL051179.

Tanaka, S., M. Ohtake, and H. Sato (2004), Tidal triggering of earthquakes in Japan related to the regional tectonic stress, *Earth Planets Space*, *56*, 511-515.

Tape, C., M. West, V. Silwal, and N. Ruppert (2013), Earthquake nucleation and triggering on an optimally oriented fault, *Earth and Planetary Science Letters*, *363*(0), 231-241, doi:http://dx.doi.org/10.1016/j.epsl.2012.11.060.

Thomas, A.M., R.M. Nadeau, and R. Burgmann (2009), Tremor-tide correlations and near-lithostatic pore pressure on the deep San Andreas fault, *Nature*, *462*(24), doi:10.1038/nature08654.

Toda, S., R.S. Stein, P.A. Reasenberg, J.H. Dieterich, and A. Yoshida (1998), Stress transferred by the 1995 M_w = 6.9 Kobe, Japan, shock: Effect on aftershocks and future earthquake probabilities, *Journal of Geophysical Research-Solid Earth*, *103*(B10), 24543-24565, doi:10.1029/98jb00765.

Toda, S., R.S. Stein, K. Richards-Dinger, and S.B. Bozkurt (2005), Forecasting the evolution of seismicity in southern California: Animations built on earthquake stress transfer, *Journal of Geophysical Research*, *110*(B5), B05S16, doi:10.1029/2004JB003415, 200.

Tuttle, M.P., and R. Hartleb (2012), Appendix E. Central and Eastern U.S.paleoliquefaction database, uncertainties associated with paleoliquefaction data, and guidance for seismic source characterization, in

The Central and Eastern U.S. Seismic Source Characterization for Nuclear Facilities, Technical Report, EPRI, Palo Alto, CA, U.S. DOE, and U.S. NRC, 135 p. plus database, http://www.ceus-ssc.com/. edited.

USGS (2013a), Groundwater-Level Response to Virginia Earthquake, August 23, 2011, edited, http://water.usgs.gov/ogw/eq/VAquake2011.html.

USGS (2013b), Mining Seismicity Source Regions, edited, http://earthquake.usgs.gov/earthquakes/eqarchives/mineblast/sources.php.

Utsu, T.,Y. Ogata, and R.S. Matsuura (1995), The centenary of the Omori formula for a decay law of aftershock activity, *Journal of Physics of the Earth*, *43*(1), 1-33.

van der Elst, N.J., and E.E. Brodsky (2010), Connecting near-field and far-field earthquake triggering to dynamic strain, *Journal of Geophysical Research-Solid Earth*, *115*, doi:10.1029/2009jb006681.

Viegas, G. (2012), Source parameters of the 16 July 2010 Mw3.4 Germantown, Maryland, Earthquake, *Seismological Research Letters*, *83*(5), doi:10.1785/0220110056.

Virginia Department of Mines (2003), Digital representation of the 1993 Geologic Map of Virginia: Virginia Department of Mines, Minerals, and Energy, Publication 174, scale 1:500,000, CD-ROM. Virginia Division of Mineral Resources, 1993, Geologic map of Virginia: Virginia Division of Mineral Resources, scale 1:500,000.

Wang, J. (1994), On the correlation of observed Gutenberg-Richter's b Value and Omori's p value for Aftershocks, Bulletin of the Seismological Society of America, 84(6), 2008-2011.

Wang, Z. (2007), Seismic hazard and risk assessment in the intraplate environment: The New Madrid seismic zone of the central United States, *Geological Society of America Special Papers*, *425*, 363-374, doi:10.1130/2007.2425(24).

Watters, T.R. (1988), Wrinkle Ridge Assemblages on the Terrestrial Planets, *J. Geophys. Res.*, *93*(B9), 10236-10254, doi:10.1029/JB093iB09p10236.

Watters, T.R. (1991), Origin of periodically spaced wrinkle ridges on the Tharsis Plateau of Mars, *Journal of Geophysical Research-Planets*, *96*(E1), 15599-15616, doi:10.1029/91je01402.

Watters, T.R., M.S. Robinson, and A. C. Cook (1998), Topography of lobate scarps on Mercury: New constraints on the planet's contraction, *Geology*, *26*(11), 991-994, doi:10.1130/0091-7613(1998)026<0991:tolsom>2.3.co;2.

Watters, T.R., R.A. Schultz, M. S. Robinson, and A. C. Cook (2002), The mechanical and thermal structure of Mercury's early lithosphere, *Geophysical Research Letters*, *29*(11), 4, doi:10.1029/2001gl014308.

Watters, T.R. (2004), Elastic dislocation modeling of wrinkle ridges on Mars, *Icarus*, *171*(2), 284-294, doi:10.1016/j.icarus.2004.05.024.

Watters, T.R., M.S. Robinson, C.R. Bina, and P.D. Spudis (2004), Thrust faults and the global contraction of Mercury, *Geophysical Research Letters*, *31*(4), 5, doi:10.1029/2003gl019171.

Watters, T.R., F. Nimmo, and M.S. Robinson (2005), Extensional troughs in the Caloris basin of Mercury: Evidence of lateral crustal flow, *Geology*, *33*(8), 669-672, doi:10.1130/g21678.

Watters, T.R., J.W. Head, S.C. Solomon, M.S. Robinson, C.R. Chapman, B.W. Denevi, C.I. Fassett, S.L. Murchie, and R.G. Strom (2009a), Evolution of the Rembrandt Impact Basin on Mercury, *Science*, *324*(5927), 618-621, doi:10.1126/science.1172109.

Watters, T.R., S.L. Murchie, M.S. Robinson, S.C. Solomon, B.W. Denevi, S.L. Andre, and J.W. Head (2009b), Emplacement and tectonic deformation of smooth plains in the Caloris basin, Mercury, *Earth and Planetary Science Letters*, *285*(3-4), 309-319, doi:10.1016/j.epsl.2009.03.040.

Watters, T.R., S.C. Solomon, M.S. Robinson, J.W. Head, S.L. Andre, S.A. Hauck, and S.L. Murchie (2009c), The tectonics of Mercury: The view after MESSENGER'S first flyby, *Earth and Planetary Science Letters*, *285*(3-4), 283-296, doi:10.1016/j.epsl.2009.01.025.

Watters, T., and C. Johnston (2010), Lunar Tectonics, in *Planetary Tectonic*, edited by T. R. Watters and R. A. Schultz, pp. 121-182, Cambridge University Press, New York, NY.

Watters, T.R., and F. Nimmo (2010), The tectonics of Mercury, in *Planetary Tectonics*, edited by T.R. Watters and R. A. Schultz, pp. 15-80, Cambridge University Press, New York.

Watters, T.R., M.S. Robinson, R.A. Beyer, M.E. Banks, J.F. Bell III, M.E. Pritchard, H. Hiesinger, C.H. van der Bogert, P.C. Thomas, E.P. Turtle, and N.R. Williams (2010), Evidence of Recent Thrust Faulting on the Moon Revealed by the Lunar Reconnaissance Orbiter Camera, *Science*, *329*(5994), 936-940, doi:10.1126/science.1189590.

Watters, T.R., and R.A. Schultz (2010), Planetary tectonics: introduction, in *Planetary Tectonics*, edited by T. R. Watters and R. A. Schultz, pp. 15-80, Cambridge University Press, New York.

Watters, T.R., P.K. Byrne, C. Klimczak, A.C. Enns, M.E. Banks, L.S. Walsh, C.M. Ernst, M.S. Robinson, J.J. Gillis-Davis, S.C. Solomon, R.S. Strom, and K. Gwinner (2011a), The Tectonics of Mercury: The View from Orbit, in *American Geophysical Union*, edited.

Watters, T.R., P.C. Thomas, and M.S. Robinson (2011b), Thrust faults and the near-surface strength of asteroid 433 Eros, *Geophysical Research Letters*, *38*, 5, doi:10.1029/2010gl045302.

Watters, T.R., S.C. Solomon, C. Klimczak, A.M. Freed, J.W. Head, C.M. Ernst, D.M. Blair, T.A. Goudge, and P.K. Byrne (2012a), Extension and contraction

within volcanically buried impact craters and basins on Mercury, *Geology*, *40*(12), 1123-1126.

Watters, T.R., M.S. Robinson, M.E. Banks, T. Tran, and B. Denevi (2012b), Recent extensional tectonics on the Moon revealed by the Lunar Reconnaissance Orbiter Camera, *Nature Geoscience*, doi:10.1038/ngeo1387.

Watters, T.R., S.C. Solomon, C. Klimczak, M.M. Selvans, L.S. Walsh, M.E. Banks, P.K. Byrne, B.W. Denevi, C.M. Ernst, S.L. Murchie, J. Oberst, F. Preusker, S.A. Hauck, II, M.T. Zuber, and R.J. Phillips (2013), Distribution of prominent lobate scarps on Mercury: Contribution to global radial contraction, *Lunar and Planetary Science Conference*, Houston, TX, Abstract #2213.

Weems, R.E., and P.E. Olsen (1997), Synthesis and revision of groups within the Newark Supergroup, eastern North America, *Geological Society of America Bulletin*, *109*(2), 195-209.

Wells, D. L., and K.J. Coppersmith (1994), New empirical relationships among magnitude, rupture length, rupture width, rupture area, and surface displacement, *Bulletin of the Seismological Society of America*, *84*(4), 974-1002.

Wheeler, R.L. (2006), Quaternary tectonic faulting in the Eastern United States, *Engineering Geology*, *82*(3), 165-186, doi:10.1016/j.enggeo.2005.10.005.

Wiemer, S. (2001), A software package to analyze seismicity: ZMAP, *Seismological Research Letters*, *72*(2), 374–383.

Wiemer, S., M. Gerstenberger, and E. Hauksson (2002), Properties of the aftershock sequence of the 1999 Mw 7.1 Hector Mine Earthquake: Implications of aftershock hazard, 92(4), 1227-1240.

Wilhelms, D.E. (1987), *The Geologic History of the Moon*, U.S. Government Printing Office, Washington, DC.

Wilhelms, D.E., and J.F. McCauley (1971), Geologic map of the nearside of the Moon.

Williams, H. (1995), *Geology of the Appalachian-Caledonian Orogen in Canada and Greenland*.

Williams, N.R., J.F.I. Bell, T.R. Watters, M.E. Banks, and M.S. Robinson (2012), Tectonic mapping of mare frigoris using lunar reconnaissance orbiter camera images, paper presented at 43rd Lunar and Planetary Science Conference.

Wilson, J.T. (1965), A new class of faults and their beiring on continental drift, *Nature*, *207*(4995), 343, doi:10.1038/207343a0.

Wolin, E., S. Stein, F. Pazzaglia, A. Meltzer, A. Kafka, and C. Berti (2012), Mineral, Virginia, earthquake illustrates seismicity of a passive-aggressive margin, *Geophysical Research Letters*, *39*(2), L02305, doi:10.1029/2011GL050310.

Wu, P. (1997), Effect of viscosity structure on fault potential and stress orientations in eastern Canada, *Geophysical Journal International*, *130*(2), 365-382, doi:10.1111/j.1365-246X.1997.tb05653.x.

Ziv, A., and A.M. Rubin (2000), Static stress transfer and earthquake triggering: No lower threshold in sight?, *Journal of Geophysical Research*, *105*(B6), 13631-13642, doi:10.1029/2000JB900081.

Zoback, M.L. (1992), Stress Field Constraints on Intraplate Seismicity in Eastern North America, *J. Geophys. Res.*, *97*(B8), 11761-11782.

Zuber, M.T., D.E. Smith, R.J. Phillips, S.C. Solomon, G.A. Neumann, S.A. Hauck, II, S.J. Peale, O.S. Barnouin, J.W. Head, C.L. Johnson, F.G. Lemoine, E. Mazarico, X. Sun, M.H. Torrence, A.M. Freed, C. Klimczak, J. Margot, J. Oberst, M.E. Perry, R.L. McNutt, Jr., J.A. Balcerski, N. Michel, M. Talpe, and D. Yang (2012), Topography of the Northern Hemisphere of Mercury from MESSENGER Laser Altimetry, *Science*, *336*(6078), 217-220, doi:10.1126/science.1218805.

Zuber, M. T., D.E. Smith, M.M. Watkins, S.W. Asmar, A.S. Konopliv, F.G. Lemoine, H.J. Melosh, G.A.Neumann, R.J. Phillips, S.C. Solomon, M.A. Wieczorek, J.G. Williams, S.J. Goossens, G. Kruizinga, E. Mazarico, R.S. Park, D.N. Yuan (2013), Gravity Field of the Moon from the Gravity Recovery and Interior Laboratory (GRAIL) Mission, *Science*, *339*(6120), 668-671, doi:10.1126/science.1231507.